PB95-269346

REPORT NO.
UCB/EERC-95/02
JUNE 1995

EARTHQUAKE ENGINEERING RESEARCH CENTER

THE ATTENUATION OF STRONG GROUND MOTION DISPLACEMENTS

by

NICHOLAS J. GREGOR

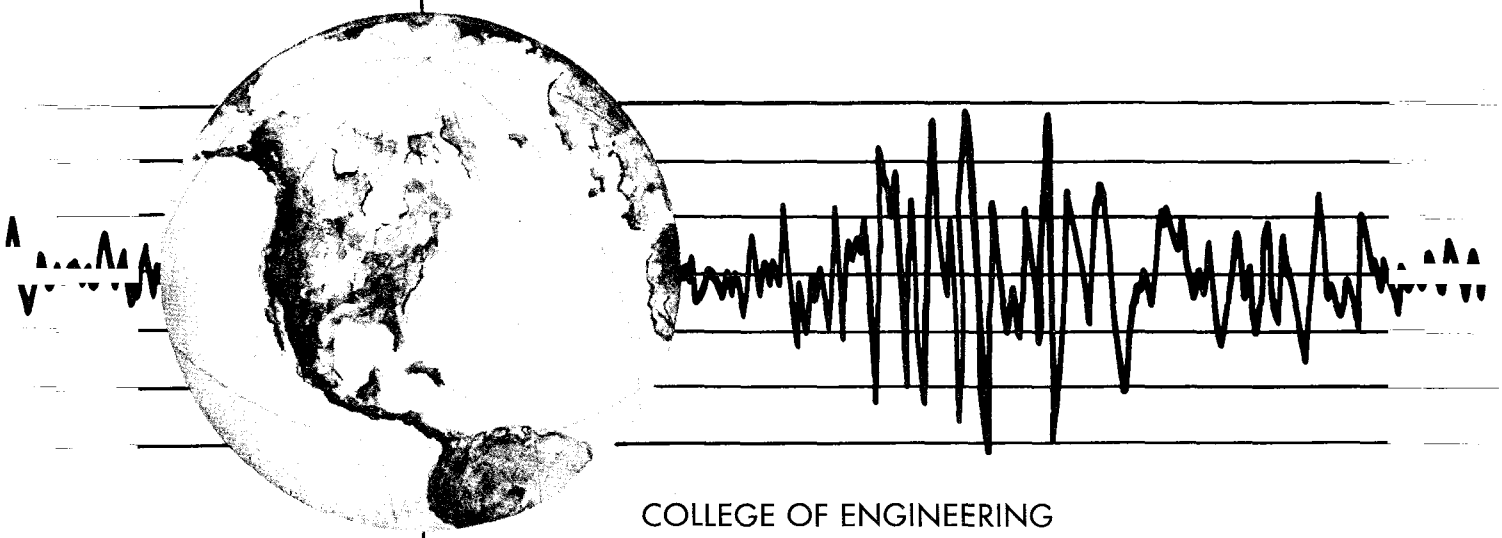

COLLEGE OF ENGINEERING

UNIVERSITY OF CALIFORNIA AT BERKELEY

For sale by the National Technical Information Service, U.S. Department of Commerce, Springfield, Virginia 22161.

See back of report for up to date listing of EERC reports.

DISCLAIMER

The Attenuation of Strong Ground Motion Displacements

by

Nicholas John Gregor

Preface

by

Bruce A. Bolt

Report No. UCB/EERC - 95/02

Earthquake Engineering Research Center

University of California at Berkeley

Berkeley, California

June 1995

Preface

This study is the sixth in a series concerned with the interpretation and analysis of seismograms of strong ground motion recorded by accelerometers. The first five were based on measurements from arrays, and dealt with the spatial variability of the ground motions, and the estimation of inputs for multi-supported structures. Such studies flourished after the large SMART1 data set became available after 1980.

The SMART1 array was installed in Taiwan in September 1980 and through June 1991 recorded strong ground motions (with some accelerations exceeding 0.3 g) from over 55 local earthquakes. The first two reports in the series are: UCB/EERC-82/18 by B. A. Bolt, C. H. Loh, J. Penzien, Y. B. Tsai, and Y. T. Yeh and UCB/EERC-85/82 by N. A. Abrahamson. In 1988, R. B. Darragh published "Analysis of Near Source Waves: Separation of Wave Types Using Strong Motion Array Recordings" in Report UCB/EERC-88/08. A research summary through 1986 was published in "Earthquake Spectra", *3*, 263-287, 1987 by N. A. Abrahamson, B. A. Bolt, R. B. Darragh, J. Penzien, and Y. B. Tsai. Two additional recent reports are: UCB/EERC-89/06 by Hong Hao, entitled "Effects of Spatial Variation of Ground Motions on Large Multiply-Supported Structures" and UCB/EERC-91/07 by S. J. Chiou, entitled "Estimation of Seismic Source Processes Using Strong Motion Array Data." A further report, giving details of the application of attenuation and coherency relations for large multi-supported structures has been published as, UCB/EERC-93/12 by B. A. Bolt and N. J. Gregor, entitled "Synthesized Strong Ground Motions for the Seismic Condition Assessment of the Eastern Portion of the San Francisco Bay Bridge."

The main thrust of the present research has been directed to the measurement of seismic ground displacements from California earthquakes, selected from those with published maps of the distribution of slip on the causative fault plane. The aim has been

to understand more clearly the variation of the maximum wave displacement amplitude, and its attenuation with distance, with engineering applications in mind.

Gregor has made a comprehensive analysis of 12 California earthquakes with strong ground motion recordings and published fault-slip distributions. Seismological interpretation criteria were used that applied seismic wave theory before statistical analysis. The theory is needed for selection of compatible ground wave displacements because of the mixing of body S waves with Love and Rayleigh surface wave trains. Seismic wave response of alluvial basins can alter dramatically the amplitudes and durations of the long period surface wave coda in a displacement record. Also, because peak displacements tend to have an order of magnitude longer period than peak ground accelerations, it is necessary to relate the displacement amplitudes and phases to the slip-history on the fault plane, rather than to the earthquake focus or some arbitrary measure, such as the nearest horizontal distance to the causative fault trace.

In this work, the attenuation distance was taken between the instrument and the point of largest slip known from published source mechanism inversions using seismograms. It is usually the case that the largest displacement amplitudes, recorded on strong ground motion instruments, occur in the predominately S wave portion of the record. These displacements are the consequence of the elastic rebound along the rupturing fault due to the work done in the dislocation by an equivalent force couple. The ensuing SH shear pulses travel outward with maximum amplitudes normal and parallel to the moving dislocation. Directivity focusing of the moving source produces further significant amplitude and frequency modulation. Evidence for the latter effect was found in this study.

The selected earthquakes were classified into two types: predominately reverse dip-slip and strike-slip mechanics. The sites of recording stations were classified as either rock or soil.

This research program has been supported by National Science Foundation (U. S.) grant BCS-93-03187. Essential financial support has been forthcoming from a grant from the California Division of Transportation (Professor H. Astaneh, Principal Investigator). This work was carried out at the Seismographic Station, U. C. Berkeley.

B. A. Bolt

Abstract

The attenuation of the maximum shear wave for strong ground displacements for large earthquakes ($5.4 < M_W < 7.2$) in California was studied from a seismological viewpoint and regression curves of attenuation were statistically estimated. The curves were computed for two different geologic classifications of the recording location (rock or soil), and two different fault mechanisms of the seismic source (strike-slip or reverse-fault). The sample consisted of eight strike-slip and four reverse-fault mechanism earthquakes with 238 soil and 100 rock measurements.

The peak ground-motion displacements were measured from the S body-wave portion of the seismograms (typical frequencies of 0.2 - 1 Hz) after seismic wave-type discrimination. The peak displacement from the surface wave energy was not considered in this analysis. A defined attenuation distance, H_{slip}, was used as the distance from the recording station to the location on the fault plane of largest slip. Two sub-samples were formed of the SH (transverse) and SV (vertical) measurements. A total of eight attenuation relations, based on source mechanism, site geologic condition, and horizontal (SH) versus vertical (SV) ground motion, were statistically estimated.

For example, the SH wave attenuation curve for a reverse-fault mechanism rock site is,

$$\mathrm{Log}_{10}(D) = -3.44 + 0.92M_W - 1.51\,\mathrm{Log}_{10}(H_{slip}), \quad \sigma_T = 0.31 ,$$

where D is the peak ground displacement in cm and σ_T is the standard deviation for the sample. The resulting mean peak displacement at H_{slip} = 10 km for a M_W = 7.0 earthquake is 31 cm.

The effect of rupture directivity on the observed peak displacements causes the greatest variation in the sample, with the largest dispersion for observations from stations which are located close to and along the strike of the propagating seismic rupture. These deviations can be predicted from seismological wave theory, as well as the scatter due to the corresponding radiation patterns. Finally, in a few cases, the individual site response of a station was observed to cause deviations from the mean greater than one standard deviation.

The set of ground-displacement attenuation curves predict greater amplitudes at sites classified as soil than rock sites. SH motion is larger than SV motion for both types of seismic source mechanisms. Finally, strike-slip attenuation relationships predict higher peak displacements for $H_{slip} > 30$ km than comparable curves for reverse-fault mechanism earthquakes.

Acknowledgments

Throughout my stay at Berkeley I have had the privilege of working under the tutelage of Professor B. A. Bolt. I also owe a debt of gratitude to Professor L. R. Johnson for reviewing my research and to Professor H. Astaneh for his interest in my research.

The comments, discussions, and computer programs provided by Dr. N. Abrahamson were much appreciated, as was the provision of digital data for a series of earthquakes by Dr. D. Wald.

I would also like to thank the faculty and staff at the Seismographic Station: Professor B. Romanowicz, Dr. R. A. Uhrhammer, R. McKenzie, D. Neuhauser and C. Paffenbarger.

The Attenuation of Strong Ground Motion Displacements

Table of Contents

1. Introduction

1.1. Importance of Peak Strong Ground Motion Displacement

The attenuation of seismic waves with large amplitudes is of fundamental importance in both seismology and earthquake engineering. Numerous empirical attenuation relations for peak strong ground motion parameters (particularly peak ground acceleration, pga) have been estimated in the last 20 years.

Much more recently, attenuation curves of peak strong-motion acceleration as a function of frequency have also been computed (for a review of attenuation models see, Joyner and Boore, 1988; Iai and Matsunaga, 1993). Such a dependence is needed for quantitative structural dynamic analysis (e.g., see Miranda, 1993). This variation of frequency spectral attenuation has been estimated based on the numerical transformation of recorded strong ground motion time histories to spectral acceleration and to pseudovelocity spectral response (see section 2.3). Many of these attenuation studies have included recordings of strong ground motion from worldwide earthquakes, while some are restricted to a specified seismically active region.

Comparable studies of the variation of maximum ground displacement as a function of distance and frequency are much fewer, although individual values for maximum ground displacements, measured observationally by regular seismographs and field strong-motion accelerometers, have been published.

Among the various strong seismic ground motion parameters that have been defined, peak ground acceleration, velocity, and displacement are key markers in seismic response studies of major engineered structures. Recently, the special importance of peak ground displacement has been stressed in performance and design considerations of certain critical structures, such as a base-isolated building

(e.g., see Buckle and Mayes, 1990; Perry et al., 1993) and multi-supported bridges (e.g., see Singh and Tabatabaie, 1991; Miranda, 1993; Bolt and Gregor, 1993; Kawashima and Hasegawa, 1994).

The use of peak ground displacement in seismic hazard assessment was first proposed by Newmark and Hall (1969). In their methodology, estimates of engineering design spectra for critical structures, such as nuclear power plants, were based on the three peak ground motion parameters - acceleration, velocity, and displacement. The design spectrum was then scaled, within certain frequency bands, by previously determined amplification values, for the various degrees of critical damping. In general, the peak ground-motion displacement values controlled the response spectrum for frequencies less than about 0.4 Hz.

Recently, there has been a greater demand from structural engineers for attenuation curves for the expected peak displacement ground motion to be used in a site specific analysis for the base isolation of a structure (Buckle and Mayes, 1990). Engineering considerations demonstrate that the longer period velocity and displacement ground motion (frequencies less than about 1 Hz), can be more critical in the vulnerability assessment of a large engineered structure than the higher frequency ground acceleration. (The theory for structural response of base-isolated structures to input seismic motion is outlined in Kelly (1990)).

The corresponding statistical regression of attenuation relations for peak ground displacement has not progressed for a number of seismological, instrumentation, and engineering reasons. In a full seismological description, maximum displacement values on a seismogram describe amplitudes of either the P and S body waves, which usually arrive during the time window of largest ground motions, or surface waves, which with their lower propagation velocities, arrive later in the time histories. Source extensions, lateral refraction, and scattering cause some mixing of these wave types throughout the wave train with different

properties in each record. For this reason, discrimination of the absolute peak values from consistent wave types requires application of criteria from seismological theory and observational experience.

On the instrumental side, recent advances in the digitization and processing of strong ground-motion time histories has increased the bandwidth of strong ground-motion records. Because displacement records are derived from double integration of the accelerograms and filter and base-line adjustment considerations are critical, these advances have improved the reliability of peak displacement measurements. Finally, as mentioned above, the need has arisen in the engineering community for peak displacement attenuation curves for use in seismic hazard assessments.

The statistical study of the attenuation properties of strong motion displacement has been significantly enhanced in the last five years by the acquisition of many strong ground motion records from large crustal earthquakes in California recorded at close to moderate distances from the fault source. Specifically, the October 17, 1989 Loma Prieta earthquake, M_W = 7.0, the June 28, 1992 Landers earthquake, M_W = 7.2, and the January 17, 1994 Northridge earthquake, M_W = 6.7 contributed an increase of about 40% to the collection of strong ground motion accelerograms which can be used for the regression of attenuation curves for peak strong ground motion displacement.

This work gives a seismological discussion of the variability of the maximum amplitude of ground displacement in strong ground shaking. As a substantial component of this analysis it describes the estimation of empirical relations which define the attenuation of peak ground displacement from 12 large crustal earthquakes in California. The estimation involves a quantitative discussion of the observational difficulties (see section 1.2), the theoretical seismological interpretations of the measured seismic waves (see chapter 3), the relevant

instrumentation processing (see section 4.15), and geological uncertainties in the estimation procedure and robustness of the results (see chapter 5).

The results are in the form of empirical attenuation equations which summarize the sample of measurements. These equations can be used in seismic vulnerability assessments to estimate the mean peak ground displacement that may occur at a given site of interest in a large earthquake of given source mechanism. The attenuation equations are computed for two separate site classifications, soil and rock, as well as for two types of earthquake faulting, strike-slip and reverse. Inferences are drawn concerning the significance of computed differences between the mean values of pairs of the eight cases, and a seismological explanation is advanced for outlying values.

1.2 Seismological Considerations

Seismological considerations are basic to the selection of peak ground displacement for the development of empirical attenuation relations. Maximum amplitudes on seismograms can be caused by either the P and S body-wave energy, or the surface-wave energy, or in the near field a mixture of both. Many empirical attenuation relations for peak ground acceleration (see Iai and Matsunaga, 1993) have been estimated without regard to the type of seismic wave attributable to the peak. The peak values of ground acceleration usually arrive during the direct S wave train and subsequent S wave coda but seismic wave types are mixed. In the same way, the peak ground displacements often are a superposition of S and disperse surface wave components traveling along extended crustal paths, and these waves are significantly modified by their propagation through complex geologic structures and alluvial basins.

As an example, the east-west components of ground acceleration, velocity, and displacement are shown in Figure 1.1 from the 1994 Northridge earthquake recorded at the Obregon Park site in the Los Angeles basin (Darragh et al., 1994b). The epicentral distance for the site is about 38 km (see Figure 4.18). The peak acceleration, velocity, and displacement values are marked on the time histories. As is clear on the records, the peak acceleration and velocity amplitudes occur in the body wave portion of the records at an arrival time of about 10 seconds. However, the largest peak ground displacement occurs in the seismic surface wave train at about 23 seconds. In the present study, travel-time and wave properties are used to discriminate between the predominate S wave and surface wave (Love and Rayleigh waves) portion of the records. Regression results for the sample of S wave maxima only are presented so that the peak ground displacement value of approximately 2.5 cm, which occurs during the seismic S body wave train, would be selected in the results given here.

Even when a correct interpretation of wave type is made, there is a basic difficulty in trying to estimate an empirical attenuation relation based on the different types of waves. The attenuation of surface waves is proportional to the inverse of the square root of the distance from the source while the attenuation of S waves is proportional to the inverse of the distance from the source (see section 3.1 and 3.2). This kinematic constraint entails that peak ground-displacement values from S body-wave pulses and from surface waves should not be mixed in the observational analysis if a mechanical interpretation of the attenuation properties in terms of geometrical spreading and intrinsic viscous damping is to be made. The different geometrical proportionality factors lead to surface waves being, on average, more pronounced at larger distances from the source (e.g., distances of the order of 10^2 km) and for sites located on deep alluvium or in sedimentary basins. The mixing of measurements from different wave types is minimized in this study by

first analyzing each displacement time history in terms of seismic wave theory and subsequently selecting the maximum peak ground-displacement value from the S body wave portion of the recorded ground motion. The empirical attenuation curves are then regressed separately for the transverse (SH) and vertical (SV) components of motion.

Throughout the studies of the variation of wave amplitude with distance, a serious problem in the regression process has been the choice of an appropriate measure of source-to-station distance. Indeed the definition of distance used in independently published attenuation relations can be quite different. In recent acceleration attenuation relationships (see section 2.1), the distances used are either the closest distance from the station to the projection of the slipped fault plane, or the slant distance to the actual fault plane (see Joyner and Boore, 1988, for a review of different distance definitions used in attenuation models).

The usual wave frequency of peak ground acceleration is above 5 Hz while for peak ground displacement it is below 1 Hz. The corresponding characteristic wavelengths between acceleration and displacement differ from short (600 meters) to long (3000 meters). Consequently, the largest arriving S wave displacement is predominately generated by a much larger patch on the slipping fault plane. Therefore, an essential aim of this study is to link the basic distance variation with the appropriate wave generation process for S displacement pulses. The adopted distance, H_{slip}, is defined as: the *distance between the source and the place on the fault plane of largest seismic slip* (see Figure 4.2).

This independent variable H_{slip} is used in the estimation of all the following empirical attenuation relations for peak ground displacement. Further, the horizontal components of motion will be rotated to the transverse (SH) and radial component relative to this hypocenter of largest slip on the fault plane for the measurement of the largest peak displacement on the SH component. As a practical

application, the graphs of the mean attenuation curves will be plotted versus the epicentral H_{slip} distance as defined: the distance on the ground surface to the epicentral location of largest slip on the fault plane. The curves are presented in this fashion for the application in seismic vulnerability assessment studies where the horizontal distance from the structure to the fault in question is the key distance parameter.

1.3 Engineering Demands

Seismic retrofitting of large structures, such as bridges, now requires the consideration of ground displacement in seismic hazard assessments (Singh and Tabatabaie, 1991; Miranda, 1993). A recent illustration is the seismic hazard assessment for the eastern span of the San Francisco Bay bridge (Bolt and Gregor, 1993). Synthetic time histories were generated for acceleration, velocity, and displacement ground motions. The peak acceleration and velocity values were determined from previously published attenuation curves and the displacement values were determined from a simple regression of peak displacement data from the 1989 Loma Prieta and the 1992 Landers earthquakes. These ground motion parameters were used as input parameters in the development of the synthetic time histories. Similar use of displacement time histories and ground wave displacement scaling of response spectra are needed for many base-isolated structures.

Base-isolated buildings are becoming more common in the regions of California that are susceptible to large earthquakes (e.g., Los Angeles and the San Francisco Bay region). A review of world-wide base-isolated structures is presented in Buckle and Mayes (1990). The seminal question for the designing engineers is the amount of spacing, D, to allocate between the seismic dampers and the stops (usually concrete walls) at the foundation of the building (see Figure 1.2). Damage

can occur to the building if the spacing is too small and pounding develops between the isolators and the building stops. The effect of pounding can lead to a peak ground motion which is greater than what would be experienced if there were no base isolators for the structure (Maison and Ventura, 1992). Because of the decision on the amount of spacing to include in the design (Buckle, 1988), engineers need estimates of the peak ground displacement from large earthquakes located close to the structure. Currently the largest design spacing in practice is approximately 60 cm (Heaton et al., 1995). However, in a case study for a hypothetical M_W=7.0 earthquake underneath downtown Los Angeles (Heaton et al., 1995), pounding between the isolators and the stops still occurred for a spacing of 60 cm. The statistical estimation of peak ground-motion attenuation curves from this research will assist in engineering studies of this type of structure.

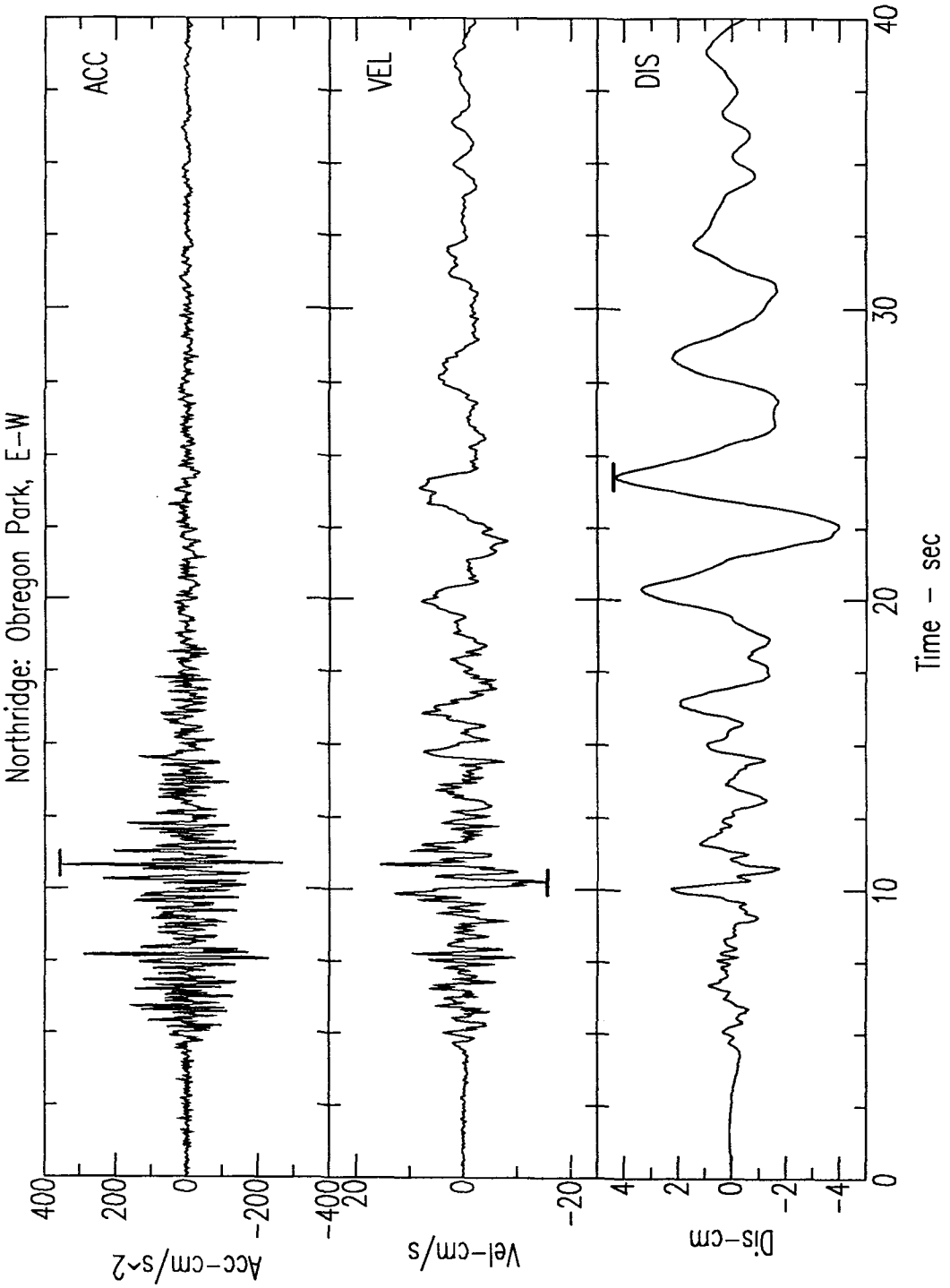

Figure 1.1 Peak strong ground motion acceleration, velocity, and displacement seismograms recorded at the Obregon Park station from the 1994 Northridge earthquake. The East-West component of motion is shown with the absolute peak acceleration, velocity, and displacement values marked.

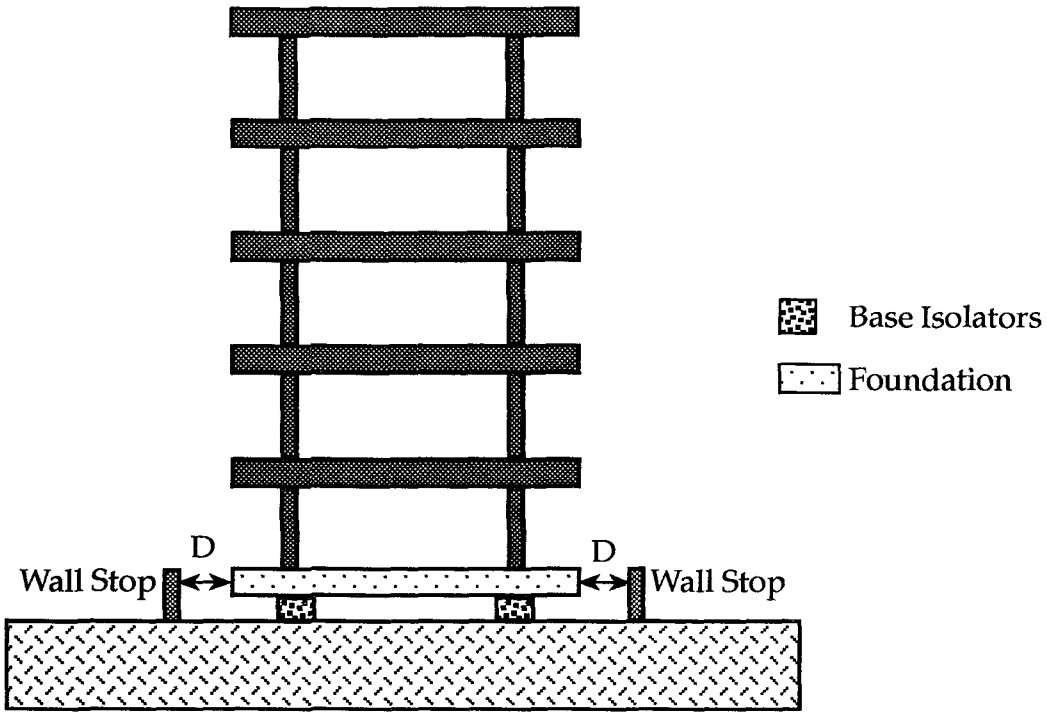

Figure 1.2 Schematic diagram of a base-isolated building.

2. Review of Attenuation Relationships

2.1 Acceleration Attenuation Relations

A central part of the present analysis is the construction of empirical peak ground displacement attenuation curves. The recorded accelerograms that are the basis of such relations have been greatly enhanced in the last five years because of instrumented measurements of seismic waves obtained from the following large earthquakes in California: 1989 Loma Prieta (M_W = 7.0), 1992 Petrolia (M_W = 7.2), 1992 Petrolia Aftershock (M_W = 7.0), 1992 Joshua Tree (M_W = 6.2), 1992 Landers (M_W = 7.2), 1992 Big Bear (M_W = 6.6), and 1994 Northridge (M_W = 6.7). However, even this sample, with only a small number of strong ground motion recordings for large earthquakes ($M_W \geq 7.0$) at close distances ($r \leq 10$ km) is limited in a number of important ways.

Several authors have estimated empirical attenuation curves for peak acceleration of strong ground motion based on the recordings from earthquakes in the western United States (for a review see Joyner and Boore, 1988; Iai and Matsunaga, 1993). A comparison of four different acceleration attenuation relations is made in Table 2.1. The sequence of the attenuation curves listed in the table reflects the updating of previously published empirical equations as newly recorded strong-motion accelerograms became available since the 1989 Loma Prieta earthquake. One common feature of three out of the four attenuation models is the accepted use of moment magnitude, M_W, for the size of each earthquake.

The moment magnitude is defined as (Hanks and Kanamori, 1979),

$$M_W = \frac{2}{3} \text{Log}(M_o) - 10.7 \quad , \tag{2.1}$$

where M_o is the seismic moment of the earthquake. Older attenuation relations (e.g., see Campbell, 1987; Idriss, 1985) used the surface wave, M_S, and Richter local magnitude,

Table 2.1 Acceleration attenuation relations.

Author	Magnitude	Distance	Site Conditions	Faulting Mechanisms
Boore, Joyner and Fumal (1993; 1994)	M_W	Closest distance to the surface projection of the fault rupture	Shear Wave velocity in the upper 30m beneath the site	No separation of faulting mechanisms
Campbell (1993)	$M_L < 6$, $M_S \geq 6$	Closest distance to the seismogenic rupture on the fault plane	Rock	Strike slip; Reverse; Intermediate strike slip and reverse mechanisms
Campbell and Bozorgnia (1994)	M_W	Closest distance to the seismogenic rupture on the fault plane	Soft rock; Hard rock; Alluvium	Strike slip; Reverse mechanisms
Sadigh (1993)	M_W	Closest distance to the fault rupture surface	Rock	Strike slip; Reverse mechanisms

M_L magnitude. However, M_W provides a better representation of the physical size of the earthquake source because of its definition with relation to the seismic moment of an earthquake (Hanks and Kanamori, 1979). Another advantage in using M_W is the lack of magnitude saturation (i.e., an upper-limit magnitude cut-off value) for high magnitude values. The M_L saturates at a M_W of approximately 6.5 while the M_S under predicts the M_W magnitude for values less than $M_W = 6.0$ (Heaton et al., 1986). For the peak acceleration attenuation relations compared in Table 2.1, the magnitude ranges from $4.7 < M_W < 7.7$. For earthquakes in which a moment magnitude was not available, Campbell and Bozorgnia (1994b) used the surface wave magnitude for $M_S \geq 6$ and the Richter magnitude for $M_L < 6.0$; this corresponds to the approximate range in which these magnitude scales are equal to M_W.

The largest difference between the individual acceleration attenuation relations is in the definition of source-to-station distance, a problem mentioned in section 1.2 and denoted R in this section. For all four attenuation models, the fault plane is determined from the location of aftershocks. The attenuation curve of Sadigh (1993) adopts R as the closest distance from the recording station to the fault plane. The attenuation models of Boore et al., (1993; 1994) define R as the shortest distance from the recording station to the vertical projection of the fault plane. For a vertical dipping fault, these two definitions of R are identical and a direct comparison of the two curves can be made. However, for a dipping fault the defined distances vary depending on the fault-to-station geometry. A third definition of R is employed by Campbell (1993) and Campbell and Bozorgnia (1994b). Their R is taken as the closest distance to the fault plane below a depth of 3 km. In a vertical strike-slip earthquake where surface rupture is observed, the closest distance for a station located directly on top of the fault plane for these two relationships (Campbell, 1993 and Campbell and Bozorgnia, 1994b) is 3 km, whereas for the other curves R is zero.

As mentioned in section 1.2 in this study of peak ground displacement a wave source relation distance $R \equiv H_{slip}$ is used. H_{slip}, is defined as the distance from the recording station to the largest slip on the fault plane (see section 4.1.2). A limitation with this definition of distance is the need for a fault slip inversion model for each earthquake to determine the location on the fault plane of largest slip. When such models are available, however, the H_{slip} distance is a physically based estimate of the distance over which the measured wave attenuation occurs.

A preliminary study was needed of the local geology near the recording sites of the measured wave displacements. A detailed geologic profile of most strong ground motion recording sites in California is presently not available, partly because the classification of recording sites into separate geological categories is not uniform for all competing attenuation models. The acceleration attenuation curves of Sadigh (1993) are restricted to rock site conditions. Campbell and Bozorgnia (1994b) subdivide the rock sites into soft rock and hard rock as well as alluvial site conditions. Boore et al., (1993; 1994) have classified the site conditions based on the seismic S wave velocity in the upper 30 meters below the site. These four site classifications are listed in Table 2.2.

Table 2.2 Boore, Joyner, and Fumal (1993;1994) site classification.

Site Category	Shear wave velocity in upper 30 meters
A	Vs > 750 m/sec
B	360<Vs<750 m/sec
C	180<Vs<360 m/sec
D	Vs<180 m/sec

Because the seismic velocity profile in the upper 30 meters directly under the site was not always available, site classifications were performed by correlating the seismic profile with recorded borehole measurements in similar geologic materials (Boore et al.,

1993; 1994). The acceleration attenuation models were not developed for site classification D because of the limited number of strong ground motion recordings. It should be noted that the B site classification contains both rock and soil sites with the sample approximately 1/3 rock and 2/3 soil sites. Deep alluvium sites are now classified as site C.

For peak ground displacement values, the site specific classification based on the shear wave velocity in the upper 30 meters is not as crucial as it is for acceleration. A characteristic wavelength of 500 meters would be estimated for a frequency of 1 Hz, which is a typical frequency for the observed peak ground displacement of the body waves, and a shear wave velocity of 500 m/sec (site B). The amplitude of these seismic waves, which have wavelengths greater than 30 meters by an order of magnitude, will not be greatly modified on the basis of the geological structure of the upper 30 meters. This classification, however, can be important for the analysis of peak acceleration, which is of a higher frequency content (and therefore shorter wavelengths) than displacement.

Recent attenuation curves for peak ground acceleration (see Table 2.1) take into account the type of earthquake faulting. All of the curves except in the Boore et al., (1993; 1994) study are computed from sub-samples formed by subdividing the strong ground motion accelerograms for strike-slip and reverse mechanisms earthquakes; separate attenuation curves are then estimated for each type of earthquake fault mechanism. In this work also, separate attenuation models were constructed for different types of faulting mechanism. A total of eight strike-slip and four reverse earthquakes were examined (see sections 4.2 and 4.3).

2.2 Velocity Attenuation Relations

A similar regression analysis for peak ground velocity versus distance from large earthquakes was made by the usual procedure for peak ground acceleration. For example, Boore et al., (1980) computed a set of empirical attenuation curves for peak ground velocity from a limited sample of strong ground motion recordings. The observations were divided into two separate groups corresponding to $5.3 < M_L < 5.7$ and $M_L = 6.4$. A simple equation of the form, $\text{Log}_{10}(\text{PGV}) = a - b\ \text{Log}_{10}\ R$, was used for the regression. Similar results for magnitudes greater than $M_L = 6.4$ were prevented by the unavailability of observations from larger earthquakes. Only 25 measurements of the peak ground velocity were available at the time for the statistical fit.

After the 1979 Imperial Valley earthquake, Joyner and Boore, (1981) updated the velocity attenuation curves to include the new strong ground motion measurements. The enhanced sample consisted of 38 points from the 1979 Imperial Valley earthquake as well as 68 points from other earthquakes. The observed peak velocity measurements were regressed with a modified equation of the following form,

$$\text{Log (PGV)} = a_1 + a_2 M_W - \text{Log } r + a_3 r + a_4 S + 0.26P\ , \qquad (2.2)$$

where $r = (d^2+h^2)^{0.5}$, PGV is the peak ground velocity in cm/sec, d is the closest distance to the surface projection of the fault plane, and S is 1 for soil sites and 0 for rock sites, and P is zero for the 50th percentile and one for the 84th percentile. The form of (2.2) is magnitude dependent and accounts for both anelastic attenuation (the a_3 coefficient) and an assumed geometrical spreading attenuation of the simple inverse of the distance (the negative unit coefficient of log r). The values of a_i (i =1, 2, 3, 4) and h are listed in Table 2.3. This empirically estimated attenuation relation for peak ground velocity is valid for predicting peak velocity from earthquakes between $5.3 < M_L < 7.4$.

More recently, Joyner and Boore (1988) updated their attenuation curves for velocity. The main difference between these curves and the previous curves is the use of a second order polynomial in magnitude in the later curves.

Table 2.3 Regression parameters from the Joyner and Boore (1981) attenuation model for peak ground velocity.

Parameter	Value
a_1	-0.67
a_2	0.489
a_3	-0.00256
a_4	0.17
h	4.0

Campbell (1987) has estimated competing empirical attenuation models for the peak ground velocity by regressing on a sample with the form,

$$\text{Ln (PGV)} = a + bM + d\text{Ln}[r + h_1\exp(h_2M)] + kr + s\,, \tag{2.3}$$

where PGV is the peak ground velocity in cm/sec, M is the surface wave magnitude (M_S) for values equal to 6.0 or greater, and M_L for values less than 6.0, r is the closest distance to the seismogenic zone, and the value of k, which represents the anelastic attenuation of seismic energy, was adopted as 0.0059 for the regression on the sample (Campbell, 1987). The final term, s, in equation (2.3) was included to incorporate the effects of fault type, fault rupture directivity, soil type, and building size. The algebraic form of s was assumed to be,

$$s = e_1K_1 + e_2K_2 + e_3K_3\tanh(e_4D) + e_5(1-K_3)\tanh(e_6D)\,, \tag{2.4}$$

where D is the depth to crystalline basement rock.

Table 2.4 Regression parameters from the Campbell (1987) attenuation model for peak ground velocity.

Parameter	Value
a	-1.584
b	1.18
d	-1.24
h_1	0.00907
h_2	0.951
e_1	0.49
e_2	0.99
e_3	0.53
e_4	0.41
e_5	0.60
e_6	0.88
k	0.0059
K_1	1 Reverse fault mechanisms
	0 Strike slip fault mechanisms
K_2	1 Rupture toward site
	0 Other
K_3	1 Shelters and buildings less than 5 stories
	0 other
σ_{Lny}	0.27

For the attenuation of peak acceleration, equation (2.4) does not include the depth to crystalline rock dependence (see, Campbell, 1987) indicating a stronger dependence on the amplitudes of relatively longer period velocity waves to the sediment layers located directly beneath the recording site. The values of a, b, d, h_i (i=1, 2), k, K_i (i=1, 2, 3) and e_i (i=1, 2, 3, 4, 5, 6)are listed in Table 2.4.

In recent years, substantial emphasis has been placed on the construction of empirical attenuation relations based on recordings from recent large earthquakes. The tendency has been to construct spectral attenuation curves which provide attenuation values at preferred frequencies. Present seismic response assessment of substantial structures usually relies on the estimated response spectra from large ground shaking (e.g., see Singh and Tabatabaie, 1991).

The response spectrum is defined as the maximum response to a single degree-of-freedom oscillator, for a given set of frequencies and a specified damping value, to a given input strong ground motion (Housner, 1970). Attenuation models for the pseudo-spectral velocity from large earthquakes have been statistically estimated recently (see section 2.4) and are replacing the use of empirical attenuation curves for peak ground velocity. However, complete seismic assessment studies for engineering purposes (Singh and Tabatabaie, 1991; Geomatrix, 1992; Miranda, 1993) must consider the peak velocity values in scaling synthetic time histories of strong ground motion.

2.3 Spectral Attenuation Relations

One aspect for the seismic vulnerability and resistance seismic assessment of large engineered structures is the need to examine the response of the structure in the frequency domain rather than the time domain. Consider a simple linear oscillator with a mass M and a stiffness k (Figure 2.1). The equation of undamped motion is given by,

$$My''(t) + ky(t) = - Mz''(t) , \tag{2.5}$$

where y(t) is the relative displacement and z''(t) is the acceleration of the base. If the oscillator has viscous damping then the response is given by,

$$y(t,\omega,n) = \frac{1}{\omega_n}\int_0^t z''(t)e^{-n\omega_n(t-\tau)}\sin\,\omega_n(t-\tau)\,d\tau\ , \qquad (2.6)$$

where n is the fraction of critical damping and $\omega_n = \omega(1-n^2)^{0.5}$. For values of critical damping less than 0.2, $\omega_n \approx \omega$. The displacement response spectrum, S_d, is defined as the maximum value of displacement, $|y(t_m,\omega,n)|$, which will occur at the time t_m (Housner, 1970). The corresponding velocity response spectrum, $|y'(t_m,\omega,n)|$, is defined as the maximum velocity at time t_m. Unlike the maximum velocity and displacement values, the maximum relative acceleration is of little direct engineering use. However, the linear combination of the relative acceleration and the acceleration of the base of the structure is of engineering interest. The absolute maximum acceleration spectrum is defined as (Housner, 1970),

$$S_a = (k/M)S_d = \omega^2 S_d\ , \qquad (2.7)$$

and attenuation curves based on the recorded seismograms of large earthquakes (e.g., see Sadigh, 1993; Boore et al., 1993; 1994) have been computed.

Another spectral response of engineering relevance is the pseudovelocity spectral response spectrum, S_{pv}. Physically, this response corresponds to the maximum relative velocity at a given frequency and is defined as (Housner, 1970),

$$S_{pv} = (1/\omega)S_a = \omega S_d\ . \qquad (2.8)$$

As is the case for the S_a response spectrum, empirical attenuation models for the S_{pv} response spectrum have been computed from a select set of recorded strong ground motions (e.g., see Boore et al., 1993; 1994; Bozorgnia and Niazi, 1993; Sadigh, 1993). The regression of the sample indicates that the shape of the pseudovelocity response

spectrum is distance, as well as, magnitude dependent (Bozorgnia and Niazi, 1993). For this reason, the scaling of the entire response spectrum by a single peak strong ground-motion parameter (e.g., peak ground acceleration) is incomplete and large deviations from the pseudovelocity relations estimated at separate frequencies can develop for periods of approximately 0.3 second and longer (Joyner and Boore, 1991). To help alleviate this problem, a statistical estimate of peak ground motion displacement can be used to estimate the scaling of long-period motion in a response spectrum.

Because of the increased demand for spectral attenuation in the last ten years, further estimation and updating of existing attenuation relationships for peak ground velocity has lagged. Perhaps surprisingly, the variability of peak ground displacement, which is usually of longer period than the observed velocity, has not been the subject of quantitative study in the last ten years even though the available data set of relevant strong ground motion displacement records is large enough to perform robust statistical regressions.

2.4 Displacement Attenuation Relations

An early attempt to estimate empirical attenuation for displacement was made by Boore et al., (1980) using a limited number of strong ground motion records. A total of 25 measurements of peak ground displacement was used in a regression of amplitudes against source-to-recorder distances. The data were divided into two separate magnitude categories, $5.3 < M_L < 5.7$ and $M_L = 6.4$. The regression equation was a simple Log - Log curve,

$$\mathrm{Log}_{10}(\mathrm{PGD}) = a - b\,\mathrm{Log}_{10}\,R\,, \tag{2.9}$$

where PGD is the peak displacement in cm and R is taken as the shortest distance (in km) between the recording station and the fault plane, as determined from aftershock locations. The values for a and b are listed in Table 2.5 and the attenuation curves are plotted in Figure 2.2. The empirical values are limited by the lack of observations for different magnitudes and distances to such an extent that they have not been adopted widely for seismic assessment studies. Even though the available library of strong ground motion accelerograms has substantially increased since 1980, no further published reference has been discovered that improves and updates these earlier empirical attenuation curves for peak ground displacement for California earthquakes.

Table 2.5 Attenuation parameters for peak ground displacement from Boore et al., 1980.

Magnitude Range	Distance Range (km)	a	b
5.3 - 5.7	5 -30	1.8	-1.2 ± 0.6
6.4	15 - 55	1.5	-0.6 ± 0.5

Although further estimation and updating of displacement attenuation based on seismic strong ground motions recorded in the United States have not occurred in the last 15 years, empirical attenuation curves for other seismotectonic regions of the world have been constructed. Kawashima et al., (1986) examined the strong ground motion recordings from 90 earthquakes in Japan with hypocentral depths of less than 60 km. A total of 197 sets of horizontal time histories was examined from 67 free-field sites. The sites were categorized into three geological sets: rock, soil, and soft soil. The regression was performed on the maximum peak ground displacement for the two combined horizontal components. A criticism is that the selection of the peak values did not consider the seismological aspects of the displacement waves (see section 1.2);

consequently, the measurements represent a sample from an unknown mixture of SH, SV and surface waves. The following equation was fit to the sample,

$$Log_{10}(PGD) = f_1 + f_2 M_{JMA} + f_3 Log_{10}(\Delta + 30)\,, \qquad (2.10)$$

where PGD is the peak ground displacement in cm, M_{JMA} is the JMA magnitude, and Δ is the epicentral distance in km. (It should be noted that M_{JMA} is approximately equal to M_W for values of $M_W < 8.0$ (Heaton et al., 1986)). The values of f_i (i=1, 2, 3) are listed in Table 2.6 for the three separate geologic site categories. The attenuation curves for each geologic site condition are plotted in Figure 2.3 for a M_{JMA}=7.0 earthquake. Each of the site condition curves is plotted over a separate distance range corresponding to the range of available recordings. The empirically estimated curve for soil sites predicts higher peak displacement values than the rock curve and the attenuation model for soft soil

sites predicts the highest peak ground displacement values for a given distance and earthquake magnitude.

Table 2.6 Attenuation coefficients for peak ground displacement from Kawashima et al., 1986.

Site Condition	f_1	f_2	f_3
Rock	-0.052	0.393	-1.390
Soil	-1.252	0.549	-1.179
Soft Soil	-1.155	0.575	-1.224

On account of the different depths of hypocenters between Japanese earthquakes from subduction sources and shallow crustal earthquakes from western North America, these curves can, but perhaps should not be used in a seismic assessment study for

tectonic regions with only crustal seismic sources. The larger depth of the Japanese subduction seismic sources is modeled in the regression equation by the addition of 30 km to the epicentral distance in the last term of equation (2.10). This value was adopted to model the characteristic size and location of the large subduction seismic sources for the region (Kawshima et al., 1986).

A more recent examination of peak ground-motion displacement attenuation has been performed for the seismically active region of Greece (Theodulidis and Papazachos, 1992). Their sample consisted of a total of 105 horizontal component seismograms from 36 shallow earthquakes, between $4.5 < M_S < 7.0$, in Greece. Because of the limited number of large earthquakes, 16 components of motion were selected from 4 shallow subduction earthquakes, between $7.2 < M_S < 7.5$, from Japan and Alaska. These records were selected because of the similar seismotectonic structure between Japan, Alaska, and Greece (Theodulidis and Papazachos, 1992). The geological site condition for each recording station was classified as either rock or soil. The latter category included sites located in alluvial and deep alluvial basins. Unlike the previous attenuation model for Japan, the two horizontal peak ground-displacement values were taken as separate data points. However, the selection of the peak ground displacement values was made without consideration of seismic wave type. The values of peak ground displacement were fit to,

$$\text{Ln (PGD)} = C_1 + C_2M + C_3\text{Ln}(R + R_o) + C_4S + \sigma_{\text{Ln}Y}P\,, \qquad (2.11)$$

where PGD is the peak ground displacement in cm, M is the surface wave magnitude M_S, R is the epicentral distance in km, S is one for rock sites and zero for soil sites, and P is zero for the 50th percentile and one for the 84th percentile. The values for C_i (i=1, 2, 3, 4) and R_o are listed in Table 2.7. Figure 2.4 shows the rock and soil attenuation curves

for a M_S = 7.0 earthquake. As is seen from the previous study, the attenuation curve for soil sites predicts higher peak displacement values than the curve for rock sites.

Table 2.7 Attenuation coefficients for peak ground displacement from Theodulidis and Papazachos, 1992.

Parameter	Value
C_1	-5.92
C_2	2.08
C_3	-1.85
R_o	5
C4	-0.97
σ_{LnY}	1.23

Given the different strong ground motion samples, meaningful comparison between the estimated attenuation relations is complicated by the different criteria for selection of measurements in each study. The Boore et al., (1980) curves are not considered for this comparison because of the limited sample used in the regression and the simple Log-Log equation. Plotted in Figure 2.5 are the two corresponding peak displacement attenuation curves for a magnitude 7.0 earthquake for the Kawashima et al., (1986) (KAT86) and Theodulidis and Papazachos (1992) (TP92) relationships for rock site conditions. As was the case before, the two curves are plotted only for epicentral distances in which there were measurements.

There is a striking difference between the slopes and offsets of the two curves. The TP92 curve predicts higher peak displacement values for distances less than approximately 60 km. Beyond 60 km the greater attenuation of the TP92 curves leads to lower peak displacement values. One possible explanation for the difference in attenuation of the two curves is the difference in the type of seismic source between the two relations. For the TP92 curve, the measurements of peak ground displacement were

from predominately shallow earthquakes in Greece with a small contribution from larger subduction earthquakes in Alaska and Japan. However, the KAT86 curve is based solely on observations from Japanese subduction seismic sources. Different rates of attenuation, due to the differences in the tectonics and geology of the two separate regions, could also be expected. Finally, as was noted earlier, the KAT86 regression equation accounts for the deeper earthquake sources with the saturation term of 30 in equation (2.10). This leads to a saturation of the curve for short distances and can be compared with a saturation term of only 5 (see equation (2.11)) for the TP92 attenuation curve.

Next, a similar comparison is made for soil site attenuation curves (see Figure 2.6). The two curves are again drawn for a magnitude 7.0 earthquake. The TP92 curve predicts higher peak ground-displacement values than the KAT86 curve for short distances. However, the cross-over distance between the two curves occurs at a distance of approximately 80 km for soil sites rather than 60 km for the rock sites. Both of the soil curves predict higher values than the corresponding rock curves and the rate of attenuation of the two soil curves is similar to that of the rock curves. The large differences in the two soil curves, as was observed for the rock sites, can be attributed to the differences between the regional tectonics and seismic sources of the respective measurements of peak ground displacement used in the regressions.

Whatever the causes of the noticeable differences between the three independent attenuation relations for peak ground displacement discussed above, some inferences can be drawn that helped in the construction of the attenuation curves for peak displacement ground motion in this research. The differing mean depths of earthquake foci used in this analysis suggest that the peak displacement attenuation curves estimated in the following sections would be expected to be more similar to the TP92 curves rather than to the KAT86 curves. The variation in ground displacement attenuation relationships will now be examined for both rock and soil sites using strong

ground-motion records from crustal earthquakes in California and a comparison with the attenuation curves discussed above will be presented in chapter 6.

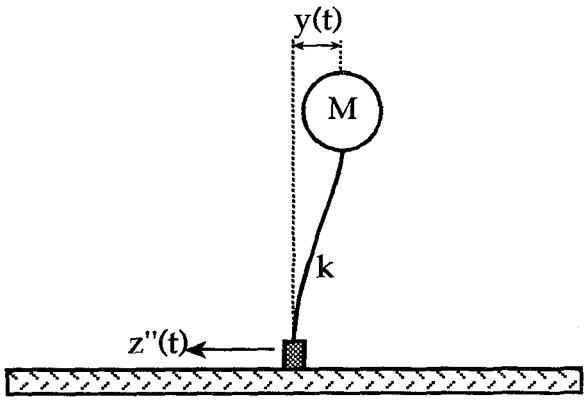

Figure 2.1 Simple linear oscillator with a mass M, a stiffness of k and a base acceleration of z"(t). See equation (2.5) for the equation of motion the system.

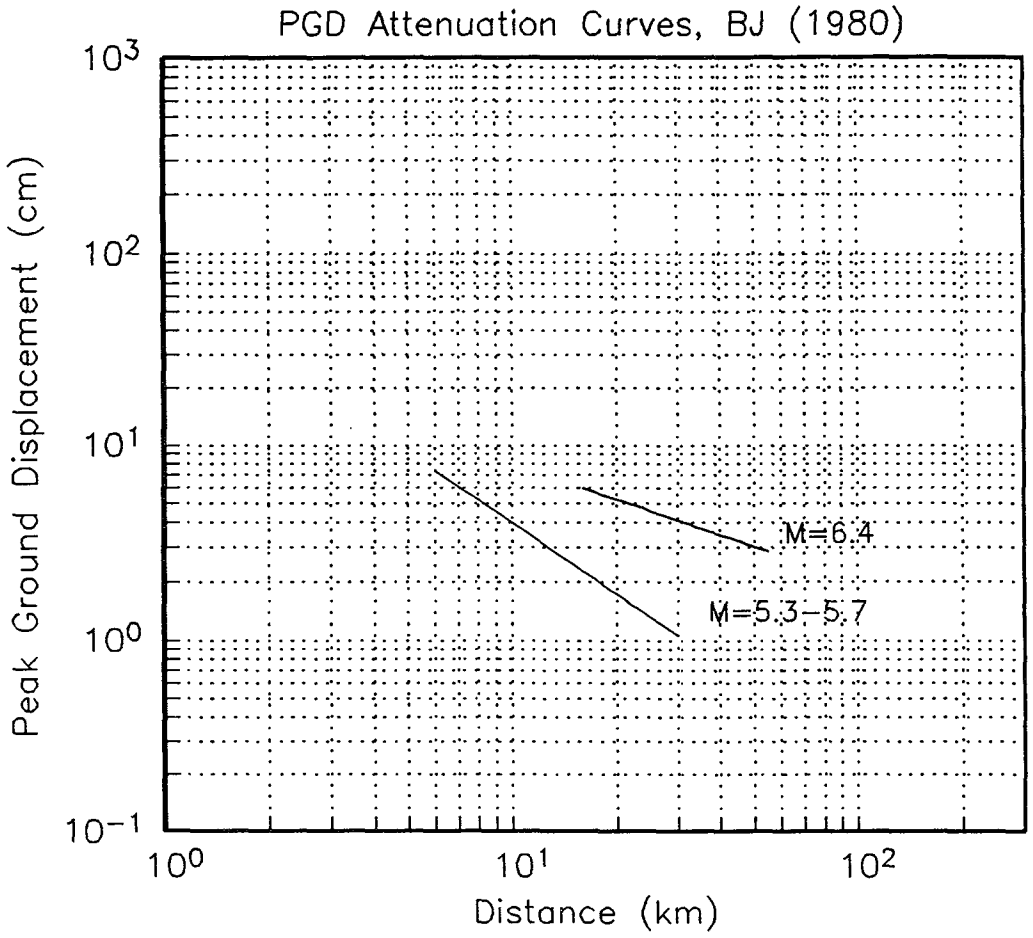

Figure 2.2 Peak ground displacement attenuation curves from Boore et al., (1980). The curves are graphed only for the distance and magnitude range of the regression sample.

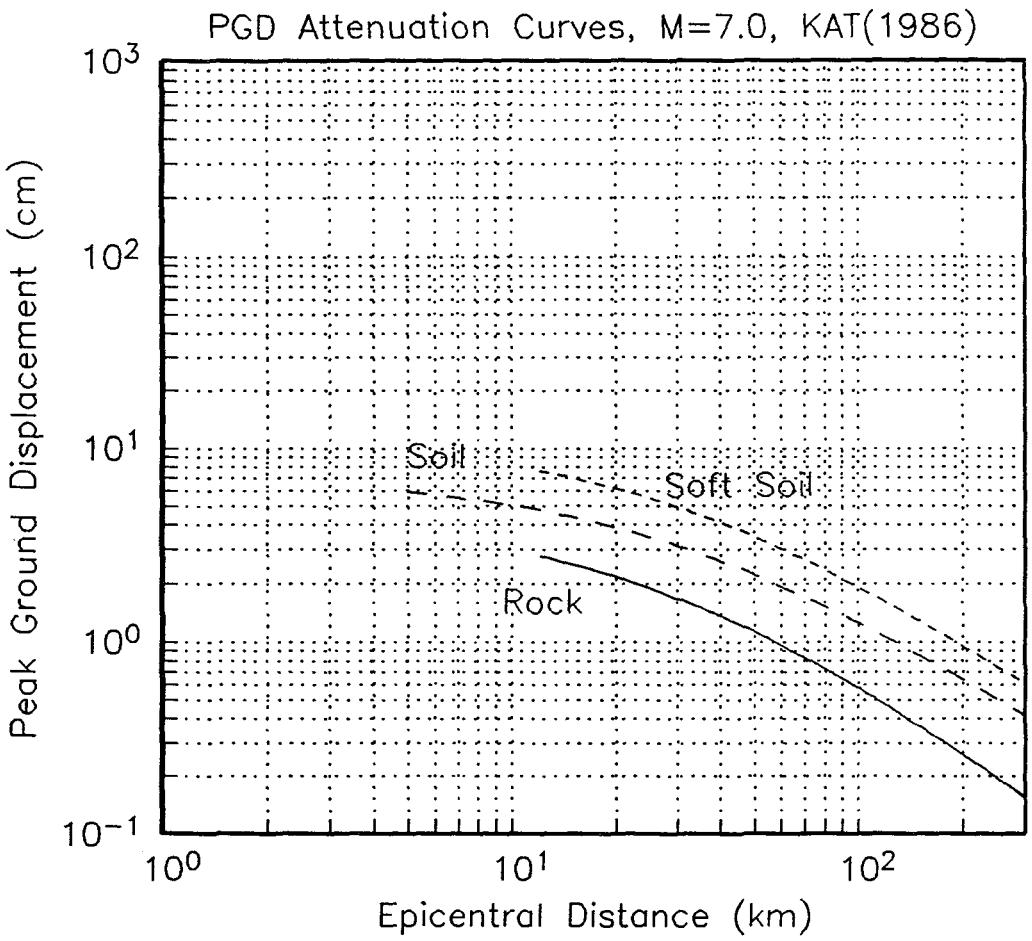

Figure 2.3 Peak ground displacement curves from Kawashima et. al., (1986) for the three separate site classifications (i.e., rock, soil, and soft soil). The curves are plotted for a M_{JMA} = 7.0 earthquake and only over the distance range of the observations.

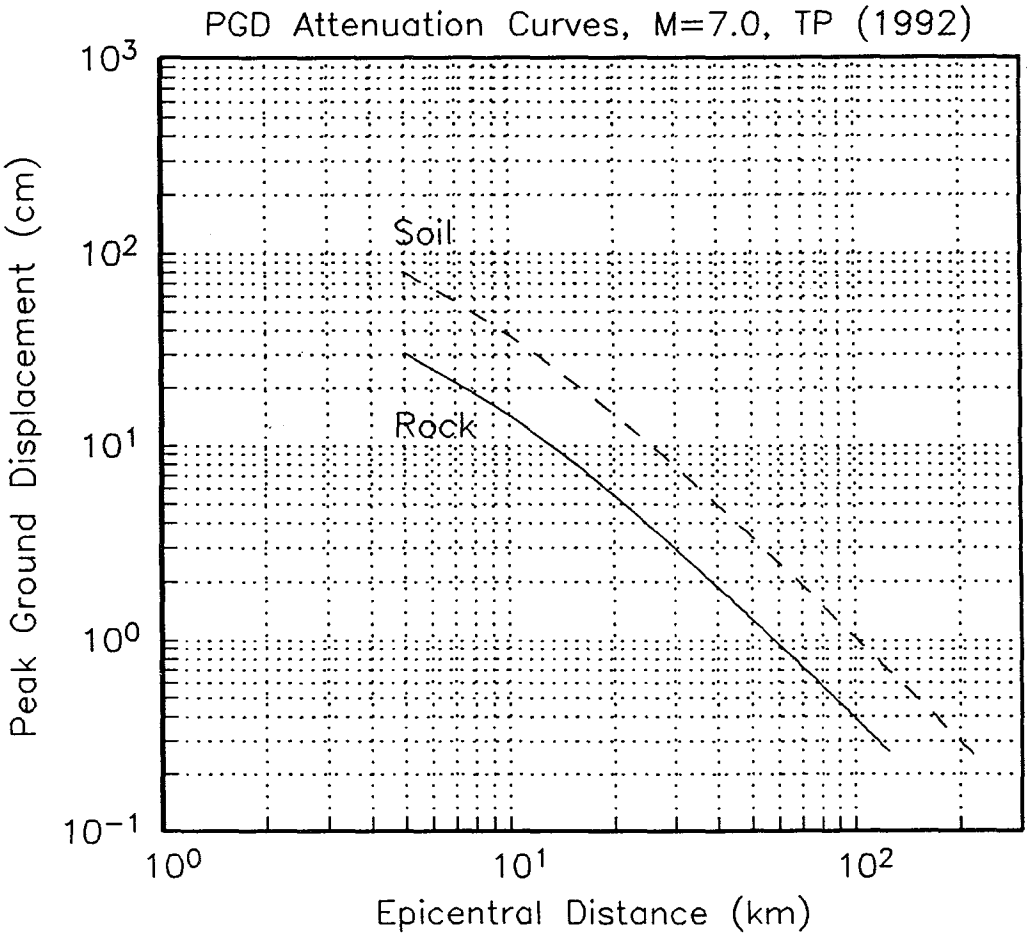

Figure 2.4 Peak displacement attenuation curves from Theodulidis and Papazachos (1992) for the two site classifications (i.e., rock and soil). The curves are plotted for a $M_S = 7.0$ earthquake and only over the distance range of the observations.

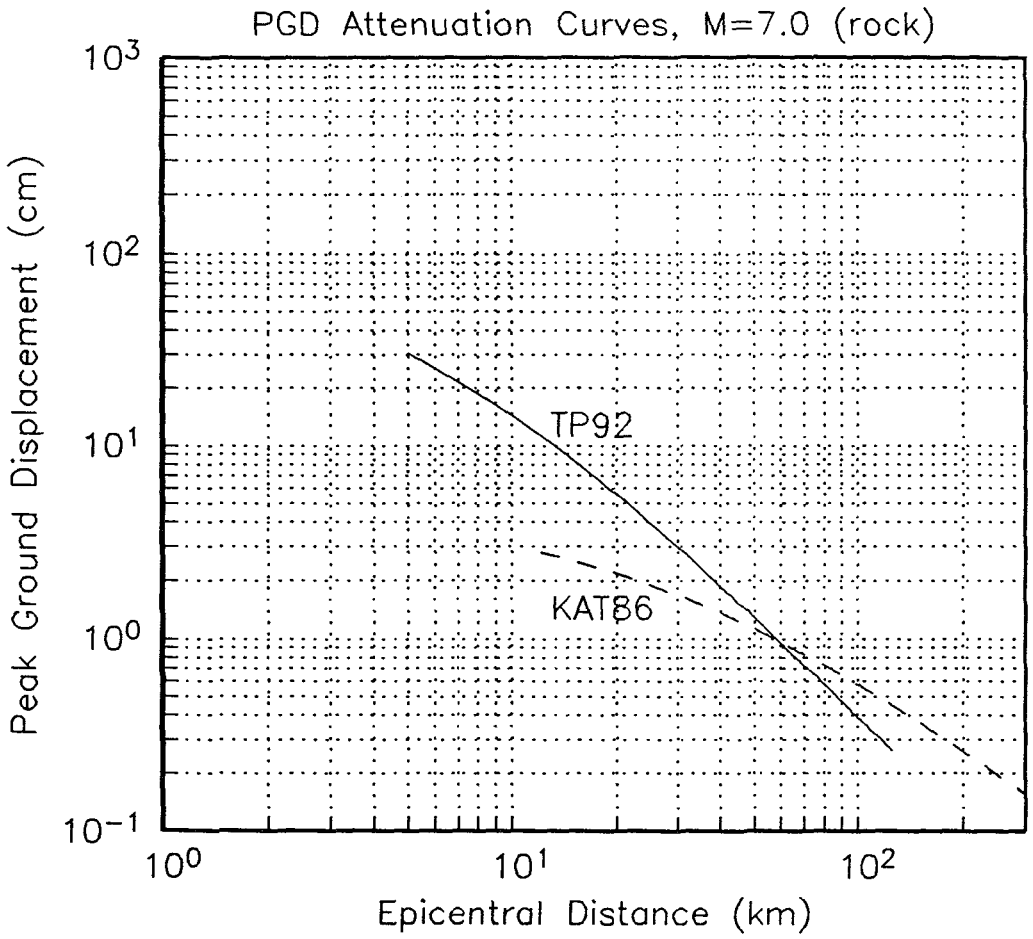

Figure 2.5 Comparison between the KAT86 and TP92 peak ground displacement attenuation curves. The comparison is made for a magnitude 7.0 earthquake for rock sites. Each curve is only drawn over the corresponding distance for which there were observations.

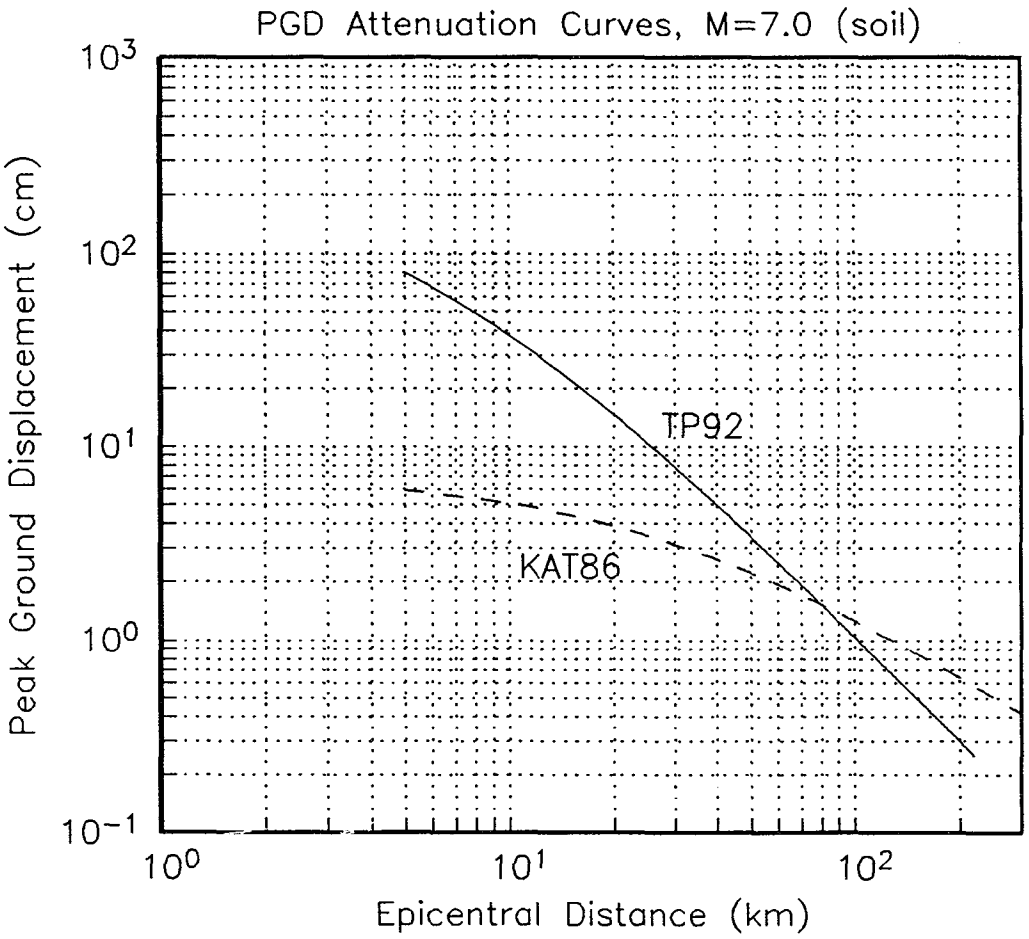

Figure 2.6 Comparison between the KAT86 and TP92 peak ground displacement attenuation curves. The comparison is made for a magnitude 7.0 earthquake for soil sites. Each curve is only drawn over the corresponding distance for which there were observations.

3. Seismological Wave Theory

As was discussed in chapter 1, the analysis of strong ground motion displacement seismograms for the determination of the maximum value must take into consideration the seismological wave type. The displacement seismogram is comprised of a combination of P and S body waves and surface waves. Seismic wave theory and the application of appropriate seismic wave travel times make it clear that in most strong ground motion accelerograms, the largest ground acceleration is attributable to the body waves (usually S waves) generated somewhere along the extend seismic source. Large ground accelerations, however, can be recorded later in the accelerogram, as was the case for the Pacoima Dam time history from the 1971 San Fernando earthquake (Bolt, 1972). For peak ground displacement the largest amplitude waves can be the later arriving surface waves (as an example see the acceleration, velocity, and displacement time history in Figure 1.1). The appropriate seismic wave theory for body waves and surface waves will be outlined in this chapter and references to its application made in later chapters.

3.1 Body Waves

This work is restricted to measurements of the amplitudes of the principal S body wave portion of the displacement seismograms. Discrimination of the wave types in typical mixing requires surface wave properties to be considered also. The source representation theorem (for a description see Aki and Richards, 1980) relates the displacement in a medium to the displacement discontinuity on a slip surface. For a homogenous, isotropic and unbounded medium, select the Cartesian axes such that the fault slip plane lies in the (x_1,x_2) plane. Figure 3.1 shows the geometry of the Cartesian axes (x_1,x_2,x_3) as well as the corresponding spherical polar coordinates $(\hat{r},\hat{\theta},\hat{\phi})$. For a

moment tensor M_{pq}, equal to the integral over the fault slip region of moment density, the displacement field is the convolution of the moment tensor with the elastodynamic Green's function for the medium (for a proof see Bullen and Bolt, 1985),

$$u_n(x,t) = M_{pq} * \frac{\partial}{\partial x_q} G_{np} \, . \tag{3.1}$$

For a double-couple solution the moment tensor can be defined using a time-dependent seismic moment,

$$M_0(t) = \mu \bar{u}(t) \, A \, , \tag{3.2}$$

where μ is the rigidity of the medium, $\bar{u}(t)$ is the average displacement slip on the fault plane, and A is the area of slip on the fault plane. The displacement field can now be expressed in spherical polar coordinates as (Aki and Richards, 1980),

$$\begin{aligned} u_n(x,t) = & \frac{1}{4\pi\rho} A^N \frac{1}{r^4} \int_{r/\alpha}^{r/\beta} \tau M_0(t-\tau) \, d\tau \\ & + \frac{1}{4\pi\rho\alpha^2} A^{IP} \frac{1}{r^2} M_0(t - \frac{r}{\alpha}) + \frac{1}{4\pi\rho\beta^2} A^{IS} \frac{1}{r^2} M_0(t - \frac{r}{\beta}) \\ & + \frac{1}{4\pi\rho\alpha^3} A^{FP} \frac{1}{r} \dot{M}_0(t - \frac{r}{\alpha}) + \frac{1}{4\pi\rho\beta^3} A^{FS} \frac{1}{r} \dot{M}_0(t - \frac{r}{\beta}) \, , \end{aligned} \tag{3.3}$$

where ρ is the density of the medium, α is the P wave seismic velocity, β is the S wave seismic velocity, and r is the distance between the source and receiver. The P and S radiation pattern for the near-field, intermediate-field, and far-field are given by,

$$\mathbf{A}^{N} = 9 \sin 2\theta \cos \phi \, \hat{\mathbf{r}} - 6(\cos 2\theta \cos \phi \, \hat{\theta} - \cos \theta \sin \phi \, \hat{\phi})$$

$$\mathbf{A}^{IP} = 4 \sin 2\theta \cos \phi \, \hat{\mathbf{r}} - 2(\cos 2\theta \cos \phi \, \hat{\theta} - \cos \theta \sin \phi \, \hat{\phi})$$

$$\mathbf{A}^{IS} = -3 \sin 2\theta \cos \phi \, \hat{\mathbf{r}} + 3(\cos 2\theta \cos \phi \, \hat{\theta} - \cos \theta \sin \phi \, \hat{\phi})$$

$$\mathbf{A}^{FP} = \sin 2\theta \cos \phi \, \hat{\mathbf{r}}$$

$$\mathbf{A}^{FS} = \cos 2\theta \cos \phi \, \hat{\theta} - \cos \theta \sin \phi \, \hat{\phi}. \qquad (3.4)$$

The first term in equation (3.3) is the near-field term which attenuates proportionally to r^{-4}. However, for a step-function time dependent seismic moment $M_o(t)$, the r^{-4} proportionality factor reduces to a r^{-2} quadratic dependence. The second and third term also attenuate proportionally to r^{-2} and are called the intermediate-field terms. Finally, the last two terms in equation (3.3) are the far-field displacement terms and attenuate proportionally to r^{-1}. Because of the differences in attenuation, individual terms dominate in certain distance ranges. For distances very close, for example, less than 15 km from the source, the near-field terms will dominate. However, at greater distances, the near-field term decreases quite rapidly because of the quadratic dependence on distance and the far-field terms dominate. Although the attenuation of the intermediate terms is proportional to the inverse square of the distance, these terms never dominate over the near-field and far-field terms.

From equation (3.3) it can be shown that depending on the distance from the source, the time history can be composed of a combination of near-field, intermediate-field and far-field P and S body wave motion, with each of the motions attenuating at different rates. Any estimation of attenuation relations for peak ground displacement must separate the different types of motion and hence theoretical attenuation. Although

the near-field term will dominate at close distances, the available strong ground motion data are very limited in the near field (see Figure 4.4). For a distance of 15 km, the near-field amplitude would be less than the far-field displacement amplitude by a factor of 5 based solely on the attenuation of amplitudes as a function of distance. For a distance of 30 km, the far-field term dominate as the near-field amplitudes would be lower by an order of magnitude. The majority of the strong ground motion acceleration time histories are recorded at distances sufficient for the far-field term to dominate.

3.2 Radiation Pattern for the Far-Field P and S Wave Displacement

The far-field P and S wave displacement radiation patterns are dependent on the fault geometry. (i.e., the fault strike (ϕ_S), dip (δ), and rake (λ)). The strike is measured clock-wise from North and the dip is measured down from horizontal. The rake is taken as the angle between the strike of the fault and the slip direction. A pure vertical right-lateral fault will have δ=90 and a λ=180. In contrast, a pure thrust fault on a 45° dipping fault plane will have δ=45 and λ=90. The fault geometry and the relative location of a station to the slip on the fault plane can greatly reduce or increase the amplitude of ground motion.

To derive the far-field radiation pattern in terms of the fault geometry, a new set of Cartesian coordinate directions, $\hat{x}$ = North, $\hat{y}$ = East, and $\hat{z}$ = vertically downward, is adopted at the epicenter. The coordinate system is illustrated in Figure 3.2. With these new coordinates, it can be shown that the far-field displacement terms in equation (3.3) can be separated into the P, SV and SH body wave components of motion (Aki and Richards, 1980),

$$\mathbf{u}^P(\mathbf{x},t) = \frac{\mathcal{F}^P \mu A}{4\pi\rho\alpha^3 r} \dot{\bar{u}}(t - \frac{r}{\alpha})\,\hat{l}$$

$$\mathbf{u}^{SV}(\mathbf{x},t) = \frac{\mathcal{F}^{SV}\mu A}{4\pi\rho\beta^3 r}\,\dot{\bar{u}}\left(t - \frac{r}{\beta}\right)\hat{\mathbf{p}}$$

$$\mathbf{u}^{SH}(\mathbf{x},t) = \frac{\mathcal{F}^{SH}\mu A}{4\pi\rho\beta^3 r}\,\dot{\bar{u}}\left(t - \frac{r}{\beta}\right)\hat{\phi}\,, \tag{3.5}$$

where the $\mathcal{F}^P$, $\mathcal{F}^{SV}$, and $\mathcal{F}^{SH}$ are the radiation patterns for the far-field displacement. The radiation patterns can be expressed in terms of the strike (ϕ_s), dip (δ), and rake (λ) of the fault plane, the angle (i_ξ) at which the seismic ray leaves the seismic source (measured up from vertical), and the source to receiver azimuth (ϕ).

$$\begin{aligned}\mathcal{F}^P = {} & \cos\lambda \sin\delta \sin^2 i_\xi \sin 2(\phi - \phi_s) \\ & + \sin\lambda \sin 2\delta(\cos^2 i_\xi - \sin^2 i_\xi \sin^2(\phi - \phi_s)) \\ & + \sin\lambda \cos 2\delta \sin 2i_\xi \sin(\phi - \phi_s)\end{aligned} \tag{3.6}$$

$$\begin{aligned}\mathcal{F}^{SV} = {} & \sin\lambda \cos 2\delta \cos 2i_\xi \sin(\phi - \phi_s) - \cos\lambda \cos\delta \cos 2i_\xi \cos(\phi - \phi_s) \\ & + \frac{1}{2}\cos\lambda \sin\delta \sin 2i_\xi \sin 2(\phi - \phi_s) \\ & - \frac{1}{2}\sin\lambda \sin 2\delta \sin 2i_\xi(1 + \sin^2(\phi - \phi_s))\end{aligned} \tag{3.7}$$

$$\begin{aligned}\mathcal{F}^{SH} = {} & \cos\lambda \cos\delta \cos i_\xi \sin(\phi - \phi_s) + \cos\lambda \sin\delta \sin i_\xi \cos 2(\phi - \phi_s) \\ & + \sin\lambda \cos 2\delta \cos i_\xi \cos(\phi - \phi_s)\end{aligned}$$

$$-\frac{1}{2}\sin\lambda \sin 2\delta \sin i_\xi \sin 2(\phi - \phi_s) \quad . \tag{3.8}$$

The amplitude of the ground motion at a given site will be modified by the radiation pattern. As an example the radiation pattern for a vertical ($\delta = 90$) right-lateral ($\lambda = 180$) strike-slip fault ($\phi_s = 180$) is plotted in Figure 3.3. The P body-wave radiation pattern is drawn in Figure 3.3a and the SH and SV radiation patterns are plotted in Figure 3.3b for a take-off angle (i_ξ) of 100° (typical values of i_ξ for the strong ground motion accelerograms are $90° < i_\xi < 120°$). For the fault geometry and i_ξ, the SH amplitude would be predicted to be larger than the SV amplitude by a factor of approximately 5. It should also be noted that the relative locations of the radiation pattern maxima for the SH and SV wave motion do not coincide and are 45° apart. The corresponding radiation patterns for a dip-slip fault (ϕ_s=180, δ=45, λ=90) are shown in Figure 3.4.

3.3 Surface Waves

Surface wave energy is bounded by the free surface of the Earth and travels in directions parallel to the ground surface. Two types of surface waves need to be considered: Rayleigh waves and Love waves. The Rayleigh wave motion is elliptical in vertical planes which are parallel to the direction of propagation of seismic motion. In contrast, the Love wave motion is constrained to planes which are perpendicular to the direction of propagation. Particle motion plots can be used to discriminate the arrival of surface wave trains because of this polarization of the Rayleigh wave and Love wave motion

For regional and teleseismic distances, the surface wave amplitude is the largest owing to the lower geometrical spreading with distance of the surface wave train (see equations (3.9) and (3.10)). For strong ground motion recordings located close to the

source, the generation of coherent surface wave trains depends upon the geologic structure and distance between the source and station. Well developed surface wave trains, however, can be clearly identified on strong ground-motion records. As an example, the strong ground motion displacement time histories from the 1979 Imperial Valley earthquake (cf., section 4.2.1) recorded at El Centro #11 are plotted in Figure 3.5. As predicted by theory, the Rayleigh wave train is clearly identifiable on the vertical and radial components and the Love wave motion is observed on the transverse component. Although the surface wave displacement amplitude is larger than the corresponding body wave amplitude, the estimation of peak attenuation relations for strong ground motion displacement will only consider peak displacements from the S body wave portion of the seismograms. In this research, the majority of absolute peak ground-displacement values occurs during the S body wave portion of the time history. In only 22% of the seismograms examined, was it found that the maximum amplitude of displacement occurred in the Rayleigh-wave portion of the time history and not the S body-wave portion. For the Love-wave motion, only 17% of the records had the largest observed peak-displacement value in the Love wave motion. A separate set of attenuation curves for the largest surface-wave peak ground-displacement values can be estimated in the future

Similar to the equation for the far-field displacement given in section 3.2 for the P and S body waves, a set of equations for the surface-wave motion can be derived for the displacement field generated by a point force for a vertically heterogeneous medium. For Love waves the motion is given by (Aki and Richards, 1980),

$$u^{LOVE} = \exp(-i\omega t) \sum_{n} \frac{(F_y \cos\phi - F_x \sin\phi)\, l_1(k_n, h, \omega)}{8cUI_1}$$

$$X \frac{1}{\sqrt{r}} \sqrt{\frac{2}{\pi k_n}} \left[l_1(k_n, z, \omega)\hat{\phi} \right] \exp\left[i\left(k_n r + \frac{\pi}{4}\right) \right], \qquad (3.9)$$

where $l_1(k_n, z, \omega)$ is a continuos eigenfunction, k_n is the wavenumber, U is the group velocity, c is the phase velocity, $Fexp(-i\omega t)$ is a point source applied at r = 0 and z = h. For Rayleigh waves the displacement field is given by,

$$u^{RAYLEIGH} = \exp(-i\omega t) \sum_n \frac{F_z r_2(k_n, h, \omega) + i(F_x \cos\phi + F_y \sin\phi)\, r_1(k_n, h, \omega)}{8cUI_1}$$

$$X \frac{1}{\sqrt{r}} \sqrt{\frac{2}{\pi k_n}} \left[r_1(k_n, z, \omega)\hat{r} + r_2(k_n, z, \omega) e^{i\pi/4} \hat{z} \right] \exp(ik_n r) \; . \qquad (3.10)$$

Dispersion can greatly affect the observed amplitudes of surface-wave motion. Rayleigh-wave motion can be easily identifiable in certain cases (e.g., see Figure 3.5) where the seismic energy is separated based on the frequency-dependent wave velocity. However, for certain geological path structures (e.g., see section 5.5.1 of Bullen and Bolt, 1985) the Rayleigh wave dispersion can be limited in a given frequency range; this would lead to a large amplitude Rayleigh wave pulse. The amount of vertical to radial displacement is also dependent on the geologic structure. The Rayleigh wave motion can either be prograde or retrograde elliptical (see Figure 5.4 of Bullen and Bolt, 1985) depending on the frequency band of motion. The dispersion of Rayleigh waves causes a partitioning of energy, and therefore amplitudes, between the radial and vertical components of motion.

A comparison between equation (3.5) and equations (3.9) and (3.10) indicates the difference in attenuation between body waves and surface waves with respect to distance, r. Surface waves attenuate proportionally to the inverse square root of the distance, while body waves in the far field attenuate proportionally to the inverse of the distance. Because of this different distance dependence, the surface wave amplitude will dominate for larger distances. As an example, for a distance of 25 km the theoretical

surface wave amplitude due to geometrical spreading will be larger than the body wave amplitude by a factor of approximately 5.

The selection of peak ground-displacement values from the individual seismograms was made with the seismic-wave type taken into consideration to prevent the mixing of peak surface wave and peak body-wave values. If the seismic wave criteria were not used then the estimated attenuation curves would be a combination of the body attenuation at close distances and the surface wave attenuation at larger distances. For scaling synthetic records and spectra, this type of hybrid curve is not satisfactory because of the variability in surface-wave energy due to the regional geology, source mechanisms, and site conditions when a diverse set of earthquakes is analyzed.

3.4 Basin Effects

Seismological recordings at sites underlain by different geologic structures have shown that the presence of slow-velocity soft-sediment layers near to the surface can greatly increase the amplitude, as well as the duration of incident seismic energy (see Aki, 1988 for a review of effects of subsurface geology on strong ground motion). Similarly, instrumental observations indicate that the presence of an alluvial basin can significantly modify the incident displacement field because of the reverberations of the seismic waves within the basin and also the generation of basin-induced surface waves. These observations are generally in agreement with the predictions of seismic wave theory in layered elastic structures with appropriate damping. Numerical finite-element modeling of Love and Rayleigh wave motion incident to a nonhorizontally-layered media indicate the surface observation of the fundamental mode of displacement will be contamination by higher modes (Drake, 1972; Drake and Bolt, 1980). As an example, Drake and Bolt (1980) concluded that the two-dimensional geologic structure of the

continental boundary in California is a barrier to the propagation of fundamental-mode Love waves. Although all of the earthquakes used in this study were crustal seismic sources, the same modification of amplitudes of ground motion, as was seen at the continental boundary, could be expected at the boundary of alluvial basins.

A dramatic example of the increase in amplitude and duration of incident seismic energy occurred from the September 19, 1985 Michoacan (M_S = 8.1) earthquake. The subduction earthquake occurred off of the western coast of Mexico in the former Michoacan Gap (Singh et al., 1988). For strong ground motion accelerometers located along the coast in the immediate epicentral area, the peak horizontal ground acceleration from this earthquake was approximately 130 cm/sec^2 (Singh et al., 1988). However, this earthquake is more typically referred to as the Mexico City earthquake because of the substantial amount of damage to buildings in Mexico city, more than 350 km away from the source. This large region of damage has been discussed in terms of the large sediment-filled valley underneath Mexico City (Singh et al., 1988).

Strong ground motion records were collected in the Mexico City area on both rock and the sediment filled lake bed, where the majority of the damage occurred (Anderson et al., 1986). As an example, the accelerograms from the University City (CUIP) station, which is located on rock and is approximately 400 km away from the epicenter, are plotted in Figure 3.6. Horizontal peak ground-acceleration values are approximately 30 cm/sec^2. In comparison, the acceleration time histories for the station Secretaria De Comunicaciones y Transportes (SCT1), which is also located approximately 400 km from the epicenter but on the soft alluvium basin, are plotted in Figure 3.7 (the horizontal and vertical scaling is amplified by a factor of three for the SCT1 station). It is evident from the comparison that the presence of a soft clay layer beneath the SCT1 station greatly amplifies, not only the amplitude of strong ground acceleration, but also the duration of seismic energy. The accelerogram from the SCT1

site is also more monochromatic in nature indicative of the resonance response of the alluvial basin.

Analysis of other strong ground motion recordings in Mexico City indicated an increase in amplitude of between 8 to 50 times between the rock sites and certain soil sites (Singh et al., 1988). The amplification in amplitude and duration can be modeled by introducing a slow velocity layer within the alluvial basin (Kawase and Aki, 1989). This model explains the long durations observed at the recording sites in the basin in terms of the amplification and resonance of seismic energy within the alluvial basin. To match the observed amplitudes and durations, a soft-surface layer in which the seismic P and S velocities are low must be introduced for the geologic model of the basin (Kawase and Aki, 1989).

The effects of alluvial basins on strong ground motion have also been observed for crustal earthquakes in Southern California (e.g., Vidale and Helmberger, 1988; Graves, 1995). Plotted in Figure 3.8 are the displacement seismograms from the 1971 San Fernando earthquake (cf., section 4.3.1) recorded at Palos Verdes. The disperse Rayleigh-wave train is clearly observable on the radial and vertical components of motion, while the Love wave is recorded on the transverse component. Vidale and Helmberger (1988) modeled these surface waves as the conversion of direct shear waves at the basin boundary into Love and Rayleigh waves that propagate across the Los Angeles alluvial basin. A similar type of basin amplification was observed in the more recent 1994 Northridge earthquake (cf., section 4.3.4) at strong ground-motion sites in the Los Angeles basin. The displacement time histories from the strong-motion station at Downey are plotted in Figure 3.9. This site is located in the center of the Los Angeles basin, southeast of the epicenter. As was the case for the San Fernando time histories, the well dispersed surface-wave trains are clearly observable in the later portion of the seismograms. Similar to the numerical modeling results of Vidale and Helmberger (1988) for the San Fernando earthquake, Graves (1995) numerically modeled the seismic

wave energy of the Northridge earthquake and attributed the generation of the observed surface waves to the conversion of body waves at the basin boundary.

Although the amplification of seismic energy due to the presence of an alluvial basin can modify the peak ground-displacement amplitudes, the estimation of attenuation relations for peak ground displacement presented here does not consider the basin generated surface waves. A further complication with the basin induced surface waves is in the location of the source of such surface waves. For these basin induced surface waves, the source of all or part of these waves may not be the fault slip source of the earthquake, but rather the edge of the basin. In order to avoid this complication, measurements of peak ground displacement values were determined by selecting the largest ground displacement values from only the S body wave portion of the time histories.

3.5 Rupture Directivity

The effect of rupture directivity on the peak ground displacement values used for the regression analysis will be address in this section. Rupture directivity from seismology is similar to the Doppler effect observed in Physics and electromagnetic wave theory (Morse and Feshbach, 1953). The effect of rupture directivity leads to the amplification of ground motion for stations located along the direction of moving rupture and deamplification of ground motion for stations located at a back-azimuth from the seismic source. The spectral content of the ground motion will also be modified with shorter period ground motion for stations in the forward azimuth relative to the back-azimuths stations (for the spectral effects of rupture directivity on strong ground motion, see Becker, 1993).

The corresponding equations for the radiation patterns of a propagating fault rupture have been derived for both P and S body waves (for a full description see Ben-

Menahem, 1982). The forms of the equations for S body waves are similar to equation (3.5). The effect of rupture directivity mandates the introduction of amplification function,

$$D(M,\Theta) = \frac{1}{1 - M\cos\Theta}, \tag{3.11}$$

where M is the seismic Mach number and Θ is the angle between the strike of the propagating rupture and the observation location. The directivity focusing effect will only modify displacement amplitudes above the corner frequency of the seismic source. As an example, the amplification coefficients for a vertical strike-slip fault are listed in Table 3.1 for typical Mach numbers of 0.9 and 0.5. The values of $D(M,\Theta)$ were computed for four different receiver locations: directly along the strike, perpendicular to the strike on both sides, and along the back-azimuth of the fault. The amplitude for stations located 180 degrees apart, along the azimuth, are predicted to be larger by a factor of approximately 19 for a Mach number of 0.9. For a lower Mach number of 0.5, the amplification is not as severe (i.e., a factor of approximately 3). It will be shown in chapter 5 that the effects of rupture directivity contribute to the observed statistical scatter in the measured values of peak ground displacement.

Table 3.1 Rupture directivity amplification coefficients.

M = 0.9	D(M,Θ)	M = 0.5	D(M,Θ)
Θ = 0	10.0	Θ = 0	2.0
Θ = 90	1.0	Θ = 90	1.0
Θ = 180	0.53	Θ = 180	0.67
Θ = 270	1.0	Θ = 270	1.0

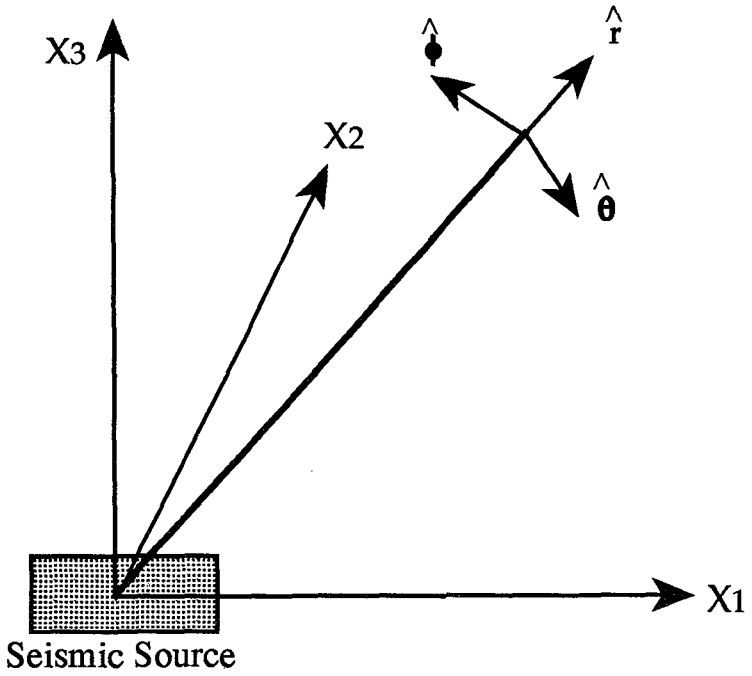

Figure 3.1 Cartesian and spherical polar coordinate system used in the theoretical equations for the displacement field (see section 3.1).

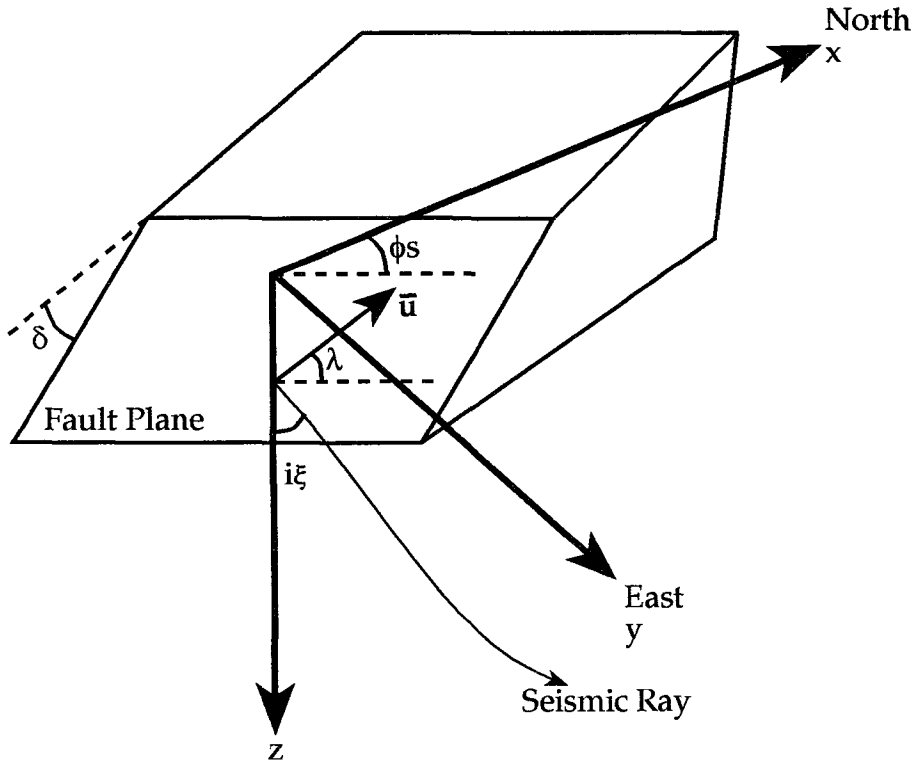

Figure 3.2 Coordinate system defined for the equations of far-field P and S body wave radiation patterns (see equations (3.6-8)). The fault strike (ϕ_S), dip (δ), and rake (λ) are indicated in the figure as well as the take-off angle (i_ξ).

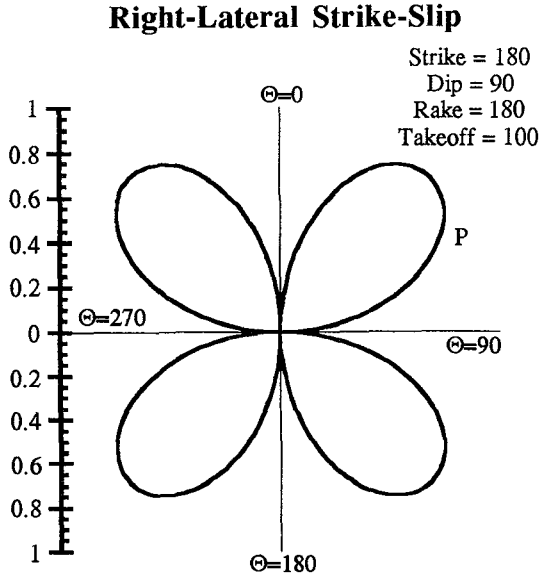

(a)

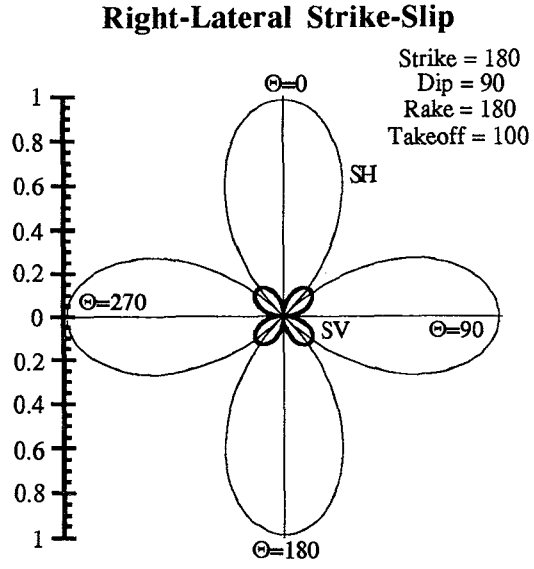

(b)

Figure 3.3 Far-field body wave radiation pattern amplitudes for a vertical right-lateral strike-slip fault and a take-off angle of 100°. (a) Radiation pattern for P body wave. (b) Radiation pattern for SH and SV body wave.

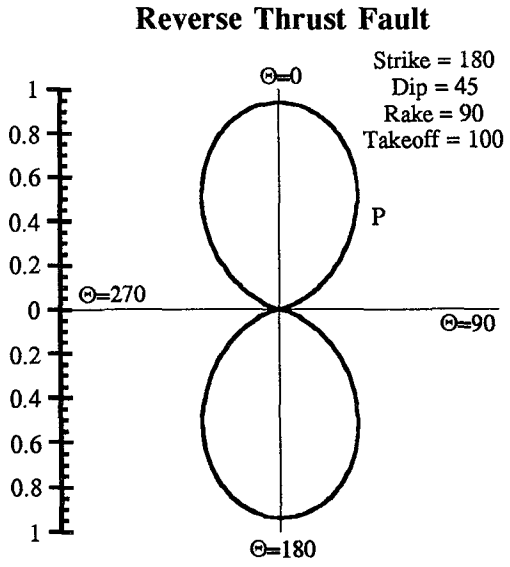

(a)

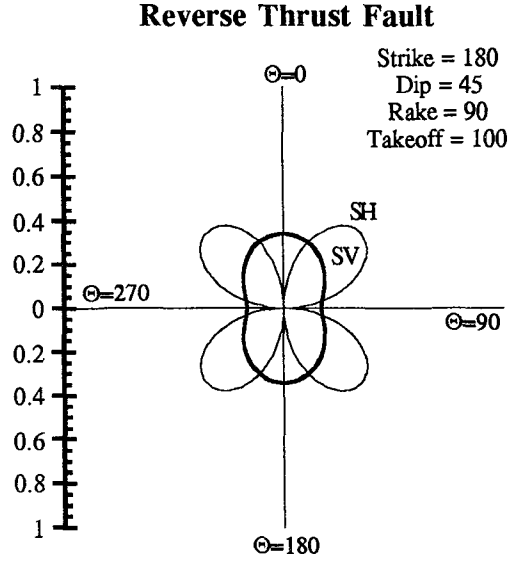

(b)

Figure 3.4 Far-field body wave radiation pattern amplitudes for a 45° dipping thrust fault and a take-off angle of 100°. (a) Radiation pattern for P body wave. (b) Radiation pattern for SH and SV body wave.

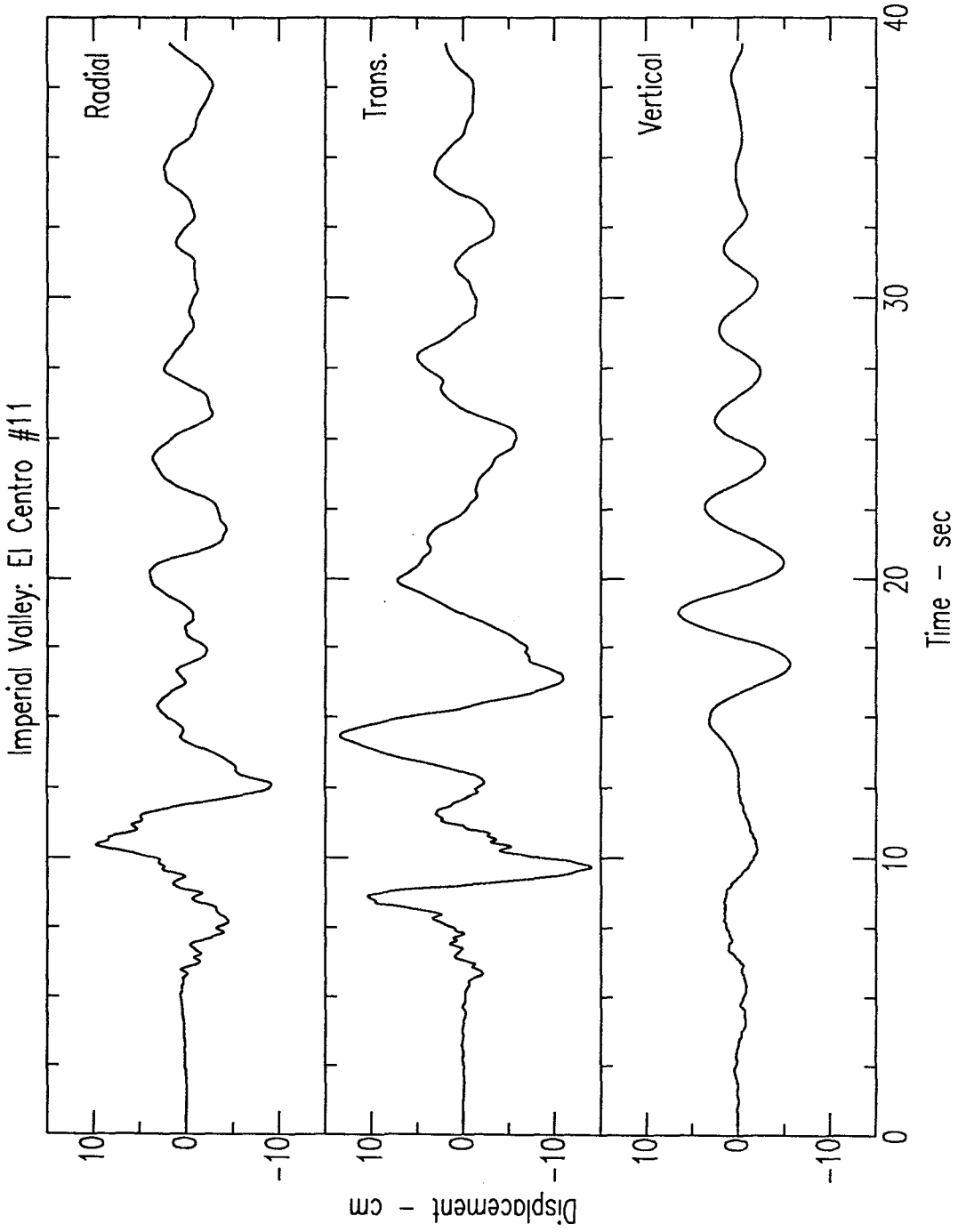

Figure 3.5 Radial, transverse, and vertical displacement seismograms from the 1979 Imperial Valley earthquake recorded at El Centro #11. Well disperse surface wave trains are observed on all three components.

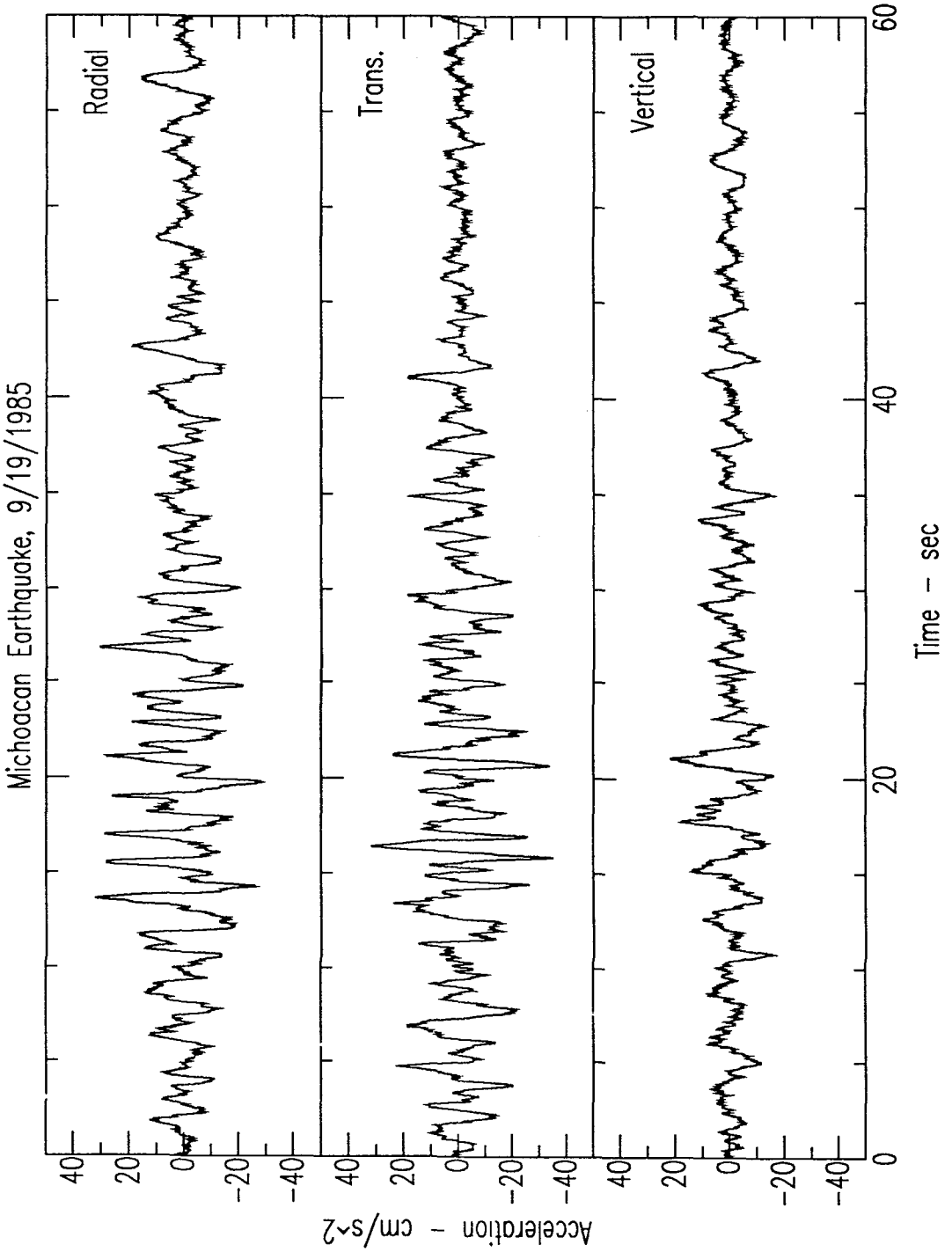

Figure 3.6 Three component accelerograms (North-South, East-West, and Vertical) recorded at the University City station (rock) from the 1985 Michoacan earthquake.

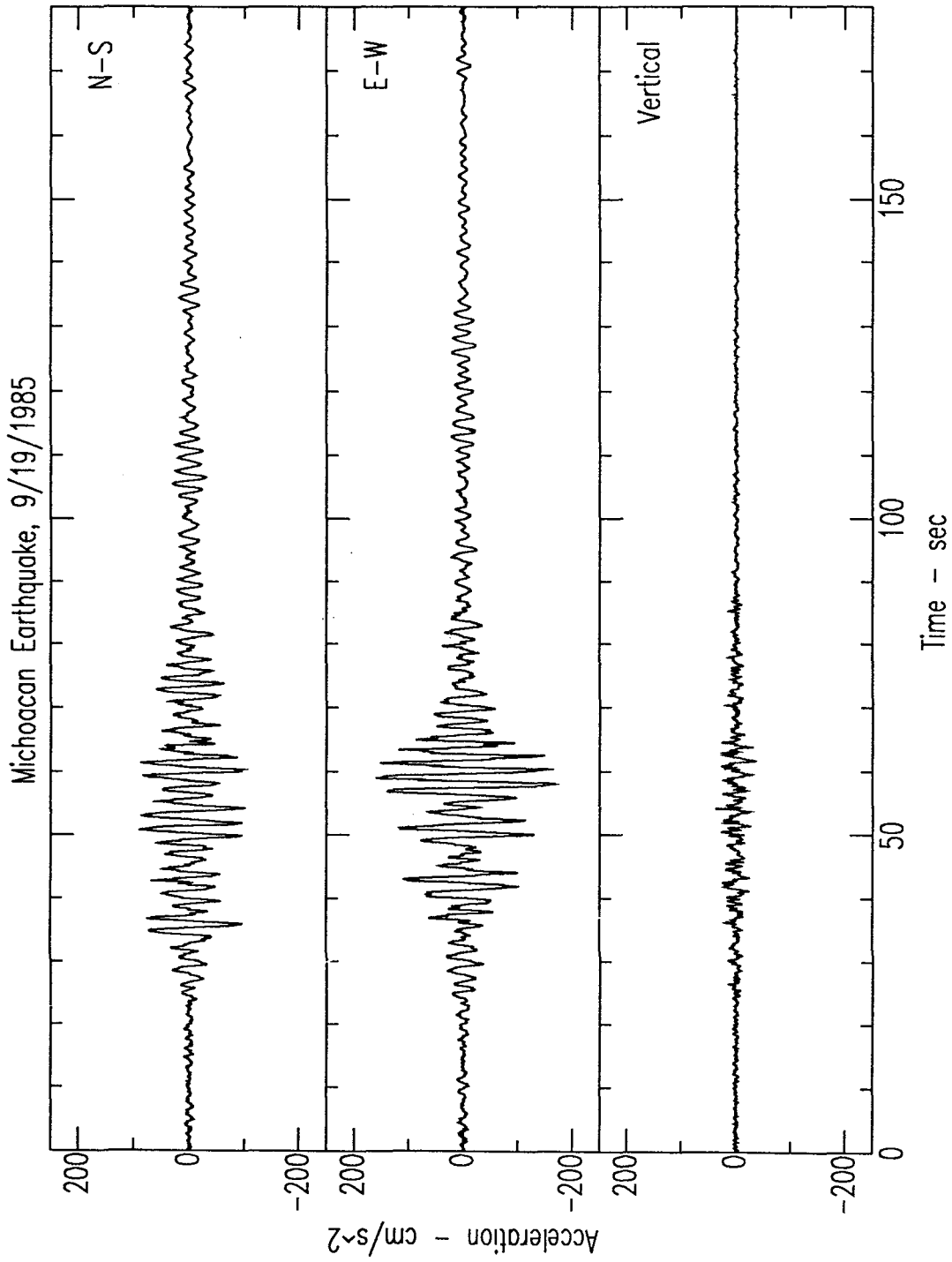

Figure 3.7 Three component accelerograms (North-South, East-West, and Vertical) recorded at the Secretaria De Communicaciones y Transportes station (soft soil) from the 1985 Michoacan earthquake (cf., Figure 3.6).

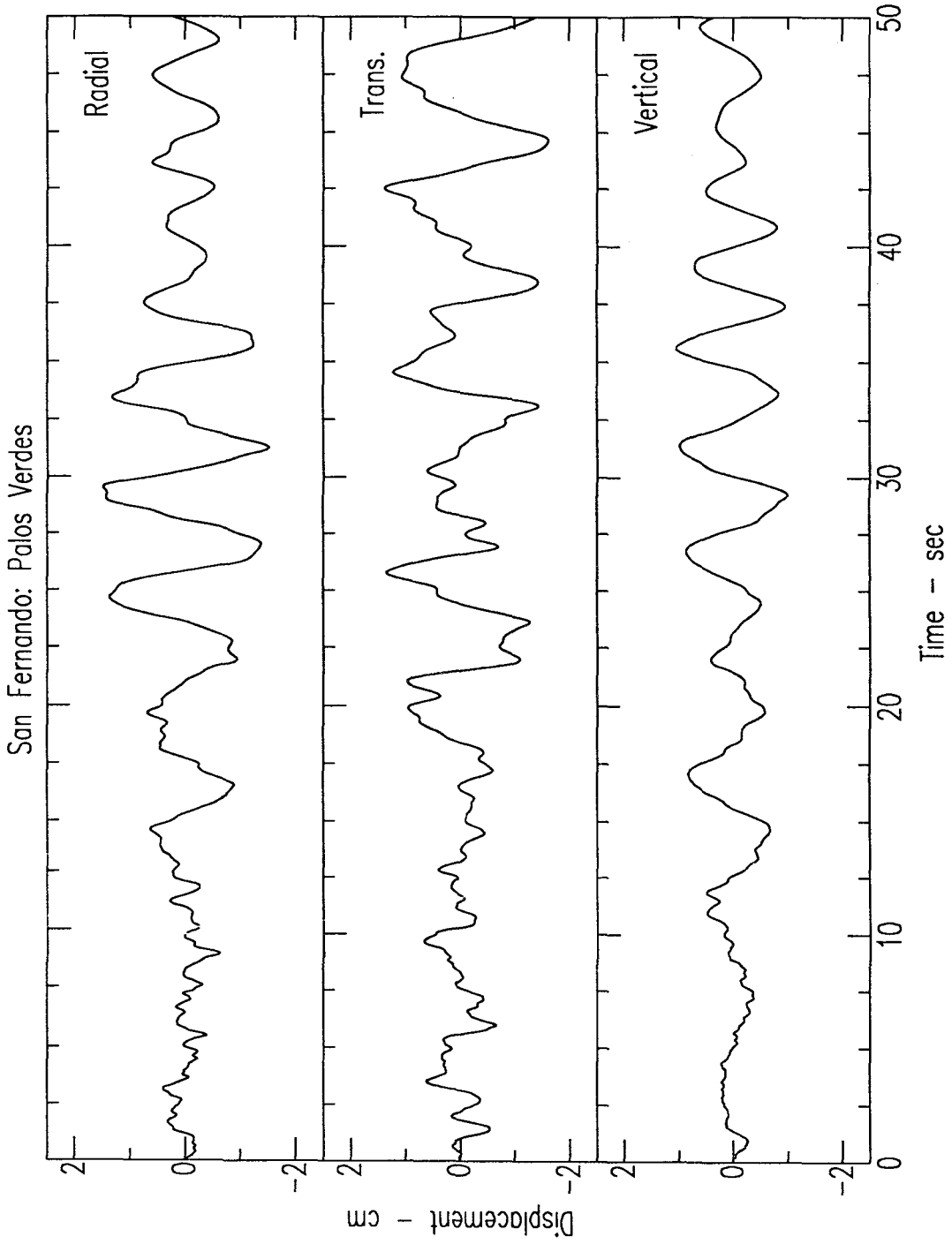

Figure 3.8 Radial, transverse, and vertical displacement seismograms from the 1971 San Fernando earthquake recorded at Palos Verdes. Well disperse surface wave trains are observed on all three components.

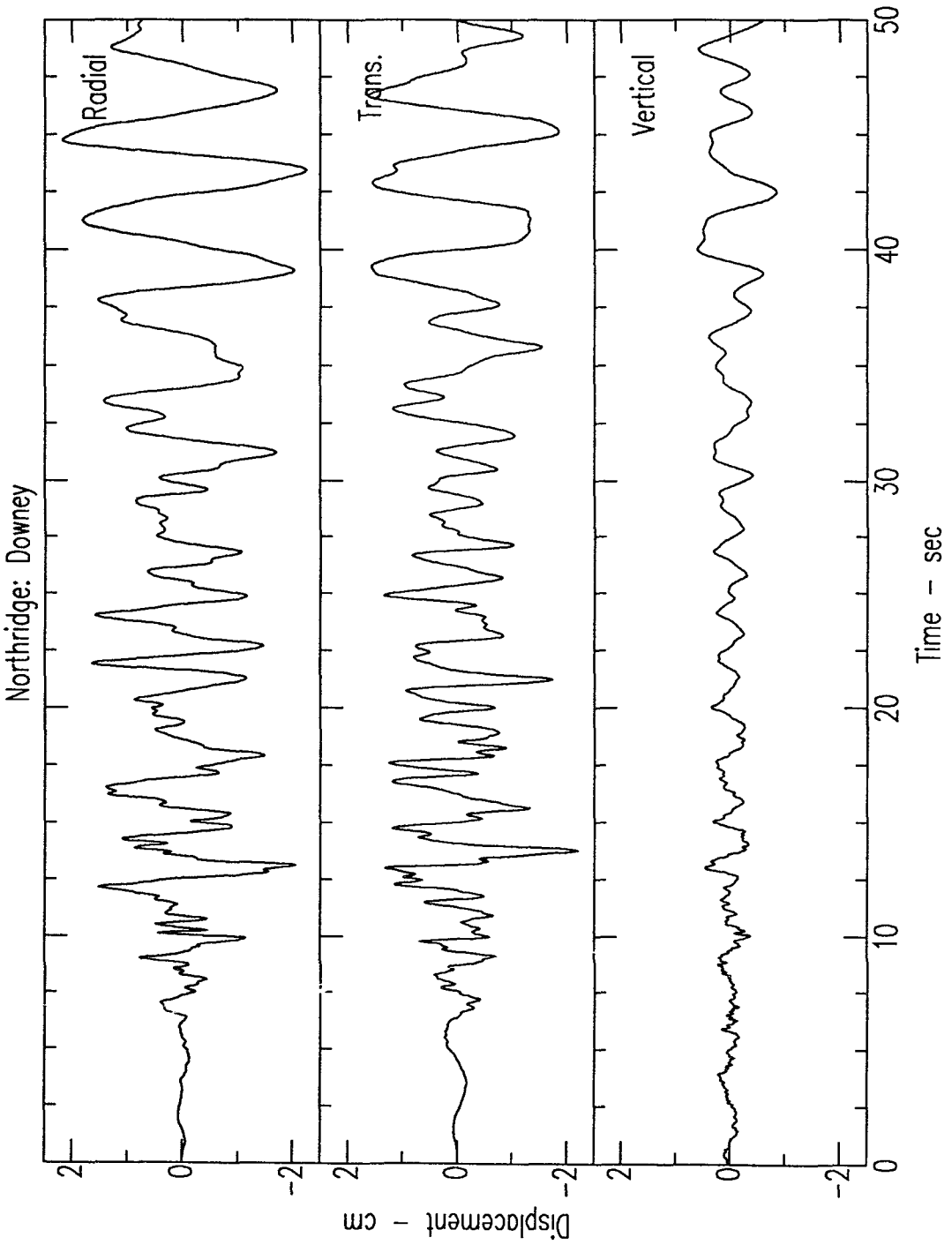

Figure 3.9 Radial, transverse, and vertical displacement seismograms from the 1994 Northridge earthquake recorded at Downey. Well disperse surface wave trains are observed on all three components.

4. Earthquake Data Set

4.1 Earthquake Selection

The occurrence of 15 moderate-to-large size (M_W = 6 - 7.2) earthquakes in California in the last 10 to 15 years (e.g., 1984 Morgan Hill, 1987 Whittier Narrows, 1989 Loma Prieta, 1992 Landers, 1992 Big Bear, 1992 Joshua Tree, 1992 Petrolia, and 1994 Northridge), has easily doubled, in principle, the number of available strong ground motion accelerations for the estimation of attenuation relations. However, the selection of earthquakes for use in the examination of attenuation of peak ground displacement is limited to those with a known fault slip model. For seismograms to be used in the analysis of peak ground displacement, a published fault slip model must be computed for the seismic source. This constraint resulted in a total of 12 earthquakes (see Table 4.1) being selected in this study. Each earthquake was classified as either a strike-slip or reverse fault mechanisms. Moment magnitude (M_W) was selected as the parameter of size because this measure does not saturate at high magnitudes (see section 2.1) and provides a dynamically consistent estimate of the earthquake source size. The mean moment magnitude for the class of strike-slip earthquakes in the selected set is M_W = 6.35 for eight earthquakes and the mean moment magnitude is M_W = 6.25 for the four reverse-fault earthquakes.

4.1.1 Earthquake Rupture History and Mechanism

As was mention above, each selected earthquake has at least one published fault slip rupture history. Fortunately, it is becoming routine for quantitative models of the fault slip histories to be published now for large earthquakes (e.g. Wald et al., 1991;

Wald and Heaton, 1994a; Wald and Heaton, 1994b). Although the resolution and uncertainty varies considerably from case to

Table 4.1 Earthquakes used in the analysis of the attenuation of peak ground displacement.

Earthquake	Mechanism	Latitude (° North)	Longitude (° West)	Depth (km)	Magnitude (M_W)
1971 San Fernando	Reverse	34.410	-118.400	8.4	6.7
1979 Imperial Valley	Strike-Slip	32.614	-115.318	12.1	6.5
1980 Livermore MS	Strike-Slip	37.826	-121.786	8.0	5.8
1980 Livermore AS	Strike-Slip	37.750	-121.712	10.0	5.4
1984 Morgan Hill	Strike-Slip	37.309	-121.678	8.4	6.1
1986 North Palm Springs	Strike-Slip	33.999	-116.608	11.1	6.2
1987 Superstition Hills	Strike-Slip	33.013	-115.838	1.7	6.6
1987 Whittier Narrows	Reverse	34.049	-118.081	14.6	6.0
1989 Loma Prieta	Strike-Slip	37.040	-121.880	17.6	7.0
1991 Sierra Madre	Reverse	34.245	-118.002	12.0	5.6
1992 Landers	Strike-Slip	34.201	-116.436	4.5	7.2
1994 Northridge	Reverse	34.213	-118.537	18.9	6.7

case, numerical inversions to compute the slip on the fault plane can use one or a combination of geodetic measurements, teleseismic seismograms, or local strong-motion recordings. For large, more recent earthquakes (e.g., the 1989 Loma Prieta and 1992 Landers earthquakes), competing inversion solutions for fault slip have been published. In this work, only one model of fault slip for each earthquake was selected to determine the location on the fault plane of largest slip and the corresponding H_{slip} distance (previously defined in section 2.1). This choice of an individual model was

based on a desire to maintain a consistency of resolution between seismic sources provided by the inversion procedure and data used. Consequently, models in which only the teleseismic seismograms were inverted for fault slip were considered only indirectly as checks, unless there were no other inversion models available. Prior to the inversion for fault slip from the local strong ground motion velocity records, the time histories were bandpassed filtered by each author between the approximate frequency range of 0.2 Hz to 2.0 Hz (the exact frequency range varies for each earthquake).

Although the individual inversion procedures for each earthquake listed in Table 4.2 differ because of the variations in the data used, fault plane grid size, and individual constraints and assumptions, the general theory for the inversion of ground motion to obtain fault slip is similar for all of the earthquakes studied in this research. The fault plane is divided into a set of subfaults determined by the length and width of the fault plane estimated from the aftershock distribution. Synthetic time histories are generated based upon a velocity structure for the region. An over-determined system of linear equations is formulated in matrix form,

$$\mathbf{A}\,x = b\,, \tag{4.1}$$

where **A** is the matrix of synthetic time histories, b is the vector of the observations, and x is the vector of dislocation for each individual subfault. Because the matrix **A** is ill-conditioned, linear constraints in the following form,

$$\begin{pmatrix} C_d^{-1}\mathbf{A} \\ \lambda\mathbf{S} \end{pmatrix} x = \begin{pmatrix} C_d^{-1}b \\ 0 \end{pmatrix}, \tag{4.2}$$

where S is a matrix of smoothing constraints in which the difference in slip on adjacent subfaults is set equal to zero, C_d^{-1} is an a priori data covariance matrix, and λ are linear weights, are applied to the system of equations before the inversion is computed. The

standard resolution and information matrices are not computed for any of the inversion models studied in this analysis.

Errors in the fit between the observed and computed waveforms for the estimation of the fault slip on the fault plane are introduced due to measurement uncertainty in the former and assumptions in the latter. Specifically, the synthetic seismograms are computed based on an adopted velocity structure for the region. However, because of the limitations of computing resources, site and path specific velocity structure models were not incorporated in any of the 12 cases in Table 4.2. For the local strong ground motion time histories, the fit could be improved by using empirical Green's functions in place of the synthetic time histories (Hartzell, 1989). However, for each earthquake studied here, empirical Green's functions from aftershocks were either not available or not used.

In all cases, the location on the fault plane of largest slip will have some uncertainty associated with it. An independent computation was made in this work to assess this uncertainty for each earthquake in the up-dip and the along-strike direction of the fault plane. (These error values are listed in Table 4.2.) For each fault slip model, the error estimate was based on the contour of 80% of the largest slip on the fault plane. In addition a subjective quality rating of the inversion results was attempted for each earthquake, with a rating of A being the best fit to the observed data. This relative judgment was based on initial analysis of each published inversion. The cases of the two Livermore earthquakes were rated as C, for example, even though the assessed error estimates are lower than the other earthquakes because the physical constraints were weak and the misfit between the model seismic moments and independently measured values (see section 4.2.3-4). At the other extreme, the case of the Northridge earthquake was rated A because of the agreement between the model and the observations and the agreement with other published fault slip inversion models (e.g., see Dreger, 1994).

Table 4.2 List of fault inversion models and error estimates used for the regression analysis.

Strike-Slip Earthquakes

Earthquake	Inversion Model	Quality	Error along Strike	Error along Dip	Data
1979 Imperial Valley	Hartzell and Heaton (1983)	B	± 3.2 km	± 1.7 km	T,S
1980 Livermore MS	Becker (1993)	C	± 1.1 km	± 1.5 km	S
1980 Livermore AS	Becker (1993)	C	± 1.3 km	± 1.2 km	S
1984 Morgan Hill	Hartzell and Heaton (1986)	B	± 0.8 km	± 1.2 km	S
1986 North Palm Springs	Hartzell (1989)	B	± 0.8 km	± 1.1 km	T,S
1987 Superstition Hills	Wald, Helmberger, and Hartzell (1990)	B	± 0.8 km	± 2.5 km	S
1989 Loma Prieta	Wald, Helmberger, and Heaton (1991)	A	± 3.0 km	± 1.9 km	T,S
1992 Landers	Wald and Heaton (1994a)	A	± 3.3 km	± 5.2 km	G,T,S

Reverse-fault Earthquakes

Earthquake	Inversion Model	Quality	Error along Strike	Error along Dip	Data
1971 San Fernando	Heaton and Helmberger (1979)	C	± 4.4 km	± 1.5 km	S
1987 Whittier Narrows	Hartzell and Iida (1990)	A	± 0.6 km	± 0.3 km	S
1991 Sierra Madre	Wald (1992)	A	± 1.4 km	± 0.6 km	T,S
1994 Northridge	Wald and Heaton (1994b)	A	± 1.6 km	± 1.5 km	S

All of the earthquakes examined were classified into two sub-sets based on the type of earthquake mechanisms: either strike-slip or reverse fault mechanisms. Even though certain earthquakes, for example, 1989 Loma Prieta earthquake, contained a substantial amount of dip slip motion (Wald et al., 1991), the overall rake for the event (145°) indicates its classification as a strike-slip seismic mechanism. Because of the limited number of observations for the four reverse-fault earthquakes, separation of the sample based on the location of the recording station on either the hanging-wall or the foot-wall was not considered in this research.

4.1.2 Distance Calculation

There are many different definitions of recorder ("site") to seismic source distance presently used with the different sets of attenuation relations for peak ground acceleration (see section 2.1). In the case of maximum displacement regression, there is a strong case for a fresh consistent definition of distance. Maximum ground displacement, which involves long wave periods (e.g., 0.5 - 2 seconds) must physically be generated over an extended area containing the region of largest energy release on the fault surface. This mechanism is observed on the horizontal components of displacement from the 1987 Superstition Hills earthquake recorded at POE (Figure 4.1). The largest displacement is generated from the large region of slip located south of the earthquake hypocenter (see section 4.2.6 for further details). The seismic energy from the closest portion of the fault plane is marked on the displacement time history. This basic generation mechanism is known to be complicated in certain cases by a multiple slip pattern giving rise to the observation of significant amplitude long wave-length motion from separate sources on the fault plane (e.g., see the discussion of multiple seismic sources for the 1994 Northridge earthquake in section 4.3.4).

In the following estimations H_{slip} for each site was determined based on the location of largest slip of the fault slip model. This location of largest slip was adopted from the published fault slip model for each earthquake and are tabulated in Table 4.3. It should be noted that, in each earthquake the location of the largest slip never coincided with the either the initial hypocenter or the

Table 4.3 Hypocentral location of largest slip on the fault plane for the 12 earthquakes used in the regression analysis.

Earthquake	Mechanism	Latitude (° North)	Longitude (° West)	Depth (km)	Magnitude (M_W)
1971 San Fernando	Reverse	34.400	-118.333	1.8	6.7
1979 Imperial Valley	Strike-Slip	32.755	-115.450	5.9	6.5
1980 Livermore MS	Strike-Slip	37.813	-121.775	7.8	5.8
1980 Livermore AS	Strike-Slip	37.756	-121.718	10.3	5.4
1984 Morgan Hill	Strike-Slip	37.192	-121.600	6.7	6.1
1986 North Palm Springs	Strike-Slip	33.992	-116.583	10.5	6.2
1987 Superstition Hills	Strike-Slip	32.957	-115.733	10.0	6.6
1987 Whittier Narrows	Reverse	34.050	-118.081	15.3	6.0
1989 Loma Prieta	Strike-Slip	37.103	-121.933	12.1	7.0
1991 Sierra Madre	Reverse	34.245	-118.015	11.3	5.6
1992 Landers	Strike-Slip	34.483	-116.508	7.1	7.2
1994 Northridge	Reverse	34.264	-118.561	14.7	6.7

closest part of the fault plane to the site. Figure 4.2 illustrates the distance definition used. In the figure, the fault slip model for the earthquake is contoured, with larger slip values indicated by the darker shading. In this case there are two localized regions of slip on the fault plane with a larger maximum slip occurring north of the initial

hypocenter and the corresponding H_{slip} distance is labeled. A map view of each earthquake showing the location of the largest slip and initial hypocenter is given in the following sections pertaining to each earthquake (sections 4.2-4.3). Figure 4.3 is a graph of the distribution of the sample for the eight strike-slip earthquakes of H_{slip} versus M_W. The top figure is for soil sites (see section 4.1.4), while the bottom figure is for rock sites. The observations are not evenly distributed over M_W and H_{slip}, with a large majority of strong ground motion recordings from moderately sized earthquakes (M_W = 6.0 - 7.0) at distances between 10 - 100 km.

4.1.3 Rotation of Horizontal Components

Prior to the processing of the strong ground motion accelerograms, a rotation of the two horizontal components into a radial and transverse component of motion was performed. A difficulty arises in determining the angle of rotation for a site located close to a moving extended source because as the rupture front passes by the site, the radial and transverse angle changes. However, for the work presented here, the rotation was computed relative to the largest slip on the fault plane (see Figure 4.2) to isolate the SH motion generated from the largest slip on the fault plane onto the transverse component of motion. However, this does not necessarily isolate the motion generated from the other regions of slip on the fault plane. For strong ground motion stations which are located close to the rupturing fault source (e.g., for distances less than 10 km), the effects of rupture directivity will modify the observed amplitudes of ground motion (see section 3.5). The rotation procedure mentioned above will not eliminate the rupture directivity effects, which will be shown later to cause a scatter in the measured peak ground displacement values from the mean estimates.

4.1.4 Site Selection

Based on published geological evidence, each strong ground motion recording site was classified as either a rock site or a soil site. A comparison will be made in chapter 6 between the mean attenuation curves for rock and soil sites. Recent attenuation relations for peak ground acceleration (Boore et. al, 1993; 1994) have further separated the local geological site conditions into four separate categories (A, B, C, and D) based upon the seismic shear velocity in the upper 30 meters below the site (see Table 2.2). As was discussed in section 2.1, this further site separation based solely on the shear wave velocities of the upper 30 meters beneath a recording site is not as critical for the longer wave-length displacement motion than for the shorter wave-length accelerations motion, and is not adopted.

For the eight strike-slip earthquakes studied, the displacement time histories from a total of 181 strong ground motion sites were used. There are more than twice as many soil sites as rock sites, with a 122 soil sites and 59 rock sites. The distribution of the sample for the rock and soil classification for strike-slip earthquakes is listed in Table 4.4. It should be noted that only the 1989 Loma Prieta and 1992 Landers earthquakes contain a sizable number of rock strong ground motion recordings.

The corresponding distribution of rock and soil sites for the four reverse fault earthquakes are listed in Table 4.5. There are a total of 42 rock sites and 115 soil sites. Approximately 83% of the total number of observations for the reverse earthquakes are from the 1987 Whittier Narrows and 1994 Northridge earthquakes in southern California. Because of this limited sampling of peak displacement measurements, the estimated attenuation curves for peak ground displacement from reverse-fault mechanism seismic sources should not be extended without consideration of the limited dataset to other tectonic regions and magnitude ranges. As was the case for the strike-

slip earthquakes, the number of soil sites is approximately twice the number of rock sites.

Table 4.4 Distribution of rock and soil strong ground motion sites for strike-slip earthquakes.

Earthquake	Magnitude (M_W)	Number of Rock Sites	Number of Soil Sites
1979 Imperial Valley	6.5	2	32
1980 Livermore MS	5.8	1	6
1980 Livermore AS	5.4	1	5
1984 Morgan Hill	6.1	7	18
1986 North Palm Springs	6.2	7	11
1987 Superstition Hills	6.6	1	10
1989 Loma Prieta	7.0	27	25
1992 Landers	7.2	13	15

Table 4.5 Distribution of rock and soil strong ground motion sites for reverse-fault earthquakes.

Earthquake	Magnitude (M_W)	Number of Rock Sites	Number of Soil Sites
1971 San Fernando	6.7	7	14
1987 Whittier Narrows	6.0	16	66
1991 Sierra Madre	5.6	3	3
1994 Northridge	6.7	16	32

4.1.5 Long Period Data Processing

All of the digital data were accessible in the form of acceleration time histories for each event. The primary source was the strong motion database run by the Southern California Earthquake Center (SCEC) (Archuleta et al., 1994). The SCEC database

contains the digital strong motion accelerograms from earthquakes since 1993 in northern and central America (Seekins et al., 1992). Additional accelerograms were obtained from the Southern California Edison (Kelly, 1992) and TERRAscope for the 1992 Landers earthquake. Digital strong ground motion accelerograms for the 1987 Superstition Hills earthquake and the 1991 Sierra Madre earthquake were obtained from D. Wald. The accelerograms from the Livermore earthquakes were provided by A. Becker. The digital data for the more recent (since the 1989 Loma Prieta earthquake) was obtained directly from the California Division of Mines and Geology (CSMIP).

Prior to the selection of the peak strong ground motion displacement, the acceleration time history must be processed to obtain the displacement seismograms There has always been a numerical difficulty with the process of integration of strong ground motion accelerograms to obtain displacement time histories mainly due to the presence of significant long period noise. To alleviate this problem, a standard procedure was adopted for all of the time histories examined in this work. First, the Fourier transform of the acceleration data was examined to determine the low end corner frequency at which the signal energy is still greater than the noise energy. For the CSMIP data, the low end frequency corner, provided from its processing procedure, was accepted. For the larger earthquakes the low end corner frequency was approximately 0.1 - 0.2 Hz. Moreover, this range was constant for each earthquake but varied depending on the individual sites.

Prior to integration of the accelerograms, the time histories had the mean value removed from them to account for any constant shift in the baseline. Next, a least-squares fit to a straight line was fit to the data and then removed from the data to account for any constant rate of drift in the record. Integration of the accelerogram was first performed using the trapezoidal method to obtain the velocity time histories and repeated again to obtain the displacement time histories. Finally, a 4-pole Butterworth high pass filter was applied with the low corner frequency being previously

determined. The time histories were passed through the filter twice to preserve the phasing of the displacement records. It should be noted that this long period data processing procedure is similar to the standard procedure implemented by CSMIP for strong ground motion accelerograms and a comparison of the two procedures return the same maximum displacement values.

The maximum recorded displacement was measured in the time window specified in each case. The instrumental response ensures that this value is close to the actual ground displacement. The distribution of peak ground displacement versus H_{slip} is shown in Figure 4.4 for both soil and rock sites from just the strike-slip earthquakes.

After the occurrence of the 1992 Landers earthquake, a processing procedure for near-field accelerograms has been proposed (Iwan and Chen, 1994) which bears on the record resolution and consistency side of the present study. Their proposed methodology is based upon the analysis of strong ground motion accelerograms from the Landers earthquake recorded at a single site. This Lucerne Valley (LCV) site is located approximately 2 km from the fault trace and is near the location of largest slip (see section 4.2.8 and Wald and Heaton, 1994). Iwan and Chen (1994) claim to be able to recover a permanent offset in displacement of a much as 2.6 meters with their new processing technique.

One key aspect of the procedure used in the processing of this Landers accelerogram was the removal of the instrument response to obtain the actual ground motion (Iwan and Chen, 1994). To obtain the instrument response, which is not flat over the entire frequency band, the SMA-2/EMA instrument from the Lucerne Valley station was retrieved and placed on a shake-table at the California Institute of Technology. This response was computed for seventeen frequencies between the values of 0.1 Hz and 40 Hz (Iwan and Chen, 1994). The instrument response begins to fall off for frequencies lower than about 0.3 Hz. At the lowest frequency tested, 0.1 Hz (10 seconds period), the amplification has already dropped by approximately 35%. The questions is how

faithfully can the adopted procedure recover the very long period motion. At frequencies lower than 0.1 Hz the amplification of the recording instrument is so low (less than 35% at a second) that the very long period energy may not be amplified above the long period noise. Based on Fourier analysis, the permanent offset seen in the Landers displacement records are attributable to seismic energy at a frequency of zero Hz. Therefore, the procedure developed by Iwan and Chen (1994) must remove the instrument response for frequencies lower than 0.1 Hz down to zero Hz. From their estimation of the instrument response curve from laboratory testing of the actual instrument (i.e., frequencies greater than 0.1 Hz), this does not appear to be the case.

Another key point in the above proposed processing scheme for near field strong ground motion records is the assumption that the ground velocity of the recorded time history physically begins and ends at zero (Iwan and Chen, 1994). Based on this assumption, the processing method applies a baseline fit to the beginning and end of the time history. For strong motion instruments with pre-event memory this criterion is valid. However, because the strong ground motion accelerograms from the site at Lucerne Valley were recorded by a *triggered* SMA-2/EMA instrument the initial assumption that the velocity is zero at the start of the record appears incorrect.

This proposed processing scheme for the strong ground motion time histories yielded peak displacement values at the Lucerne Valley station that are substantially higher than previously recorded and processed displacement values (Iwan and Chen, 1994). The reported value is a peak displacement of 260 cm for the transverse component of motion and 146 cm for the longitudinal motion. In this work, based on the uncertainties described above in the lower frequency processing of the time histories, the standard processing procedure used for the other seismograms in the sample outlined above was adopted for the Lucerne Valley accelerograms. Using this standard integration and filtering procedure, the peak displacement in the transverse component of motion is 43.7 cm for the Lucerne Valley site.

4.2 Strike-Slip Faulting Earthquakes

The analysis of strong ground motion displacement seismograms from large crustal earthquakes in California will be divided into two separate categories based on the type of fault mechanism of the earthquake. Strike-slip faulting mechanism earthquakes will be discussed first with the discussion of reverse mechanism sources being deferred to the next section (4.3). The strong ground motion data from a total of eight strike-slip events from California (see Table 4.1) were selected for the estimation of peak ground motion displacement attenuation models and will be presented individually in the following sections.

4.2.1 1979 Imperial Valley

The Imperial Valley earthquake (M_W = 6.5) on October 15, 1979 was generated by rupture of the Imperial fault located in the Imperial Valley in Southern California near the California-Mexico boarder (see Figure 4.5). The Imperial Valley region was well instrumented with strong ground motion accelerometers which recorded the ground motion from the earthquake. A majority of the strong ground motion stations in the region consisted of the 13 stations of the El Centro strong ground motion array, which runs in an NE to SW direction and transverses the Imperial Fault north of the epicenter. Because of the alluvial conditions prevalent throughout the Imperial Valley region, there are only two strong ground motion stations on rock which recorded the earthquake.

The epicenter was located in Mexico at a latitude of 32.614° N, a longitude of -115.318° W, and a depth of 12.1 km (see Figure 4.5). Examination of the large amplitudes recorded on the El Centro array stations relative to the other strong ground motion stations surrounding the fault source indicated a northerly propagating rupture

on the Imperial fault (e.g., Niazi, 1982; Spudich and Cranswick, 1982). Hartzell and Heaton (1983) performed an inversion on the strong ground motion time histories, as well as, the teleseismic seismograms to obtain a model of the fault slip. The teleseismic data constrained the dip of the fault to be $90^{o} \pm 5^{o}$ down from horizontal. The strike of the fault was fixed at N 143^{o} W, which corresponds to the average surface trend of the Imperial fault. The rake angle was allowed to vary from pure right lateral strike-slip to pure dip-slip, however, the amount of dip-slip motion for their final fault slip inversion is negligible when compared to the strike-slip motion.

The final inversion model of Hartzell and Heaton (1983) represents the seismic source as a northerly propagating rupture with a maximum slip of approximately 190 cm located 14 km north of the epicenter. This adopted region of largest energy release on the fault plane for the Imperial Valley earthquake and is indicated in Figure 4.5 (also see Table 4.3). The estimates of the error in location of the largest slip on the fault plane are presented in Table 4.2 for both the along-strike and up-dip direction. The total seismic moment for the final model of Hartzell and Heaton (1983) is 5.0e25 dyne-cm, which corresponds to a moment magnitude of $M_W = 6.5$.

Figure 4.5 shows the Imperial Valley region of southern California with the strong ground motion stations plotted with solid squares. The azimuthal coverage relative to the largest slip on the fault plane is relatively uniform. A total of 35 strong motion stations were examined for the determination of attenuation relations for peak ground motion displacement. Approximately one third of all of the strong motion stations were located north of the region of largest energy release (see Figure 4.5). Because of the amplitude magnification effects due to the rupture directivity (see section 3.5) of the northerly propagating rupture, the stations located north of the region of largest energy release were expected to experience higher peak ground displacements. This hypothesis was confirmed observationally; the largest recorded peak displacement for the Imperial Valley earthquake was recorded at station E06

located just east of the Imperial fault (see Figure 4.5). The peak transverse displacement was 48.6 cm and the peak vertical displacement was 16.3 cm.

4.2.2 1980 Livermore 1/24/80

The Livermore Valley region of Central California experienced a moderate, M_w = 5.8, earthquake on the morning of January 24, 1980. The epicenter was located at a latitude of 37.826° N and at a longitude of -121.786° W with a depth of 8 km (Becker, 1993) (see Figure 4.6). Despite the relative small size of the earthquake, the event was recorded on number of strong ground motion sites in and around the San Francisco Bay region. Surface faulting was observed and the earthquake is assumed to be produced by fault slip at depth on the Marsh Creek - Greenville fault system (Bolt et al., 1981). The aftershocks within the first 24 hours indicated that the fault rupture propagated to the southeast from the initial epicentral location (Boatwright and Boore, 1982). A large (M_w = 5.4) aftershock occurred approximately 14 km south of the mainshock three days later on January 27, 1980 and will be discussed in the following section.

Past examinations of the strong ground motion, as well as, broad-band recordings from the earthquake indicated a southeasterly propagating rupture on a nearly vertical right lateral strike-slip fault (Bolt et al., 1981; Schechter, 1981; Boatwright and Boore, 1982). A more recent study (Becker, 1993), examined the strong ground motion data from the Livermore Valley earthquake to investigate the effects of directivity. The Livermore Valley earthquake triggered 33 strong motion instruments in the immediate source region. However, only ten sites contained recordings of high enough quality for digitization to be used in an isochron inversion for the fault slip model of the seismic source (Becker, 1993). The strike of the fault was assumed to be N34°W, with a dip of 86° to the SW. The final slip model is characterized by a region of high slip (maximum slip of 256 cm) initiating near the hypocenter and propagating

southeast along the fault. The location parameters for the largest energy release are listed in Table 4.3 and the corresponding uncertainties in its location are listed in Table 4.2. The seismic moment computed from the isochron slip model is 3.0e25 dyne-cm. However, this is larger by an order of magnitude than the estimates of the seismic moment by other authors, Bolt et al., (1981). Because of the uncertainties discussed by Becker (1993), the estimate of seismic moment for the Livermore Valley mainshock earthquake is taken to be 5.3e24 dyne-cm (Bolt et al., 1981).

The epicenter of the mainshock is plotted in Figure 4.6 along with the strong ground motion stations. Although the time histories from ten stations were initially digitized (Becker, 1993), only eight stations were selected as being acceptable for this study. Two stations were rejected because of their location inside of a large building or engineered structure, which can influence the response of the recording instrument in the longer periods of interest. The azimuthal distribution of the strong motion stations relative to the largest slip is not ideal with the majority of the stations located southwest of the earthquake. A large amplification of ground accelerations due to rupture directivity for stations to the south, as has been argued by previous authors, Boatwright and Boore (1982), can also be seen in the peak ground displacements.

Only the station at the California State University, Hayward Stadium (HSG) was located on rock. The other seven sites are classified as soil sites. This moderate moment earthquake did not produce large amounts of seismic energy above the noise level in the long period range, so that the time histories were high-passed filtered with a low frequency corner of between 0.3 - 0.45 Hz before integration from acceleration to displacement.

The largest peak displacement occurs at the KOD site with a transverse amplitude of 3.6 cm and a vertical amplitude of 0.5 cm. However, as was noted by previous studies (Boatwright and Boore, 1982; Becker, 1993), the peak ground motions at the KOD are anomalous when compared to the other peak ground motions in the

area and the large amplification is attributable to a large site response. More specifically, the peak ground displacement amplitudes at the nearest site, SRM, are lower by a factor of 8 for the transverse and a factor of 2 for the vertical component. Because of the presence of the large site response at KOD, these peak ground displacement values were not used in this research. Disregarding KOD, the largest peak ground displacement for the earthquake occurs at the LVA station with a SH peak displacement of 2.6 cm and a SV peak displacement of 0.6 cm.

4.2.3 1980 Livermore 1/27/80

Three days after the Livermore Valley earthquake on January 24, 1980, a large aftershock of M_W = 5.4 struck the Livermore Valley region. The epicenter of this aftershock was located at the southern end of the primary rupture area for the mainshock on January 24 and was at a latitude of 37.750° N and a longitude of -121.712° W, with a depth of about 10 km (Becker, 1993) (see Figure 4.7). As was the case for the mainshock, this earthquake was recorded on several strong ground motion sites in the San Francisco Bay region.

Aftershocks from the January 27 earthquake indicated that the rupture propagated in a northwesterly direction, opposite of the mainshock earthquake three days earlier (Cockerham et al., 1980). Becker (1993), performed an isochron inversion on the recorded displacement time histories from the aftershock to obtain the fault slip model. The identical fault strike of N34°W and dip of 86° SW as assumed for the mainshock, was adopted for this inversion. The largest slip on the fault plane (a maximum slip of 138 cm) for the aftershock is located near the hypocenter (see Table 4.3). The estimated error uncertainties are listed in Table 4.2. For the final inversion model, the fault rupture propagated unilaterally to the NW along the fault plane. As was the case for the mainshock, the seismic moment, 4.1e24 dyne-cm, computed from

the isochron inversion slip model is higher than the estimated seismic moment of 1.3e24 dyne-cm by other authors (Bolt et al., 1981). Once again the lower estimate for the seismic moment was taken for the aftershock of the Livermore earthquake.

Only six of the strong ground motion stations that recorded the mainshock were operable and recorded the aftershock (Figure 4.7). The Tracy (TRA) station, did not record the aftershock. As was the case for the mainshock, the azimuthal coverage of the stations is not ideal. HSG was again the only rock site of the six stations.

Unlike the mainshock, it was observed that due to rupture directivity effects (see section 3.5) the amplitudes of ground accelerations were increased at the northerly stations instead of the southerly stations (Boatwright and Boore, 1982). For the peak displacement values, the effect of directivity is not as observable because the peak values at the northerly station ANT are of the same order as the rest of the measurements. Similar to the time histories for the mainshock, the aftershock time histories were high-passed filtered with a low corner frequency of between 0.3 - 0.6 Hz before integration from acceleration to displacement to remove the long period noise.

The peak displacement values at the KOD strong motion station were again anomalously high for the aftershock. The peak transverse displacement of 2.6 cm was larger than the peak value for the nearby SRM site by a factor of approximately 6. The amplification between the two sites for the vertical displacement was not as great (i.e. approximately a factor of 3). The anomalous time histories recorded at the KOD site from the aftershock were discussed in previous studies (Boatwright and Boore, 1982; Becker, 1993) as being caused by a site response and hence were not used in the empirical development of peak displacement attenuation curves.

4.2.4 1984 Morgan Hill

The moderate size (M_W = 6.1) Morgan Hill earthquake was felt throughout Central California. The earthquake occurred on April 24, 1984 and had an epicentral location of 37.309° N, -121.678° W, and a depth of 8.4 km (see Figure 4.8). The earthquake is assumed to have been caused by fault rupture on the Calaveras fault. Damage from the earthquake was concentrated in the town of Morgan Hill and at the southern end of Anderson Reservoir. Aftershock locations, as well as the first motion plots for the mainshock, indicate a right-lateral strike slip movement to the south of the epicenter (Hoose, 1987). Visual examination of the strong ground motion time histories and simple earthquake location estimates, indicated an second energetic source located 16 - 20 km south of the epicenter near the southern end of rupture (Bakun et al., 1984).

The general fault strike of the Calaveras fault in the ruptured portion is N27°W, although individual segments in the area vary in strike by as much as 24° (Hoose, 1987). Hartzell and Heaton (1986) performed an fault slip inversion using the recorded strong ground motion velocity time histories from 11 stations. The strike and dip of the fault plane were constrained to be N32°W and 90° down from horizontal, respectively. Based on aftershock locations, the length of the fault was determined to be 32 km and the width was 11.5 km. (The majority of elastic dislocation, determined from their inversion model, only occurs over a fault length of approximately 25 km.) The slip on the fault plane can be divided into two main regions of slip, with the larger region of slip (amplitudes larger by a factor of 3 with a maximum of approximately 110 cm) located about 14 km south of the hypocenter (Hartzell and Heaton, 1986). The errors in location are listed in Table 4.2. The strong ground motion stations are plotted in Figure 4.8. The seismic moment computed from the fault slip model is 2.1e25 dyne-cm (Hartzell and Heaton, 1986), which is similar to the geodetic estimate of 1.9e25 dyne-cm (Prescott et al., 1984).

Due to the number of strong ground motion accelerometers located in Central California, the Morgan Hill earthquake was recorded on 75 instruments ranging in epicentral distance of 4 km to 100 km. However, only a total of 25 strong motion stations had digital records available and were used in this work. Seven of these sites were rock sites and 18 were soil sites (see Table 4.4). The azimuthal distribution of stations is not ideal with a approximately half of the station located southwest of the earthquake along the strike of the fault. Large ground motions would be expected for these stations due to rupture directivity (see section 3.5) from the unilaterally propagating seismic source.

4.2.5 1986 North Palm Springs

On July 8, 1986 a moderate earthquake (M_W = 6.2) occurred approximately 12 km north of the city of North Palm Springs in Southern California. The epicenter of the event was located between the Mission Creek and Banning strands of the San Andreas fault at a latitude of 33.999° N, a longitude of -116.608° W, and a depth of 11.1 km (see Figure 4.9). The location of the aftershocks indicated that the event was caused by fault slip on the Banning strand of the San Andreas fault. The hypocenters of the aftershocks map out a fault plane with a surface trend of approximately N60°W and dipping about 50° to the northeast (Jones et al., 1986).

The earthquake epicenter lies in the northern section of the Coachella Valley alluvial basin. The northeasterly edge of the Coachella Valley is bounded by the Mission Creek fault. Located southwest of the Mission Creek fault is the Banning fault which bisects the northern end of the Coachella Valley and eventually joins the Mission Creek fault approximately 40 km southeast of the epicenter (Jones et al., 1986).

Accelerograms from 18 strong ground motion sites (Figure 4.9) were used to generate the displacement records from the North Palm Springs earthquake. Eleven of

the 18 stations were classified as soil sites and the other seven were as rock sites (see Table 4.4). Eight of the strong ground motion sites are part of the linear array of stations located approximately 30 - 65 km southwest of the epicenter (see Figure 4.9). The array consists of four rock sites and four soil sites and, as would be expected, the waveforms between the individual stations of the array are similar.

Hartzell (1989) inverted the teleseismic seismograms and the local strong ground motion time histories to estimate a rupture model for the North Palm Springs earthquake. The fault was parameterized with a strike of 287° and a dip of 46°. The length of the fault was determined, based on the locations of aftershocks to be 22 km and extend from a depth of 4 km to a depth of 15 km. The fault slip model based on the observed strong ground motion time histories had a problem in fitting the later arriving phases on the time histories (Hartzell, 1989). For this reason, the teleseismic fault slip inversion model was adopted in this research to determine the largest slip on the fault plane. From the teleseismic inversion model, the strike-slip component of fault slip is approximately twice as large as the dip-slip, with a maximum slip of approximately 88 cm located east and up-dip of the hypocenter. Even though there is a dip-slip component of motion for the final fault slip inversion model, this earthquake is classified as a strike-slip mechanism earthquake because the average rake angle is 154°. The uncertainties in the location of largest slip were again computed based on the contours of 80% of the maximum slip and are listed in Table 4.2. The seismic moment from the inversion model is 1.7e25 dyne-cm (Hartzell, 1989).

4.2.6 1987 Superstition Hills

The Superstition Hills earthquake (M_W = 6.6) occurred on November 24, 1987 in the western region of the Imperial Valley in Southern California. The epicenter of the earthquake was southwest of the Salton Sea at a latitude of 33.013° N and a longitude of

-115.838° W (see Figure 4.10). The estimated depth of the focus of the earthquake was 2 km. Seismic waves were generated by fault slip on the northwest trending Superstition Hills fault and right-lateral surface offset was observed along the fault trace (Wald et al., 1990).

The Superstition Hills fault lies to the west of the Salton Trough which is the major tectonic feature of the region. The fault marks the southwestern boundary of the badlands area of the western side of the Imperial Valley (Sharp, 1982). The Imperial Valley is a deep alluvium valley with sediment depths greater than over 6 km (Sharpe, 1982) along the northwest-southeast trending center axis.

Accelerograms from 11 strong ground motion stations (see Figure 4.10) in the region were used for the measurement of peak ground displacement values. Only the Superstition Mountain (SSM) strong motion site is classified as a rock site and the other ten sites are classified as soil sites (see Table 4.4). The digital acceleration time histories for all sites except for the Imperial Valley Liquefaction Array (IVW), were kindly made available by D. Wald. Only the horizontal components of motion were digitized (Wald et al., 1990) for these ten stations. The digital data, both horizontal and vertical components, from the IVW station was obtained from the USGS (Porcella et al., 1987b).

Wald et al., (1990) inverted the strong ground motion time histories from the ten stations in the epicentral region to obtain a model of the fault slip. As was noted by these authors, the fault rupture of the Superstition Hills earthquake can be characterized by three separate sub-events. Wald et al. (1990), computed the seismic moment of the third sub-source to be roughly twice that of the other two sub-sources which is supported by the relative amplitudes of a triplet of arriving SH body waves on the transverse component displacement seismogram from the Parachute Test Site (PTS).

For the fault slip inversion, the fault plane was assumed to have a strike of 127°, a vertical dip of 90°, and the slip was constrained to be right-lateral. A fault length of 20 km and a depth of 12 km was selected based the locations of aftershocks (Wald et al.,

1990). The fault rupture propagates unilaterally in a southeasterly direction away form the hypocenter. The largest slip on the fault plane (maximum slip of 191 cm) is located approximately 12 km along the strike from the hypocenter (see Table 4.3 for location parameters) and the estimated errors in the location are listed in Table 4.2. The total seismic moment for this earthquake, estimated from the inversion, is 4.8e25 dyne-cm with the third sub-event contributing 3.5e25 dyne-cm (Wald et al., 1990).

4.2.7 1989 Loma Prieta

The 1989 Loma Prieta (M_W = 6.9) earthquake took place on October 17, 1989 and was felt widely throughout Central California. Damage was widespread throughout the San Francisco Bay area with a relatively severe region occurring in the northern San Francisco Bay at an epicentral distance of approximately 100 km (see Lomax and Bolt, 1992 for a discussion). This region incorporates the Marina district in San Francisco, the failed span of the San Francisco Bay bridge, and the collapsed section of the Cypress Street viaduct. The epicenter of the earthquake was located at a latitude of 37.040° N and a longitude of -121.880° W, with a focal depth of 17.6 km (Figure 4.11).

The earthquake epicenter is located in the rugged Santa Cruz Mountains which separates the Santa Clara Valley to the northeast from the northern margin of the Monterey Bay to the southwest (Hanks and Krawinkler, 1991). The strike of the San Andreas fault changes in the southern end of the Santa Cruz mountains as it passes through a restraining bend (Ponti and Wells, 1991). The dip of the San Andreas fault also changes from the more typical 90° vertical fault to a dip of 60-70° in the Santa Cruz Mountains (Dietz and Ellsworth, 1990).

The Loma Prieta earthquake was recorded on accelerographs throughout the San Francisco Bay region. A total of 53 digital strong motion sites (Figure 4.11) were obtained from both the U.S.G.S. (Brady and Mork, 1990) and CSMIP (CSMIP, 1989;

Huang et al., 1990a; and Huang et al., 1990b). The sites were equally divided between rock and soil with 25 soil sites and 27 rock sites (see Table 4.4). As can be seen in Figure 4.11, there is a high density of strong ground motion stations located in and around the city of San Francisco (a total of 11 stations) at a distance of approximately 100 km from the source.

The strong ground motion for stations located in the region around the city of San Francisco have a very coherent and large transverse SH displacement pulse, which can be seen at all sites in the region. Two causes for the increase in seismic energy at given locations in San Francisco have been discussed in previous studies. Somerville and Yoshimura (1990) concluded that a significant contribution to the enhanced seismic energy at these distances was due to the critical reflection of seismic energy off of the base of the crust. Later, Lomax and Bolt (1992) examined the 3-D effect of SH wave propagation in the San Francisco Bay region and concluded that part of the horizontal focusing of seismic energy in San Francisco can be attributed to the lateral crustal velocity contrast across the San Andreas fault. Both of the these wave propagation effects contribute to the relative increase in the observed peak displacement values in San Francisco.

Several fault slip inversion models have been published for the Loma Prieta earthquake (e.g., Choy and Boatwright, 1990; Beroza, 1991; Hartzell et al., 1991; Steidl et al., 1991; Wald et al., 1991). The overall general characteristics of slip distribution from each model are similar (i.e., bilateral rupture with two large regions of slip located approximately equidistant from the hypocenter) and demonstrate the robust estimation for fault slip of the earthquake. All of the inferred models have limited slip occurring up-dip of the hypocenter. The slip model of Wald et al. (1991) combined the inversion of both the teleseismic seismograms and strong ground motion time histories, unlike the other models which based their inversions on either just the teleseismic or strong

ground motion data. For this reason the fault slip model of Wald et al. (1991) was selected to determine the location on the fault plane of largest slip.

The fault plane was modeled with a length of 40 km long, strike of N 128° E, and dip of 70° to the southwest (Wald et al., 1991). The dimension of the fault plane were determined based on the location of major aftershock activity while the strike and dip were selected based on the teleseismic broadband inversion results of Kanamori and Satake (1990). The rupture history can be described by two large regions of slip, with the largest slip (a maximum slip value of approximately 350 cm) being located about 6 km northwest of the hypocenter and the other smaller localized slip region being located approximately 5 km southeast of the hypocenter. The error in the location of largest slip is listed in Table 4.2. The computed seismic moment for the fault slip inversion model is 3.0e26 dyne-cm (Wald et al., 1991).

4.2.8 1992 Landers

The Landers California earthquake (M_W = 7.2) occurred on June 28, 1992 in the desert region of southern California located east of the Los Angeles metropolitan area (see Figure 4.12). The Landers earthquake is the largest to strike southern California since the 1952 Kern County earthquake (M_W = 7.4). Strong-motion instruments recorded the earthquake over a wide distance range (i.e., from 2 km from the fault rupture to 200 km at sites located in the Los Angeles basin).

The hypocenter of the Landers earthquake was at a latitude of 34.201° N, longitude -116.436° W, and a depth of 4.5 km (SCEC catalog). The earthquake ruptured over three faults (Johnson Valley, Homestead Valley, and Camp Rock/Emerson fault) for a total length of approximately 70 km. The rupture started on the Johnson Valley fault and propagated unilaterally to the north. There was some rupture in the southern direction for approximately 10 km, however, this seismic energy release for this section

of the fault plane is small in comparison to the northern segment (Wald and Heaton, 1994a).

A fault slip inversion model has been computed by inverting the near field strong motion time histories (see Wald and Heaton, 1994a). They modeled the Landers earthquake as a combination of three separate faults, each with a different strike. The rupture is fixed to be right-lateral strike-slip. From their inversion model, the largest slip (slip of over 6 meters) occurs approximately 32 km north of the hypocenter (on the Homestead Valley fault). This location is indicated in Figure 4.11 (see Table 4.3 for location parameters). This location on the fault plane also agrees with the observed surface location of largest seismic offset (Wald and Heaton, 1994a). The corresponding errors for the largest slip location from the inversion model are listed in Table 4.2. The total seismic moment for the Landers earthquake from the inversion model was computed to be 7.7e26 dyne-cm (Wald and Heaton, 1994a).

There were a total of 28 strong ground motion stations for the Landers earthquake (Figure 4.12), with 15 soil sites and 13 rock sites (see Table 4.4). Digital accelerograms were obtained from three separate sources: California Strong Motion Instrumentation Program (CSMIP), TERRAscope, and Southern California Edison (SCE). The azimuthal distribution of strong-motion stations nearly ideal, with an azimuthal gap of approximately 25° located to the northwest of the earthquake.

A data set of digital strong motion accelerograms from the Los Angeles basin processed and operated by the University of Southern California (U. S. C.) was initially analyzed. Strong motion time histories from 27 sites, which were all located in the Los Angeles basin, were examined. The peak ground displacements selected from the U. S. C. sites were smaller in absolute value than the peak displacement values from nearby CSMIP strong motion sites. Not only were the peak values different, but the frequency content and phasing of the time histories were strikingly different. All of the time histories in the Los Angeles basin processed by CSMIP showed a large surface wave

pulse with a period of approximately 10 seconds. However, this large displacement pulse was not observed on any of the U. S. C. sites in the Los Angeles basin. To investigate the differences between the sets of time histories, two U. S. C. stations, COM and LBC, and one CSMIP station, DOW were examined. All three stations are located approximately 165 km from the earthquake (see Figure 4.12). The transverse component of displacement for the three stations are plotted in Figure 4.13. The discrepancy in the peak displacement amplitudes as well as the frequency content of the time histories are noticeable. Figure 4.14 shows the transverse components of motion for the three stations with the DOW seismogram high passed filtered (4-pole Butterworth) with a corner frequency at 0.3 Hz. This processing of the DOW record produces similar displacement time histories in amplitude and phasing. These results along with other comparisons demonstrate that the U. S. C. strong motion data has been high passed filtered with a relatively high cut-off frequency (i.e., approximately 0.3 Hz) and is not compatible with the spectral frequency range used in measuring the peak displacement values on the other displacement seismograms in this study (basically a spectral range of 0.1 Hz to 23.0 Hz). As a consequence, the U. S. C. observations were not used in this research.

There were two strong motion stations provided by SCE (Lucerne Valley (LCV) and Coolwater Generation Plant (COL)) that were located close to the fault (see Figure 4.12). The COL station is classified as a soil site and the LCV site is classified as rock. In the processing of the strong motion accelerograms to obtain the peak ground displacement, a high pass filter (4-pole Butterworth) with a corner frequency of 0.4 Hz was adopted to reduced the long period noise in the time history (see section 4.1.5). Due to this relatively high corner frequency, the measured peak ground displacements were considered to be underestimated, as was noted for the U. S. C. strong ground motion sites, and was not used for this study. The long period processing of the LCV accelerograms was previously discussed in section 4.1.5.

Rupture directivity effects greatly effects the peak ground displacement values for the Landers earthquake due to the predominately unilateral rupture of the event (see section 3.5). Stations located to the north (e.g., Barstow (BRS)) exhibit greater amplitudes and shorter duration of ground displacement than stations located to the south (e.g., Desert Hot Springs (DSP)). In contrast, stations located to the east and west of the seismic source have amplitudes and durations of intermediate size.

4.3 Reverse Faulting Earthquakes

A total of four earthquakes (see Table 4.1) from California were examined for the estimation of attenuation relations of peak ground displacement from reverse fault mechanism earthquakes. All of the earthquakes were located in the greater Los Angeles basin region. The sample of strong ground motion records from the four earthquakes is dominated by the measurements from the 1987 Whittier Narrows and 1994 Northridge earthquakes, which make up approximately 80% of the dataset (see Table 4.5). Each of the four earthquakes will be examined and presented in the following sections.

4.3.1 1971 San Fernando

The San Fernando earthquake (M_W = 6.7) occurred on February 9, 1971 with an epicentral location in the San Gabriel Mountains (34.410° N, -118.400° W) and a hypocenter depth of 8.4 km (see Figure 4.15). Major damage occurred in the cities of San Fernando and Sylmar located in the northwestern part of the San Fernando Valley. At the time of the earthquake the regions around the San Fernando and Los Angeles basins were instrumented with strong ground motion accelerometers and these recorded accelerograms provided the first large set of time histories for use in studies of

attenuation of seismic waves from a large earthquake and other aspects of seismic intensity.

The initial fault plane solution for the earthquake indicated thrust motion on a fault plane striking approximately N70°W and dipping approximately 50° NE (Allen et al., 1975). This is in agreement with the regional tectonic setting of the San Gabriel Mountains, which form a rugged barrier separating the Mohave Desert to the north from the San Fernando, San Gabriel, and Pomona valleys to the south (Ehlig, 1975). The elevation of the San Gabriel Mountains is attributable to the uplift resulting from reverse faulting along the southern boundary of the mountains and from arching along the northern boundary (Ehlig, 1975). Sediments in both the San Gabriel and San Fernando basins reach depths of approximately 3 km, while sediments in the Los Angeles basin reached structural depths of up to 9 km (Graves, 1995). The effect of geometry and rock types in such basins on ground motion has been previously discussed in section 3.4.

As was the case for the strike-slip earthquakes, the fault rupture history must be known for the earthquake to determine H_{slip} for the regression analysis. Because the methodology of fault slip history inversion from local strong ground motion time histories for regional velocity and geologic structure (see section 4.1.1) had not been routinely performed for earthquakes prior to 1971, the estimation of the fault rupture slip was estimated with a forward modeling procedure by Heaton and Helmberger (1979). This methodology used generalized rays to compute models of fault slip on a fault. In their comparison with observed seismic waves, only four strong ground motion stations were selected in the study due to the labor at that time of the calculations performed for each source to station geometry. They adopted two separate fault plane sections hinged together at a depth of 5 km, which is in agreement with teleseismic studies of the event (Langston, 1978). The lower portion of the fault plane had a dip of 53° and the upper section had a shallower dip of 29° (Heaton and Helmberger, 1979).

Their best fitting model for the fault slip is characterized by two main regions of slip on the fault surface. A broad region of slip of approximately 2 meters begins at the hypocenter and propagates up-dip in a southerly direction. The largest fault slip (amplitude of approximately 5 meters) occurs on the upper portion of the hinged fault plane, at a depth of 1.8 km (see Table 4.3 for the location parameters). The error in location of the region of largest slip have been estimated based on the 80% of the maximum slip contour. The errors along strike are $\pm$ 4.4 km and $\pm$ 1.5 km along the dip of the upper section of the fault plane (see Table 4.2). Because of the non-uniqueness in the forward modeling procedure used for the San Fernando earthquake, the quality of the resolution of the fault slip history is low and was classified as C. The total seismic moment for the earthquake model was computed to be 1.4e26 dyne-cm (Heaton and Helmberger, 1979).

A total of 21 strong ground motion stations (Figure 4.15) were examined with seven sites being classified as rock and 14 as soil (see Table 4.5). The stations range in H_{slip} distance of 8.4 km at Pacoima Dam (PDW) to 179.7 km at Anza Post Office (AZP). The largest displacement (17.2 cm horizontal and 12.3 cm vertical) occurred at the PDW, located up-dip from the hypocenter.

4.3.2 1987 Whittier Narrows

Sixteen years after the 1971 San Fernando earthquake, the 1987 Whittier Narrows (M_w = 6.0) earthquake occurred east of Los Angeles. It was the largest earthquake to occur west of the San Andreas fault in southern California since 1971 (Hauksson and Jones, 1989). The epicenter was located in the northeastern portion of the Los Angeles basin at a latitude of 34.049° N and a longitude of -118.081° W, with a hypocentral depth of 14.6 km (Hauksson and Jones, 1989) (see Figure 4.16). After the 1971 San Fernando earthquake two independent strong ground motion instrumentation

programs for the Los Angeles basin were instituted by the CSMIP and by the University of Southern California. Approximately 300 strong-motion instruments recorded the Whittier Narrows earthquake in the greater Los Angeles region (Hauksson and Stein, 1989).

Prior to the Whittier Narrows earthquake, the major seismic hazard in the Los Angeles basin was dominated by earthquakes which would be generated by slip on the west striking reverse faults of the Transverse Ranges and the north to northwest striking strike-slip faults of the Peninsular Ranges (Hauksson and Jones, 1989). However, the source of the Whittier Narrows earthquake was located south of the reverse Sierra Madre fault and northwest of the strike-slip Whittier fault. Aftershock locations indicated that the Whittier Narrows earthquake was generated by fault slip on a north dipping reverse fault at depths between 10 to 16 km (Hauksson and Jones, 1989). No surface faulting was observed from this blind thrust fault and all the evidence indicates that the Whittier Narrows earthquake was generated by slip on a blind thrust fault which is part of the Elysian Park fault system (Hauksson and Jones, 1989). The Elysian Park fault system of a series of blind thrust faults which gently dip to the north and strikes in a westerly direction beneath the Los Angeles basin. The identification of this fault system, as well as the possibility of other earthquakes generated on separate blind thrust faults in the Los Angeles region and the strong ground motion data obtained from the 1994 Northridge earthquake, has increased the need for updated and more current estimates of peak parameter ground motion for large acceleration, velocity, and displacement (Heaton et al., 1995).

Because of the high density of strong ground motion stations in the Los Angeles basin (see Figure 4.16) at the time of the earthquake, the inversion for the fault slip history of the Whittier Narrows earthquakes has the best station azimuthal distribution of any of the 12 earthquakes examined in this study (i.e., the fault inversion model was classified as A, see Table 4.2). Hartzell and Iida (1990) performed an inversion based on

the velocity time histories from 17 strong ground motion stations located less than 15 km from the epicenter. The fault plane was modeled with strike of 280° and a dip of 30°. Both the down-dip and along strike distance was taken as 10 km, to encompass the distribution of aftershocks. Their final inversion model for fault slip can be characterized by four separate regions of high slip, which agrees with other published results on the source complexity (e.g., see Bent and Helmberger, 1989). The largest slip on the fault plane of 90 cm is located down dip and to the north of the epicenter (Hartzell and Iida, 1990). This large slip is located at a depth of 15.3 km, which is 0.7 km deeper than the hypocenter (see Table 4.3 for latitude and longitude parameters). The error estimates for this location are listed in Table 4.2. The estimated seismic moment for the Whittier Narrows earthquake is 1e25 dyne-cm, based on the inverted fault slip model (Hartzell and Iida, 1990).

A total of 82 free field strong ground motion stations were selected from the available strong ground motion database for the Whittier Narrows earthquake (see Table 4.5) and are plotted in Figure 4.16. A total of 16 strong ground motion stations were classified as rock sites, while the remaining 66 sites were classified as soil sites (see Table 4.5). It should be noted that the Whittier Narrows earthquake contributes the largest percentage of displacement records of any of the 12 earthquakes examined here (see Table 4.4 and 4.5). The stations range in H_{slip} distance of 16.0 km at San Gabriel (SGS) to a distance of 108.7 km at Hemet Fire Station (H05). The largest SH peak displacement from the earthquake of 5.24 cm was recorded at Santa Fe Springs (SFS).

4.3.3 1991 Sierra Madre

Four years after the 1987 Whittier Narrows earthquake, the northeastern portion of the Los Angeles basin experienced another moderately sized thrust earthquake. The Sierra Madre earthquake (M_W = 5.6) occurred on June 28, 1991 with an epicentral

location of 34.262° N and -118.002° W (see Figure 4.17). The hypocenter was located at a depth of 12 km. The earthquake was generated by slip at depth on the Clamshell-Sawpit fault (Wald, 1992). This fault is part of the tectonic boundary of reverse faults between the Transverse Ranges and the northern boundary of the Los Angeles basin. The Sierra Madre fault is an extension of Clamshell-Sawpit fault to the west.

A model of the fault slip history had been published based on the inversion of broadband teleseismic and strong ground motion wave forms (Wald, 1992). The fault plane was selected with a strike of S 62° W and a dip of 50 to the NW. The lateral extent of 7 km along strike and a down-dip width of 6 km was estimated based on the locations of the major aftershocks of the earthquake. The inverted slip history is characterized by a broad region of high slip (maximum slip amplitude of approximately 80 cm) with a location up-dip and southeast of the hypocenter (see Wald, 1992). The errors in the location of largest slip were estimated as $\pm$ 0.7 km along strike and $\pm$ 0.6 km along dip (see Table 4.2) and the estimated seismic moment from the fault slip history model is 2.8e24 dyne-cm (Wald, 1992).

Although the Los Angeles basin was widely instrumented with strong ground motion accelerometers in the epicentral region at the time of the earthquake (e.g., see Figure 4.16 for the Whittier Narrows earthquake), the relative small size of this earthquake did not demand the immediate digitization of strong ground motion time histories. A select set of accelerograms were personally digitized by D. Wald at the California Institute of Technology for the fault slip inversion modeling (Wald, 1992) and were kindly provided to me for the estimation of peak ground displacement values. A total of six strong ground motion stations were analyzed with an even distribution of three rock and three soil sites.

4.3.4 1994 Northridge

The most damaging earthquake (M_W = 6.7) to ever occur in the Los Angeles basin had its origin on January 17, 1994 in the San Fernando Valley. Its epicenter was located approximately 30 km northwest of the city of Los Angeles at a latitude of 34.213° N and a longitude of -118.537° W (Southern California Earthquake Center, 1994); the hypocentral depth of the mainshock was 18.4 km (see Figure 4.18). As was the case in the Whittier Narrows earthquake, no surface faulting was observed from the Northridge event, but suggests that the Northridge earthquake was caused by slip on either an eastward extension of the Oak Ridge fault system or on a southerly dipping blind thrust fault (Dreger, 1994). Aftershock epicenters covered a surface area of about 30 km by 25 km, with the majority located north of the mainshock epicenter (see Figure 4.18). The aftershock hypocenters map out a dipping fault plane with a south dip of approximately 45° (Scientists of the U.S.G.S. and the Southern California Earthquake Center, 1994).

Preliminary analysis of the strong ground motion acceleration and velocity time histories in the immediate epicentral region indicated a multiple stage fault rupture process for the Northridge earthquake (e.g., Bolt and Gregor, 1995). Multiple stages in the fault rupture process for large earthquakes have been well established observationally (e.g., Wyss and Brune, 1967; Trifunac and Brune, 1970; Kanamori and Stewart, 1978; Abrahamson and Darragh, 1985; Choy and Kind, 1987; Choy and Boatwright, 1990). These inferences were based on cross correlation of identifiable P and S phases on seismograms, either from different regional or teleseismic seismographic sites or independently from inversions for fault slip evolution models, using recorded strong ground motions at near-field and far-field distances. The Northridge earthquake provides a further example of a multiple seismic source where at least a significant

mechanism doublet (and perhaps a triplet (Thio and Kanamori, 1994)) can be identified from the strong ground motion records.

Visual analysis of the wave pattern on strong ground motion seismograms makes evident the rupture complexity of the source process of the Northridge earthquake (see Figure 1.1). Such complexity of near-source ground motion is not unusual, but what is striking in this case is that the time histories from strong motion stations in the immediate source area show a large coherent phase (called S_2) arriving with similar time lags of approximately 3 to 5 seconds after the initial S wave arrival (called S_1). This secondary phase is more pronounced on the velocity seismograms than the acceleration and displacement time histories. For certain velocity time histories, the S wave coda energy following the initial S_1 wave onset is too large to discriminate unambiguously the onset of the S_2 phase, but the S_2 phase at 12 strong ground motion stations from different distances and azimuths (see Table 4.6) could reliably be identified for the Northridge mainshock. This secondary phase does not correspond to the arrival of either the Love or Rayleigh wave train predicted from a standard velocity model of the basin and crust. An a prior hypothesis that the secondary phase can be attributed to an initiation point of a second rupture source on the fault plane is tested. Specifically, an attempt is made to locate a secondary (lagged) hypocenter (called H_2) relative to the initial hypocenter location (called H_1) from the arrival times of the onset of the S_2 phases. The establishment of such a second source is important in providing insight into the overall rupture process of the Northridge earthquake and in the discrimination of the predominate shear wave portion of the displacement time histories.

Measurement of the arrival times of the secondary S_2 phase was facilitated by first rotating each horizontal component to the radial and transverse component relative to the mainshock hypocenter location H_1. Because all of the analog strong ground motion records used in this study (except for the Pasadena station records) have no pre-

event memory, the arrival time of the initial P wave cannot be determined. However, the initial S_1, and in some cases, the secondary S_2 wave arrival times can be confidently read within 0.1 sec on selected seismograms. In some cases, joint comparisons of the wave patterns of the corresponding accelerations, velocity, and displacement records were helpful in identifying S_1 and S_2 onsets but the adopted arrival times of both the initial S_1 and secondary S_2 wave phases were determined from the velocity seismograms.

Seventeen S_1 wave arrival times and 12 S_2 arrival times were retained as the most reliable for the hypocenter calculations (see Table 4.6). The hypocenter location algorithm, HYPOELLIPSE (Lahr, 1989) was used to compute the location of the initiation of the assumed secondary source H_2 on the fault plane. A local shear wave velocity model for Southern California developed by Dreger and Helmberger (1991) was used for the location procedure. Station S travel-time corrections were first estimated by keeping the hypocenter and origin time of the initial source H_1 fixed at the values given by Southern California Earthquake Center (1994) and substituting the initial S_1 phase arrival times in the location program (see Table 4.6). The resulting mean S wave station correction for the 17 sites used in the calculations was 0.35 seconds with a maximum of 1.50 seconds at the 116th Street School station. This latter site is located in the Los Angeles basin and the large station correction can be attributed to the slow shear wave velocity characteristics of the alluvium layers of the basin. Other strong motion sites in the Los Angeles basin also show a large positive station correction due to the alluvium layers (see Table 4.6). In contrast, negative station corrections are associated with rock sites.

Table 4.6 **Arrival times, station corrections, and residuals for the initial source H_1 and secondary source H_2.**

	Initial Source		Secondary Source	
Station	Arrival Time*	Station Correction	Arrival Time*	Residual
Pacoima, Kagel Canyon	2.70	-0.29	7.66	1.27
Sylmar	3.18	0.55	6.36	-0.03
U.C.L.A.	3.62	0.33	8.52	-0.47
Newhall	4.03	0.58	5.60	-1.36
Century City	4.38	0.78	9.40	-0.38
Hollywood	5.06	0.83	10.15	-0.12
Malibu	6.48	-0.20	---	---
Moorpark	6.95	0.31	12.17	0.99
Pasadena	6.97	-0.11	11.62	-0.30
Vasquez	7.12	-0.44	9.99	-0.48
Alhambra	8.51	0.29	---	---
Castaic	8.67	0.16	---	---
Lake Hughes #9	9.15	-0.32	---	---
Mount Wilson	9.17	-0.41	15.49	1.56
Obregon Park	9.30	1.23	14.73	-0.03
San Marino	9.36	1.13	---	---
116th Street School	10.13	1.50	15.34	-0.65

* Arrival time in seconds after 12 h 31 min 00 seconds.

The location of H_2 was constrained to lie on the primary fault plane determined by Dreger et al. (1994) with a strike of 121° and a dip of 43°. This assumption is reasonable because no fault inversion models to date (Dreger, 1994; Wald and Heaton, 1994b) have indicated that any significant region of rupture occurred on a separate fault plane with similar strike. All of the arrival times were given equal weighting in the determination of the hypocenter. The calculated coordinates and uncertainties of H_2 are latitude 34.263 ± 0.003° N, longitude 118.537 ± 0.003° W, depth 14.1 ± 1.3 km and origin

time of 12:31 00.2 UTC (see Table 4.6 for station residuals). This location is about 7 km up-dip and north of the mainshock hypocenter and is lagged by about 4.8 seconds. With allowance for the various uncertainties, the corresponding constant rupture velocity is between 1.4 and 2.0 km/sec and continues at a significant higher velocity. The second rupture event may, however, initiate after a delay in the elastic dislocation process.

Figure 4.18 compares the epicentral locations of the first and second sub-sources plotted with all the aftershocks of magnitude 4.0 and larger for the first month after the mainshock. It should be noted that the location of H_2 corresponds to a region of relatively few aftershocks. The small size of station residuals is evidence that the location of the initial rupture of a secondary source can explain the onsets of the S_2 pulse, within the usual observational uncertainties in hypocentral location.

There is an independent comparison that provides some confirmation to the doublet model as an explanation of the recorded doublet pulse. Two fault slip inversion models for the Northridge earthquake for the overall mainshock seismic source from regional and strong-motion wave forms are now published (Dreger, 1994; Wald and Heaton, 1994b). Although differing in minor ways, both studies lead to fault slip models with characteristically large amplitude slip regions (local slip about 3.3 m), located about 8 km up-dip of the initial hypocenter (local slip about 2.5 to 3.0 m). The computed location of the initiation point of the second source H_2 lies within this larger region of high amplitude slip on the fault plane.

The fault slip inversion model of Wald and Heaton (1994b) was selected for the estimation of the largest slip on the fault plane to maintain consistency with previously examined fault inversion models from other earthquakes (see Table 4.2). For their model the fault plane was selected with a strike of 122°, which is an average strike of the teleseismic estimates and the dip was constrained to be 42° based on the distribution of aftershocks. The overall dimension of the fault plane was determined based on the teleseismic time function generating a fault length of 18 km and a down-dip width of

20.9 km (Wald and Heaton, 1994b). The strong ground motion velocity time histories used in the inversion were bandpassed filtered between 0.1 - 1.0 Hz.

As was previously stated, the complex source rupture of the Northridge earthquake can be closely fitted by a process with two seismic sources separated by approximately 8 km (Wald and Heaton, 1994b). Their fault slip model is characterized by a large amount of slip (maximum slip of 390 cm) up-dip from the hypocenter (Wald and Heaton, 1994b). The location parameters for the maximum slip point are listed in Table 4.3. The uncertainty on the fault plane of the largest slip is again estimated based on the contour of 80% of the peak slip (see Table 4.2) and the error along strike is $\pm$ 1.6 km and is $\pm$ 1.4 km along the dip. The estimated seismic moment for the fault slip model is 1.2 $\pm$ 0.2e26 dyne-cm (Wald and Heaton, 1994b).

The digital accelerograms from 48 stations from the Northridge earthquake in the Los Angeles region were used in this work and are plotted in Figure 4.20. This dataset consists of a total of 16 rock sites and 32 soil sites (see Table 4.5). The H_{slip} distance ranges from 18.8 km at Arleta (ARL) to 157.8 km at San Jacinto (SJF) and the largest peak SH displacement of 24.2 cm and SV displacement of 16.2 cm was observed at the Tarzana (TAR) station.

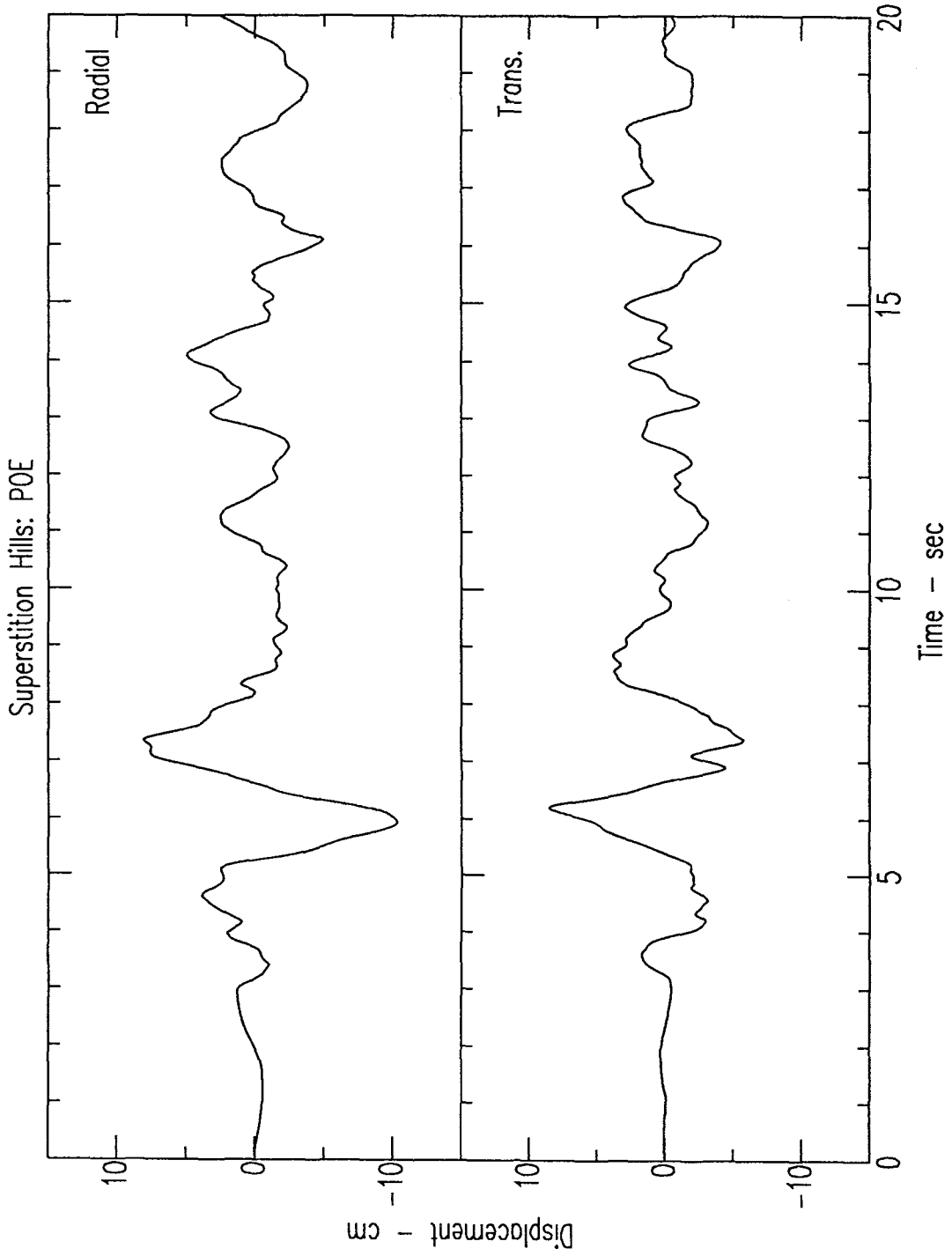

Figure 4.1 Radial and transverse displacement seismograms from the 1987 Superstition Hills earthquake recorded at POE (see Figure 4.10). Two distinct SH pulses are observed on the records, with the largest SH pulse (8.5 cm at 6 seconds) attributable to the largest slip on the fault plane.

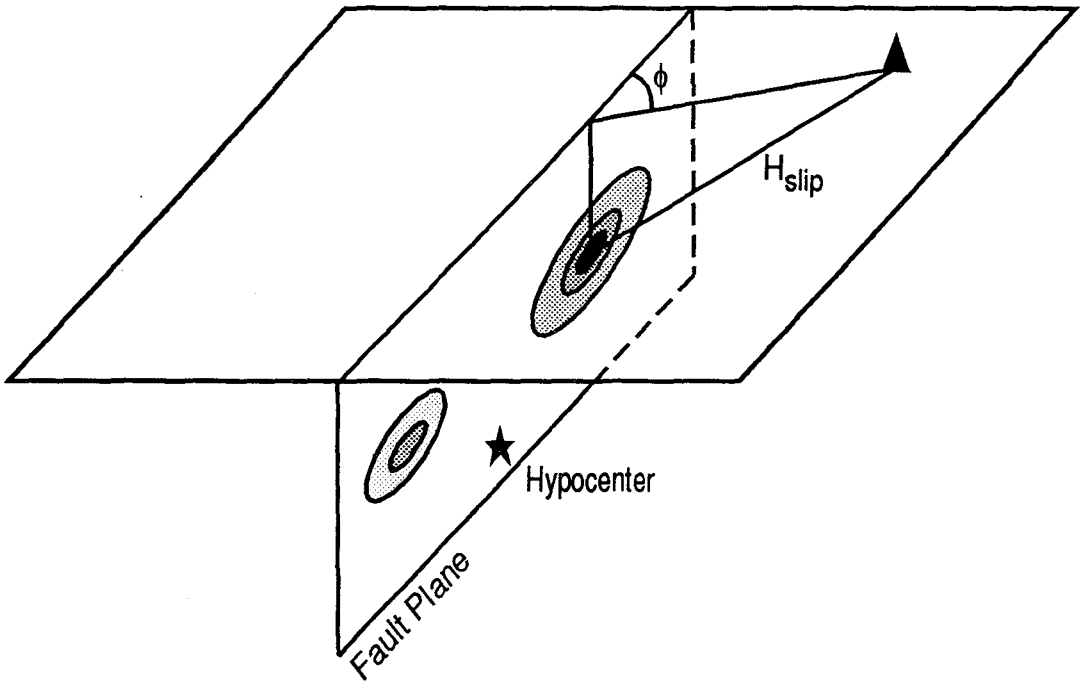

Figure 4.2 Inverted fault slip model for a vertical fault plane. The amplitude of slip on the fault plane is contoured with the darker shading indicating higher values of slip. The defined distance H_{slip} is indicated as well as the angle of rotation, ϕ for the radial and transverse strong ground motion displacement seismograms.

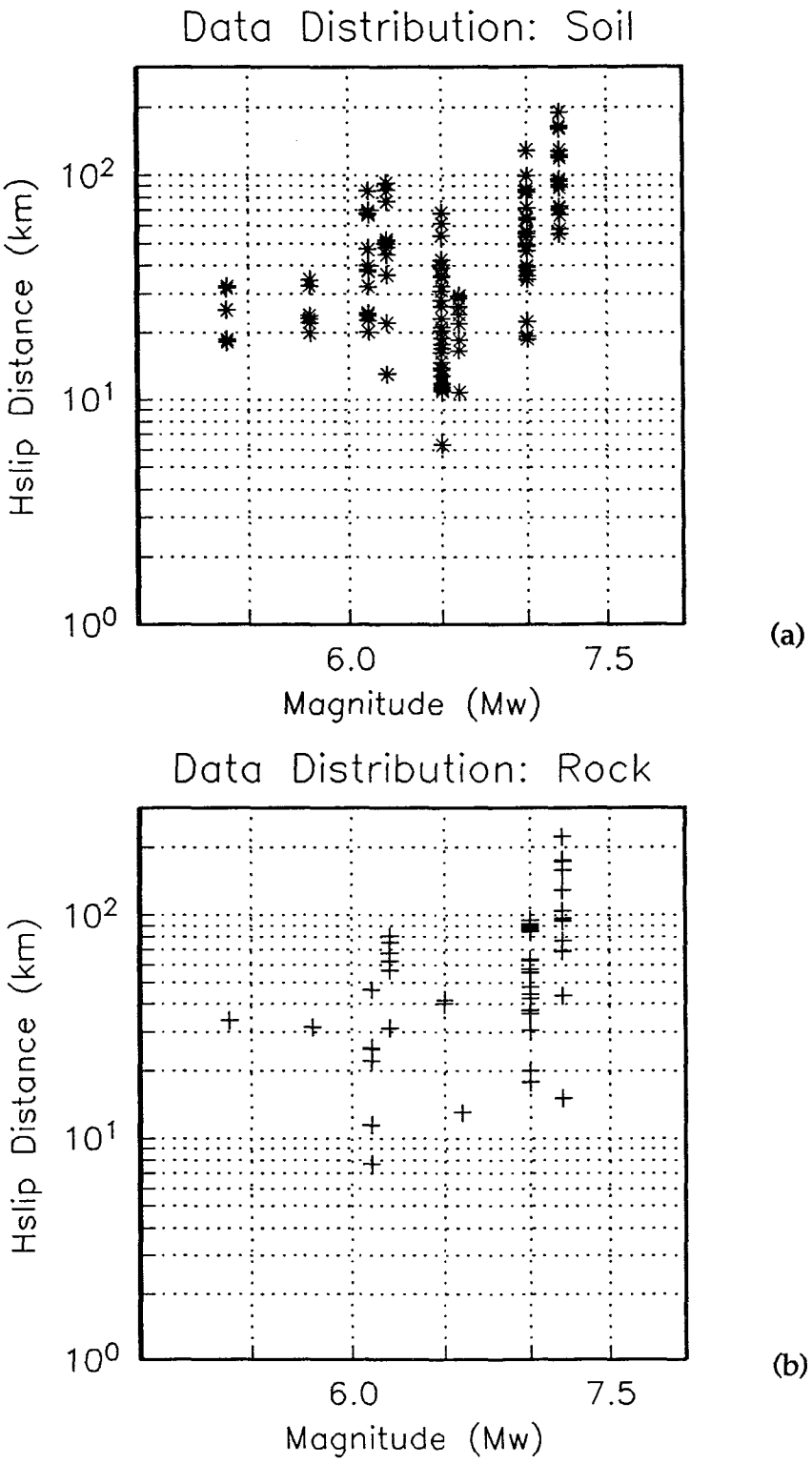

Figure 4.3 Data distribution plot for the SH observations from the eight strike-slip earthquakes. Both the soil and rock sample are limited for close H_{slip} distances and large earthquakes. (a) Soil sample distribution. (b) Rock sample distribution.

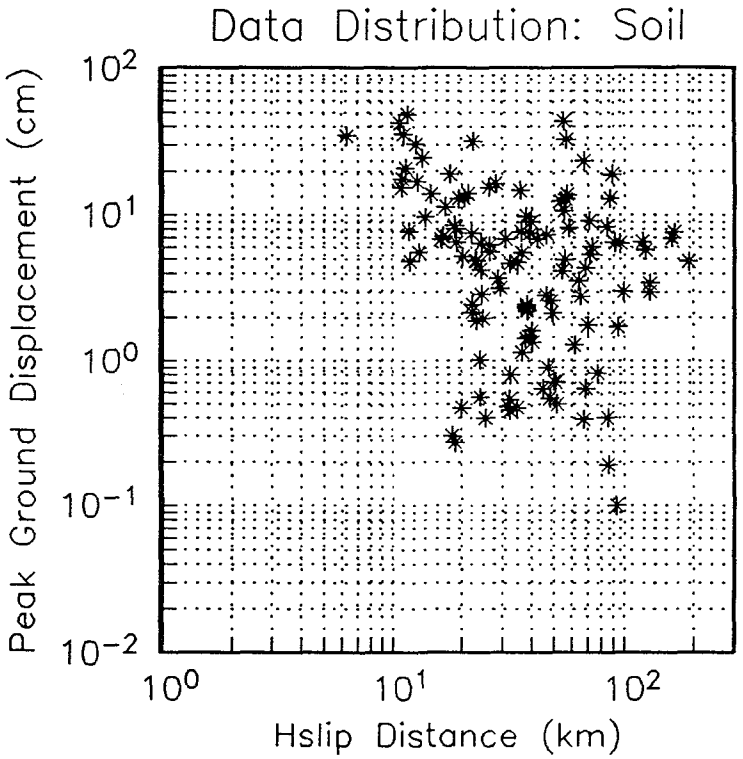

(a)

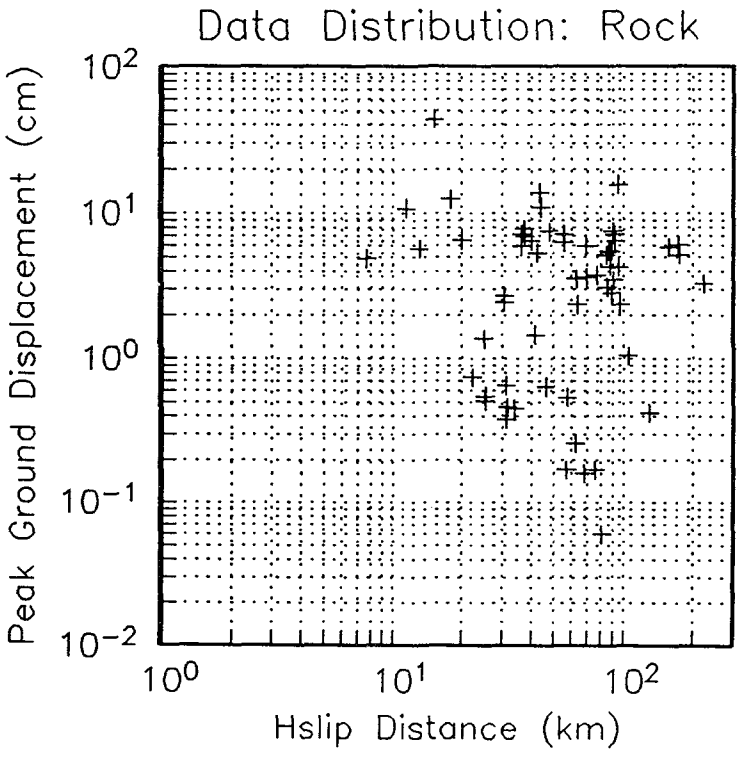

(b)

Figure 4.4 Peak (SH) ground displacement measurements versus H_{slip} distance for the eight strike-slip earthquakes examined. (a) Soil sample distribution. (b) Rock sample distribution.

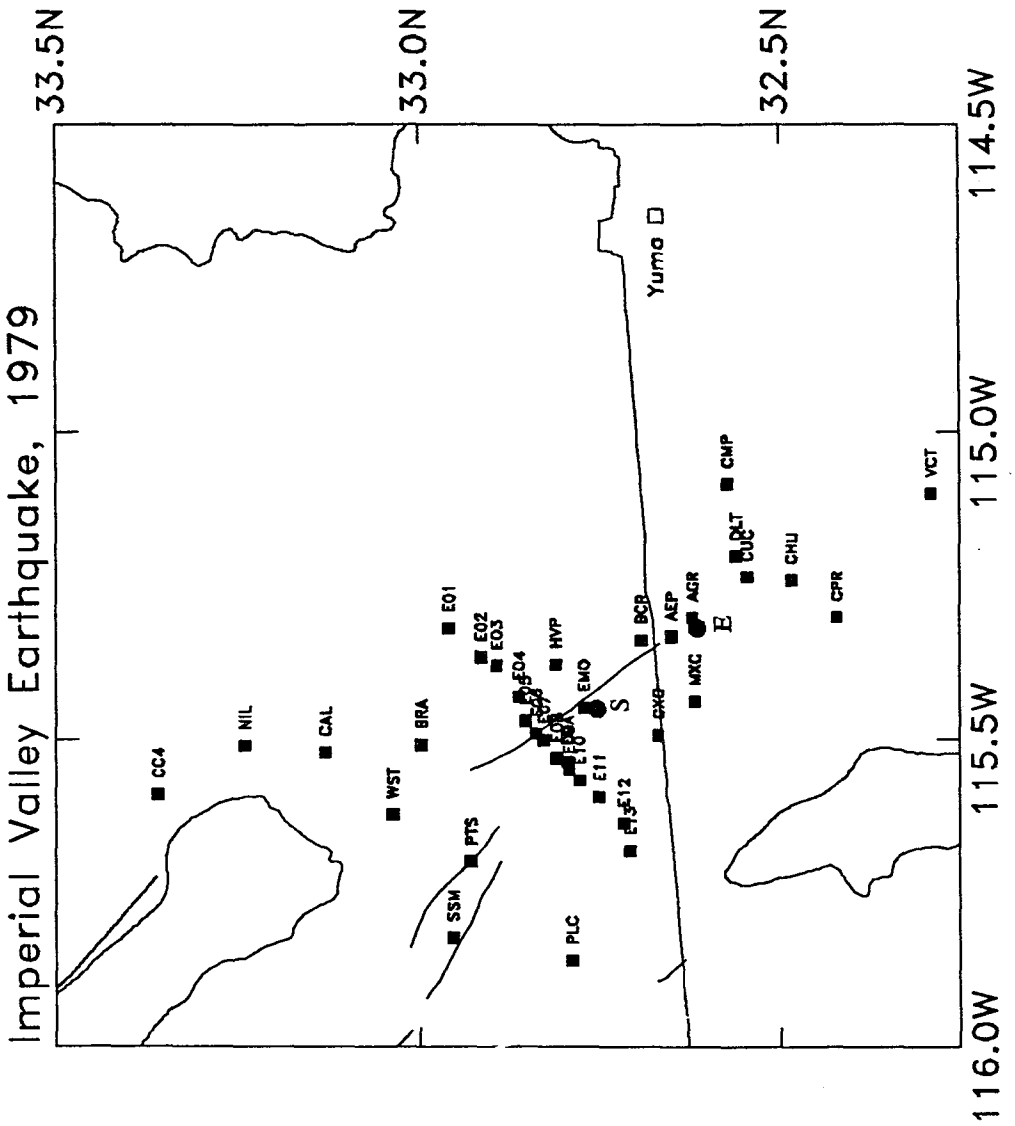

Figure 4.5 Strong ground motion stations from the 1979 Imperial Valley earthquake (M_W = 6.5). The epicenter (E) and adopted largest slip on the fault plane (S) are marked.

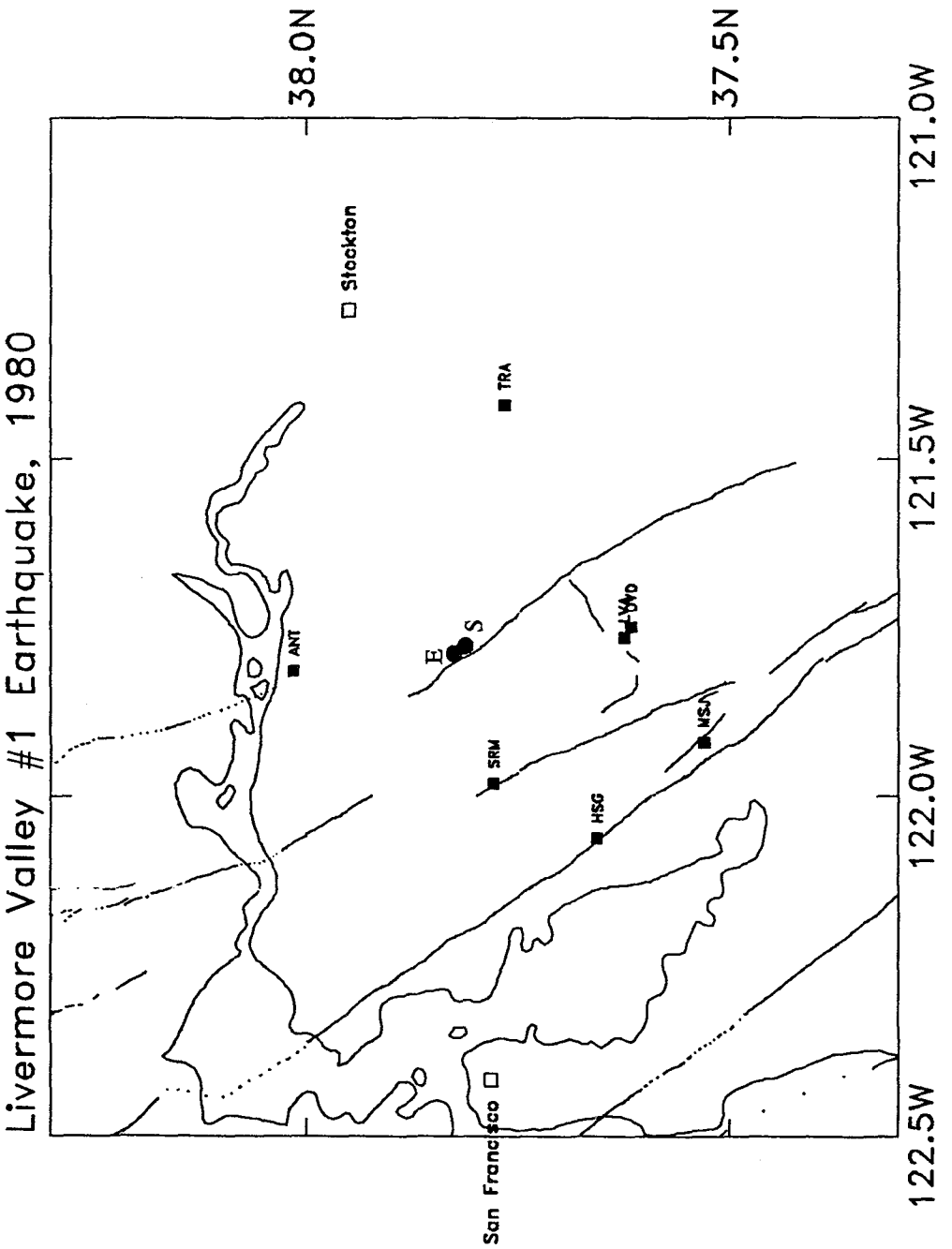

Figure 4.6 Strong ground motion stations from the 1980 Livermore Valley #1 earthquake (M_W = 5.8). The epicenter (E) and adopted largest slip on the fault plane (S) are marked.

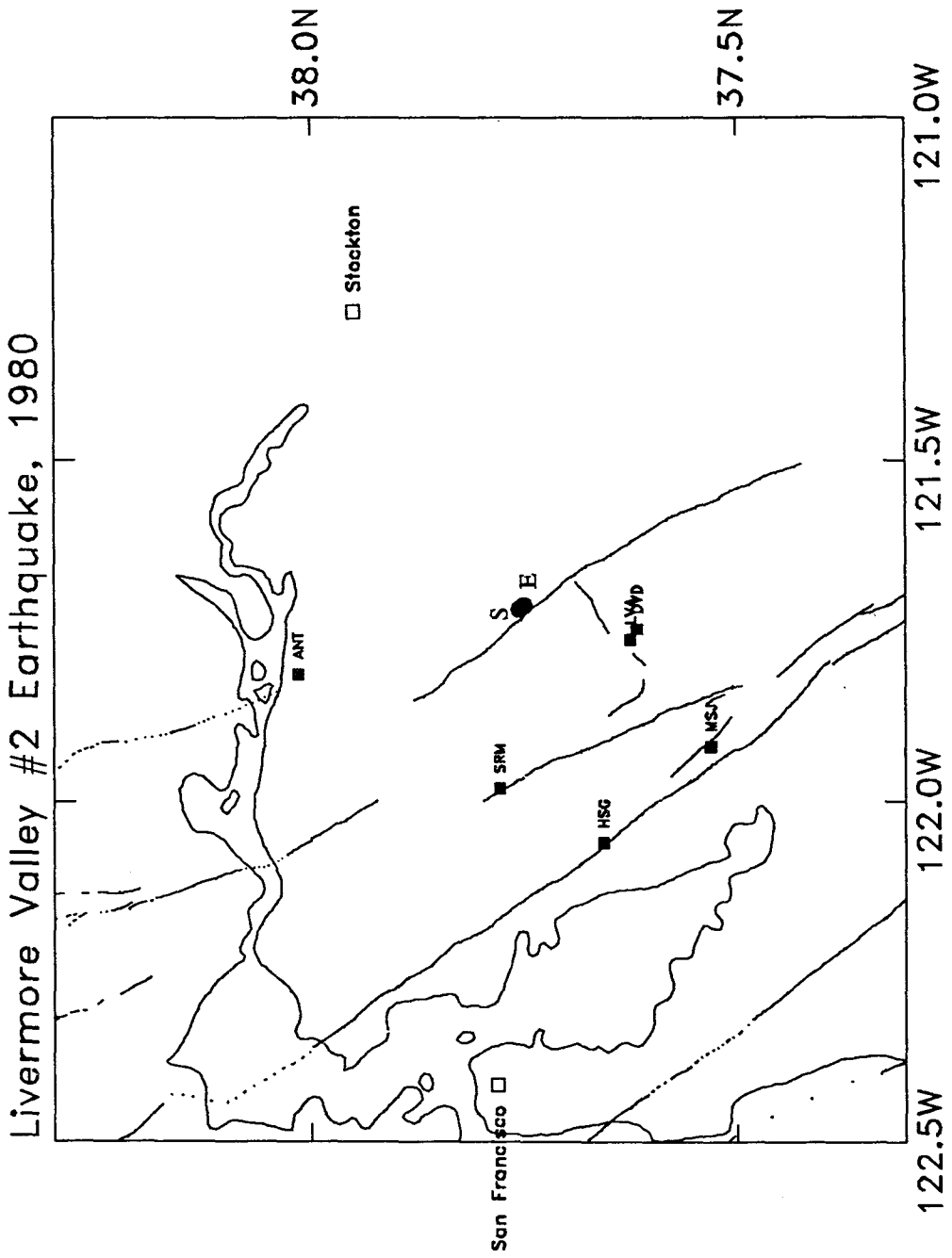

Figure 4.7 Strong ground motion stations from the 1980 Livermore Valley #2 earthquake (M_W = 5.4). The epicenter (E) and adopted largest slip on the fault plane (S) are marked.

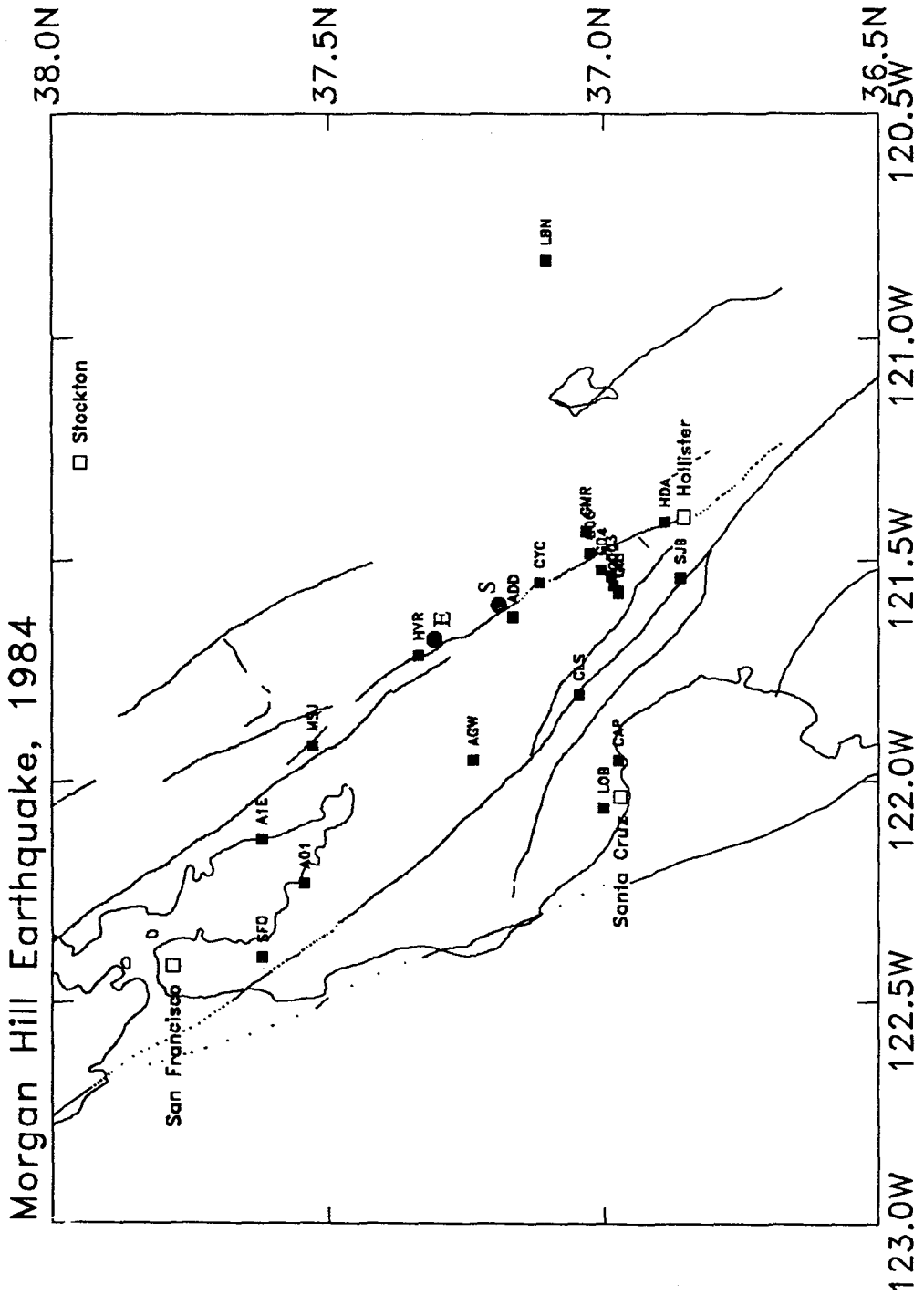

Figure 4.8 Strong ground motion stations from the 1984 Morgan Hill earthquake (M_W = 6.1). The epicenter (E) and adopted largest slip on the fault plane (S) are marked.

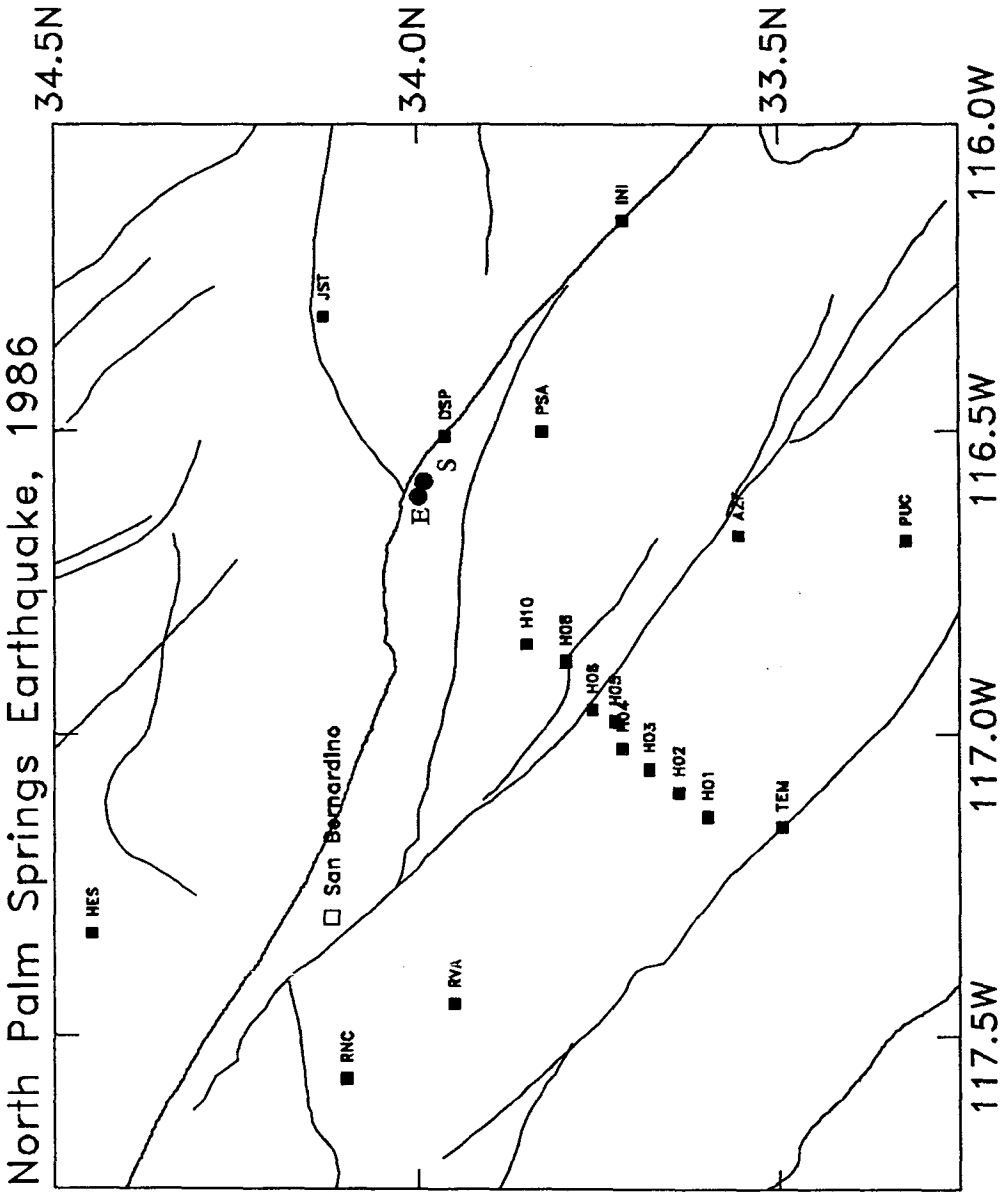

Figure 4.9 Strong ground motion stations from the 1986 North Palm Springs earthquake (M_W = 6.2). The epicenter (E) and adopted largest slip on the fault plane (S) are marked.

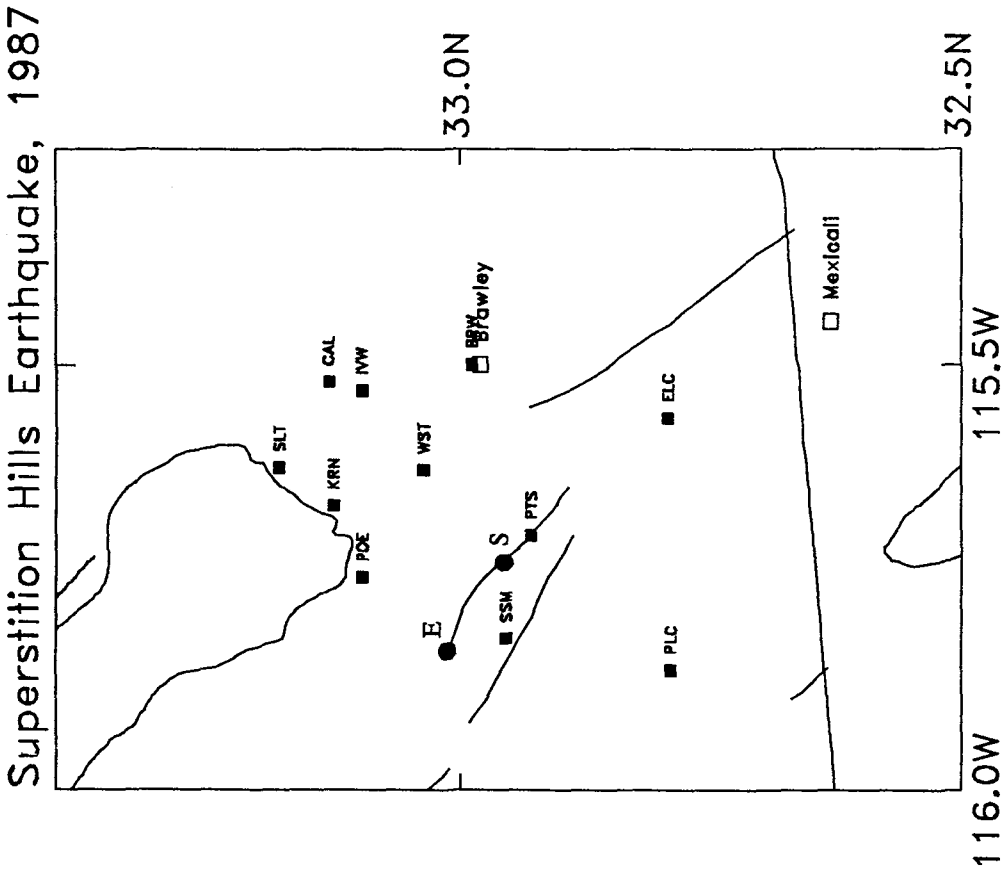

Figure 4.10 Strong ground motion stations from the 1987 Superstition Hills earthquake (M_W = 6.6). The epicenter (E) and adopted largest slip on the fault plane (S) are marked.

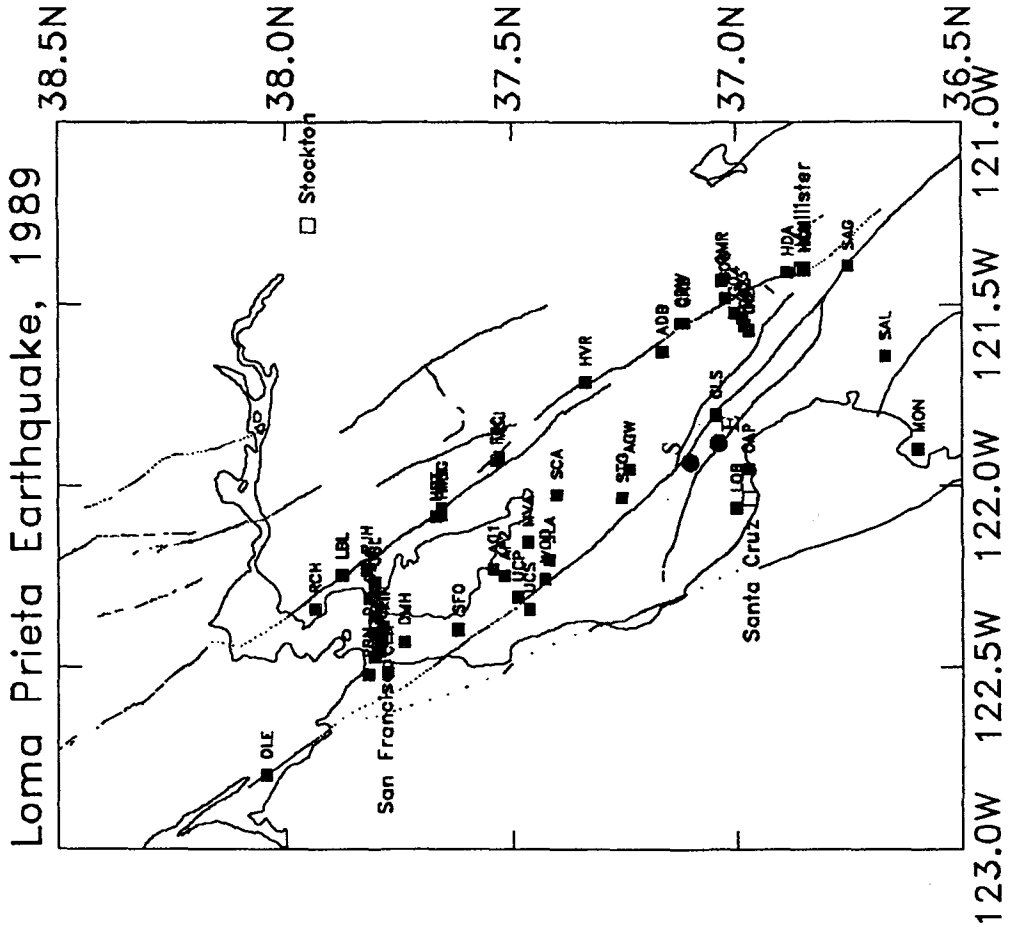

Figure 4.11 Strong ground motion stations from the 1989 Loma Prieta earthquake (M_W = 7.0). The epicenter (E) and adopted largest slip on the fault plane (S) are marked.

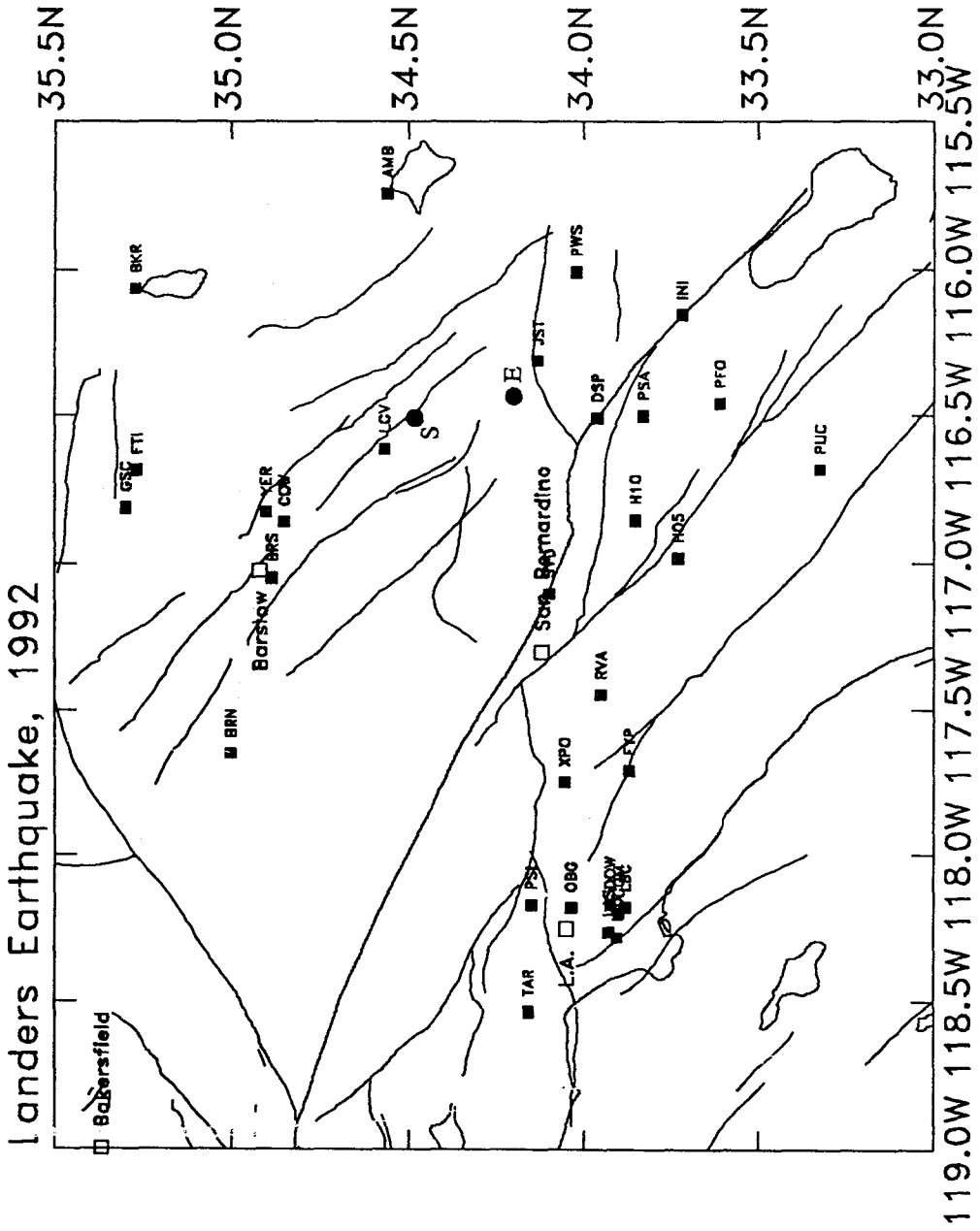

Figure 4.12 Strong ground motion stations from the 1992 Landers earthquake (M_W = 7.2). The epicenter (E) and adopted largest slip on the fault plane (S) are marked.

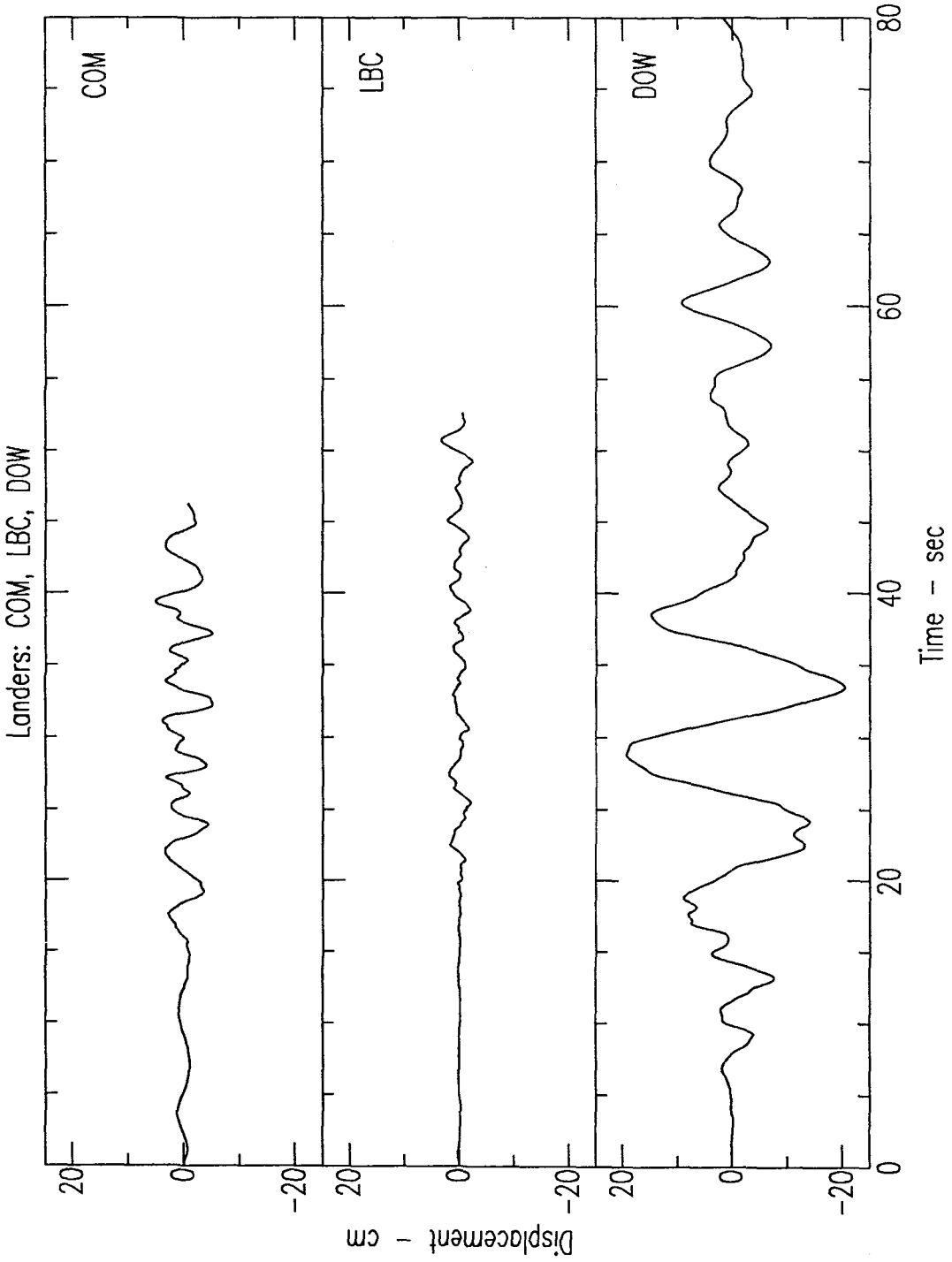

Figure 4.13 Comparison of the transverse component of motion from the 1992 Landers earthquake recorded at COM, LBC, and DOW in the Los Angeles basin (see Figure 4.12). Both COM and LBC were released by U.S.C., while the DOW records were processed and released from CSMIP.

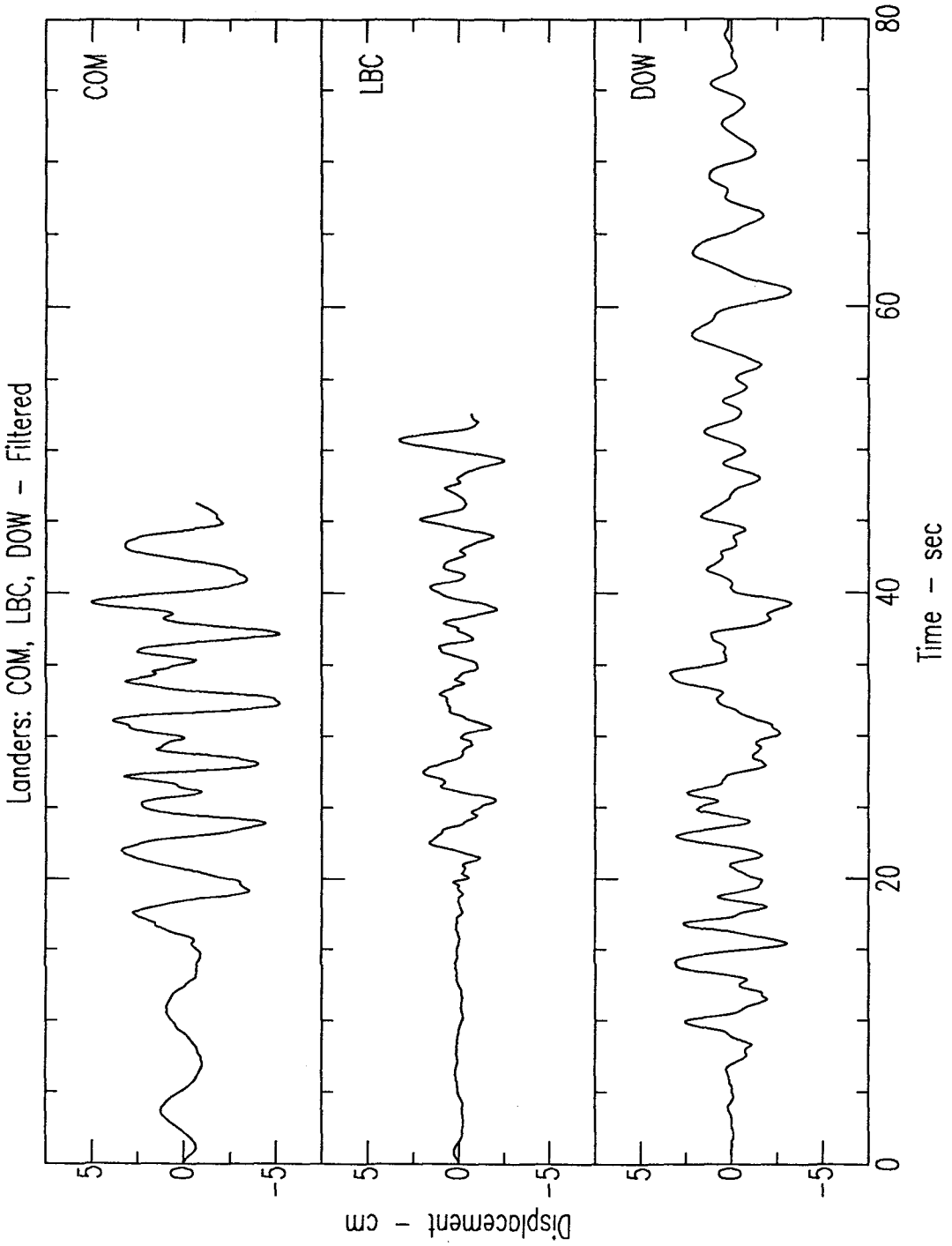

Figure 4.14 Comparison of the transverse component of motion from the 1992 Landers earthquake recorded at COM, LBC, and DOW in the Los Angeles basin (see Figure 4.12). The DOW seismogram has been high-passed filtered (4-pole Butterworth) with a corner frequency of 0.3 Hz.

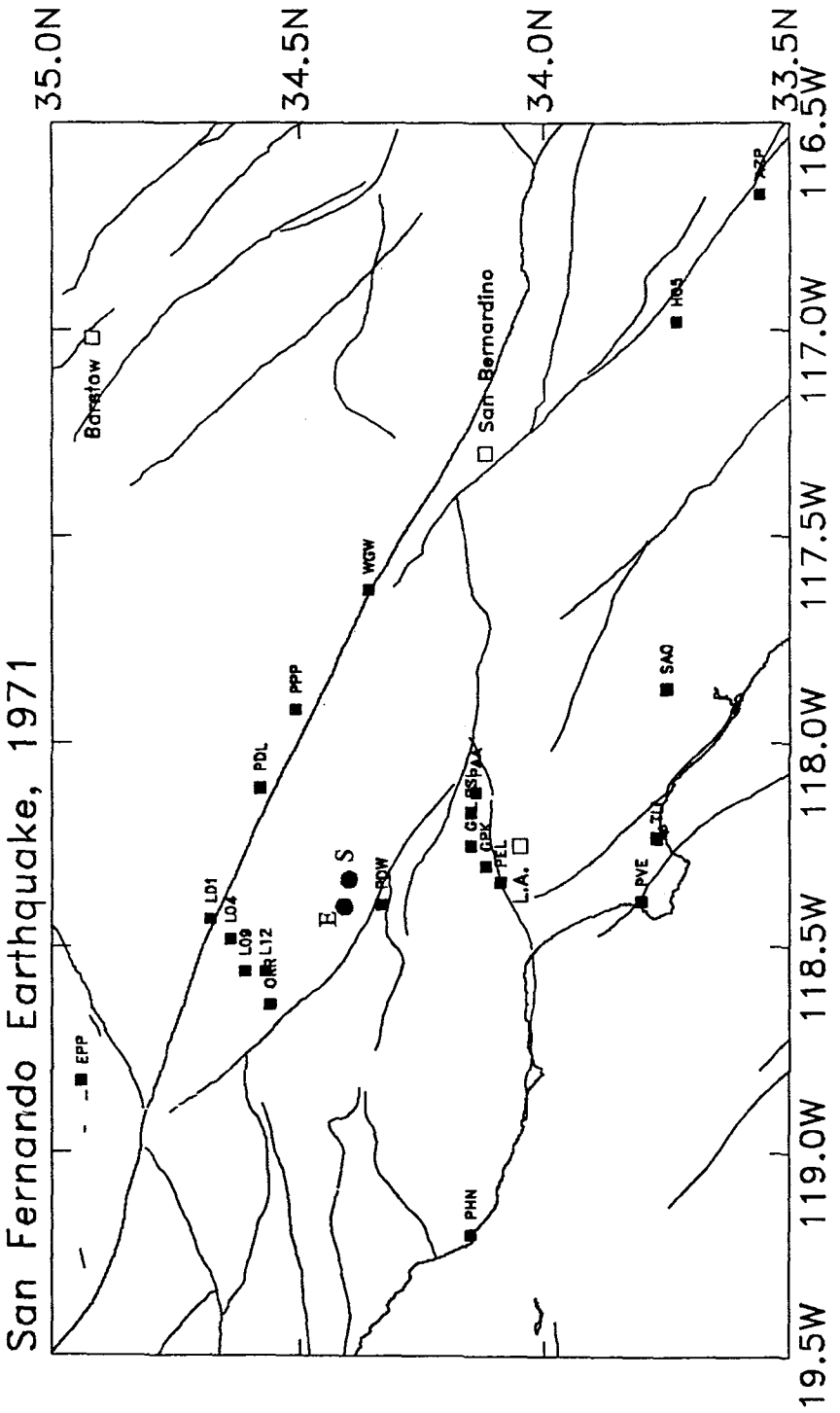

Figure 4.15 Strong ground motion stations from the 1971 San Fernando earthquake (M_W = 6.7). The epicenter (E) and adopted largest slip on the fault plane (S) are marked.

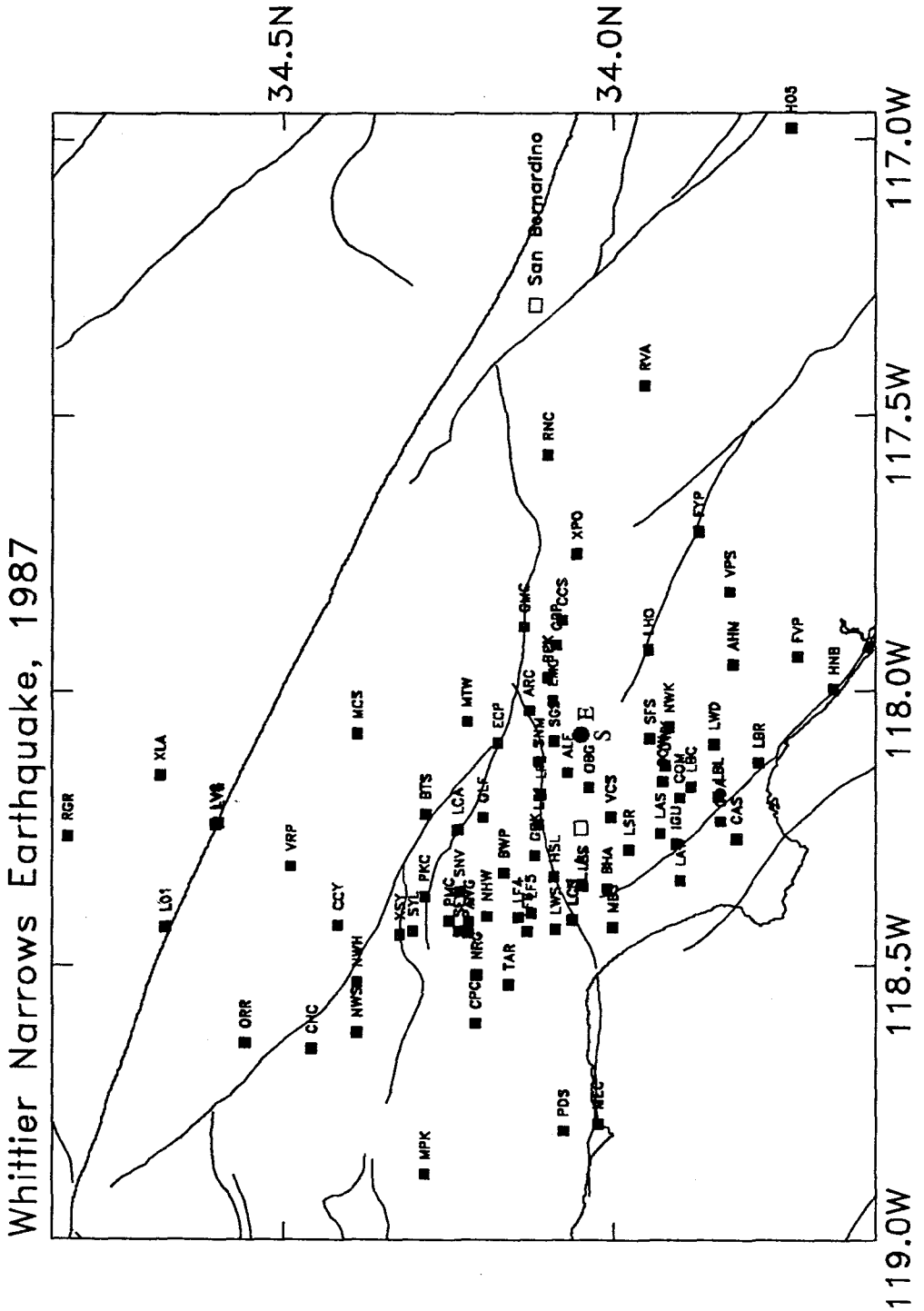

Figure 4.16 Strong ground motion stations from the 1987 Whittier Narrows earthquake (M_W = 6.0). The epicenter (E) and adopted largest slip on the fault plane (S) are marked.

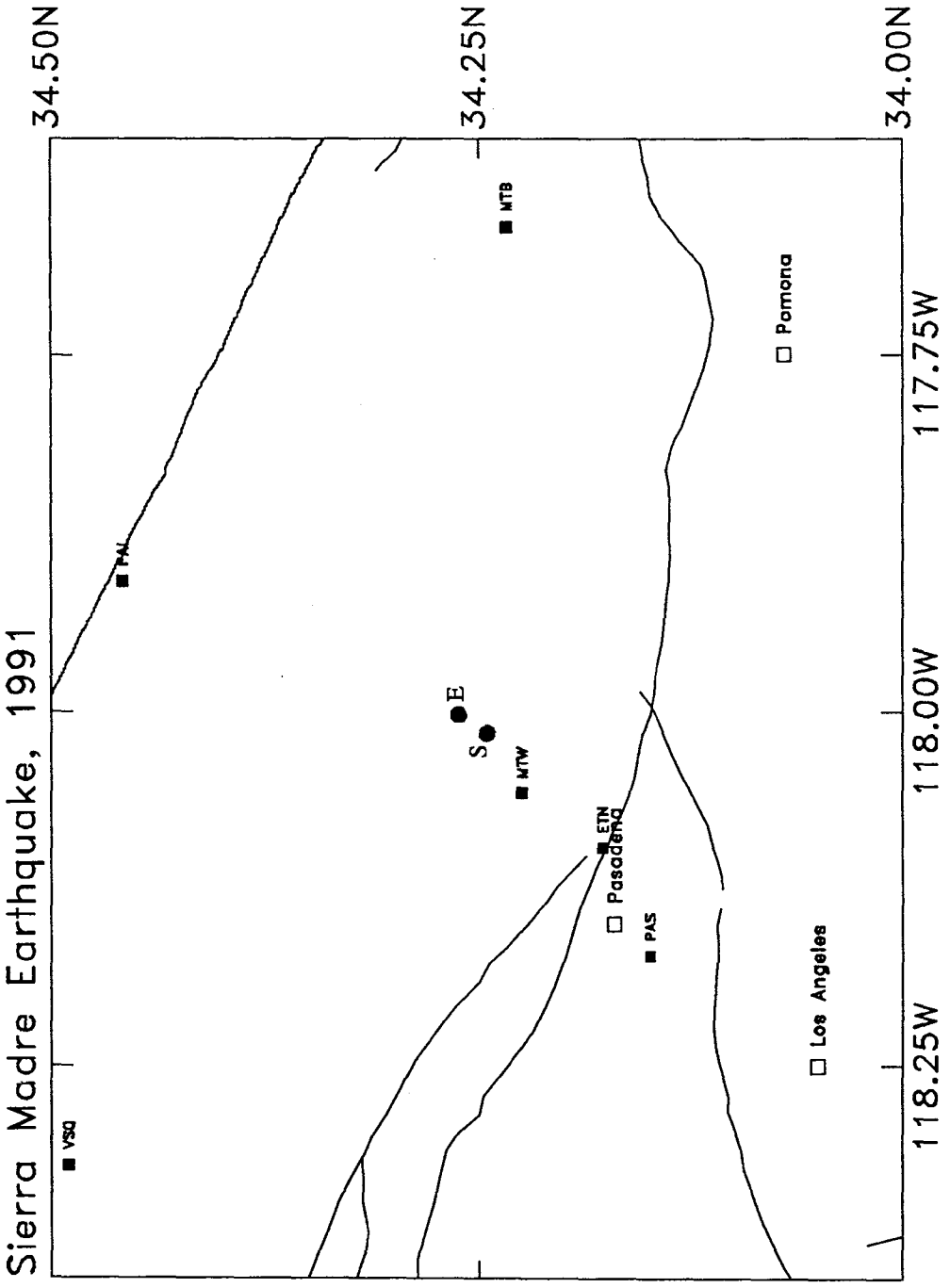

Figure 4.17 Strong ground motion stations from the 1991 Sierra Madre earthquake (M_W = 5.6). The epicenter (E) and adopted largest slip on the fault plane (S) are marked.

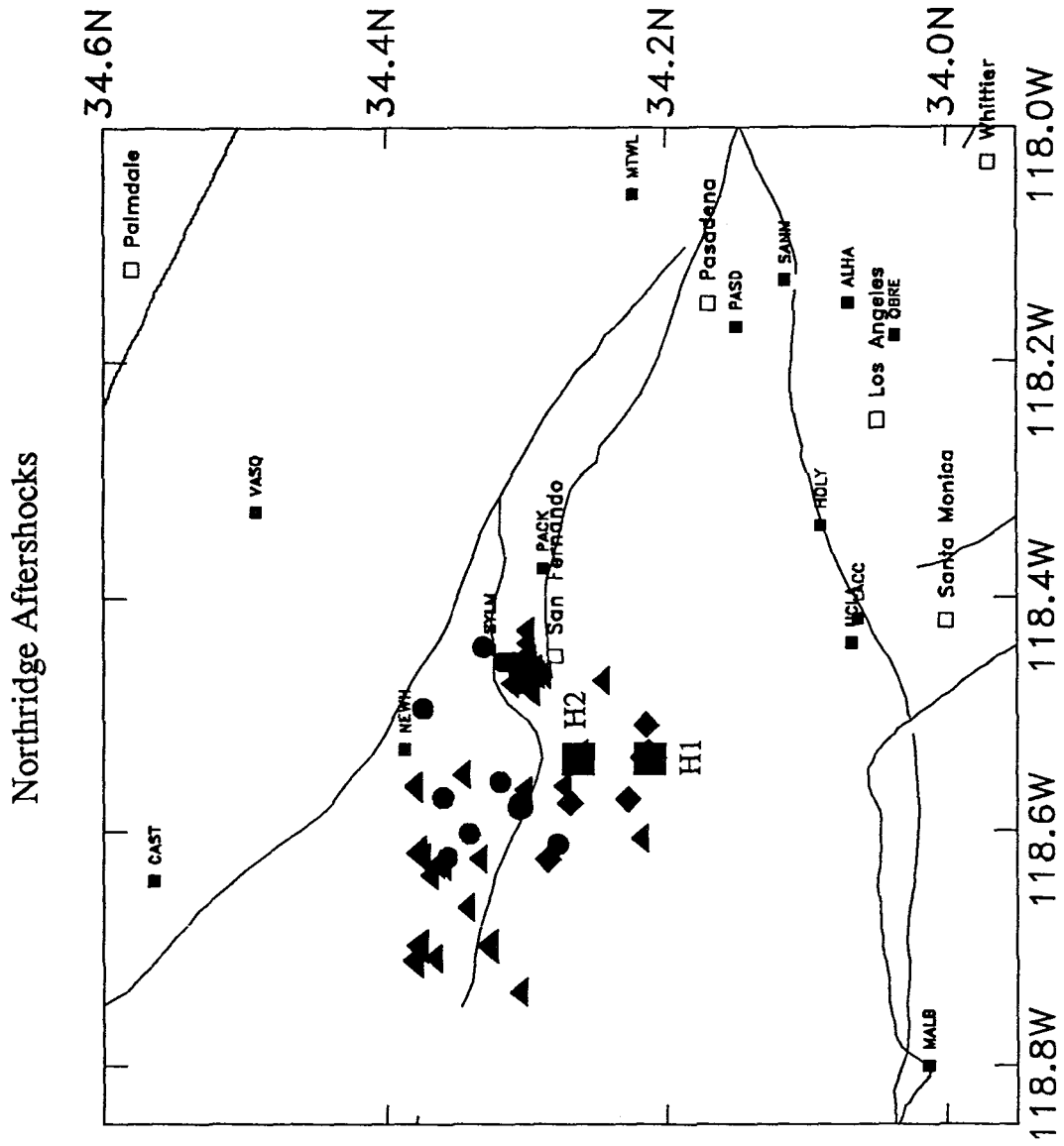

Figure 4.18 Epicentral map of the 1994 Northridge earthquake (M_W = 6.7) and all aftershocks of $M_W \geq 4.0$ for the time period January 17 - February 17, 1994. The epicentral location of the initial H_1 and secondary H_2 source is plotted (squares). Stations used in the computations are indicated. Aftershocks are plotted according to depth; diamonds > 15 km, triangles = 5 - 15 km, circles = 0 - 5 km.

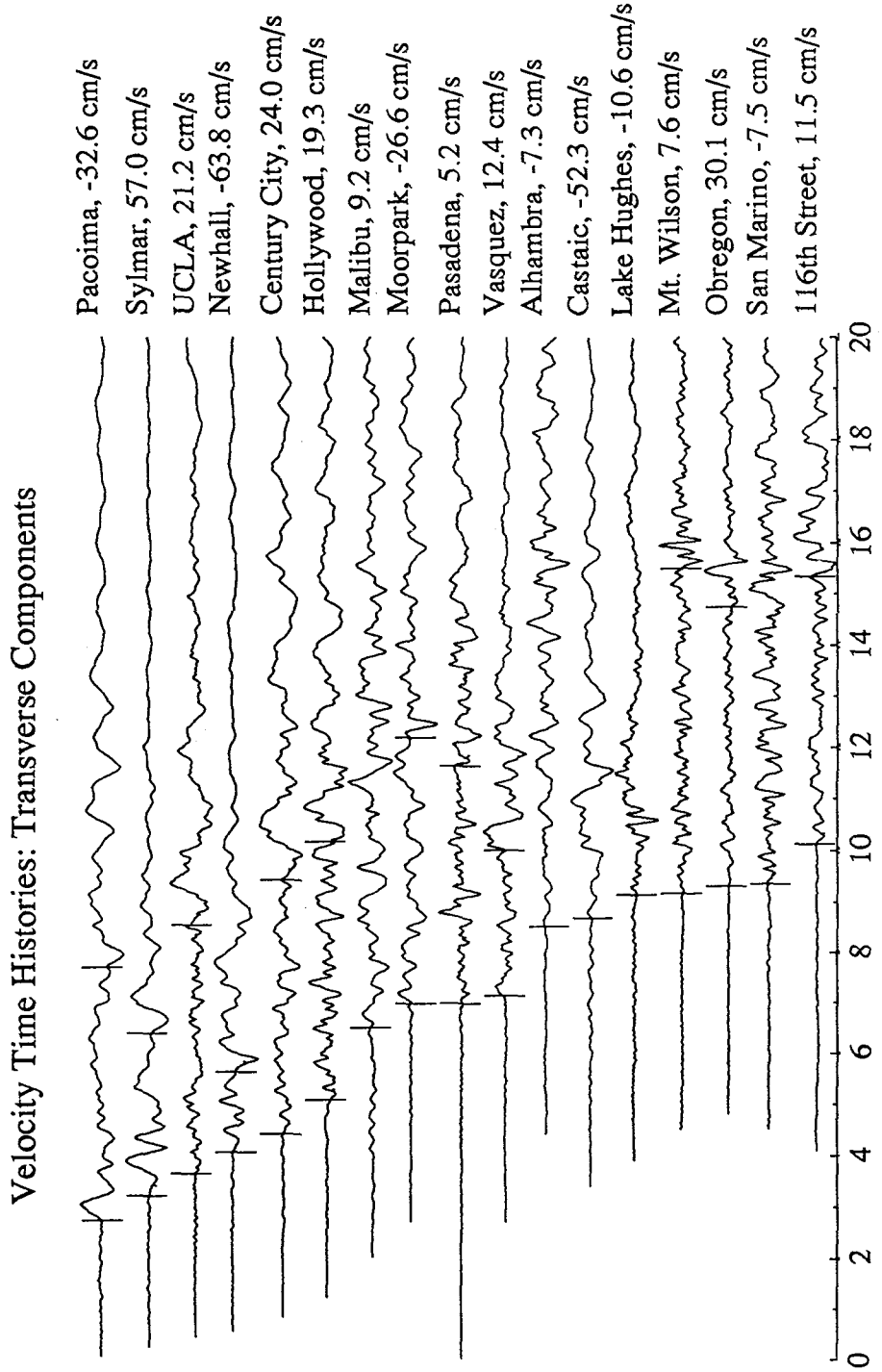

Figure 4.19 Velocity seismograms for the transverse components of motion relative to the initial hypocenter location. Both the initial S_1 and secondary S_2 phases are marked by a vertical bar on the velocity record. Peak ground motion values are indicated on the right for each seismogram.

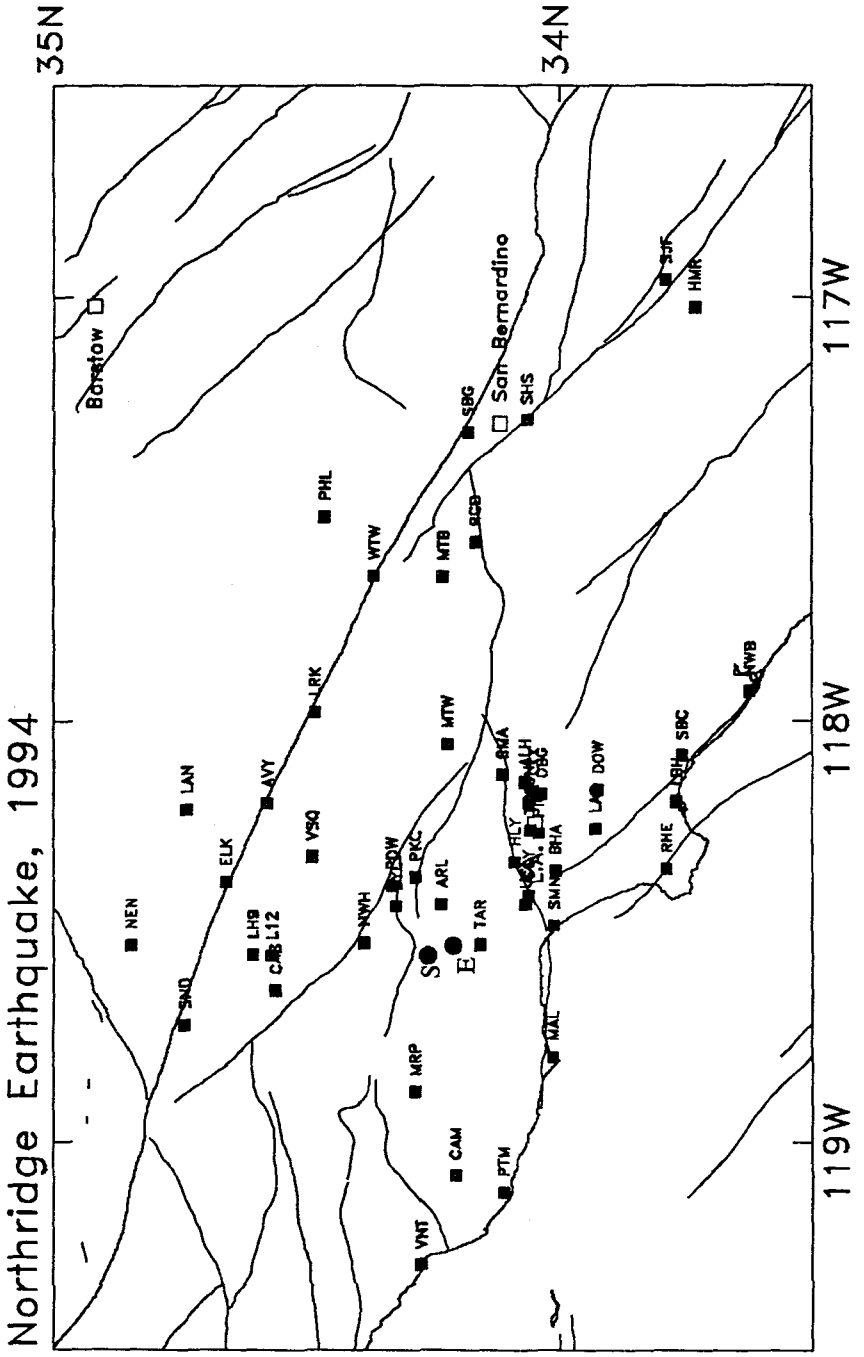

Figure 4.20 Strong ground motion stations from the 1994 Northridge earthquake (M_W = 6.7). The epicenter (E) and adopted largest slip on the fault plane (S) are marked.

5. Statistical Analysis

Attenuation regression curves for peak ground displacement will be statistically estimated in this chapter. Separate curves will be computed for rock and soil site conditions as well as strike-slip versus reverse-fault mechanisms. The horizontal SH peak displacement values and the vertical SV peak displacement values will form the sample on which the regression is performed. The statistical outliers in each regression case will be discussed in terms of possible irregularities due to the seismic source, wave propagation, and site conditions. The nomenclature for the eight attenuation curves is listed in Table 5.1 and will be used in the next two chapters.

Table 5.1 Nomenclature for the Peak Displacement Attenuation Curves.

Name	Mechanisms	Component	Site Condition
SSHR	Strike-slip	SH	Rock
SSVR	Strike-slip	SV	Rock
SSHS	Strike-slip	SH	Soil
SSVS	Strike-slip	SV	Soil
RSHR	Reverse	SH	Rock
RSVR	Reverse	SV	Rock
RSHS	Reverse	SH	Soil
RSVS	Reverse	SV	Soil

5.1 Maximum Likelihood Regression Analysis

The peak ground motion displacement measurements are regressed using a maximum likelihood algorithm for a random effects model (Abrahamson and Youngs, 1992). Abrahamson and Youngs modified the maximum likelihood algorithm of Brillinger and Preisler (1985) and this new procedure, which is applicable for the

estimation of the random effects model, is more stable than the Brillinger and Preisler (1985) version, but is less efficient. A fixed effects model has the following form,

$$\text{Ln } y_{ij} = f(M_i, r_{ij}, \theta) + \varepsilon_{ij} \ , \tag{5.1}$$

where y_{ij} is the ground motion parameter (peak ground displacement in this case), $f(M,r,\theta)$ is the attenuation equation (see section 5.2), M is the moment magnitude of the earthquake i, r is the distance, θ is the vector of attenuation model parameters, and ε_{ij} is the error term. The indices i and j refer to the jth recordings from the ith earthquake. The error is assumed to be normally distributed (Abrahamson and Youngs, 1992). A random effects model, however, will partition the fixed effects model error, ε_{ij}, into the inter-earthquake term and intra-earthquake term

$$\text{Ln } y_{ij} = f(M_i, r_{ij}, \theta) + \eta_i + \varepsilon_{ij} \ , \tag{5.2}$$

where η_i is the inter-earthquake error term and ε_{ij} is the intra-earthquake error term.

The inter-earthquake error is the uncertainties between measurements from different earthquakes. The intra-earthquake error, on the other hand, is the observed uncertainties in measurements at separate locations from the same seismic source. Each error term is assumed to be independent normally distributed variates with variances τ^2 for the inter-earthquake term and σ^2 for the intra-earthquake term (Abrahamson and Youngs, 1992). The total variance is given by,

$$\sigma_T^2 = \tau^2 + \sigma^2 \tag{5.3}$$

for the entire sample. The variances for the eight attenuation curves are listed in Table 5.2. It should be noted that for the reverse-fault mechanism curves the inter-earthquake

variance is zero due to the limited number of measurements from two out of the four earthquake sources (see Table 4.5).

Table 5.2 Inter-earthquake , τ^2, and Intra-earthquake , σ^2, variances for the eight attenuation models of peak ground displacement.

Attenuation Model	τ^2	σ^2	σ_T^2
SSHR	0.03	0.11	0.14
SSVR	0.01	0.07	0.08
SSHS	0.01	0.08	0.09
SSVS	0.00	0.06	0.06
RSHR	0.00	0.10	0.10
RSVR	0.01	0.05	0.06
RSHS	0.00	0.07	0.07
RSVS	0.00	0.07	0.07

The likelihood equation for a random effects model of normally distributed data is given by (Searle, 1971),

$$\text{Ln } L = -\frac{1}{2} N \ln (2\pi) - \frac{1}{2} (N - M) \ln (\sigma^2) - \frac{1}{2} \sum_{i=1}^{M} \ln (\sigma^2 n_i \tau^2)$$

$$\frac{1}{2\sigma^2} \sum_{i=1}^{M} \sum_{j=1}^{n_i} (y_{ij} - \bar{Y}_i)^2 - \frac{1}{2} \sum_{i=1}^{M} \frac{n_i (\bar{Y}_i - \bar{\mu}_i)^2}{\sigma^2 + n_i \tau^2}, \qquad (5.4)$$

where N is the total number of data points, M is the number of earthquakes, n_i is the number of recordings for the ith earthquake, y_{ij} are the observed values,

$$\bar{Y}_i = \frac{1}{n_i} \sum_{j=1}^{n_i} y_{ij} \qquad (5.5)$$

$$\bar{\mu}_i = \frac{1}{n_i} \sum_{j=1}^{n_i} \mu_{ij} , \tag{5.6}$$

and μ_{ij} is the predicted value of the attenuation model. The algorithm numerically maximizes equation (5.4) because there is no analytical solution.

The Abrahamson and Youngs (1992) algorithm is more stable than the algorithm of Brillinger and Preisler (1985) because it is not sensitive to the starting estimated values for the parameters (for a comparison of the two algorithms see, Abrahamson and Youngs, 1992). For too large of a starting estimate of the ratio τ^2/σ^2, the final model parameters determined by the Brillinger and Preisler (1985) methodology can be different by up to an order of magnitude. However, the Abrahamson and Youngs (1992) algorithm converges to the same results for either a large initial estimate and a more appropriate starting estimate.

Although the maximum likelihood algorithm allows for uneven weighting of the sample points, a uniform weighting scheme was implemented for this research where each peak displacement value was given a weight of unity. Uneven weighting was not used due to the limited sample size for the rock attenuation curves (i. e., see Table 4.4 and 4.5).

5.2 Forms for the Attenuation Equation

For the attenuation of acceleration and velocity from strong ground motion records there have been many different functional forms for the attenuation curves (e.g., see Bolt and Abrahamson, 1982; Joyner and Boore, 1988; Iai and Matsunaga, 1993) developed by different authors. For the estimation of attenuation models of peak ground displacement, an function of the form,

$$y = \frac{k}{r} e^{-qr}, \tag{5.7}$$

was initially selected. (compare equation (5.7) to (3.5) for the far-field displacement field). The exponential term represents the anelastic attenuation of seismic energy.

A preliminary estimation (Bolt and Gregor, 1993) of the attenuation of peak ground displacement was performed using the peak displacement measurements from only the 1989 Loma Prieta and 1992 Landers earthquakes. The sample was regressed with the following equation,

$$\mathrm{Log}_{10}(D) = \alpha_1 + \alpha_2 M - \mathrm{Log}_{10} r + \alpha_3 r, \quad \sigma_T^2, \tag{5.8}$$

with,

$$r^2 = d^2 + 12.0^2,$$

where D is the peak ground displacement in cm, M is the moment magnitude of the earthquake, d is the distance between the site and the estimated position on the fault plane of largest slip, σ^2_T is the total variance, and the values of α_i (i=1, 2, 3) are estimated from the maximum likelihood algorithm. Equation (5.8) was selected because of its similar form of the Joyner and Boore (1981) attenuation equation.

The estimation of the α_i values in equation (5.8) was performed on the complete sample from the 12 earthquakes examined (see Table 4.1). However, the estimates for α_3 were positive, a physically unacceptable result because it entails an increase in seismic energy for larger distances and yields unrealistic estimates of peak ground displacement at larger distances (i.e., for distances greater than approximately 100 km) The same positive dependence on the linear term in distance for the attenuation of peak ground motion acceleration was found by Boore et al., (1993; 1994). Consequently, in

their regression for peak acceleration, they eliminated the linear dependence on distance because of this unreasonable behavior.

In this work also, the linear term was not included in the final regression estimates. The complete sample from strike-slip and thrust earthquakes was regressed using the following functional form,

$$\text{Log}_{10}(D) = \theta_1 + \theta_2 M + \theta_3 \text{Log}_{10}(H_{slip}), \quad \sigma_T^2, \tag{5.9}$$

where D is the peak ground displacement in cm, M is moment magnitude, H_{slip} is the distance from the station to the largest slip on the fault plane, estimated from inversion models, and σ^2_T is the total variance.

Based on wave theory for far-field displacement waves (see section 3.2), the estimates of the θ_3 term should be identically equal to one for a homogenous isotropic medium. However, the estimates values of θ_3 are not equal to unity (see sections 5.3 - 5.4). These differences can be explained by many separate factors. The assumption of a homogenous medium is not representative of the diversity of the different geological structures for most of the selected earthquakes. The assumption of a homogenous medium through which the seismic energy is transmitted is an over simplification for these observations. Scattering near the recorder and basin effects (see section 3.4) can also lead to a non-unity value for θ_3 due to the amplification of peak ground displacement over a certain distance range. Finally, no attempt is made to separate the anelastic attenuation of seismic energy with the attenuation equation. The effect of anelastic attenuation will tend to increase the θ_3 leading to a value of larger than unity and yielding a greater attenuation of peak ground displacement with distance.

5.3 Strike-Slip Fault Mechanisms

The empirical attenuation curves for peak ground displacement in strike-slip earthquakes will be discussed in this section. The dataset consists of 8 earthquakes with magnitude range of $5.4 < M_W < 7.2$ (see Table 4.1), all of which have been previously examined in chapter 4. The statistical outliers for each earthquake will be discussed in terms of the seismic source, wave propagation, or site conditions.

5.3.1 Rock Displacement for SH Waves

A total of 59 peak ground displacement SH values were used in the regression analysis (see Table 4.4) for the SSHR attenuation curve,

$$\text{Log}_{10}(D) = -5.00 + 1.02M - 0.87\,\text{Log}_{10}(H_{slip}), \quad \sigma_T = 0.38 \tag{5.10}$$

where D is the peak displacement in cm and H_{slip} is the previously defined distance to the largest slip on the fault plane in kilometers.

The residuals of the observed peak displacement values minus the predicted values from equation (5.10) are plotted in Figure 5.1 as both a histogram and versus H_{slip} distance. The mean residual value for the SSHR curve is $\mu = 1.3 \pm 4.1$. The largest residual of 22.8 occurs at the Lucerne Valley station from the Landers earthquake (see section 4.15 for a detailed discussion of this peak ground displacement value).

To examine statistically the measured values which lie beyond one standard deviations from the mean, the log of the ratio of the observed peak ground displacement to the predicted peak ground displacement are computed and plotted in Figure 5.2. The data for each earthquake is plotted with a different symbol versus H_{slip}. A perfect fit to the data would return a ratio value of zero. The mean ratio for the SSHR

sample is $\mu = 0.00 \pm 0.37$. Plotted in Figure 5.3 are the computed ratios versus M_w (also see Table 5.2 for the mean values for each earthquake). I now discuss separately the measurements from each earthquake.

Table 5.3 Mean ratio estimates for each of the 8 strike-slip earthquakes for the SSHR attenuation curve.

Earthquake	Number of Data Points	SH Mean Ratio
1979 Imperial Valley	2	0.25 ± 0.45
1980 Livermore MS	1	0.05
1980 Livermore AS	1	0.47
1984 Morgan Hill	7	0.06 ± 0.36
1986 North Palm Springs	7	-0.50 ± 0.21
1987 Superstition Hills	1	-0.01
1989 Loma Prieta	27	0.06 ± 0.29
1992 Landers	13	0.03 ± 0.42
Total Dataset	59	0.00 ± 0.37

In the discussion that follows, only the graph of the peak displacement attenuation relation corresponding to the earthquake with the largest number of measurements will be presented. The corresponding graphs for the other individual earthquakes can be found in Gregor (1995). It should be noted that for this plot and all of the following plots of attenuation curves, the curves are plotted versus epicentral distance to the largest slip on the fault plane. This distance was selected for the ease of use of these empirical curves in seismic hazard analysis, where the depth and location of largest slip is not necessarily estimated. The dashed lines indicate the plus and minus one standard deviation curves.

There are only two strong ground motion stations (CPR and SSM) which are classified as rock sites in the 1979 Imperial Valley earthquake (cf., section 4.2.1). The largest peak SH displacement of 6.4 cm occurs at the CPR station at a H_{slip} distance of

40 km. Although at similar distances, the two stations are located in opposite directions from the fault rupture (see Figure 4.5). Both are located within 20° of the strike of the rupturing fault plane. The amplification of the recorded peak ground displacement would be expected for these azimuths because the radiation pattern for the SH displacement field (see section 3.2) in this case has amplitude maxima near this direction.

There was only one rock data point (HSG) from the Livermore mainshock earthquake (cf., section 4.2.2). The HSG strong ground motion station is located east of the fault of rupture at a H_{slip} distance of 31.5 km and recorded a peak SH ground displacement of 0.46 cm. The ratio value for this point is approximately zero (Table 5.3) indicating a good agreement between the observed peak displacement value and the mean estimate from the SSHR curve.

The peak displacement measurement at the HSG station (i.e., 0.45 cm) for the Livermore aftershock (cf., section 4.2.3), is approximately equal to the mainshock value. However, the moment magnitude of the aftershock is 0.4 unit lower (see Table 4.1). There is a large misfit between the mean SSHR curve and the observed data point. The misfit is also evident in Figure 5.2 which shows the log of the ratio (i.e., a ratio value of 0.41). A comparison of the displacement time histories from the Livermore mainshock and the Livermore aftershock is presented in Figure 5.4. The time histories are quite different in their overall phase and amplitude. Because of the similar path and identical site response for the two sets of records, the noticeable difference in the time histories is almost certainly caused by a difference in the respective seismic sources.

Seven measurements from rock sites were obtained for the 1984 Morgan Hill earthquake (cf., section 4.2.4). The largest SH peak displacement value (pgd = 10.8 cm) for a rock classified site was recorded at the CYC station. CYC is located directly down-strike of the direction of fault rupture (see Figure 4.8) and the observed large displacement pulse and short duration evident in the displacement seismograms can be

explained readily as due to rupture directivity (see section 3.5). The directivity enhancement effect is consistent with the observation that only the ratio value from the CYC station is greater than one standard deviation for the mean ratio value of this earthquake (see Figure 5.2 and Table 5.3).

The data from the 1986 North Palm springs earthquake (cf., section 4.2.5) consisted of seven classified rock stations. As is evident (see Figure 5.3), the mean SSHR curve systematically over-predicts the observed peak displacement values. The mean of the ratio for the seven sites is $\mu = -0.50 \pm 0.21$ (see Table 5.3). Only the RVA station is greater than one standard deviation from this mean in the negative direction. Similarly, RVA experienced low peak ground displacement values in three other earthquakes examined in this research, possibly indicating a large site response causing the reduced amplitudes.

The overall under-prediction of the peak ground displacement values can be addressed by looking at the far-field radiation pattern for the earthquake. The 1986 North Palm Springs earthquake was a strike-slip mechanism that occurred on a dipping fault (dip = 46°). All of the stations are located to the west and southwest of the earthquake with the exception of the JST station which is located to the northeast (see Figure 4.9). The RVA station is located near a SH node which can explain the low amplitude for this specific earthquake. However, the other rock sites are not located on an SH node and so another explanation must be proposed. Because the observation at JST, which is in a separate quadrant of the radiation pattern than the other rock stations, is near a maximum, but is also low in amplitude, the source of the earthquake is suggested as the cause of the systematic reduction in observed peak values.

Only one rock site (SSM) was recorded for the 1986 Superstition Hills earthquake (cf., section 4.2.6). SSM recorded a peak SH displacement of 5.7 cm which agrees with the predicted peak displacement value.

The 1989 Loma Prieta earthquake (cf., section 4.2.7), with a total of 27 rock classified sites, provided the largest single set of rock strong ground motion recordings for any of the eight strike-slip earthquakes (see Table 4.4). The SH peak ground motion values are plotted along with the mean SSHR curve for the Loma Prieta earthquake in Figure 5.5. The clustering of data points at distances of approximately 100 km are from the strong ground motion sites in and around San Francisco. These sites were noted to have higher ground motion values due to the lateral refraction of seismic energy (Lomax and Bolt, 1992) and the reflection of seismic energy from the Moho discontinuity in the crust (Somerville and Yoshimura, 1990). This amplification of ground motion is evident in the observed peak SH displacement values The mean value for log of the ratio is $\mu = 0.06 \pm 0.29$ (see Table 5.3) as the individual values are plotted in Figure 5.2.

The Monterey (MON) strong ground motion site recorded peak amplitude values which were approximately an order of magnitude lower than the rest of the dataset. A partial explanation for the low amplitudes can be provided by the rupture directivity of the seismic source because the MON station is located at the back azimuth of the rupturing fault (see Figure 4.11). (The SH component of motion is characterized by low amplitude and long duration motion as would be expected at back azimuth locations.) The MON station is located close to a node on the SH radiation pattern, which also provides a reason for the low amplitude. Finally, the crustal structure between the source and site is geologically complicated. The Monterey Basin, located between the source and the station, is a deep sea basin and lateral refraction of seismic energy away from the station could be a contributing factor to the low amplitudes of ground motion recorded at MON.

The 1992 Landers (cf., section 4.2.8) portion of the data set consisted of 13 rocks sites. The closest site was LCV at an H_{slip} distance of 13.5 km and had an observed SH peak ground displacement of 43.7 cm. The mean ratio value is $\mu = -0.03 \pm 0.42$ (see Table

5.3), for the 13 rock SH values. The peak displacement value at PLC has the largest deviation from the mean (in a negative direction). There are two factors which are contributing to the low observed peak ground displacement values at the PLC station. First, the station is located south of the northerly propagating rupture. Hence, lower peak ground displacement values would be expected at this site due to rupture directivity (see section 3.5). Secondly, the radiation pattern for the corresponding fault geometry predicts low amplitudes because of the proximity of PLC to a SH node. The low observed values at RVA can be attributed to a site response because low amplitudes of ground displacement were observed at this site for other earthquakes in the sample (e.g., see the Landers, North Palms Springs and Whittier Narrows earthquakes).

The largest positive deviation from the mean occurs for GSC which is located north along the strike of the fault plane (see Figure 4.12). The higher amplitudes of ground motion can be predicted based on the northerly propagating fault rupture for the Landers earthquake (see section 3.5). This amplification of observed peak ground displacement was consistent with the other soil sites located at the northern end of the fault plane (see section 5.3.3 - 4).

It is illuminating to graph the log of the ratios as a quadrant division based on the azimuth from the seismic source. On the average, stations located to the north exhibit positive ratios, while stations to the south exhibit negative ratios due to rupture directivity. Stations located in the Los Angeles basin also exhibit positive ratios due to the amplification of ground motion caused by the large alluvial basin (see section 3.4). The amplification and de-amplification of ground motion was also noted in the analysis of peak ground acceleration from the Landers earthquake (Campbell and Bozorgnia, 1994a).

5.3.2 Rock Displacement for SV Waves

I now consider the vertically polarized shear wave denoted, SV. A total of 58 peak SV displacement observations were used in the regression. The vertical component of strong ground motion from the 1986 Superstition Hills have not been digitized and therefore not available (Wald et al., 1990). The SSVR curve is,

$$\text{Log}_{10}(D) = -5.56 + 1.11M - 1.10\,\text{Log}_{10}(H_{slip}), \quad \sigma_T = 0.29, \tag{5.11}$$

where D is the peak SV displacement in cm and H_{slip} is in kilometers. The histogram of residuals for the SV sample ($\mu = 0.4 \pm 1.2$) is shown in Figure 5.6. For the corresponding ratio plot see Figure 5.2. The mean ratio for the SV data points is $\mu = 0.01 \pm 0.29$ and the values for each earthquake are listed in Table 5.4. As can be seen in Figures 5.2 and 5.6, the SV observations are more evenly distributed with a smaller amount of dispersion around the mean, than for the SH data for rock sites.

Table 5.4 Mean ratio estimates for each of the 8 strike-slip earthquakes for the SSVR attenuation curve.

Earthquake	Number of Data Points	SH Mean Ratio
1979 Imperial Valley	2	0.34 ± 0.50
1980 Livermore MS	1	-0.28
1980 Livermore AS	1	0.29
1984 Morgan Hill	7	0.06 ± 0.19
1986 North Palm Springs	7	-0.24 ± 0.26
1987 Superstition Hills	---	---
1989 Loma Prieta	27	0.09 ± 0.25
1992 Landers	13	-0.10 ± 0.29
Total Dataset	58	0.01 ± 0.29

The maximum SV displacement of 3.9 cm from the 1979 Imperial Valley earthquake was recorded at CPR, which also had an anomalously high SH peak displacement value. Because this station is located at a back-azimuth from the propagating source, the effect of rupture directivity would lead to a prediction of a deamplification of observed ground motion (see section 3.5). For the SH motion, the far-field radiation pattern is near a maxima for this azimuth. However, the SV radiation pattern is near a minimum and consequently the amplification is caused by either a propagation effect or a site response at CPR.

The observed displacement value from the Livermore mainshock recorded at HSG is low, as would be predicted from the near nodal position of the SV radiation pattern for this azimuth. For the Livermore aftershock (cf., section 4.2.3), the observed value for the aftershock recorded at HSG is statistically higher than the predicted value and can be explained by the source anomaly for this event, as was discussed in the previous section for the SH displacement motion.

As was observed for the SH data from the 1984 Morgan Hill earthquake, the peak SV displacement value at the station CYC is greater than one standard deviation above the predicted value. In both cases, this increase in ground motion can be explained as amplification due to the rupture propagating towards the site (see equation (3.13)). The observed lower measurement of the SV relative to the SH motion arises probably from the lower amplification between the SV and SH radiation patterns (see Figure 3.3b). The other six data points all fall within one standard deviation of the attenuation curve and the mean ratio estimate is $\mu = 0.06 \pm 0.19$ (see Figure 5.2).

As was observed in the SH data from the 1986 North Palm Springs earthquake, there is a systematic over-prediction of peak SV displacement values for all of the sites except one (JST) which has been discussed as being related to a source effect (see section 5.3.1). The mean ratio for the SV data is $\mu = -0.24 \pm 0.26$ (see Figure 5.2) which is lower than the SH values by approximately 50 percent. The largest excursion from the mean is

from the RVA station and can be indicative of a site response as has been previously discussed.

The largest subset of sample points is from the 1989 Loma Prieta earthquake (cf., section 4.2.7). A total of 27 SV data points are plotted in Figure 5.7 along with the mean SSVR curve. Seven observed displacement values are greater than plus or minus one σ_T from the mean. Four of these sites are located in San Francisco and an explanation for their high amplitudes have previously been attempted. The highest deviation from the mean for the SV data is from the measurement at the SLA station. The SH amplitude for this station was not a statistical outlier as is the case for the SV amplitude (see Figure 5.2). The displacement seismograms are plotted in Figure 5.8. The observed SV amplitude is only smaller than the observed SH amplitude by a factor of about 22 percent. For this azimuth, the radiation patterns would predict a lower SV displacement value of about 50 percent. This discrepancy at the SLA site could be explained in terms of a increased site response for the vertically polarized SV ground motion.

The likely reason for the low SH and SV amplitudes observed at the MON site have been previously discussed (see section 5.3.1). The observed SV amplitude of motion at the PJH station is lower than the mean SSVR curve by greater than one σ_T. Well developed surface wave trains are clearly identifiable on the displacement records in Figure 5.9. The seismograms from the LBL station (similar azimuth and greater distance from the source) also show well developed surface waves. However, none of the San Francisco seismograms, which are at approximately the same distance but different azimuths, indicate the development of surface wave trains. Due to the partition of the seismic energy into surface wave motion, the deamplification of SV motion at PJH can be classified as a propagation effect.

The 1992 Landers (cf., section 4.2.8) data consist of 13 vertical rock recordings (see Table 4.4). A total of five data points are greater than plus or minus one σ_T from the mean. The mean ratio for the data is $\mu = -0.10 \pm 0.29$ (see Figure 5.2). The low amplitude

at the PLC and RVA station have been discussed in the previous section. For this seismic source, the low amplitude SV value for the PFO station is attributable to the rupture directivity (see equation (3.13)), with the fault source propagating away from the station (see Figure 4.17). The low SV amplitude recorded at SVD is an artifact of the near nodal location of the station for the SV radiation pattern. The increased amplitude at the most distant station, ISA, can be explained from the rupture directivity focusing of the seismic energy in a direction towards the station.

5.3.3 Soil Displacement for SH Waves

I now discuss the mean estimation for the horizontally polarized SH peak ground displacement curve at soil sites (SSHS). A total of 122 peak SH displacement values were used in the regression for soil sites (see Table 4.4). The SSHS equation is,

$$\text{Log}_{10}(D) = -4.81 + 1.10M - 1.15\,\text{Log}_{10}(H_{slip}), \quad \sigma_T = 0.29, \tag{5.12}$$

where D is the peak SH displacement in cm and H_{slip} is in kilometers. The corresponding graphs of the residuals are shown in Figure 5.10. The largest residual of 35.6 occurs for the E06 station for the Imperial Valley earthquake. The observed amplification of peak displacement at this station will be explained below as an effect of rupture directivity. The mean residual for the SSHS curve is $\mu = 1.8 \pm 7.3$. The log values of the ratio of the observed to predicted peak SH ground displacement are shown in Figure 5.11 and 5.12. The mean ratio for the entire SH soil sample is $\mu = 0.01 \pm 0.30$ and the corresponding mean values for each earthquake are listed in Table 5.5. The soil SH data has a smaller dispersion about the zero line than the rock SH data (cf., Figure 5.2), but there are still some statistical outliers in the sample which will be discussed.

Table 5.5 **Mean ratio estimates for each of the 8 strike-slip earthquakes for the SSHS attenuation curve.**

Earthquake	Number of Data Points	SH Mean Ratio
1979 Imperial Valley	32	0.14 ± 0.27
1980 Livermore MS	6	-0.01 ± 0.30
1980 Livermore AS	5	0.03 ± 0.25
1984 Morgan Hill	18	0.10 ± 0.25
1986 North Palm Springs	11	-0.26 ± 0.23
1987 Superstition Hills	10	-0.03 ± 0.23
1989 Loma Prieta	25	-0.09 ± 0.32
1992 Landers	15	0.06 ± 0.29
Total Dataset	122	0.01 ± 0.30

The 1979 Imperial Valley earthquake (cf., section 4.2.1) produced the most soil seismograms for a strike-slip source of all the earthquakes studied. A total of 32 peak SH values were measured and are plotted in Figure 5.13 along with the mean SSHS curve for a $M_w = 6.5$ earthquake. The mean ratio value is $\mu = 0.14 \pm 0.27$ for the SH sample (see Table 5.5).

The distribution of all of the data points greater than one standard deviation from the mean can be explained in terms of the amplification of ground motion from rupture directivity (see section 3.5). These stations are all located to the north of the northerly propagating rupture (see Figure 4.5). The El Centro array stations are located at H_{slip} distances of approximately 15 km, and the ground motion from these stations are amplified due to rupture directivity (see equation (3.13)). Three data points fall below the minus one σ_T in Figure 5.13. The CMP station, at a H_{slip} distance of 40 km, is probably de-amplified due to the fault rupture propagating away from the station. The other two stations (CXO and PLS) which have low observed peak displacement amplitudes are located near a node of the SH radiation pattern.

The 1980 Livermore mainshock (cf., section 4.2.2) was recorded on a total of six soil sites and the mean ratio values is $\mu = -0.01 \pm 0.30$ (see Table 5.5). The two stations (LVA and DVD) with high amplitudes of ground motion are located along the direction of rupture propagation and these amplitudes can be predicted in terms of rupture directivity (see section 3.5). The peak SH displacement at SRM is lower than one standard deviation from the attenuation curve and can be accounted for based on the location of the station near to a minimum of the SH radiation pattern.

There are five classified soil site measurements from the 1980 Livermore aftershock (cf., section 4.2.3). Unlike the rock measurements, which showed a systematic over-prediction of the peak values with the mean SSHR curve, the observed SH data points are evenly distributed around the mean SSHS curve. This even distribution can also be seen in the plot of the log of the ratio values in Figure 5.11 where the mean value for this sample is $\mu = 0.03 \pm 0.25$ (see Table 5.5). The two peak displacement values which are lower than the mean SSHS curve can again for this source be attributed to the rupture directivity (equation (3.13)) because these two stations (DVD and LVA) are located at a back-azimuth from the propagating rupture. Rupture directivity may also cause the relatively high observed amplitude motion at ANT which is located approximately along strike in the direction of the fault rupture.

The peak SH displacement data from the 1984 Morgan Hill earthquake (cf., section 4.2.4) consisted of 18 soil sites. The highest SH peak displacement (5.2 cm) was recorded at HVR station which is located along the strike of the fault plane (see Figure 4.8), but in the opposite direction of rupture propagation. This larger than predicted amplitude is caused by the measurement being made near the maximum node of the SH radiation pattern. Rupture directivity increases the amplitude of motion at stations located approximately along the strike (e.g., the Gilroy Array and the Hollister Differential Array). AGN has the largest negative ratio (see Figure 5.11) and may be caused by the station being located near a node of the SH radiation pattern. The largest

positive ratio of 0.47 occurs at the LBN station located in the Great Central Valley of Central California. Because the station is not located along the azimuth of the fault plane, rupture directivity cannot explain the increase in motion. However, the station is located at the edge of the large sedimentary basin which can cause the amplification of ground motion (see section 3.4). The mean ratio for the 1984 Morgan Hill data is $\mu = 0.10 \pm 0.25$ (see Table 5.5) indicating a small over-prediction of the mean attenuation curve versus the observed measurements.

For the measurements from the 1986 North Palm Springs earthquake, there is a systematic over-prediction of peak displacement motion from the mean SSHS curve. Because the same systematic over-prediction in motion was also observed for the rock sites, the discrepancy between the observed and predicted values by exhaustion of alternatives may be explained by a faulting source property (such as an over-estimated seismic moment for the source which would lead to larger mean estimates of peak ground displacement). The two stations, HES and RNC have the largest misfit to the mean SSHS curve (see the ratio plot of Figure 5.11). These two sites would be expected to have a low amplitude based on the SH radiation pattern for the earthquake (see section 3.2). The mean ratio for the event is, $\mu = -0.26 \pm 0.23$ (see Table 5.5).

A sample of ten soil sites (see Table 4.4) was available from the 1987 Superstition Hills earthquake (cf., section 4.2.6). All of the data points except for two (PTS and ELC) have observed measurements lower than the predicted mean SSHS curve. As in a number of earlier cases discussed, larger than expected amplitudes are predicted by the directivity focusing mechanism. Because both of these stations are located approximately along the strike in the direction of fault rupture (see Figure 4.10). The mean ratio is $\mu = -0.03 \pm 0.23$ (see Table 5.5).

For soil sites, the second largest sample of maximum displacement measurements after the Imperial Valley earthquake is from the 1989 Loma Prieta earthquake (cf., section 4.2.7). Twenty-five strong ground motion records from such

sites were processed (see Table 4.4). The scatter in the Loma Prieta data is larger than for the other earthquakes, with a mean ratio of $\mu = -0.09 \pm 0.32$ (see Table 5.5) which could be caused by the previously noted amplification of ground motion at distances of approximately 100 km. Most of the low values can be expected based on the variations arising from the radiation pattern of the SH component of motion for this source mechanism. The large observed displacement at OSW (at a distance of approximately 85 km) corresponds with the increase in seismic energy due to lateral refraction for stations located in the San Francisco region (e.g., see Lomax and Bolt, 1992). The largest peak SH displacement (32.7 cm) occurs at the HOL site located southeast of the earthquake and is explained in terms of a large site response. This can be substantiated by comparing the peak ground displacement observed at two separate strong ground motion stations, HDA and HCH, located approximately 1 and 5 km away from the HOL station (see Figure 4.11). Both of these stations have peak SH amplitudes of about 12 cm. The clear suggestion is that a significant a large site response is present at the HOL station to cause an increase in the SH motion by a factor of about 3.

The soil data set from the Landers earthquake (cf., section 4.2.8) consists of measurements from 15 stations. The stations are well distributed over all azimuths, but the closest site is at a H_{slip} distance of over 40 km (see Figure 4.12) so that this sample contributes little to the overall regression curve at near source distances. The mean ratio for the SH stations is, $\mu = 0.06 \pm 0.29$ (see Table 5.5).

As was the case for the rock sites, the amplification of ground motion due to rupture directivity can be observed by the positive ratio values for sites located to the north, and negative ratio values for sites located to the south (see Figure 4.12). The sites located in the Los Angeles basin (OBG and DOW) have positive ratios due to the amplification of ground motion in the large alluvial Los Angeles basin (see section 3.4).

5.3.4 Soil Displacement for SV Waves

As in the case of SV wave measurements mode on rock formations, I now consider the measurements made from soil sites. A total of 113 peak SV displacement values were used in this regression. The mean SSVS attenuation curve for peak SV displacement on soil is,

$$\text{Log}_{10}(D) = -4.95 + 1.07M - 1.24\,\text{Log}_{10}(H_{slip}), \quad \sigma_T = 0.24, \tag{5.13}$$

where D is the peak SV displacement in cm and H_{slip} is in kilometers. The standard deviation for the SV soil sites is the lowest estimated standard deviation for any of the regression results previously presented. The residuals, which have a mean value of μ = 0.4 $\pm$ 2.3, are plotted in Figure 5.14. The largest residual (14.9) occurs for the ELC station from the Imperial Valley earthquake (see section 4.2.1). The SV ratio values for the entire data set is graphed in Figure 5.11 versus H_{slip} and Figure 5.25 versus M_W. The mean ratio value is, μ = 0.00 $\pm$ 0.24. Table 5.6 lists the computed mean ratio for each earthquake subsets.

Table 5.6 Mean ratio estimates for each of the 8 strike-slip earthquakes for the SSVS attenuation curve.

Earthquake	Number of Data Points	SV Mean Ratio
1979 Imperial Valley	33	-0.02 $\pm$ 0.27
1980 Livermore MS	6	-0.12 $\pm$ 0.19
1980 Livermore AS	5	-0.01 $\pm$ 0.17
1984 Morgan Hill	18	0.10 $\pm$ 0.18
1986 North Palm Springs	10	-0.02 $\pm$ 0.27
1987 Superstition Hills	1	0.45
1989 Loma Prieta	25	-0.04 $\pm$ 0.24
1992 Landers	15	0.05 $\pm$ 0.18
Total Dataset	113	0.00 $\pm$ 0.24

The vertical SV data (33 sample points) from the 1979 Imperial Valley earthquake (cf., section 4.2.1) are graphed in Figure 5.15 along with the mean SSVS curve. As was the case for the rock sample, the stations located to the north of the rupture (see Figure 4.5) had an increased amplitude in peak ground motion probably resulting from the effect of rupture directivity. In support of this explanation, the opposite effect of de-amplification was also observed at stations located to the south of the earthquake. For the vertical ground displacement motion, the two stations at CXO and MXC have SV values which are lower than the mean estimate by more than one standard deviation and are located perpendicular to the fault plane. The SV radiation pattern predicts relative low amplitudes at these two stations. The mean ratio value for the Imperial Valley data is $\mu = -0.02 \pm 0.27$ (see Table 5.6).

The observed values from the six soil sites from the 1980 Livermore mainshock (cf., section 4.2.2) are systematically under-valued (the mean ratio value for the sample is $\mu = -0.12 \pm 0.19$) for distances larger than approximately 35 km. Again the largest outliers can be expected from the theory of rupture directivity (see section 3.5), where large amplification is observed at LVA while the de-amplification is observed at ANT in a back azimuth direction (see Figure 4.6).

The five sample points from the Livermore aftershock (cf., section 4.2.3) are uniformly distributed around the mean SSVS curve (i.e., the mean of the ratio value is $\mu = -0.01 \pm 0.17$). The largest outlier was observed at DVD with a lower-than-expected peak displacement value but the reduction would be expected as the rupture front propagated away from this station.

The sample from the 1984 Morgan Hill earthquake (cf., section 4.2.5) consisted of 18 SV measurements from soil sites. The largest ratio occurs at LBN due to the increase in SV wave amplitude probably because of the same basin effect as discussed for the SH component. The largest negative ratio occurs at the G07 station with an azimuth that locates it near the node of the SV radiation pattern of the seismic source. The radiation

pattern also contributes to the increase in the peak displacement at the SJB station. The mean ratio for the earthquake is $\mu = 0.10 \pm 0.18$ (see Table 5.6).

As has been previously discussed for the other displacement results, the observed peak ground motion values from the 1986 North Palm Springs (cf., section 4.2.5) are systematically lower than the mean SSVS curve indicating a possible error in the over-estimation of the seismic moment. The two largest positive ratio values (PSA and DSP) are both located in the approximate direction of rupture propagation. The PSA value, which is higher than the mean by approximately one σ_T, is also located closer to the maximum of the SV radiation pattern than the DSP station. The mean ratio value for the ten data points from the earthquake is $\mu = -0.02 \pm 0.27$ (see Table 5.6).

Only one digital vertical displacement seismogram was available from the 1987 Superstition Hills earthquake (cf., section 4.2.6). With only having one data point, the statistical significance of the positive ratio value (see Table 5.6) is not clear, but larger than expected amplitudes would be expected at the station (IVW) based on the radiation pattern for the SV motion.

A sample of 25 measurements from the 1989 Loma Prieta earthquake (cf., section 4.2.7) for soil classified sites was used in the regression procedure. The SV data are not as widely disperse around the mean estimate when compared with the SH data (i.e., the SV sample has a mean ratio value of $\mu = -0.04 \pm 0.24$ (see Table 5.6)). The two positive data points (STG and OLE) may be accounted for by rupture directivity (see section 3.5) and lateral refraction of seismic energy (e.g., see Lomax and Bolt, 1992), respectively. The large number of negative ratio values can be partially explained by the radiation pattern for the SV motion. For example, the MVA station has the largest negative ratio value and is located near a SV radiation pattern node. The peak amplitudes for the soil site, A01, less than 4 km away from the AP2, are higher by a factor of approximately 3 indicating a de-amplification site response at the AP2 station relative to the A01 site.

The soil SV data set from the Landers earthquake consists of values from 15 stations. Only three observations (H05, XPO, and FYP) are greater than one σ_T away from the mean and all three have observed peak displacement values which are lower than the mean predicted values. These sites cluster, however, to the southwest of the mainly northerly propagating fault rupture. Although not directly in azimuth with the propagating rupture front, a numerical calculation (see equation (3.13)) suggests that the de-amplification of ground motion would be expected at these sites. Moreover, the nodal location of the three stations on the SV radiation pattern also contributes to the lower than expected peak SV displacement values. The mean ratio value for the SV sample is $\mu = 0.05 \pm 0.18$ (see Table 5.6).

5.4 Reverse-Fault Mechanisms

The empirically estimated attenuation curves for peak ground displacement produced by reverse fault mechanism earthquakes will be discussed in this section. The sample consists of only four earthquakes all from the Los Angeles region of southern California with a magnitude range of $5.6 < M_W < 6.7$ (see Table 4.1). Each earthquake has been previously described in chapter 4. The statistical outliers for each earthquake will be discussed in terms of the seismic source, wave propagation, or site response.

5.4.1 Rock Displacement for SH Waves

A total of 42 peak ground displacement SH measurements were used in the regression analysis (see Table 4.5). The mean RSHR curve,

$$\text{Log}_{10}(D) = -3.44 + 0.92M - 1.51\,\text{Log}_{10}(H_{slip}), \quad \sigma_T = 0.31, \tag{5.14}$$

where D is the peak SH displacement in cm and H_{slip} is in kilometers. Figure 5.16 shows a histogram of the residuals of the observed peak displacement values minus the predicted mean values from the RSHR curve as well as the residuals values versus H_{slip} distance. The residuals have a unimodal distribution, with a mean of $\mu = 0.33 \pm 1.81$ for the entire SH rock data set. The largest residual of 9.91 occurs from the strong ground motion recording from the 1994 Northridge earthquake at the CAS station. A total of six residuals are greater than one standard deviation from the mean; these outliers will be discussed separately for each earthquake.

The log of the ratio of the observed to predicted peak SH displacement values are plotted in Figure 5.17 for the entire reverse-fault mechanism rock sample versus H_{slip} distance. The corresponding graph versus M_w is in Figure 5.18. The mean ratio is $\mu = 0.00 \pm 0.31$ and the individual mean ratio estimates for each of the four earthquakes are listed in Table 5.7 along with the number of data points for each earthquake.

Table 5.7 Mean ratio estimates for each of the four reverse fault mechanism earthquakes for the RSHR attenuation curve.

Earthquake	Number of Data Points	SH Mean Ratio
1971 San Fernando	7	-0.14 ± 0.31
1987 Whittier Narrows	16	-0.03 ± 0.35
1991 Sierra Madre	3	0.09 ± 0.07
1994 Northridge	16	0.07 ± 0.30
Total Dataset	42	0.00 ± 0.31

First consider separately the 1971 San Fernando earthquake (cf., section 4.3.1) which has seven strong ground motion recording sites located on rock. The largest SH peak ground displacement (17.2 cm) for this earthquake was recorded at the PDW station (see Figure 4.15). The mean ratio value from the San Fernando earthquake is, $\mu = -0.14 \pm 0.31$ (see Table 5.7). Three observed peak SH displacement values (GPK, L04, and

L09) deviate from the mean value by more than one σ_T. The GPK station is located in a forward azimuth from the seismic source and the L04 and L09 station are located in a back azimuth from the seismic source. From the discussion of rupture directivity (see section 3.5), the observed amplification at GPK and deamplification at L04 and L09 is to be expected.

Next consider the 16 strong ground motion recordings from rock sites for the 1987 Whittier Narrows earthquake (cf., section 4.3.2). The mean ratio value for this sample is $\mu = -0.03 \pm 0.35$ (Table 5.7). Six observed displacement values (LBR, ORP, MTW, HNB, LBR, and RVA) are greater than one σ_T from the mean RSHR curve. The amplification of ground motion for the LBR and ORP stations would be expected for these azimuths because the radiation pattern for the SH displacement field (see section 3.2) in this case has amplitude maxima at these azimuths. Conversely, the deamplification of ground motion would be expected for the other four outlier observations (LBR, ORP, MTW, and LBR) based on the radiation pattern for the seismic source. The observed deamplification at RVA has been attributed to a site response because lower than expected peak displacement values have been measured at this site in other earthquakes.

Thirdly, consider the 1991 Sierra Madre earthquake (cf. section 4.3.3), which is the smallest event ($M_W = 5.6$) in the reverse-fault mechanism sample. Only three strong ground motion time histories for rock sites were used in the regression (see Figure 4.17). All three of the peak displacement SH values are within one σ_T of the mean RSHR attenuation curve. The computed mean ratio value is $\mu = 0.09 \pm 0.07$ (Table 5.7) for this earthquake.

Fourthly, the reverse mechanism rock sample consisted of 16 recordings from the 1994 Northridge earthquake (cf., section 4.3.4). The mean RSHR attenuation curve is graphically illustrated in Figure 5.19 along with the observed measurements. There are three observed displacement values (CAS, SND, and MTW) which are greater than one

standard deviation away from the mean curve. The observed amplification of ground motion at both the CAS and SND stations (see Figure 4.20), which are located north of the fault plane, can be attributed to the rupture directivity effects from the up-dip rupture of the seismic source (see section 3.5). The negative ratio for the MTW station would be expected from the near nodal location of the station for the SH radiation pattern from the seismic source. The mean ratio values for the Northridge measurements is $\mu = 0.07 \pm 0.31$ (see Table 5.7).

5.4.2 Rock Displacement for SV Waves

A total of 42 peak ground displacement SV measurements were used in the regression analysis (see Table 4.5). The empirically estimated mean RSVR attenuation curve is,

$$\text{Log}_{10}(D) = -3.57 + 0.88M - 1.49 \log_{10}(H_{slip}), \quad \sigma_T = 0.24, \tag{5.15}$$

where D is the peak SV displacement in cm and H_{slip} is in kilometers. Figure 5.20 shows the histogram for the residuals which have a unimodal distribution, with a mean of $\mu = 0.19 \pm 0.85$ for the entire SV rock sample. The largest residual of 4.7 occurs from the strong ground motion recording from the 1971 San Fernando earthquake at the PDW station (see Figure 4.15). Only two residuals are larger than one standard deviation from the mean and these will be discussed separately for each earthquake.

The ratio values for the rock SV peak displacement values were plotted in Figure 5.17 versus H_{slip} distance. The mean value for the SV sample is $\mu = -0.01 \pm 0.24$. The individual estimates for the mean ratio value of each of the four earthquakes is listed in Table 5.8 along with the number of data points.

Table 5.8 Mean ratio estimates for each of the four reverse fault mechanism earthquakes for the RSVR attenuation curve.

Earthquake	Number of Data Points	SV Mean Ratio
1971 San Fernando	7	-0.02 ± 0.17
1987 Whittier Narrows	16	-0.12 ± 0.25
1991 Sierra Madre	3	0.21 ± 0.20
1994 Northridge	16	0.06 ± 0.23
Total Dataset	42	-0.01 ± 0.24

First, seven observed vertical SV peak displacement values were used in the regression for the 1971 San Fernando earthquake (cf., section 4.3.1). Only one observation (PSL) is greater than one σ_T from the mean curve. The low amplitude displacement value at PSL can be attributed to the radiation pattern for the seismic source at that azimuth (see section 3.2). The mean value is $\mu = -0.02 \pm 0.17$ (Table 5.8).

Secondly, a total of 16 vertical peak SV displacement values were used in the regression analysis from the 1987 Whittier Narrows earthquake (cf., section 4.3.2). The larger than expected observed SV peak displacement at CAS could be caused by a site response which amplifies the vertical ground motion. To test this hypothesis, a comparison is made between the CAS vertical ground motion and the vertical ground motion from the CDA station, located approximately 4 km away (see Figure 4.16). The CDA peak SV amplitude was lower by a factor of 2 even though CDA is on soil, which based on the regression analysis (see equation (5.17) predicts higher peak ground displacement.

There are five observed data points (MTW, MCS, VPS, NHB, and RVA) which fall below the minus one σ_T curve. Although these stations are not clustered together (see Figure 4.16), the relative minimums of the SV radiation pattern for each of the separate azimuths would cause a deamplification of the SV observed ground motion.

The low amplitude observed at RVA is also caused by a local site effect as low peak displacement values were observed on both components for a set of different earthquakes. The mean ratio value for the Whittier SV sample is $\mu = -0.12 \pm 0.25$ (Table 5.8).

The peak SV displacement values from the 1991 Sierra Madre earthquake (cf., section 4.3.3) consisted of three stations. The PAL station recorded a higher than expected SV peak displacement value. Although the station is located at a back azimuth away from the up-dip rupture on the fault plane (see Figure 4.17) and hence directivity focusing is not responsible, the SV radiation amplitude pattern predicts higher ground motions at PAL than at other azimuths. The mean ratio value for the three data points is $\mu = 0.21 \pm 0.20$ (Table 5.8).

Finally, the mean RSVR attenuation curve for a representative $M_W = 6.7$ earthquake is plotted in Figure 5.21 along with the observations from the 1994 Northridge earthquake (cf., section 4.3.4). The vertical SV data show less dispersion about the mean curve than the SH data from the Northridge event (i.e., compare Figure 5.19 with Figure 5.21). The largest peak SV displacement of 4.5 cm was recorded at the PKC station. This larger than expected amplitude can be predicted from the rupture directivity focusing effect (see section 3.5) and the SV radiation pattern (see section 3.2). Rupture directivity also contributes to the amplification of the observed SV ground motion at the SND station located north of the seismic source (see Figure 4.20). By contrast, the NWB station is located to the south, but the larger-than-predicted peak SV amplitude probably is caused because of its location near to a maximum on the SV radiation pattern. The average ratio value for the Northridge SV data from the rock sites is $\mu = 0.06 \pm 0.23$ (see Table 5.8).

5.4.3 Soil Displacement for SH Waves

I now consider the empirical regression of the 115 peak ground displacement SH values recorded on soil (see Table 4.5). In this case the mean RSHS attenuation curve is,

$$\text{Log}_{10}(D) = -3.26 + 0.91M - 1.53\,\text{Log}_{10}(H_{slip}), \quad \sigma_T = 0.27, \tag{5.16}$$

where D is the peak SH displacement in cm and H_{slip} is in kilometers. Figure 5.22 shows a histogram plot of the residuals of observed peak displacement values minus the predicted values from the model. As was the case for the rock residuals, the residuals have a unimodal distribution, with a mean of $\mu = 0.4 \pm 2.1$ for the entire SH soil sample. The largest residual of 16.1 occurs from the strong ground motion recording from the 1994 Northridge earthquake at the TAR station. A total of nine residuals are greater than one standard deviation from the mean and are discussed separately for each earthquake.

The log of the ratio of the observed to predicted peak SH displacement values are plotted in Figure 5.23 for the soil site, reverse-fault mechanism sample versus H_{slip}

Table 5.9 Mean ratio estimates for each of the four reverse fault mechanism earthquakes for SH soil attenuation curve.

Earthquake	Number of Data Points	SH Mean Ratio
1971 San Fernando	14	-0.11 ± 0.30
1987 Whittier Narrows	66	0.00 ± 0.26
1991 Sierra Madre	3	0.13 ± 0.27
1994 Northridge	32	0.06 ± 0.28
Total Dataset	115	0.00 ± 0.27

distance. The corresponding plot versus M_W is in Figure 5.24. The mean ratio is $\mu = 0.00 \pm 0.27$. The individual mean ratio estimates for each of the four earthquakes are listed in Table 5.9 along with the number of data points for each earthquake.

The soil site observations for the 1971 San Fernando earthquake (cf., section 4.3.1) consisted of 14 measurements. Five data points are greater than one σ_T away from the mean. The two high values (GDL and SAO) are along the approximate azimuth which corresponds with a SH radiation pattern maximum. The three low observations (L12, PPP, and WTW) can also be predicted from the relative low amplitude of the radiation pattern for each of the three separate azimuths. However, as will be shown in the next section, a path and site effect for the L12 and WTW station may also be contributing to the lower-than-expected amplitudes. The mean ratio value is $\mu = -0.11 \pm 0.30$ (Table 5.9).

The sample for soil classified sites from reverse mechanism earthquakes is dominated by the strong ground motion recordings from the 1987 Whittier Narrows earthquake (cf., section 4.3.2) with 66 peak SH values in the total sample of 115 values. The Whittier Narrows observations are plotted in Figure 5.25 along with the corresponding mean RSHS attenuation curve. The data span the range $15 < H_{slip} < 115$ km (see Figure 4.16 for a map of the station locations). The observations in Figure 5.25 show a wide dispersion about the mean curve. The mean ratio value is $\mu = 0.00 \pm 0.26$ (see Table 5.9). The low amplitude of the observed values which are greater than σ_T can be accounted for by the SH amplitude radiation pattern for the seismic source (see section 3.2).

Consider next the 1991 Sierra Madre (cf., section 4.3.3) observed peak SH displacement values. The ETN station is the closest soil station and the measured peak displacement value for this station is above the σ_T. This station is located up-dip from the seismic source (see Figure 4.17) and the amplification of peak ground motion could well be caused by the effects of rupture directivity (see section 3.5). The mean ratio value for the soil sample is $\mu = 0.13 \pm 0.27$ (see Table 5.9).

Thirty two strong ground motion records were processed to determine the peak SH displacement from soil sites in the 1994 Northridge earthquake (cf., section 4.3.4). As was the case for the rock data (see section 5.4.1) from the Northridge earthquake, the soil data are dispersed about the mean attenuation curve. The computed mean ratio value is $\mu = 0.06 \pm 0.28$ (see Table 5.9). The largest peak SH ground displacement was observed at Tarzana (TAR). This site (see Figure 4.20) experienced extremely high peak ground accelerations (e.g., many peaks over 1 g) for the mainshock and subsequent aftershocks recorded on portable instruments (Spudich et. al, 1995). Spectral site response analysis of the recorded aftershocks indicate the likelihood of the large amplitude ground motions to be caused mainly by a resonance of the entire hill structure (Spudich, et al., 1995).

The other outlier point Sylmar (SYL), which is at approximately the same distance as TAR, has a high amplitude of peak ground displacement due to the rupture directivity effect of the seismic source (see section 3.5). This site is located nearly up-dip from the fault plane. The cluster of low amplitude stations at a distance of approximately 45 km is located on the northern edge of the Los Angeles basin. A possible explanation for the lower-than-expected values could be due to the partitioning of seismic body wave energy into basin generated surface waves, thereby reducing the body wave amplitude. The other values which are less than one σ_T can be accounted for by the SH radiation pattern for this thrust seismic source (see section 3.2).

5.4.4 Soil Displacement for SV Waves

The analysis of the four classifications is now completed by regressing the 112 peak ground displacement values for the SV displacement measured at soil sites (see Table 4.5). The mean empirical RSVS curve is,

$$\text{Log}_{10}(D) = -4.81 + 1.05M - 1.31\,\text{Log}_{10}(H_{slip}), \quad \sigma_T = 0.26, \tag{5.17}$$

where D is the peak SV displacement in cm and H_{slip} is in kilometers. Figure 5.26 shows a histogram of the residuals of the observed peak displacement values minus the predicted values from the model and a graph of the residuals versus H_{slip}. The residuals have a unimodal distribution, with a mean of $\mu = 0.2 \pm 1.5$ for the entire SV soil data set. The largest residual of 12.8 occurs from the strong ground motion recording from the 1994 Northridge earthquake at the TAR station where the recorded seismic wave field has been previously discussed (see section 5.4.3). Only five residuals are larger than one standard deviation from the mean. As in the previous section, the observations from each earthquake will be discussed.

The ratio values for the soil SV peak displacement values were plotted in Figure 5.23 versus H_{slip} distance. The mean value for the SV soil data is $\mu = 0.00 \pm 0.26$ and the computed mean estimates for the ratio values are listed in Table 5.10 for each of the four reverse fault mechanism earthquakes.

Table 5.10 Mean ratio estimates for each of the four reverse fault mechanism earthquakes for the RSVS attenuation curve.

Earthquake	Number of Data Points	SV Mean Ratio
1971 San Fernando	14	-0.04 ± 0.29
1987 Whittier Narrows	64	-0.02 ± 0.24
1991 Sierra Madre	2	0.44 ± 0.09
1994 Northridge	32	0.03 ± 0.27
Total Dataset	112	0.00 ± 0.26

In the same sequence as previously, first consider the SV soil dataset from the 1971 San Fernando earthquake (cf., section 4.3.1) consisting of 14 observations (Figure 5.63). Five data points are greater than one σ_T from the mean curve. The two values EPP

and SAO) which are $+\sigma_T$ are located at a distance of approximately 70 km (see Figure 4.20) and are both located near a SV radiation pattern maxima (see section 3.2). As was foreshadowed in the previous section for the SH component of displacement, the emphasized L12 and WTW station experienced both low peak SV and SH amplitudes. Although located near a SH radiation pattern minimum, these stations are located near a SV radiation pattern maximum. Hence, another explanation is needed to account for the reduction is peak amplitude at these two stations. For the L12, there is a suggestion that local structural response could be controlling the peak amplitude because nearby stations are not similarly reduced in peak ground motion amplitude. For the WTW station, one hypothesis is that the conversion of incident body-wave seismic energy near the margin of the Antelope Valley into surface wave seismic energy leads to a reduction in the observed body-wave peak displacement (see section 3.4). The computed mean ratio value for the SV is $\mu = -0.04 \pm 0.29$ (see Table 5.10).

Secondly, the 1987 Whittier Narrows earthquake (cf., section 4.3.2) provided 64 SV peak displacement values. Figure 5.27 shows the point values and the mean RSVS attenuation curve. Dispersion of sample points increases for distances greater than about 30 km and the ratio values have a mean of $\mu = -0.02 \pm 0.24$ (Table 5.10). The sample of stations that are greater in peak amplitude than one σ_T can be accounted for by their relatively close location to the SV amplitude radiation pattern maxima (see section 3.2). The low observed peak SV values, however, do not all correspond to a SV radiation pattern minima. For the sites located in the Los Angeles basin the low amplitude in SV peak displacement ground motion may appear for the same hypothesis as outlined for the 1971 San Fernando earthquake. The basin structure may convert seismic body wave energy into basin induced seismic waves. For the sites that are not located in the Los Angeles basin, the radiation pattern minima can predict the low amplitude in peak SV ground motion.

Only two peak SV data points were used from the 1991 Sierra Madre earthquake (cf., section 4.3.3) as the low amplitudes on the vertical component time history from the VSQ station were not readable. Both points lie above the one σ_T curve. However, these stations are both located on a SV radiation pattern maxima and moreover, are located in the up-dip direction of the seismic source (i.e., the directivity focusing of the seismic source would produce amplified peak ground displacement values (see section 3.5)). The mean ratio values for the two points is $\mu = 0.44 \pm 0.09$ (Table 5.10).

Finally, the data from the 1994 Northridge earthquake consisted of 32 peak SV displacement measurements. The largest peak SV displacement was observed at TAR where evidence for a resonant site response has already been discussed in the previous section. The high amplitude values for the other sites greater than one σ_T can be accounted for by either the station being located near a SV radiation pattern maxima (see section 3.2) or the effects of rupture directivity (see section 3.5). As was the case for the San Fernando earthquake, the observed peak SV displacement value at L12 is lower than one σ_T from the mean curve and this inter-earthquake correlation is evidence for a local geological explanation. The mean ratio value for the Northridge earthquake is $\mu = 0.03 \pm 0.27$ (Table 5.10).

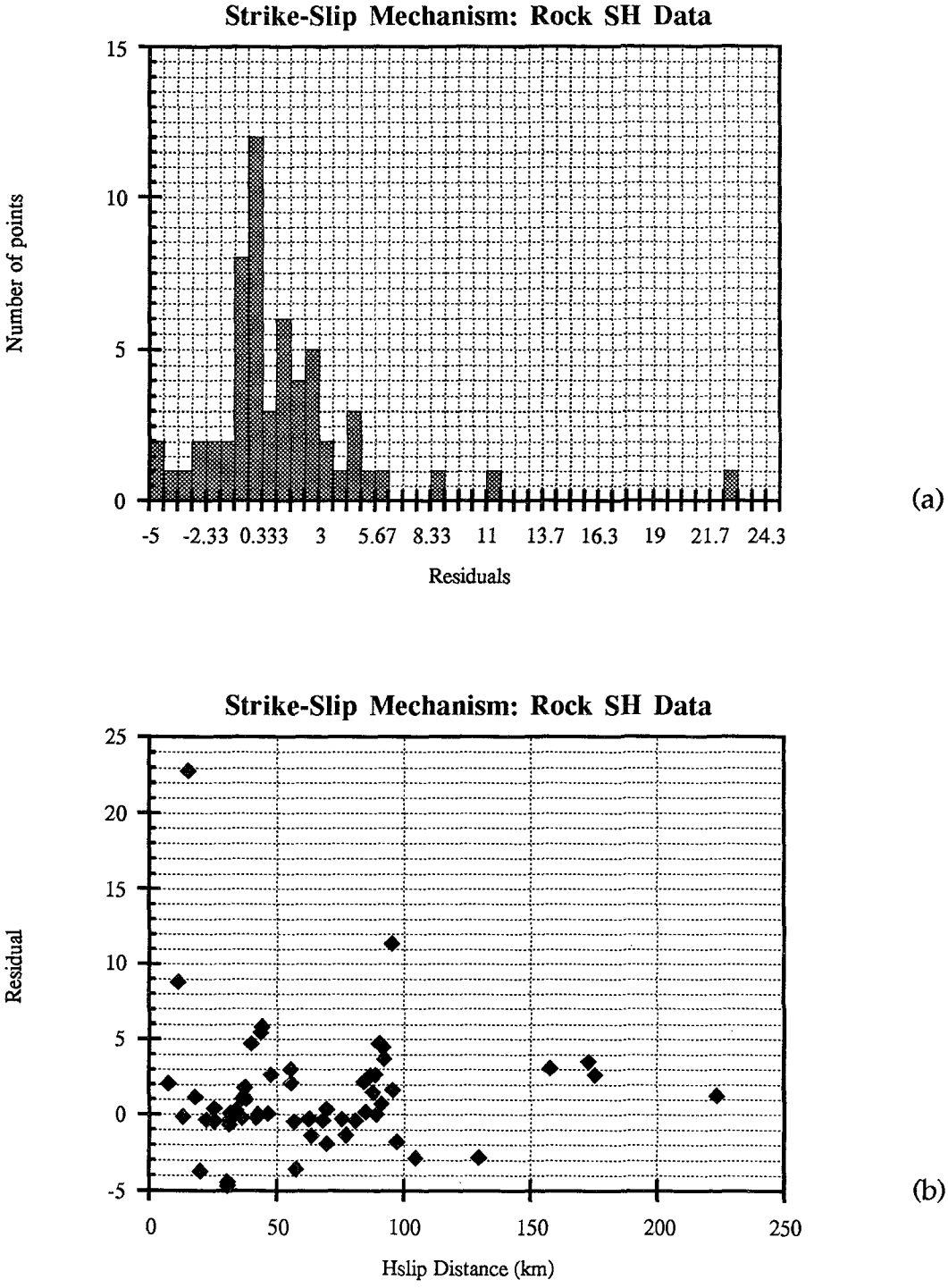

Figure 5.1 Histogram of the residuals (observed minus predicted) from the mean SSHR attenuation curve. (a) Binned histogram plot. (b) Residuals plotted versus H_{slip} distance.

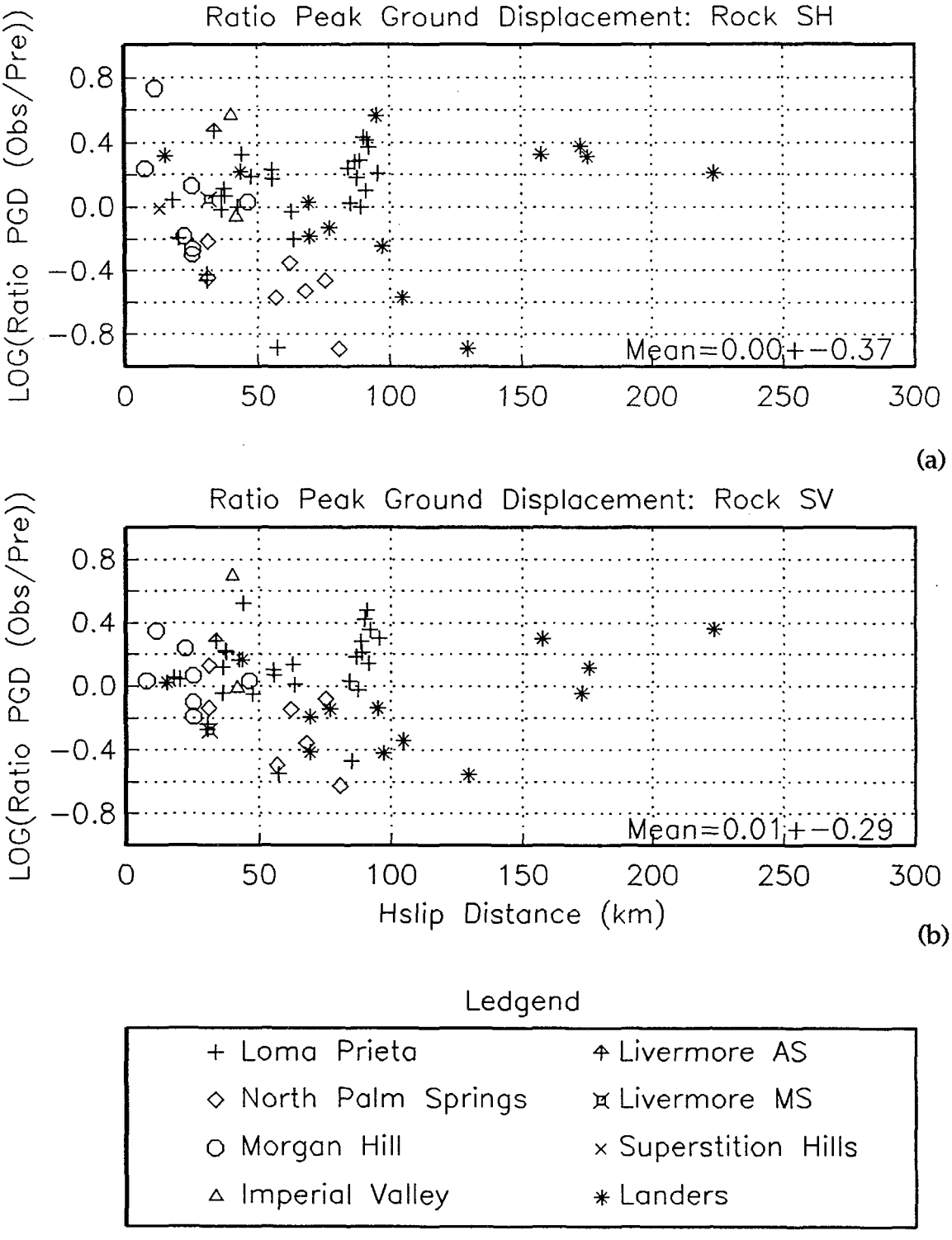

Figure 5.2 Log of the ratio of the observed peak ground displacement (Obs) divided by the predicted peak ground displacement (Pre) from the mean strike-slip rock attenuation curve versus H_{slip} distance. (a) SH component. (b) SV component.

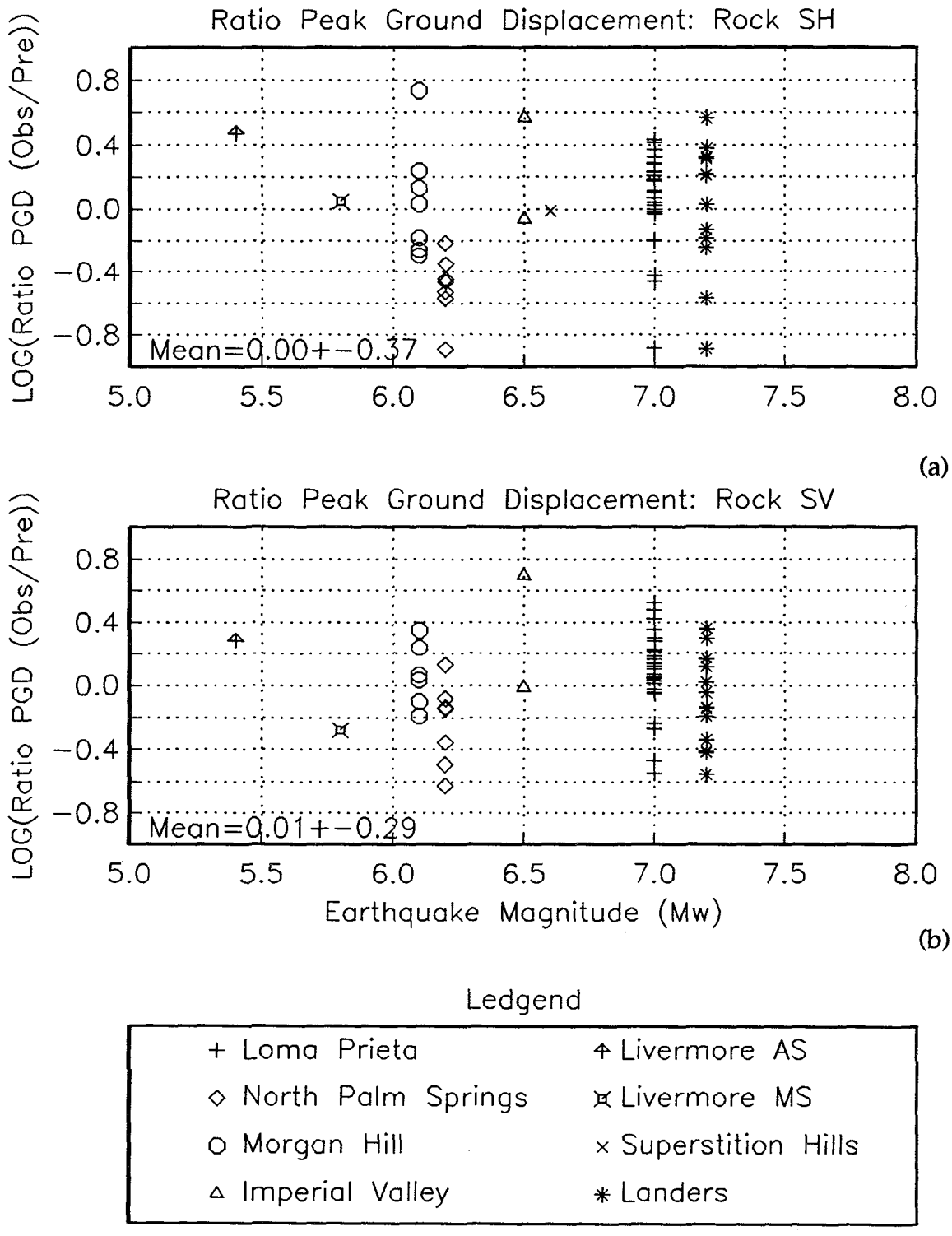

Figure 5.3 Log of the ratio of the observed peak ground displacement (Obs) divided by the predicted peak ground displacement (Pre) from the mean strike-slip rock attenuation curve versus M_W. (a) SH component. (b) SV component.

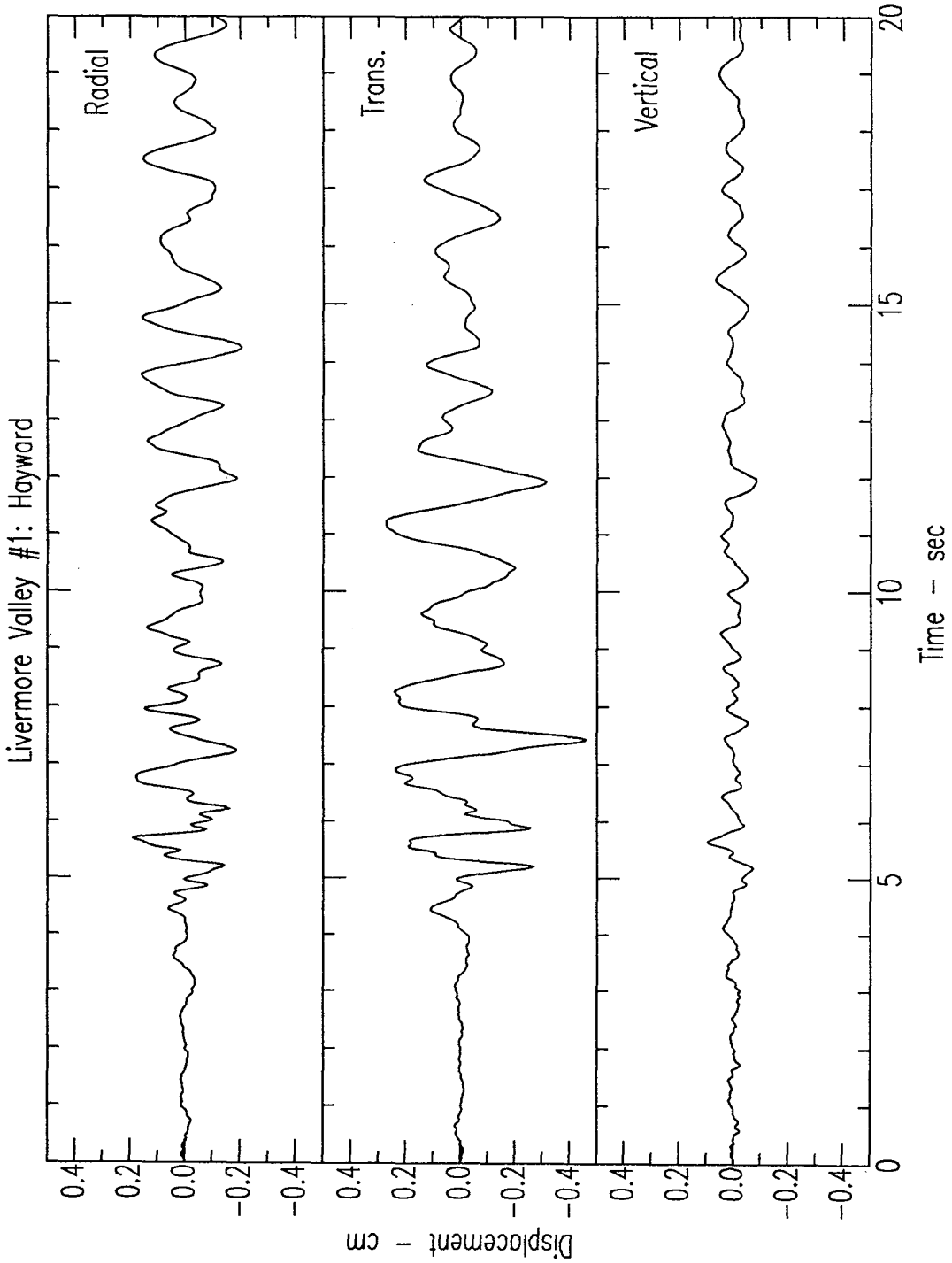

Figure 5.4a Radial, transverse, and vertical displacement seismograms from the 1980 Livermore Valley #1 earthquake recorded at Hayward Stadium Grounds.

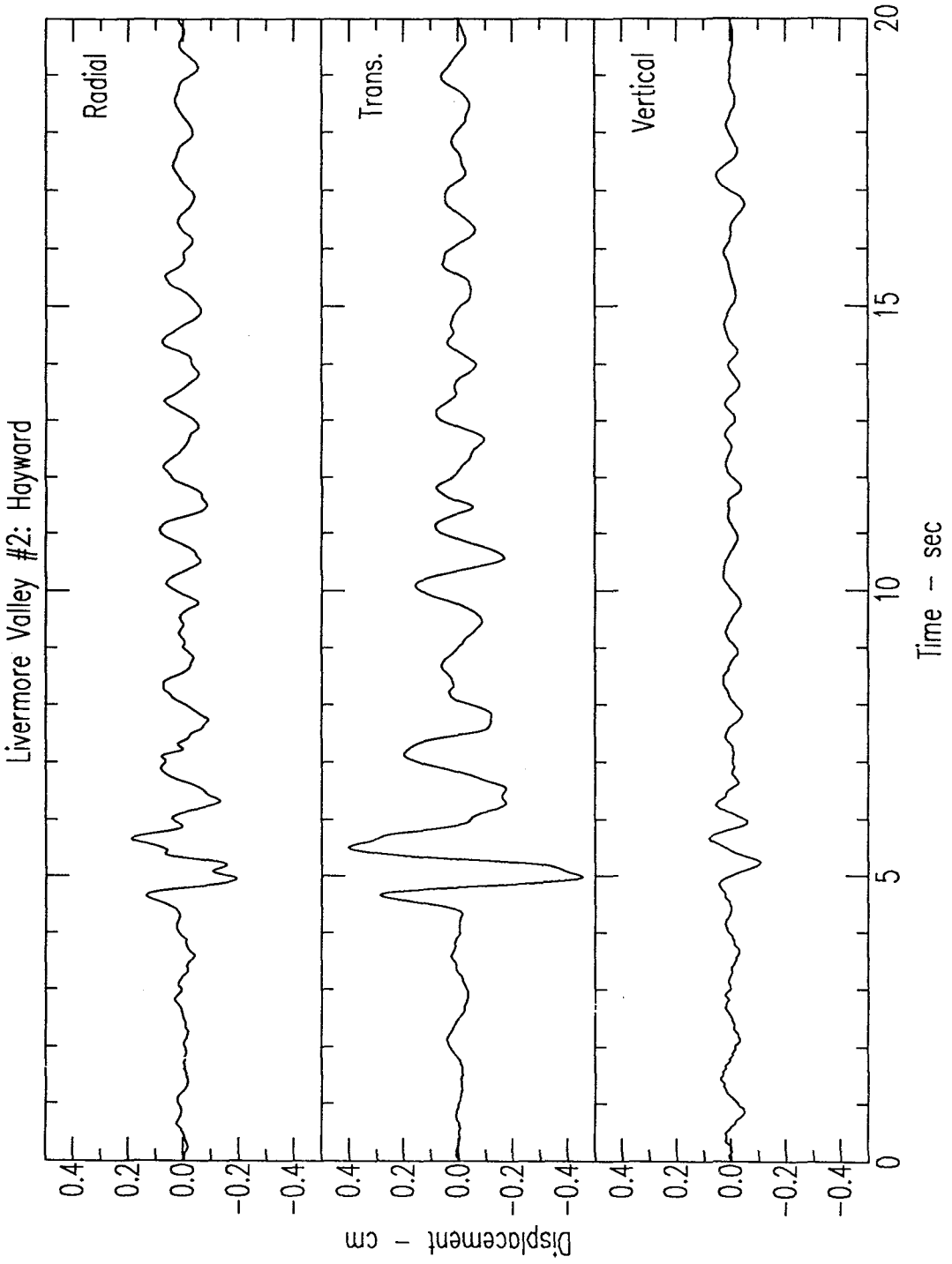

Figure 5.4b Radial, transverse, and vertical displacement seismograms from the 1980 Livermore Valley #2 earthquake recorded at Hayward Stadium Grounds.

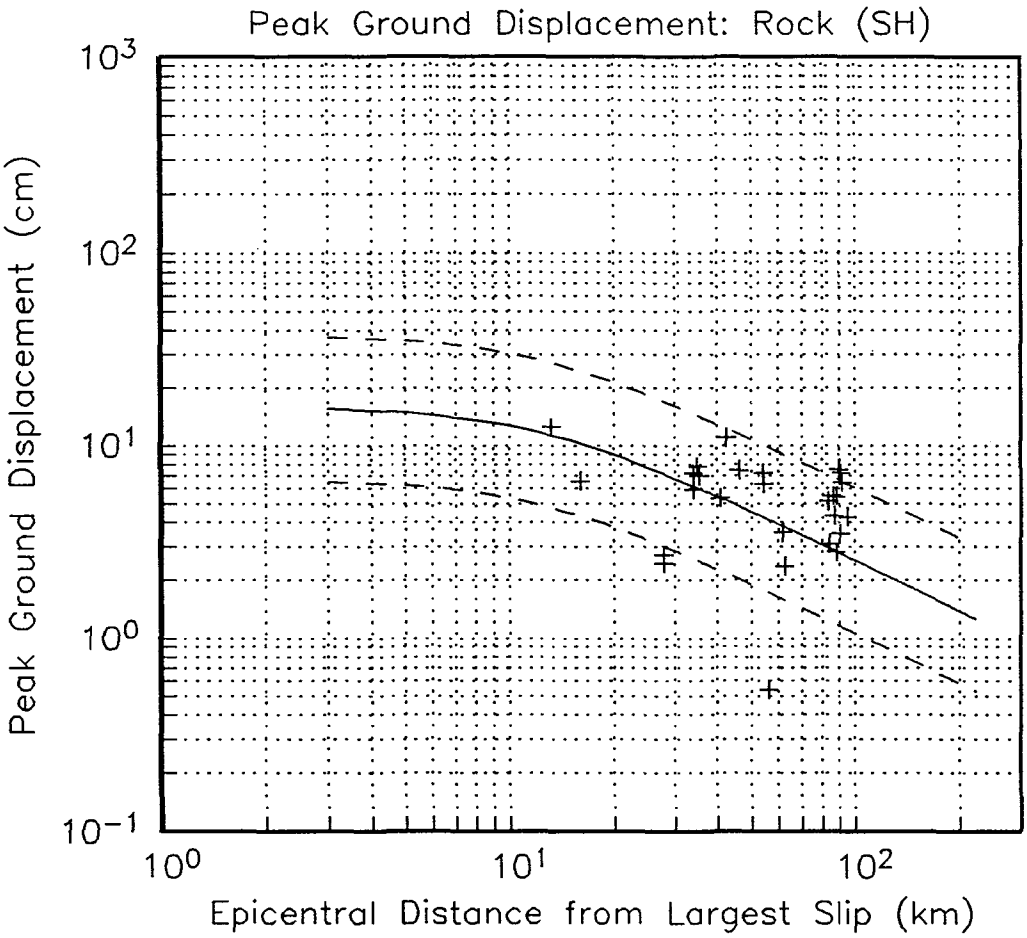

Figure 5.5 Mean SSHR attenuation curve plotted with the peak ground displacement observations from the 1989 Loma Prieta (M_w = 7.0) earthquake. Plus and minus one σ_T are indicated with the dashed lines.

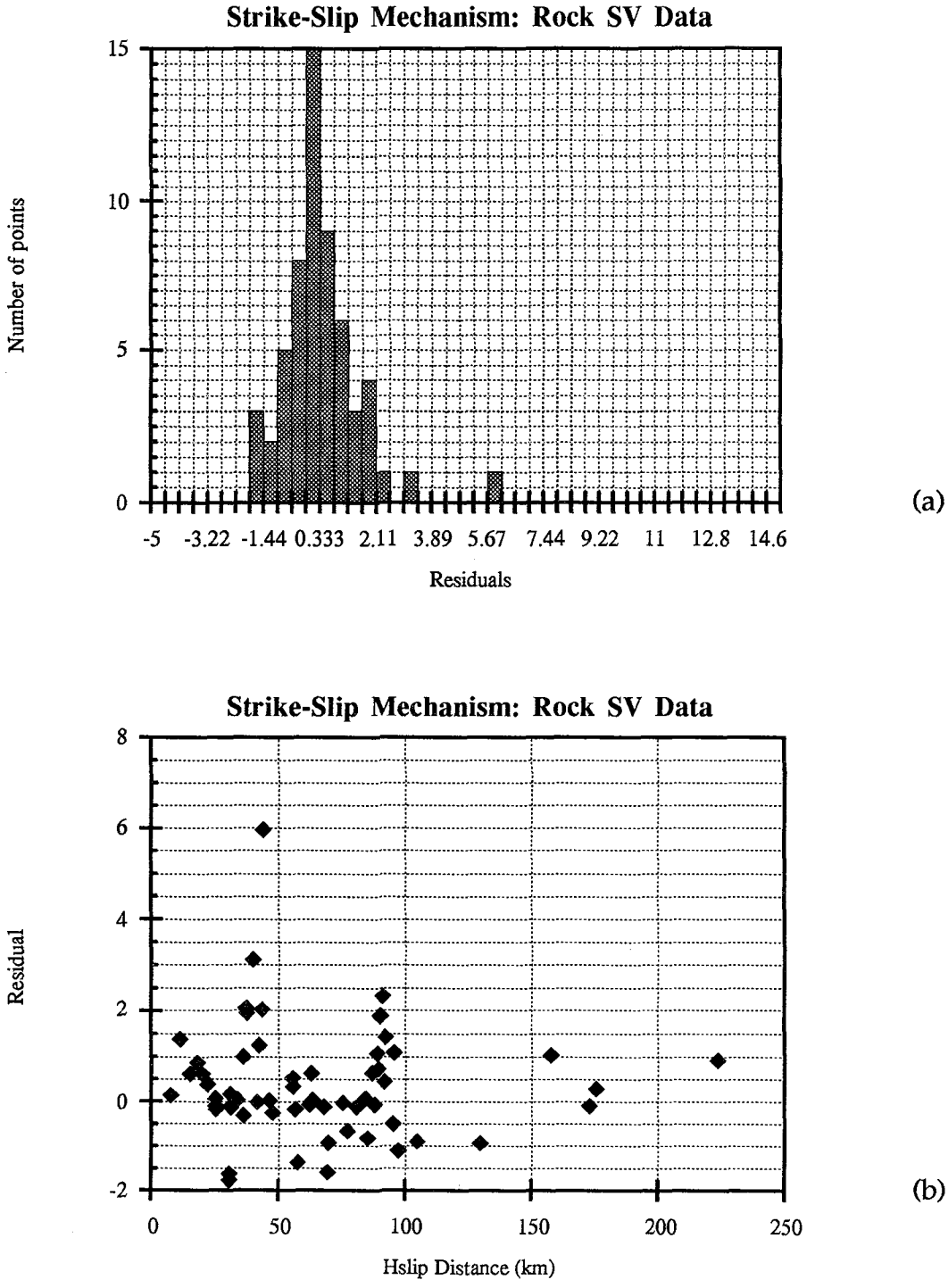

Figure 5.6 Histogram of the residuals (observed minus predicted) from the mean SSVR attenuation curve. (a) Binned histogram plot. (b) Residuals plotted versus H_{slip} distance.

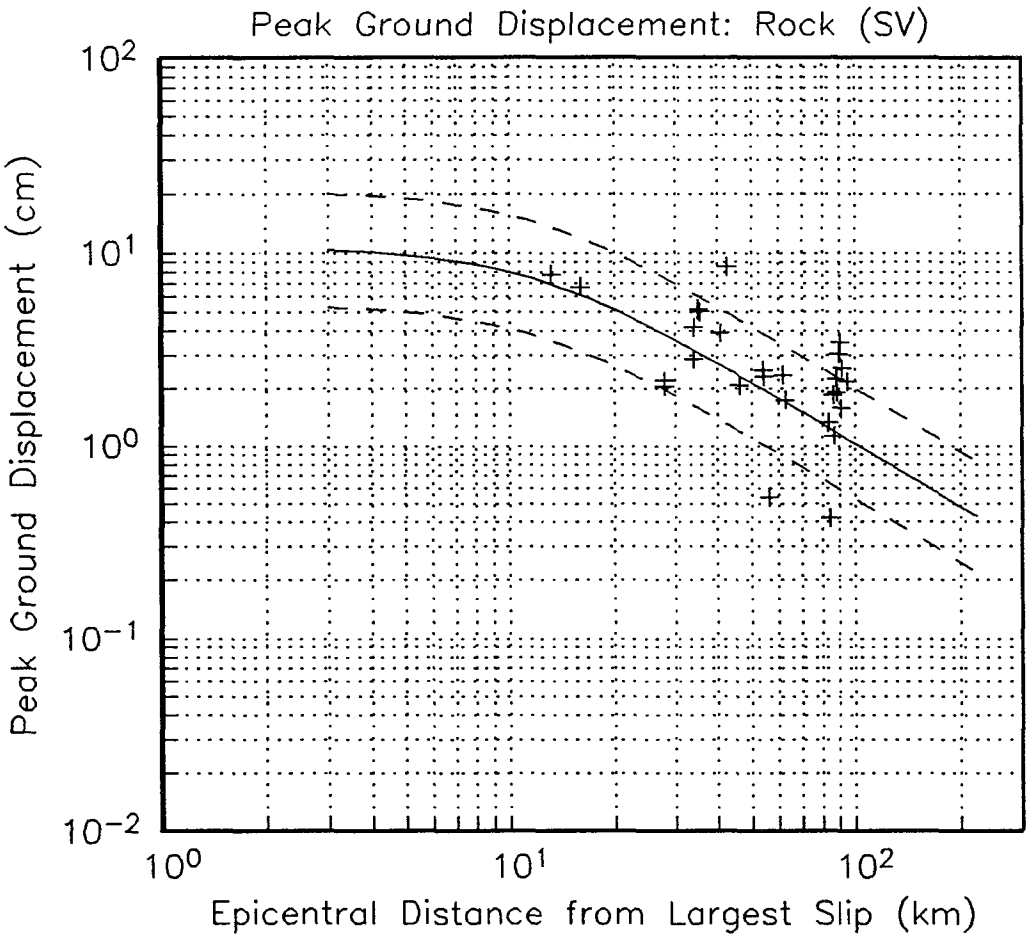

Figure 5.7 Mean SSVR attenuation curve plotted with the peak ground displacement observations from the 1989 Loma Prieta (M_w = 7.0) earthquake. Plus and minus one σ_T are indicated with the dashed lines.

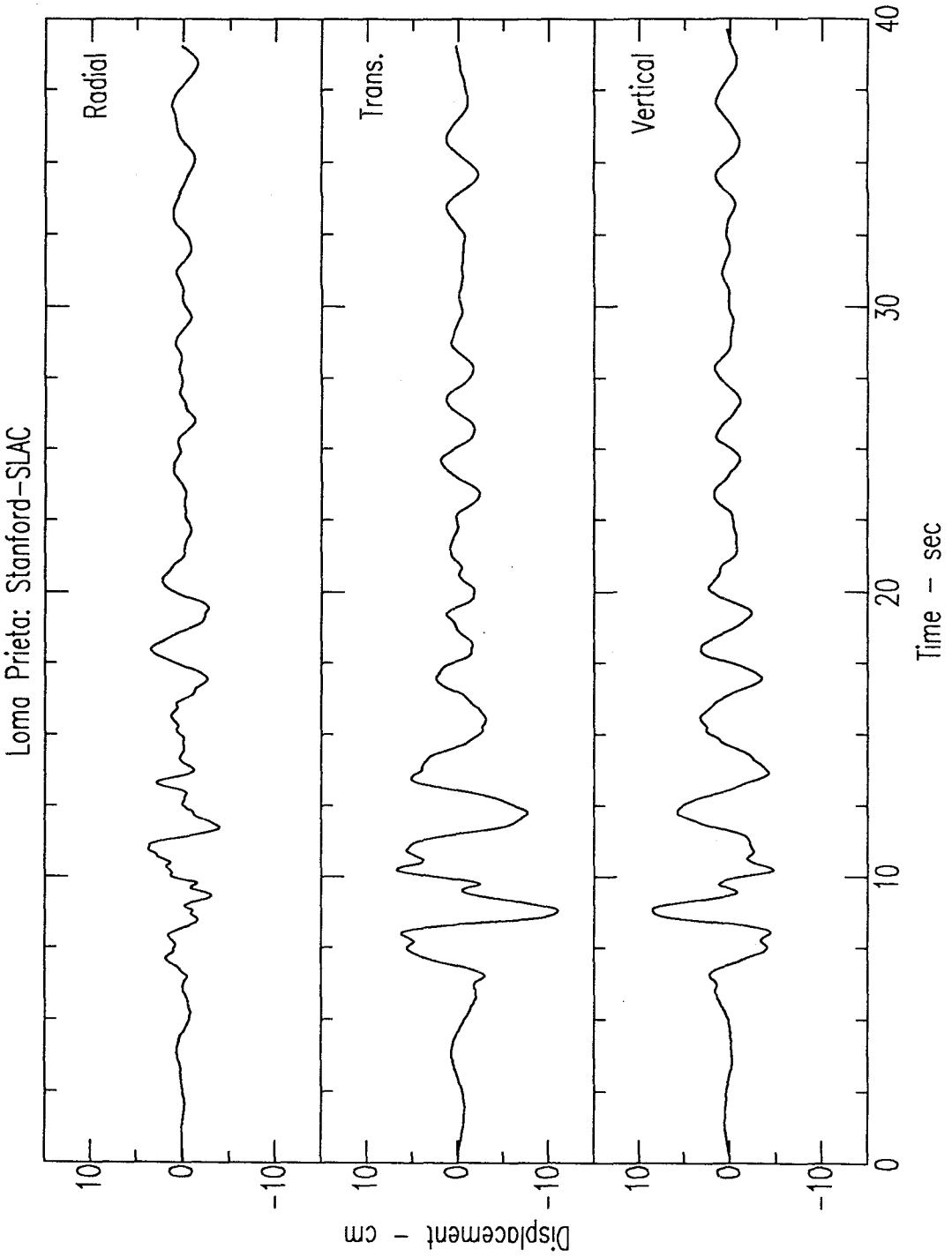

Figure 5.8 Radial, transverse, and vertical displacement seismograms from the 1989 Loma Prieta earthquake recorded at Stanford-SLAC.

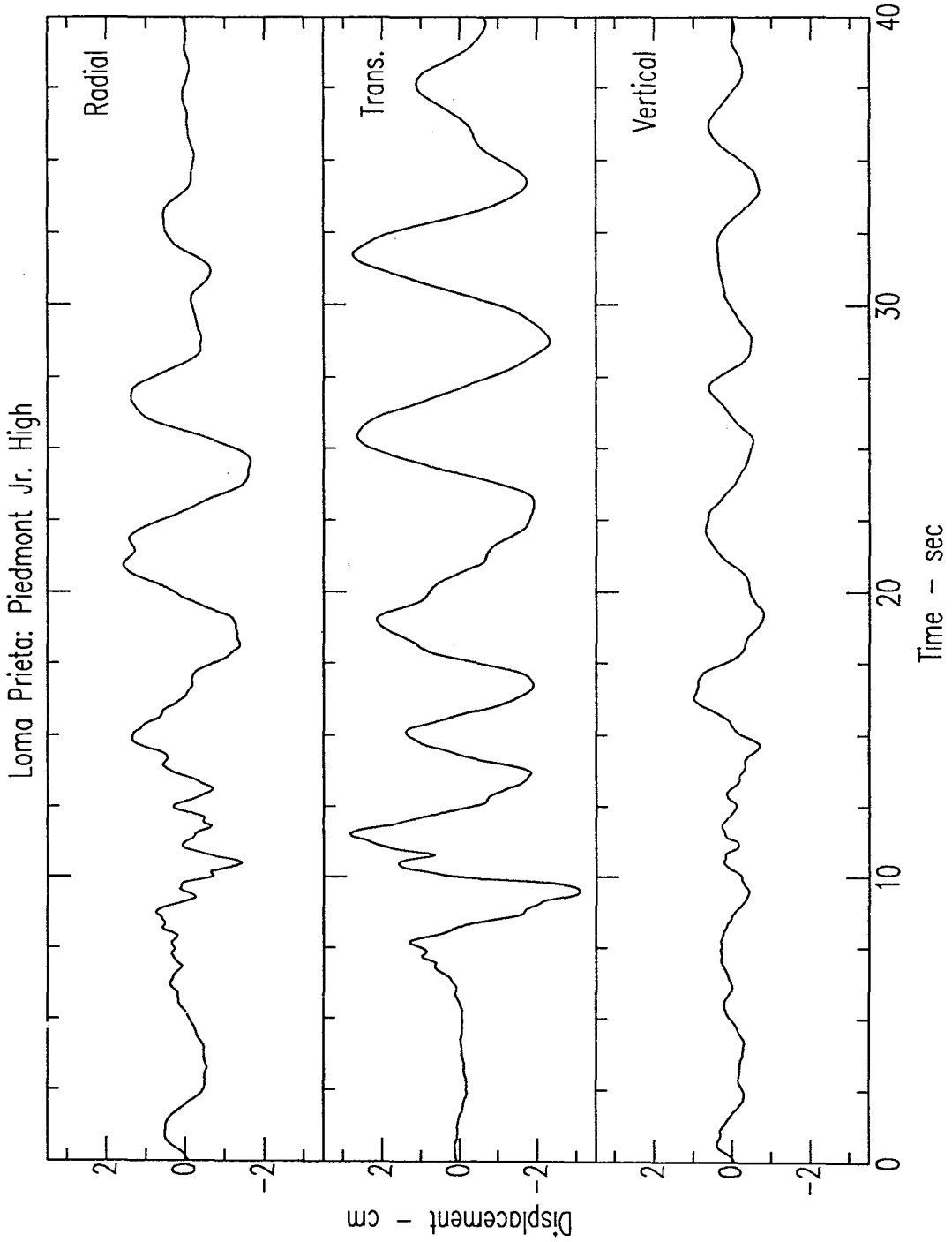

Figure 5.9 Radial, transverse, and vertical displacement seismograms from the 1989 Loma Prieta earthquake recorded at Piedmont Junior High School.

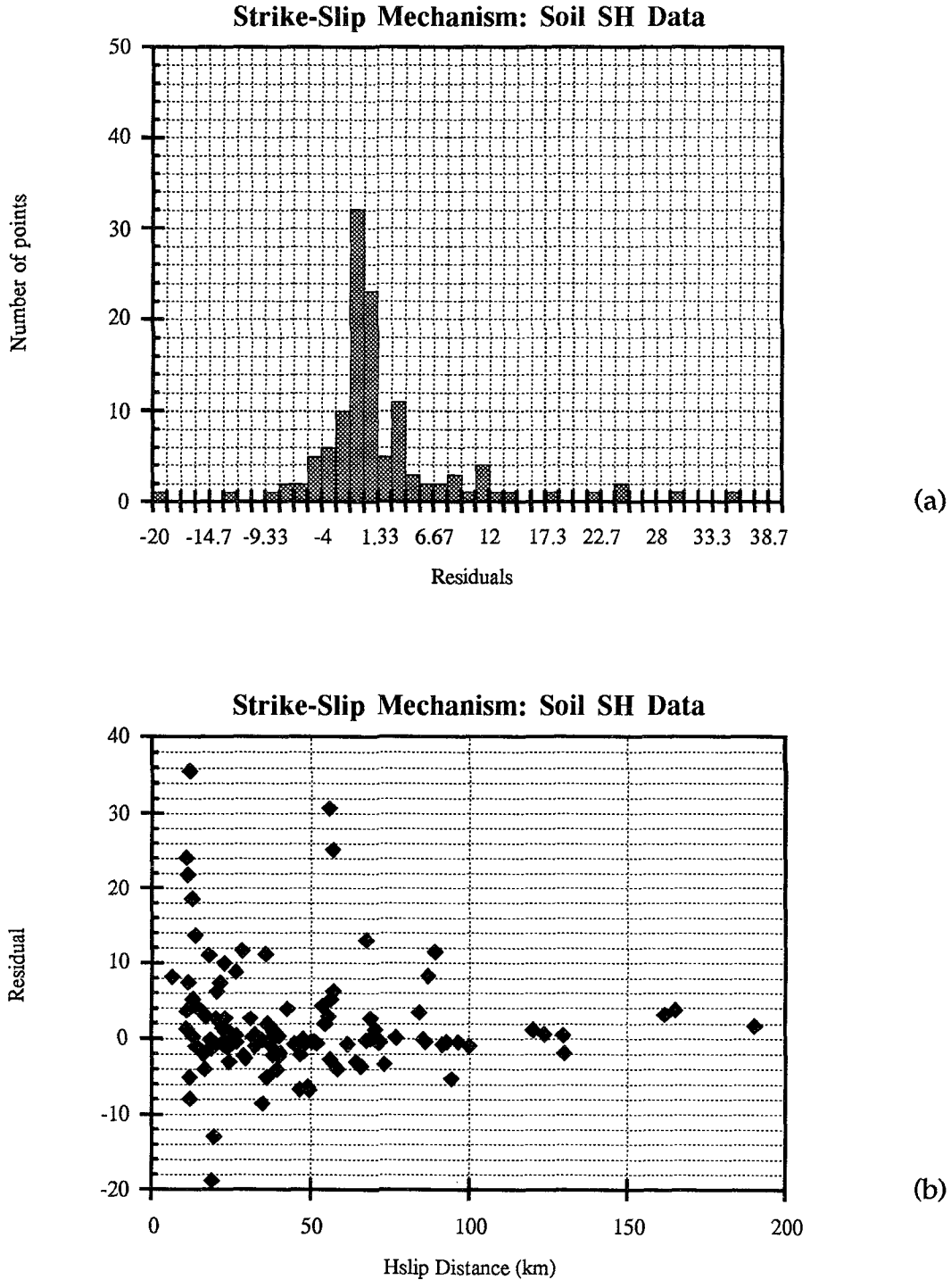

Figure 5.10 Histogram of the residuals (observed minus predicted) from the mean SSHS attenuation curve. (a) Binned histogram plot. (b) Residuals plotted versus H_{slip} distance.

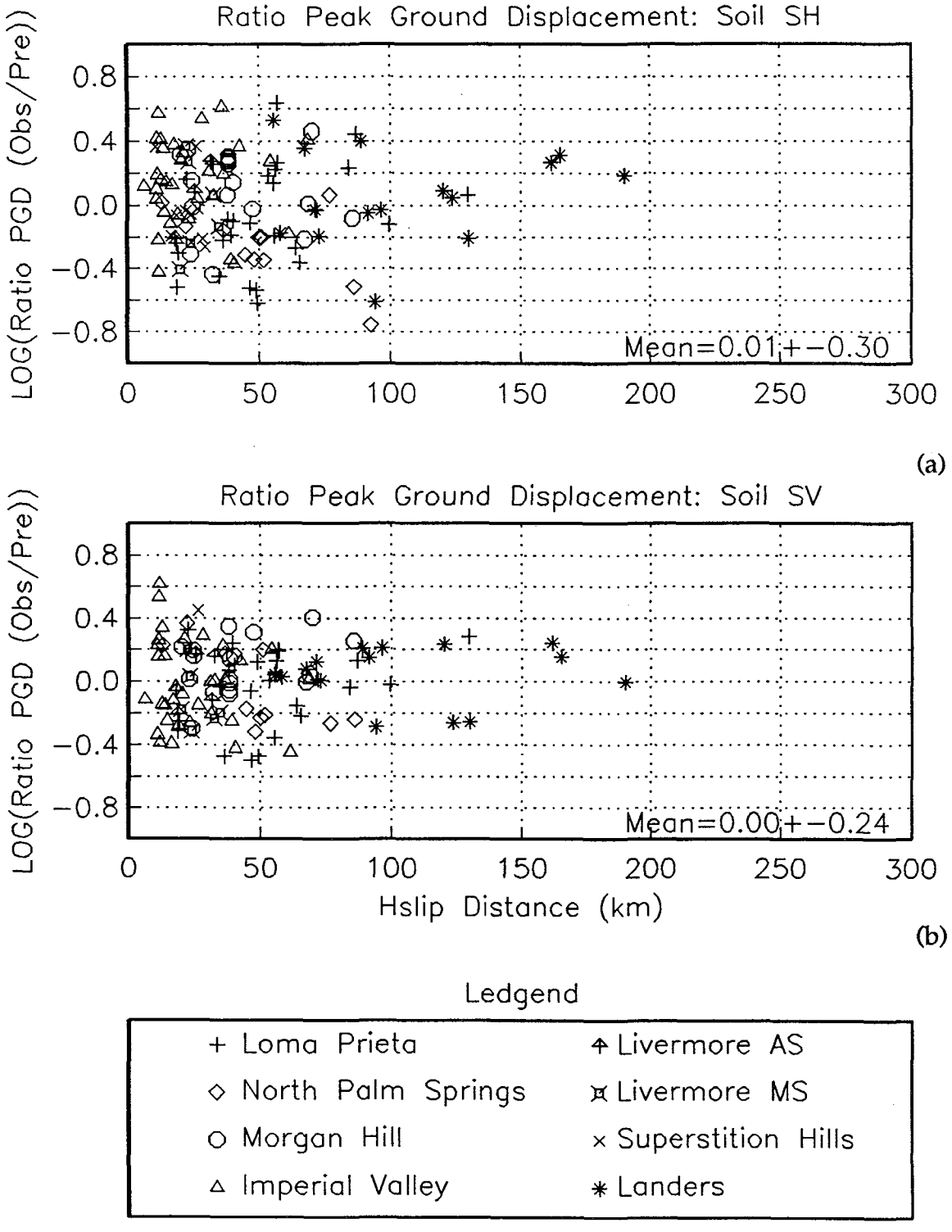

Figure 5.11 Log of the ratio of the observed peak ground displacement (Obs) divided by the predicted peak ground displacement (Pre) from the mean strike-slip soil attenuation curve versus H_{slip} distance. (a) SH component. (b) SV component.

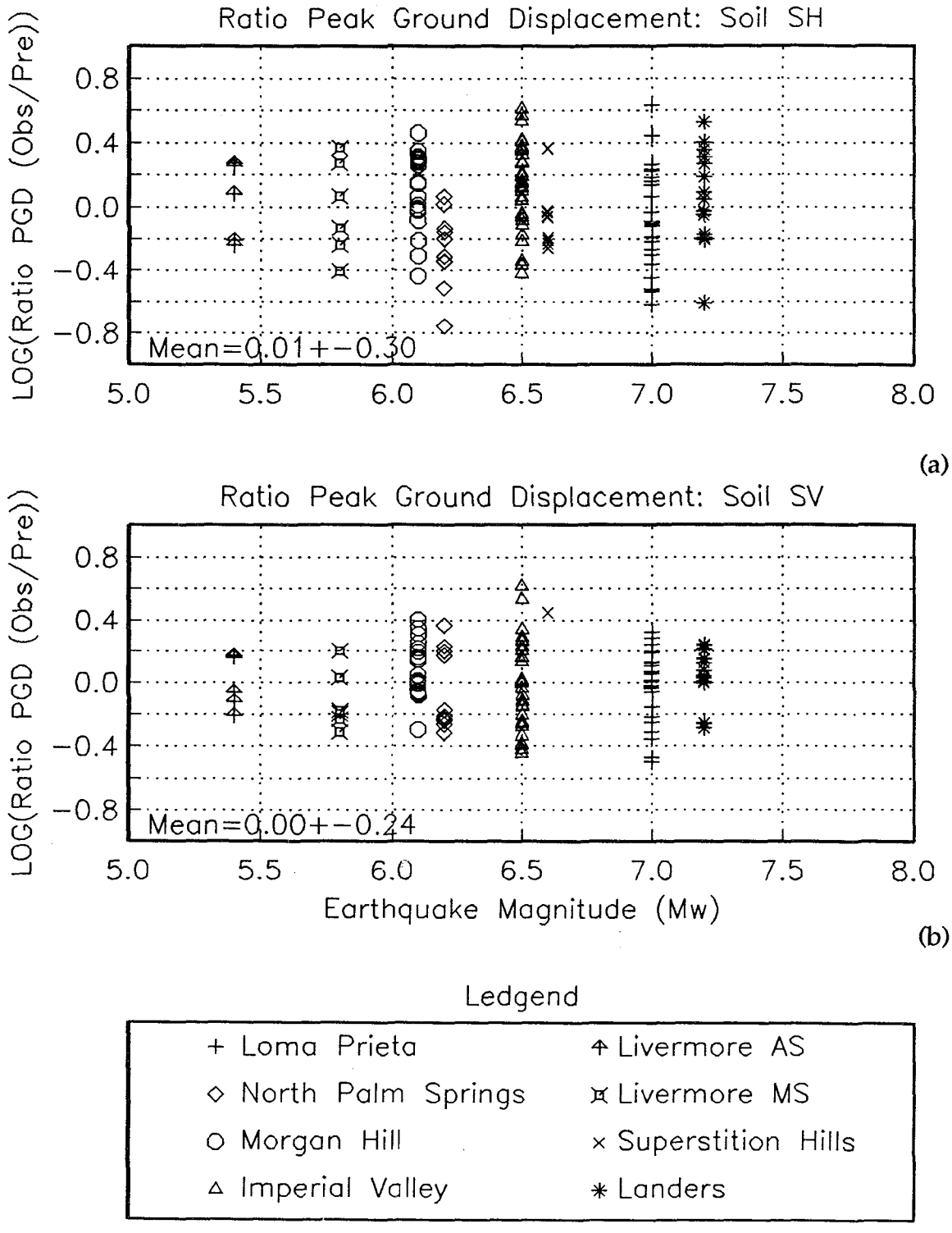

Figure 5.12 Log of the ratio of the observed peak ground displacement (Obs) divided by the predicted peak ground displacement (Pre) from the mean strike-slip soil attenuation curve versus M_W. (a) SH component. (b) SV component.

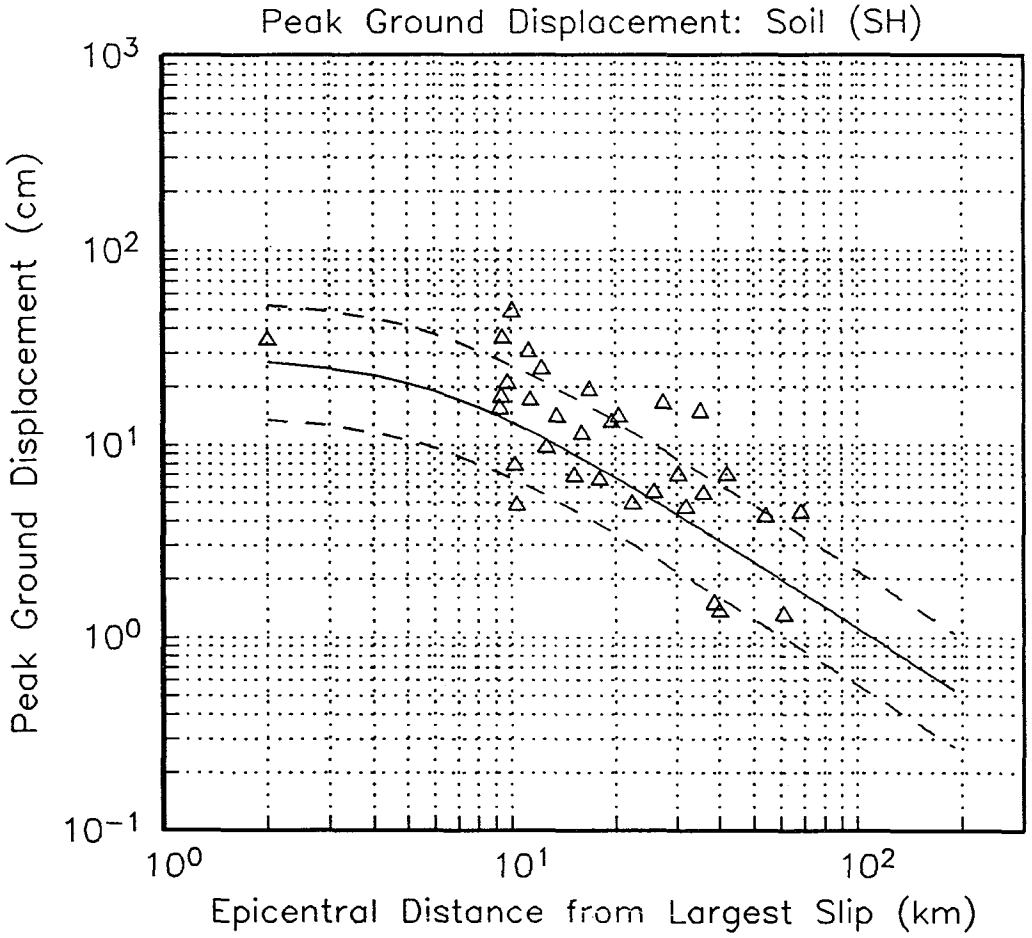

Figure 5.13 Mean SSHS attenuation curve plotted with the peak ground displacement observations from the 1979 Imperial Valley (M_w = 6.5) earthquake. Plus and minus one σ_T are indicated with the dashed lines.

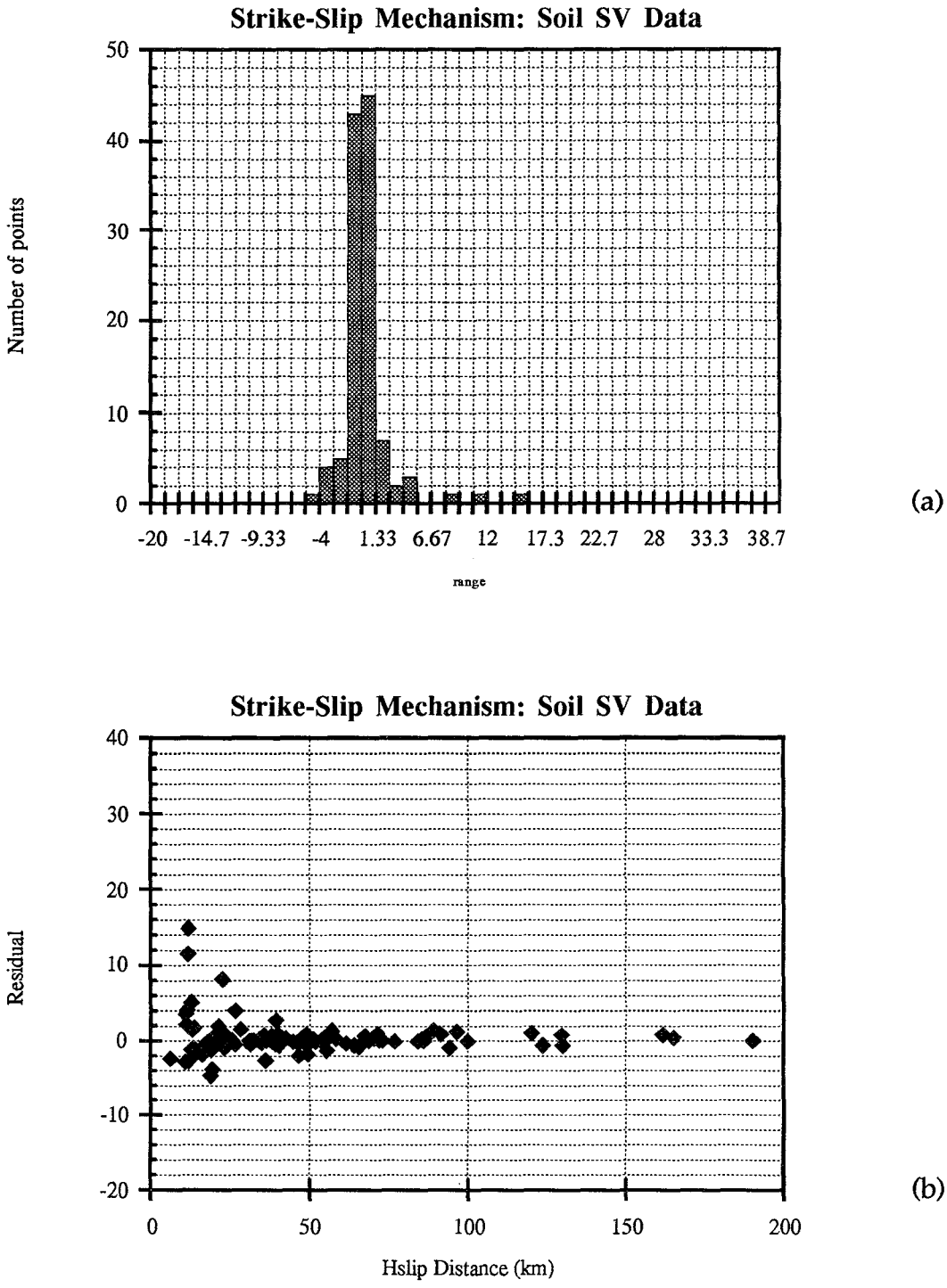

Figure 5.14 Histogram of the residuals (observed minus predicted) from the mean SSVS attenuation curve. (a) Binned histogram plot. (b) Residuals plotted versus H_{slip} distance.

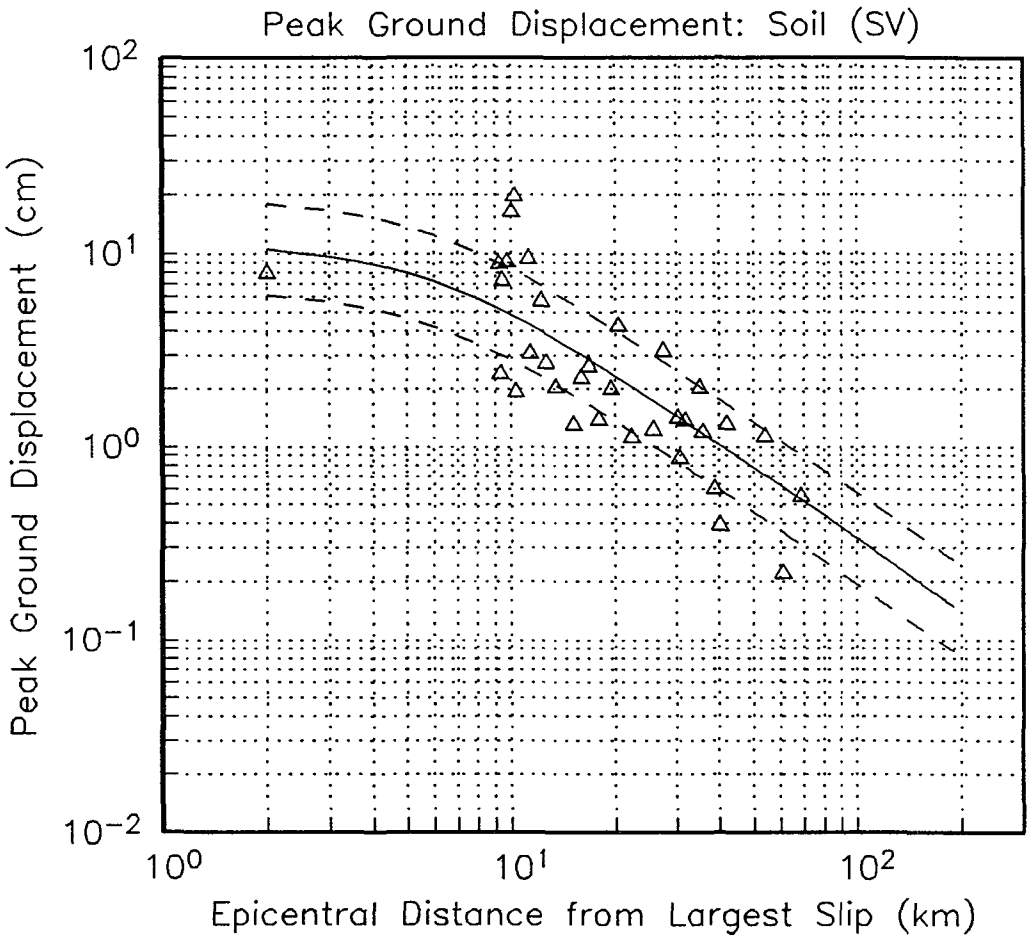

Figure 5.15 Mean SSVS attenuation curve plotted with the peak ground displacement observations from the 1979 Imperial Valley (M_W = 6.5) earthquake. Plus and minus one σ_T are indicated with the dashed lines.

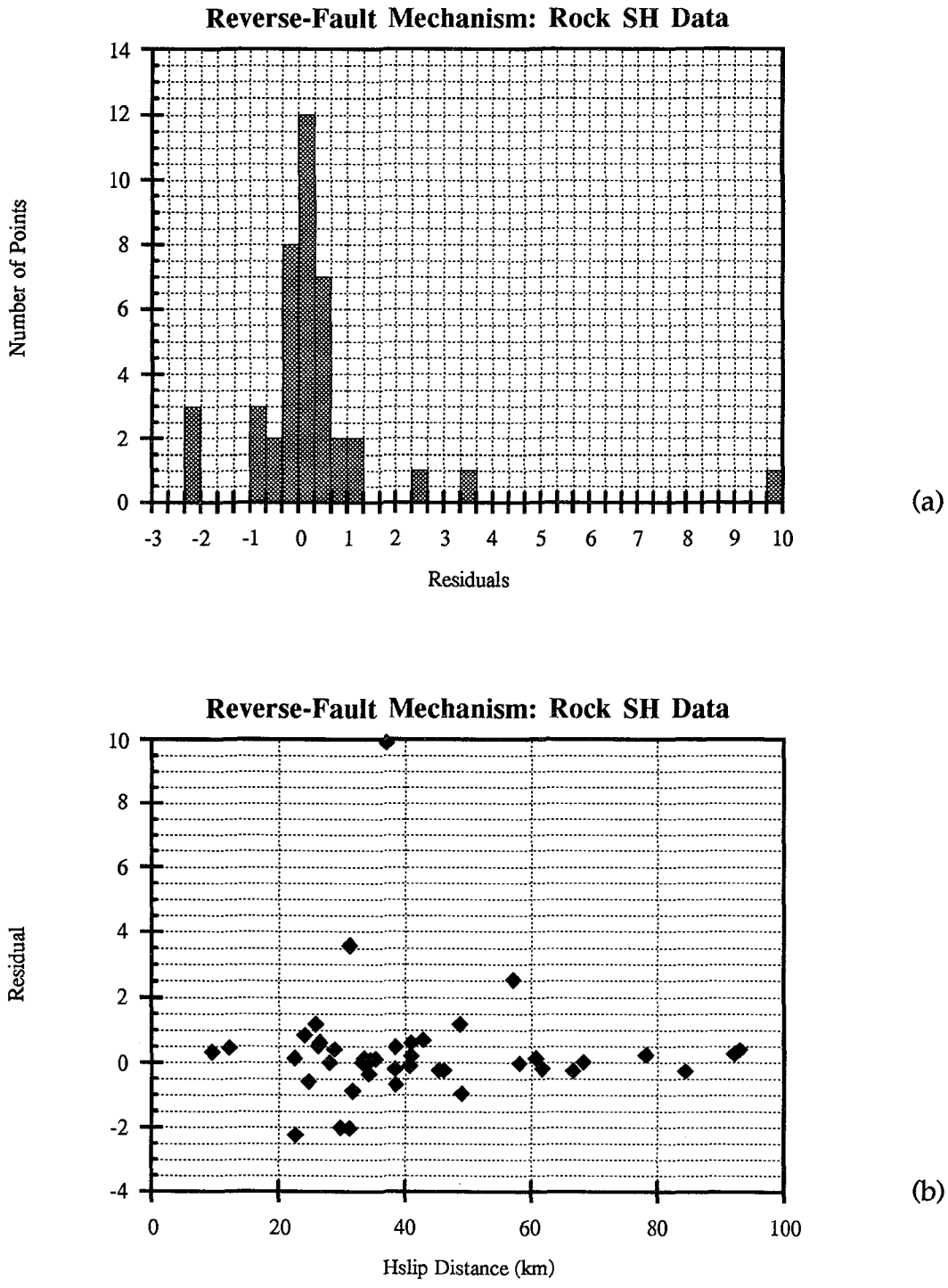

Figure 5.16 Histogram of the residuals (observed minus predicted) from the mean RSHR attenuation curve. (a) Binned histogram plot. (b) Residuals plotted versus H_{slip} distance.

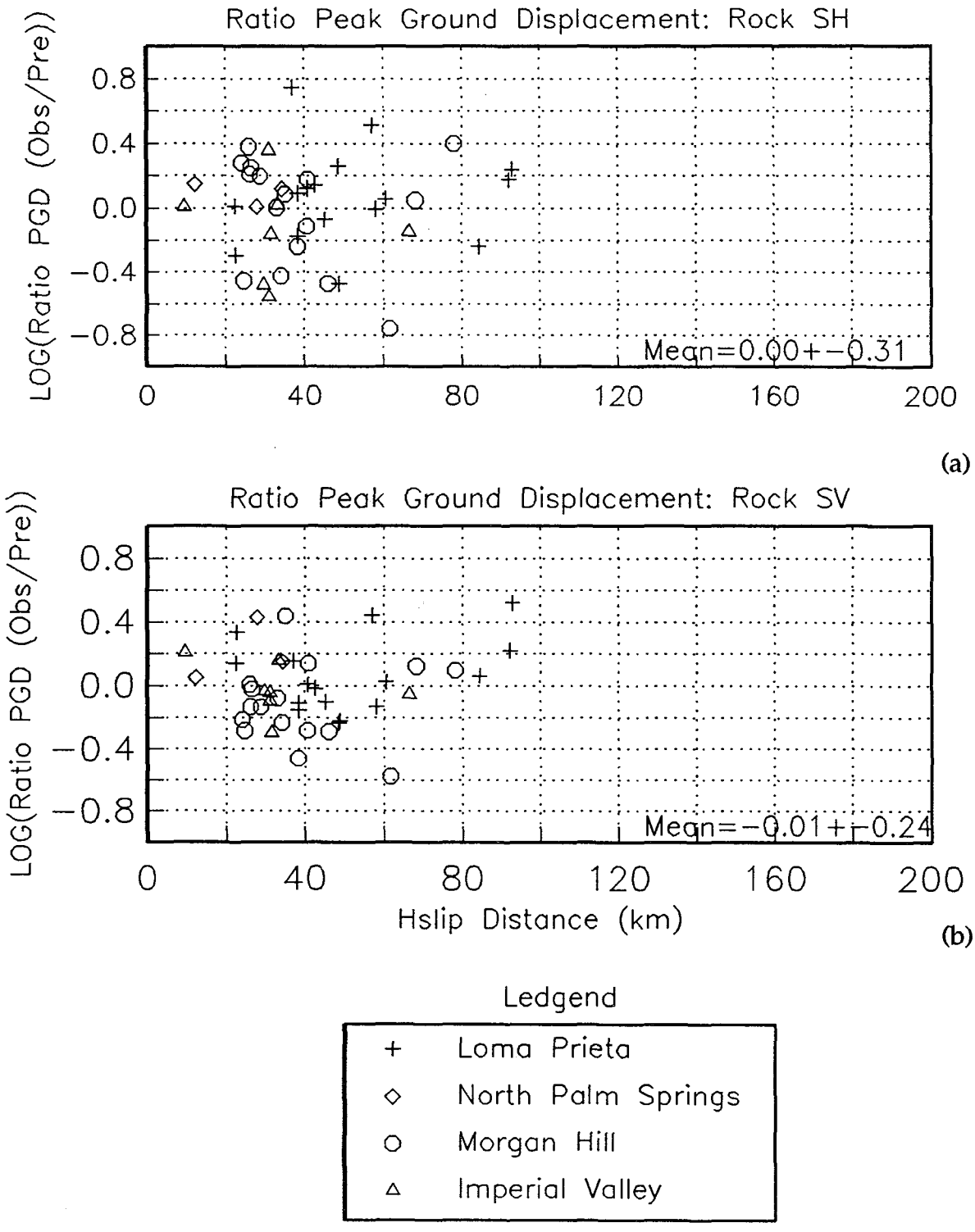

Figure 5.17 Log of the ratio of the observed peak ground displacement (Obs) divided by the predicted peak ground displacement (Pre) from the mean reverse-fault rock attenuation curve versus H_{slip} distance. (a) SH component. (b) SV component.

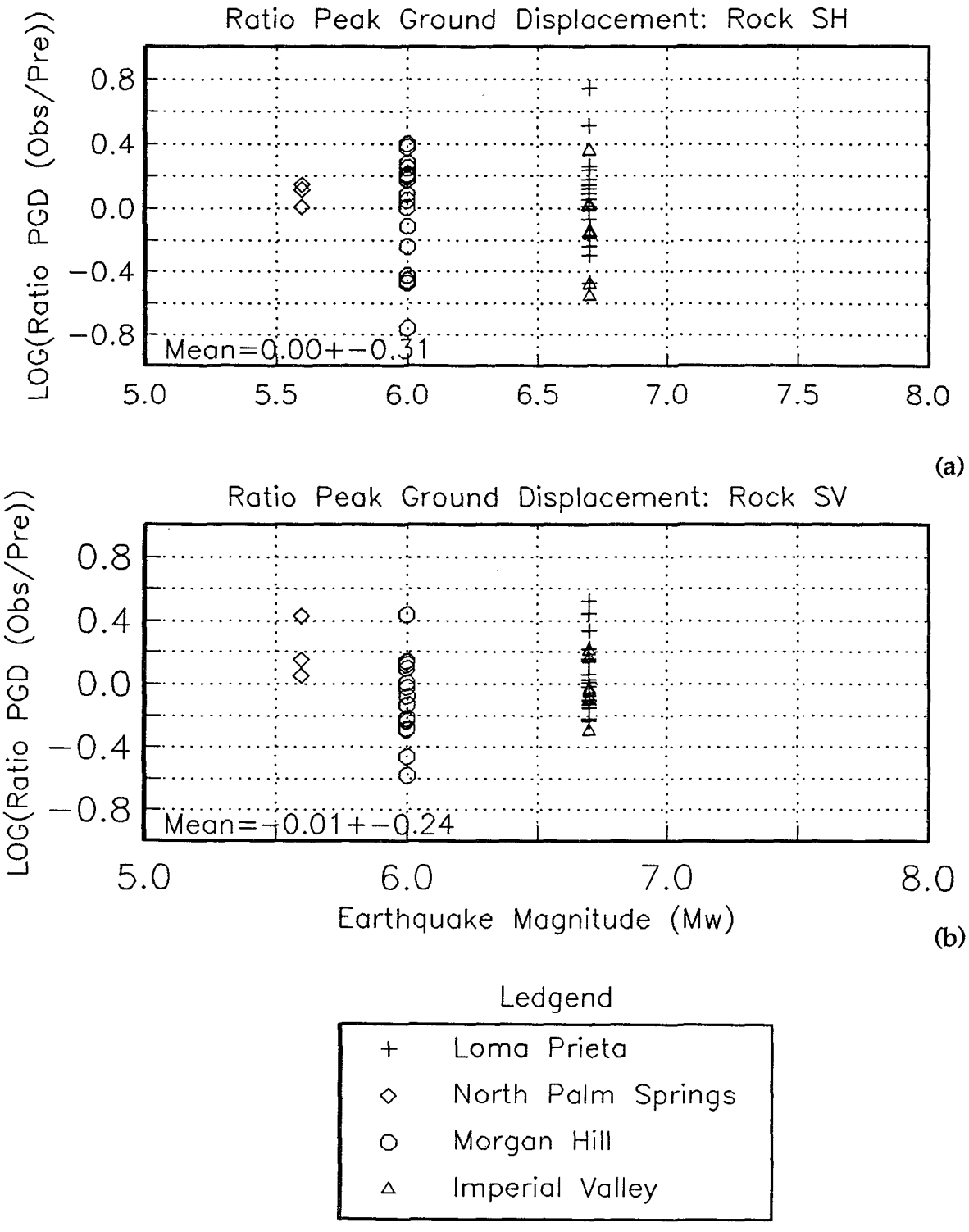

Figure 5.18 Log of the ratio of the observed peak ground displacement (Obs) divided by the predicted peak ground displacement (Pre) from the mean reverse-fault rock attenuation curve versus M_W. (a) SH component. (b) SV component.

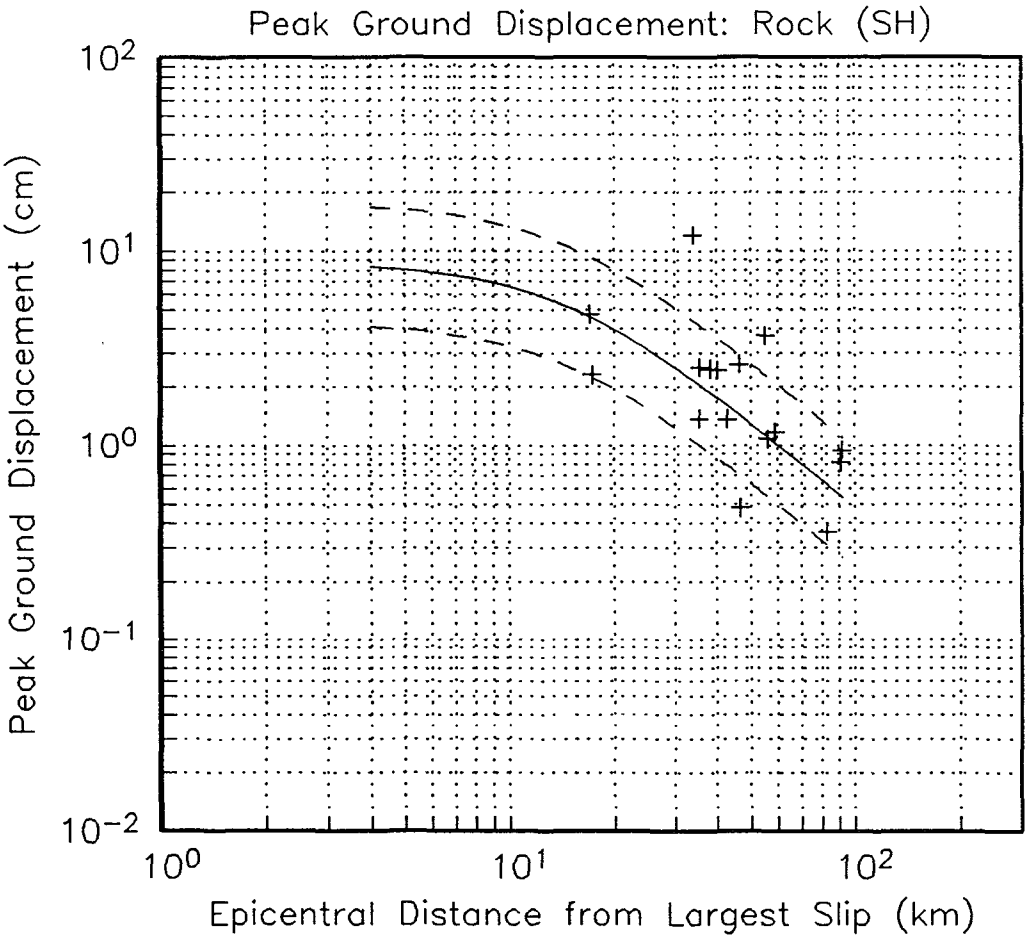

Figure 5.19 Mean RSHR attenuation curve plotted with the peak ground displacement observations from the 1994 Northridge (M_w = 6.7) earthquake. Plus and minus one σ_T are indicated with the dashed lines.

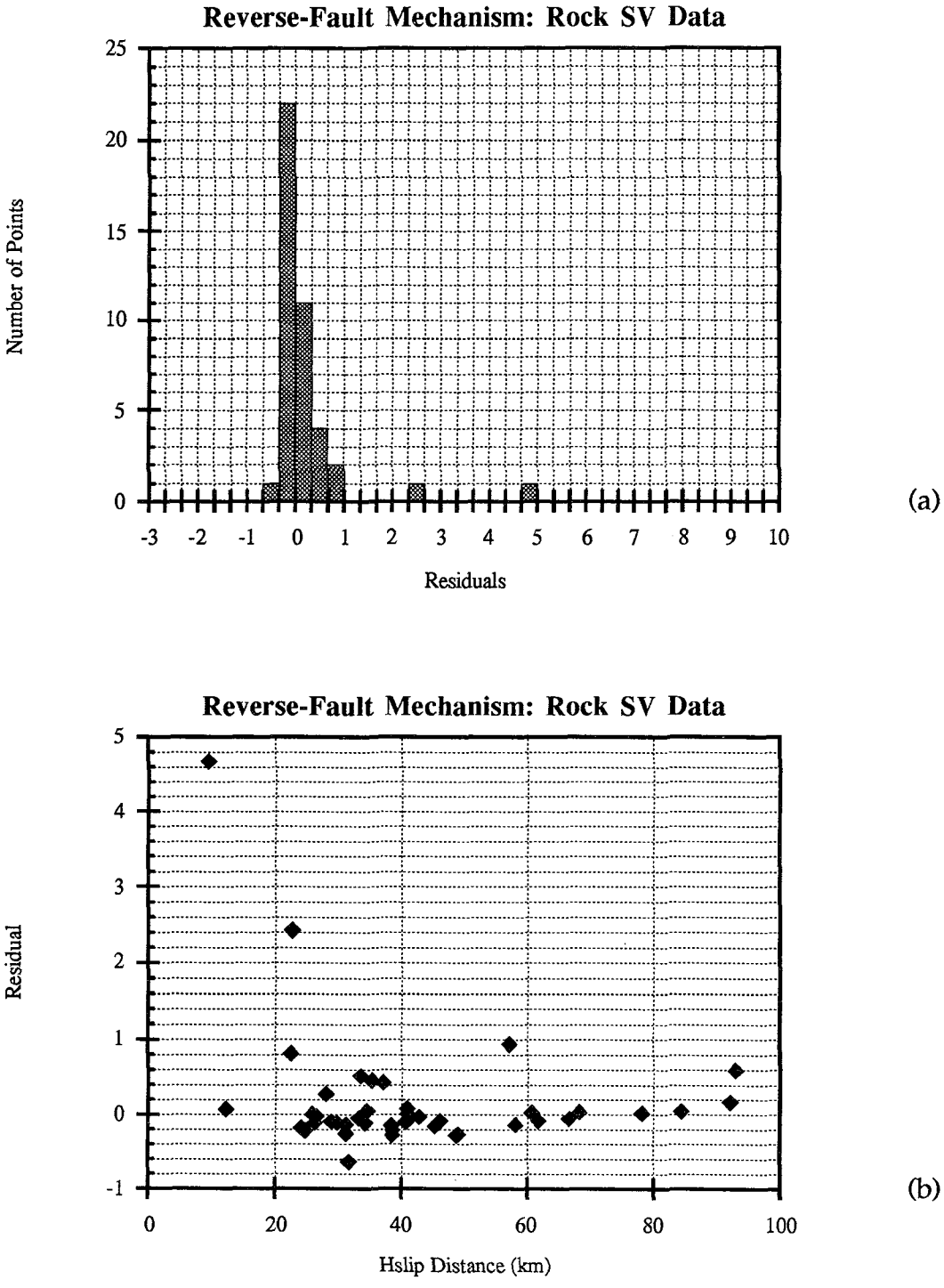

Figure 5.20 Histogram of the residuals (observed minus predicted) from the mean RSVR attenuation curve. (a) Binned histogram plot. (b) Residuals plotted versus H_{slip} distance.

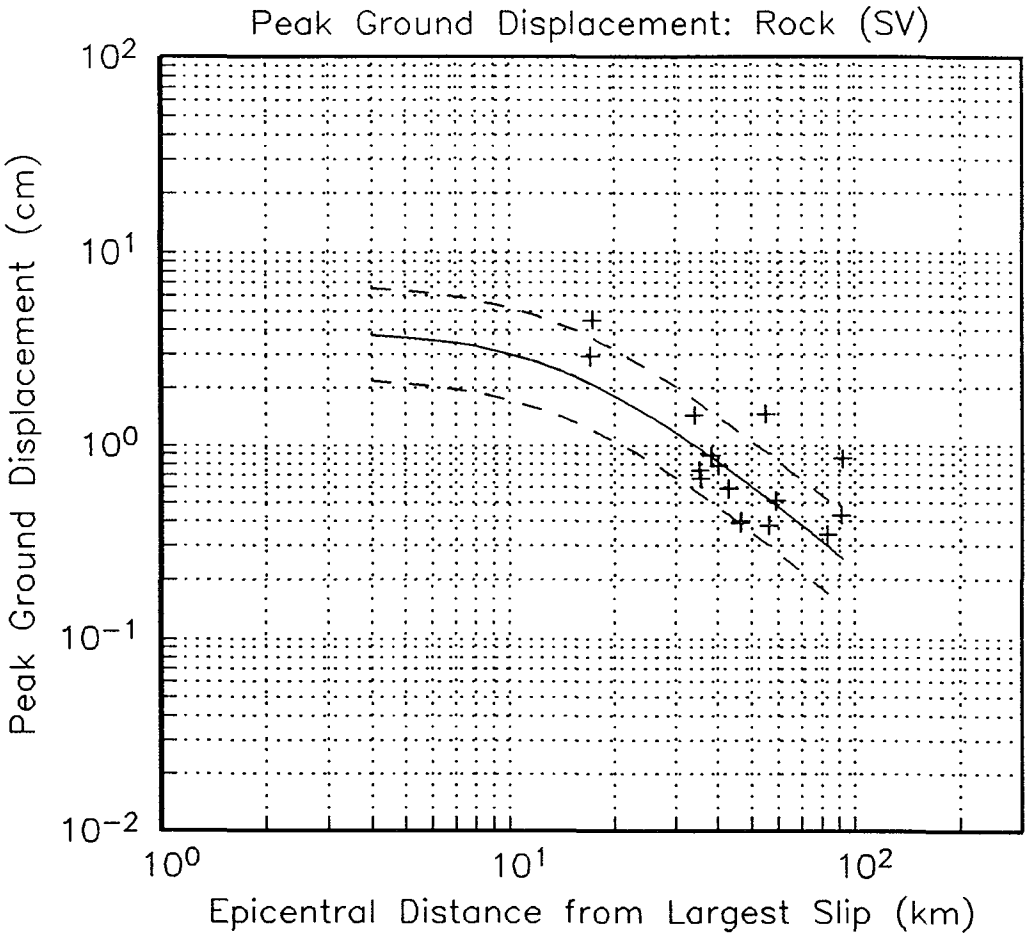

Figure 5.21 Mean RSVR attenuation curve plotted with the peak ground displacement observations from the 1994 Northridge (M_w = 6.7) earthquake. Plus and minus one σ_T are indicated with the dashed lines.

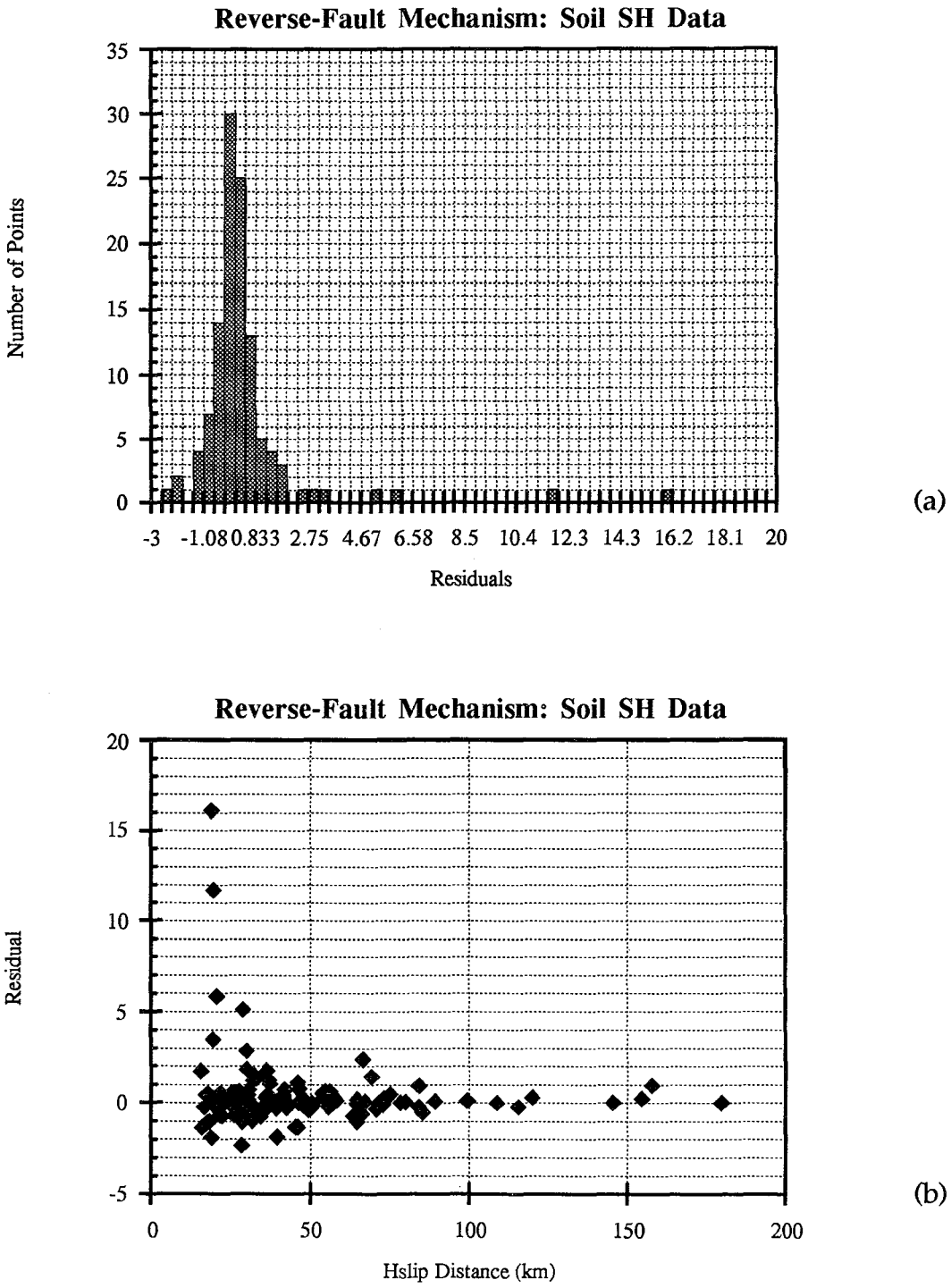

Figure 5.22 Histogram of the residuals (observed minus predicted) from the mean RSHS attenuation curve. (a) Binned histogram plot. (b) Residuals plotted versus H_{slip} distance.

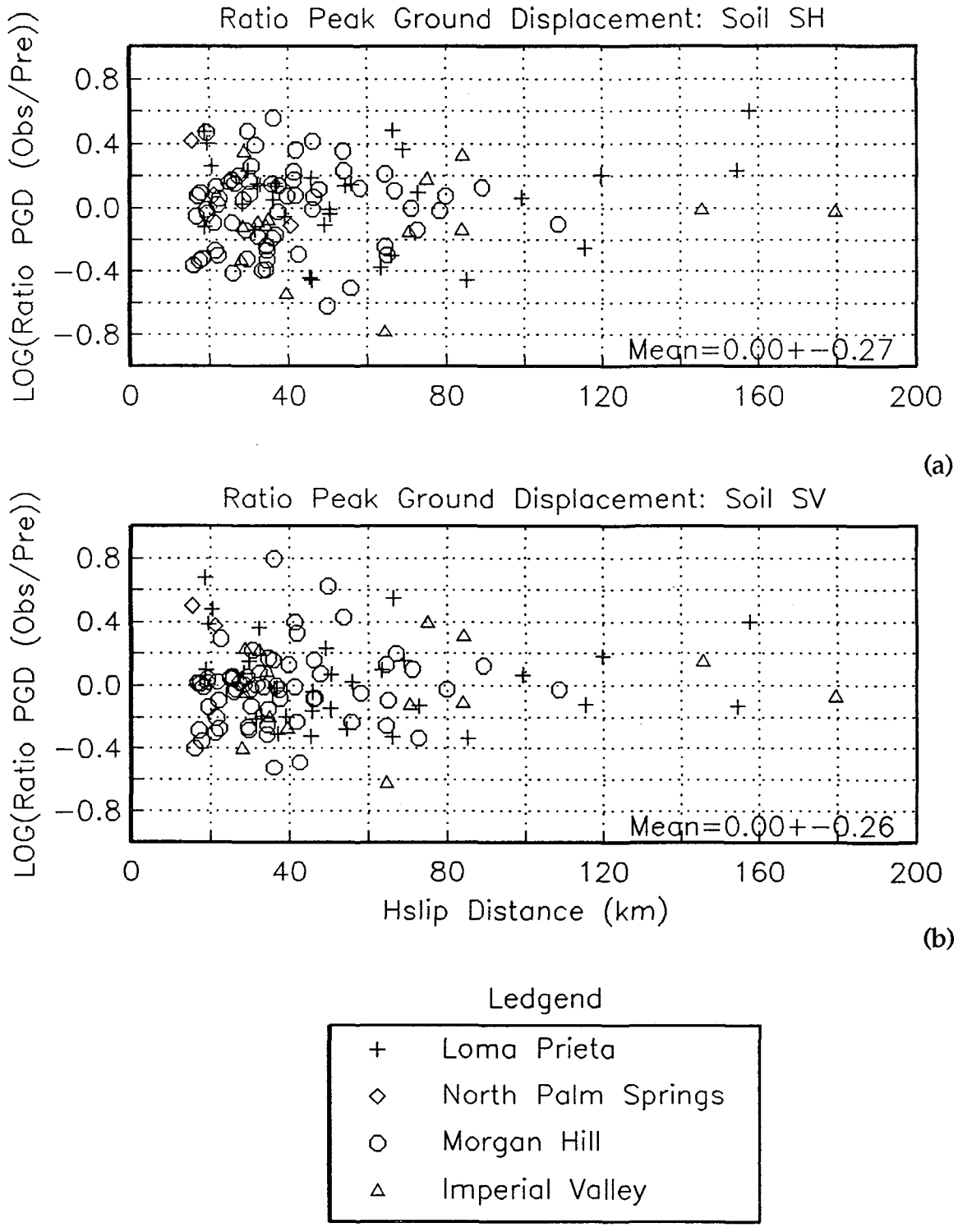

Figure 5.23 Log of the ratio of the observed peak ground displacement (Obs) divided by the predicted peak ground displacement (Pre) from the mean reverse-fault soil attenuation curve versus H_{slip} distance. (a) SH component. (b) SV component.

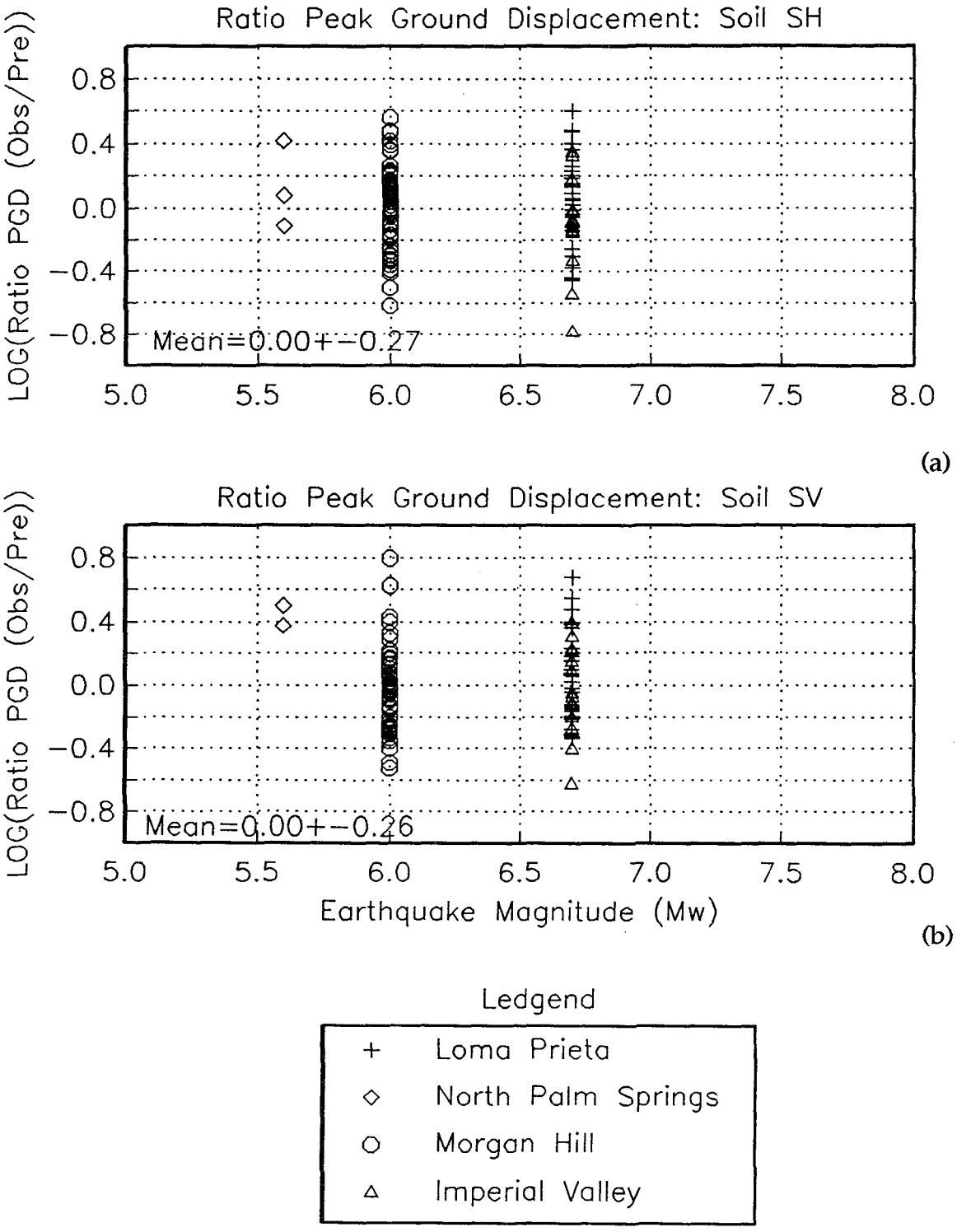

Figure 5.24 Log of the ratio of the observed peak ground displacement (Obs) divided by the predicted peak ground displacement (Pre) from the mean reverse-fault soil attenuation curve versus M_W. (a) SH component. (b) SV component.

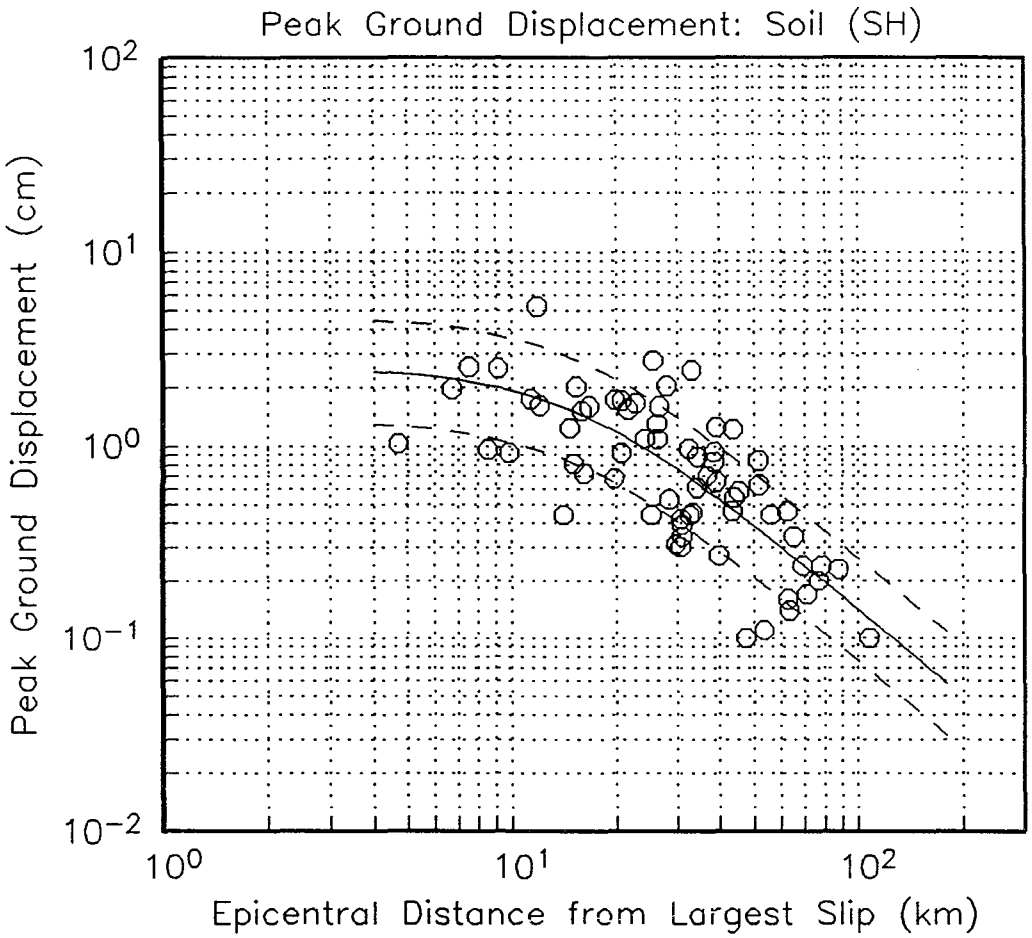

Figure 5.25 Mean RSHS attenuation curve plotted with the peak ground displacement observations from the 1987 Whittier Narrows (M_w = 6.0) earthquake. Plus and minus one σ_T are indicated with the dashed lines.

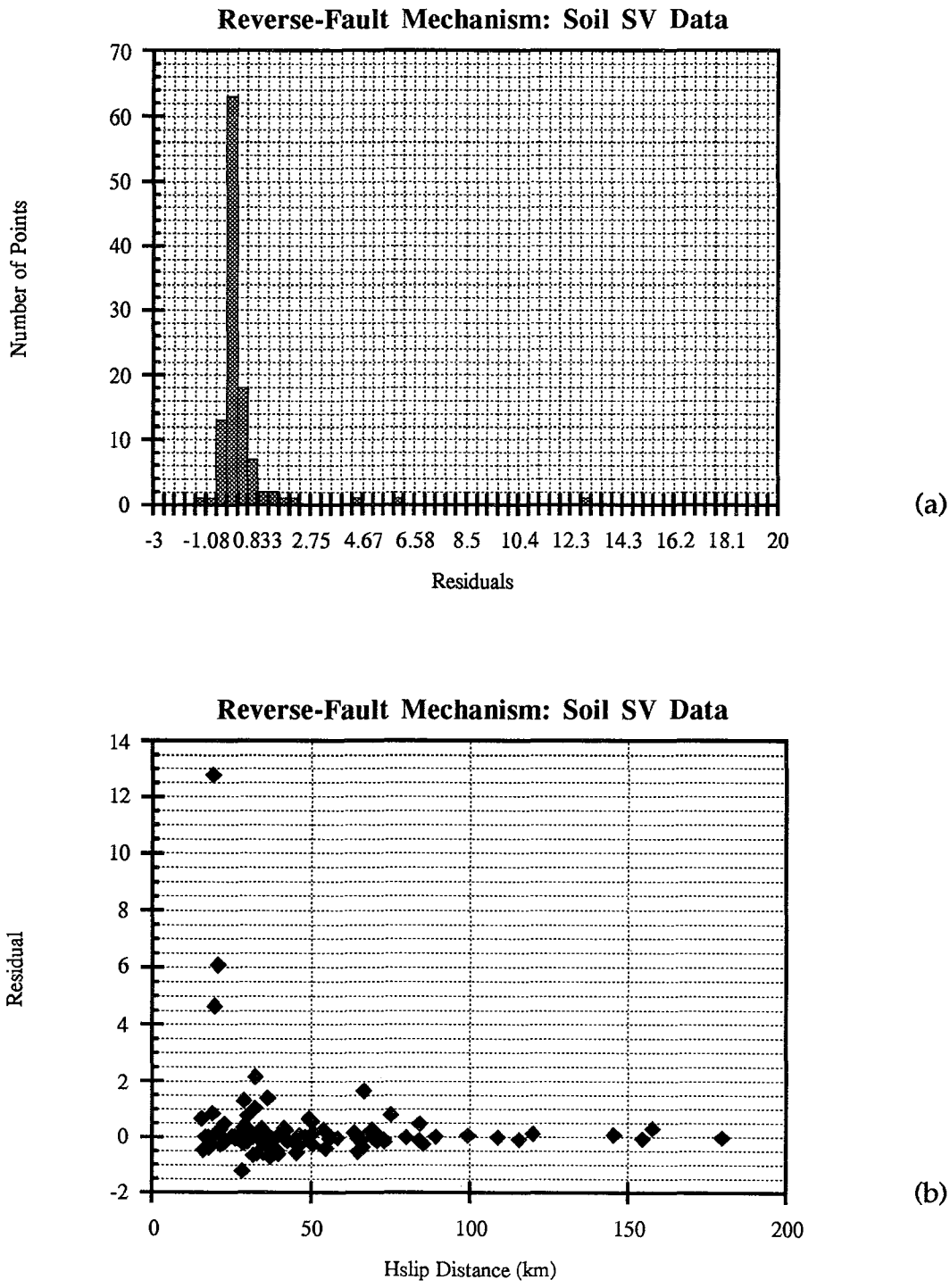

Figure 5.26 Histogram of the residuals (observed minus predicted) from the mean RSVS attenuation curve. (a) Binned histogram plot. (b) Residuals plotted versus H_{slip} distance.

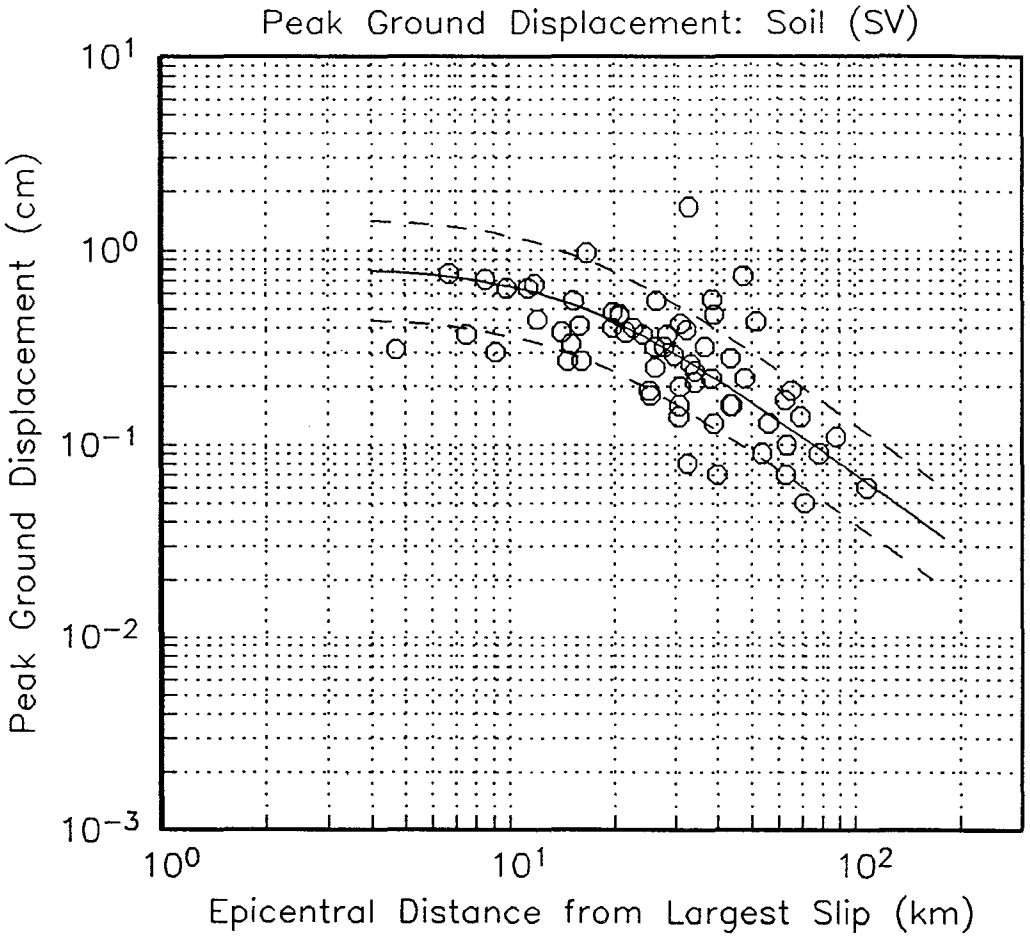

Figure 5.27 Mean RSVS attenuation curve plotted with the peak ground displacement observations from the 1987 Whittier Narrows (M_w = 6.0) earthquake. Plus and minus one σ_T are indicated with the dashed lines.

6. Conclusions and Recommendations

The goals of this research were to explore, explain, and summarize the variations of peak seismic ground displacement as a function of seismic source type, site classification, and horizontal versus vertical components of motion. Preliminary studies led to the restriction of the observational sample to 12 well recorded crustal California earthquakes, all of which have published inverted fault slip models (see Table 4.2). The peak displacements were selected and measured with the wave types of the seismological wave field taken into consideration. This procedure eliminated the selection of any displacement measurements occurring in the surface wave time window of the seismogram (see Figure 1.1). The attenuation curves, which are presented here, are based on the largest peak SH and SV body wave displacement, which corresponds with the time of largest ground acceleration. The SH and SV wave forms selected for measurement of the peak ground displacement had wave periods lying between 1 sec and 5 sec; the modal period was about 2 sec.

Eight peak displacement attenuation curves have been estimated in terms of inter-variable and intra-variable statistics (see Table 5.2) and a discussion given in the previous sections. The estimated coefficients for each attenuation curve are listed in Table 6.1. The total sample for the soil sites is approximately twice the size of the rock sample in all cases. For the reverse-fault mechanism sample, the four earthquakes were all recorded in the Los Angeles basin region so that the transferability of the estimated attenuation relations to other seismic regions could not be tested. The strike-slip models, on the other hand, contained observations from both northern and southern California and the significance of the inter-earthquake variability could be assessed (see Table 5.2). In brief, this analysis showed that within the estimated precision the same strike-slip source mechanism curve can be applied within all of crustal California. No analysis was

done to test if the same transferability of the curves is valid for other geologic regions outside California.

Table 6.1 Peak displacement attenuation coefficients for the eight separate mean attenuation curves.

Attenuation Curve	θ_1	θ_2	θ_3	σ_T
SSHR	-5.00	1.02	-0.82	0.38
SSVR	-5.56	1.11	-1.10	0.29
SSHS	-4.81	1.10	-1.15	0.29
SSVS	-4.94	1.07	-1.24	0.24
RSHR	-3.44	0.92	-1.51	0.31
RSVR	-3.57	0.88	-1.49	0.24
RSHS	-3.26	0.91	-1.53	0.27
RSVS	-4.81	1.05	-1.31	0.26

Lets us now make a comparison of the mean attenuation curves for each specific seismic source mechanism, site condition, and component of motion. For this purpose I selected, as a convenience, a standard reference M_W = 7.0 earthquake with a point of largest slip on the fault plane at a depth of 10.0 km. As was the case in all of the previous graphs (see chapters 2, 3, and 5), the abscissa of the mean attenuation curves is the epicentral distance (in km) defined here as the surface point above the largest slip on the fault plane (see section 5.3). Units of peak ground displacement are centimeters. The plus and minus one σ_T curves are also plotted. The mean attenuation curves will only be drawn for the distance range in which there are observations.

A standard Student t-test was computed for each of the following comparisons to estimate the statistical significance between the mean curves based on the empirically-estimated variances (see Table 5.2). The probability density function is graphed for each mean attenuation-curve comparison and discussed. The probability density function

indicates the probability, that by chance alone, the difference in the two means is significant. A value of unity indicates that the two mean estimates are not significantly different, whereas a value of 0.05 indicates that the two curves are significantly different at the 95% confidence level.

Figure 6.1 compares the strike-slip SH rock (SSHR) and the strike-slip SV rock (SSVR) (see Table 5.1 for nomenclature) mean attenuation curves. The SSHR curve (heavy line) lies above the SSVR curve (light line) and is statistically significant above the 95% confidence level at all distances. Theoretical considerations predict that the SSHR attenuation curve is higher than the SSVR curve by a factor of approximately 3 solely on the basis of the average radiation pattern coefficient for SH and SV body waves (see section 3.2) from a vertical strike-slip source (Boore and Boatwright, 1984). For $r > 20$ km the attenuation rate of the SSHR curve is lower than for the SSVR curve leading to a larger separation at greater distances. There is some evidence that this slower attenuation of the SSHR curve at larger distances may not be universal, but is an artifact of the lateral refraction and amplification of seismic energy (see section 5.3) that was observed in the 1989 Loma Prieta earthquake (Lomax and Bolt, 1992) and 1992 Landers earthquake (about 20% of the sample consists of these stations).

Next, compare the SSHS (heavy line) and SSVS (light line) attenuation curves (Figure 6.2). The two mean curves have nearly identical curvature, but there is a constant shift upward (on the log-log graph) of the SSHS curve and the mean estimates are statistically different. Again from the respective radiation patterns, SSHS curve would be expected to have a greater amplitude than the SSVS curve. For $r > 20$ km there is no difference between the two rates of attenuation. Although the rock sites from the Loma Prieta earthquake indicated an amplification of seismic energy at $r > 75$ km beyond which there was a systematic increase in the observations, the soil sites yield values from this earthquake that are very dispersed, varying by an order of magnitude. The classification of a site as a soil site includes a wide range of soil structures defined

by the thickness of soil layers and their respective elastic moduli. The wide scatter of data points can be an artifact of the wide range of soil conditions at each site, which would each have its own characteristic site response. For larger distances, the slower attenuation rate that was observed in the SSHR attenuation curve is masked by the scatter of the data points from the individual site responses.

Next a comparison is made between the SSHR and SSHS mean attenuation curves (see Figure 6.3). Previous examination of peak ground-acceleration attenuation models (Aki, 1988), has indicated that longer period motion is amplified on soil sites relative to rock sites and that the opposite is true for shorter period motion. The empirical mean attenuation curves from this research support the amplification of long-period motion (displacement in this case) on soil sites relative to rock sites. The SSHS curve predicts values which are significantly higher than the SSHR curve for $r < 150$ km. Clearly the two curves have a different rate of attenuation, as was discussed above. For $r > 150$ km the mean curves converge and the estimated peak displacement values are similar in a statistical definition (see the probability density function).

The corresponding plot for the SSVR and SSVS curves is in Figure 6.4. In contrast to the SH wave case, at shorter distances, the SSVS curve is greater than the SSVR for $r <$ 55 km (at the 95% confidence level). For $r > 100$ km the predicted peak displacement values from the two curves are identical within the variances of the curves.

The comparison between the RSHR and RSVR cases is presented in Figure 6.5. In agreement with the regression for strike-slip earthquakes, the mean RSHR regression is significantly higher than the mean RSVR curve at all distances. This result is perhaps theoretically unexpected. For a purely dip-slip source on a dipping fault plane of 30°, the opposite effect is predicted, based on the SH and SV radiation patterns (Boore and Boatwright, 1984). A closer special analysis is needed in this case. In the available sampling, seventy-six percent of data points for the rock stations from the set of four reverse-fault mechanism earthquakes are from the 1987 Whittier Narrows earthquake

and the 1994 Northridge earthquake (see Table 4.5). The source inversion model for the Whittier Narrows earthquake (Hartzell and Iida, 1990) indicated that the seismic source propagated *down-dip*, and hence away from the ground surface. This slip would tend to reduce the strong ground motion on the surface because of rupture directivity and also have a greater effect on the vertical component of motion. For the Northridge earthquake, the opposite is true, with the seismic source rupture up-dip. However, the scarcity of rock strong ground-motion stations located up-dip from the source leads to an under-sampling of these amplified ground motions.

Increased amplitude of the SH motion is also observed for the soil sites from the reverse-fault mechanism earthquakes (see Figure 6.6 for a comparison between RSHS and RSVS). The RSHS curve has a higher rate of attenuation and begins to approach the value of the RSVS curve for $r > 100$ km. However, over the available sample range, the two mean estimates are significantly different. The dispersion about the mean attenuation curve for the soil sites (see section 5.4) is larger than the dispersion for the rock sites (see section 5.3), as was also observed in the peak displacement measurements from the strike-slip earthquakes. This larger dispersion of the observations will control the rate of attenuation in the empirically estimated attenuation model and can be attributed to the individual site responses of the soil sites as was the case for the strike-slip sample values.

Figure 6.7 shows the comparison between the RSHR and RSHS mean attenuation curves. As is expected from the other empirical comparisons between the mean curves for soil and rock sites, the RSHS curve predicts larger peak SH ground displacement values for distances less than approximately 65 km (at the 95% confidence level). The RSHS curve has a higher rate of attenuation than the RSHR curve. This higher rate of attenuation for the soil sites was also observed for the strike-slip earthquakes (see Figure 6.3).

In comparison, the curves for the SV component for reverse-fault mechanisms do not exhibit a different rate of attenuation. The RSVR and RSVS curves are drawn in Figure 6.8. The soil site regression trend is systematically shifted higher and statistically different over the entire distance range, but the two curves have identical rates of attenuation for all practical purposes. Care must be taken, however, in the comparison between the rock and soil site estimates of peak ground displacement, because the amplitude sampling for the rock sites is rather limited. The rock sample consists of only 42 observations with the majority at distances between 20-60 km (see section 5.4.1). Because of the limited sample, the rate of attenuation of the mean RSHR and RSVR curves is not well constrained. The soil site attenuation curves, on the other hand, are fitted with a more uniformly distributed sample.

Next, a different behavior is found in the attenuation curves for the two types of seismic source mechanisms. Plotted in Figure 6.9 are the SSHR and RSHR mean attenuation curves. The strike-slip curve (SSHR) predicts lower values for $r < 15$ km and greater values for $r > 15$ km, due to a slower rate of attenuation (the lower rate of attenuation of the SSHR curve was addressed earlier). However, the mean estimates are only significantly different for $r > 25$ km at the 95% confidence level. The relative poor sampling of the RSHR curve for $r > 60$ km can also be contributing to the large observed differences between the two curves. Theoretically, the strike-slip amplitudes (SSHR) should be higher than the reverse-fault amplitudes (RSHR) based only on the coefficients of the radiation pattern by a factor of approximately 1.5 (Boore and Boatwright, 1984).

The variation of SSVR and RSVR attenuation is presented in Figure 6.10. The RSVR mean attenuation model predicts smaller values than the SSVR curve for all distances plotted, and is significantly different for $r > 15$ km at the 95% confidence level. As was noted for the SH curves, the strike-slip SV attenuation curve (SSVR) has a slower rate of attenuation than the reverse-fault SV attenuation curve (RSVR). The faster

rate of attenuation of the reverse-fault mechanism attenuation curve could possibly be an artifact of the nature of the rupture directivity (see section 5.4) of the reverse-fault mechanism earthquakes studied.

The mean soil attenuation curves for each seismic source mechanism are plotted in Figure 6.11. Unlike the comparison for the rock sites (see Figure 6.9) which were statistically significant only for r > 25 km (at the 95 % confidence level), the mean SSHS curve is statistically different than the mean RSHS curve at all distances. For the soil reverse-fault mechanism sample, over half of the data points are from the 1987 Whittier Narrows earthquake, which had a downward propagating seismic rupture. The ground motions on the surface would be reduced in amplitude based on the effects of directivity focusing (see section 3.5) and this reduction would contribute to the statistical estimate of greater average SH soil values for the strike-slip mechanism.

Finally, the soil site SV curves are plotted in Figure 6.12. The two curves, SSVS and RSVS are nearly identical, but the t-test indicates that the means are still statistically different, with the RSVS curve predicting slightly lower values. The similarity between the two curves indicates that the effects of rupture directivity discussed earlier are not as pronounced for the SV component as for the SH component of wave displacement, or that the regional attenuation of SV motion is lower than the regional attenuation of SH motion from reverse-fault mechanism earthquakes (i.e., the southern California region attenuation). A summary of the various comparison outlined above are given in Table 6.2.

Table 6.2 Summary of the comparison results between the eight separate mean attenuation curves.

Comparison	Mean Curve	Rate of Attenuation	Figure Number
SSHR/SSVR	Significant over all r	SSVR greater	6.1
SSHS/SSVS	Significant over all r	Identical	6.2
SSHR/SSHS	Significant over r < 150 km	SSHS greater	6.3
SSVR/SSVS	Significant over r < 50 km	SSVS greater	6.4
RSHR/RSVR	Significant over all r	Identical	6.5
RSHS/RSVS	Significant over all r	RSHS greater	6.6
RSHR/RSHS	Significant over r < 65 km	RSHS greater	6.7
RSVR/RSVS	Significant over all r	Identical	6.8
SSHR/RSHR	Significant over r > 25 km	RSHR greater	6.9
SSVR/RSVR	Significant over r > 10 km	RSVR greater	6.10
SSHS/RSHS	Significant over all r	RSHS greater	6.11
SSVS/RSVS	Significant over all r	Identical	6.12

The above inter classification analysis also allows a number of general conclusions.

- The largest scatter in the observed peak ground displacement measurements from the mean attenuation curves appears to be attributable to the effects of *rupture directivity* (see section 3.5). As the individual discussion in sections 5.3 and 5.4 suggest, each of the 12 earthquakes examined provided observations which were either increased or decreased in amplitude due to the propagating seismic rupture on the slipping fault. The more noticeable effect was for stations located along the direction of rupture which had a large increase in peak ground displacement amplitude (e.g., see the section on the Imperial Valley, Morgan Hill, Landers, and Northridge earthquakes). The effects of the increased amplitude of peak ground motion was observable on both the SH and SV components, and it was more prominent for stations located at $H_{slip} < 40$ km.

• The calculated curves are restricted in their sample distribution for distance and magnitude (see Table 6.3). The strike-slip attenuation models were regressed based on the sample from earthquakes with magnitude range $5.4 < M_W < 7.2$. The extrapolation of the relationships to higher magnitude earthquakes remains uncertain although the S wave generation and propagation from larger fault sources should not change in a fundamental way. The reverse fault mechanism attenuation curves were even more restricted in magnitude size (i. e., $5.6 < M_W < 6.7$).

Table 6.3 Applicability range in M_W and H_{slip} for the eight mean attenuation curves.

Attenuation Curve	M_W range	H_{slip} range
SSHR	5.4 - 7.2	3 - 224 km
SSVR	5.4 - 7.2	3 - 224 km
SSHS	5.4 - 7.2	2 - 190 km
SSVS	5.4 - 7.2	2 - 190 km
RSHR	5.6 - 6.7	4 - 92 km
RSVR	5.6 - 6.7	4 - 92 km
RSHS	5.6 - 6.7	4 - 180 km
RSVS	5.6 - 6.7	4 - 180 km

• The set of mean attenuation curves are limited in their H_{slip} range. The applicability of the attenuation curves for M_W and H_{slip} is listed in Table 6.3. The extension of the estimates of peak ground displacement to H_{slip} distances less than the closest observations also remains uncertain. The same uncertainties arise when extended the attenuation curves to H_{slip} distances larger than in the sample.

A comparison between the mean attenuation curves regressed in this study and the few independent peak ground displacement attenuation relations (see section 2.3) is of interest. As was mentioned in section 2.3, the use of different definitions of distance

limits somewhat direct comparisons. The mean attenuation curves calculated in this research predict peak displacement values which are greater than both the Kawashima et al. (1986) (KAT86) and Theodulidis and Papazachos (1992) (TP92) curves by a factor of about 2. This comparison is made for strike-slip seismic sources. The differences in earthquake observations used in the respective regressions probably accounts for these differences as both the KAT86 and TP92 curves include measurements from deeper occurring subduction earthquakes, while this study only examined crustal California earthquakes.

Recently a number of recorded strong ground motion seismograms from the 1994 Hyogo-Ken Nanbu (M_W = 6.9) earthquake have been released (Nakamura et al., 1995). Although there are no published fault slip inversion models at this time, a simple comparison of the peak ground displacement observations can be made with the mean empirical attenuation curves. Three strong ground motion accelerometers (Nakamura et al., 1995) were located within 10 kilometers of the strike-slip fault plane (no site classification is given in the report). The largest peak displacement value of 42 cm (north-south component) was recorded at the Takatori train station located within 2 km from the seismic fault (Nakamura et al., 1995). Takarazuka is located at the northeast end of the rupturing fault and the observed peak displacement is 25 cm (north-south component). The Nishi-Akashi station is located about 4 km northwest of the fault plane and had a peak displacement of 7 cm (north-south component). In comparison, the mean estimated peak ground displacement from the SSHR curve (see Figure 6.1) is approximately 12 cm at a H_{slip} distance of 10 km. The peak ground displacement at Takarazuka and Nishi-Akashi fall within one standard deviation of the mean; the Takatori recording does not. However, the amplification of ground motion at Takatori, which is located along the fault in the direction of rupture propagation, would be expected to be increased from the directivity focusing of the seismic source (cf., section

4.2.8). The same amplification due to directivity focusing is observed at the Takarazuka station.

The interpretation and statistical work described has provided the first exhaustive set of attenuation relations for peak strong ground motion displacement for crustal California earthquakes. These attenuation curves are available for use as scale parameters in seismic hazard assessments of a large engineered structure or a base-isolated building. The attenuation curves can also be used as reasonably robust estimates in standard probabilistic seismic hazard algorithms to estimate the probability of exceeding a given ground displacement level. However, the caveats should be stressed above should be used in applying the numerical results.

As more strong ground motion recordings become available from future earthquakes enough tabulation is given in this work for the attenuation models presented to be updated and modified. Displacement from past earthquakes should be added as fault slip inversion models are published for the fault rupture sources. A key aspect in the entire procedure in this work is knowledge of the position of largest slip on the fault plane. Determination of the slip model for past recorded California earthquakes (e. g. , the 1983 Coalinga, M_W = 6.7; the 1991 Big Bear, M_W = 5.6; the 1992 Joshua Tree earthquake, M_W = 6.2; and the 1992 Petrolia earthquake, M_W = 7.2), would easily double the available sample on which to regress. The inclusion of observations from other reverse-fault mechanism earthquakes would facilitate the determination of robustness and transferability of the reverse models presented here, which were regressed based on strong ground motion recordings restricted to southern California strong ground motion stations.

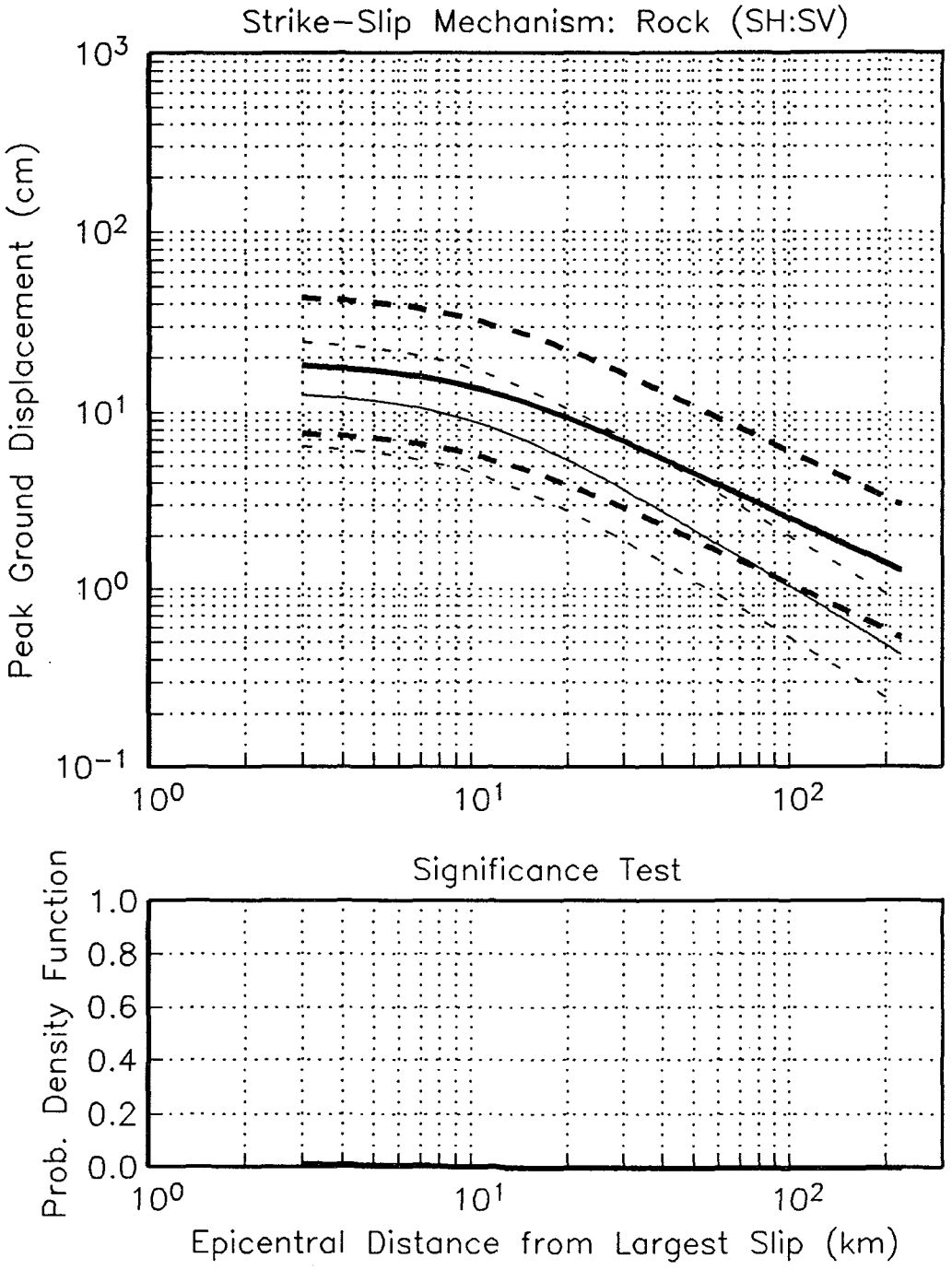

Figure 6.1 Comparison between SSHR (heavy line) and SSVR (light line) attenuation curves. The plus and minus one σ_T curves are drawn as dashed lines. The curves are for a $M_w = 7.0$ earthquake and are plotted over the applicable distance range based on the observations. (a) Peak ground displacement curves. (b) Probability density function from a student's t-test.

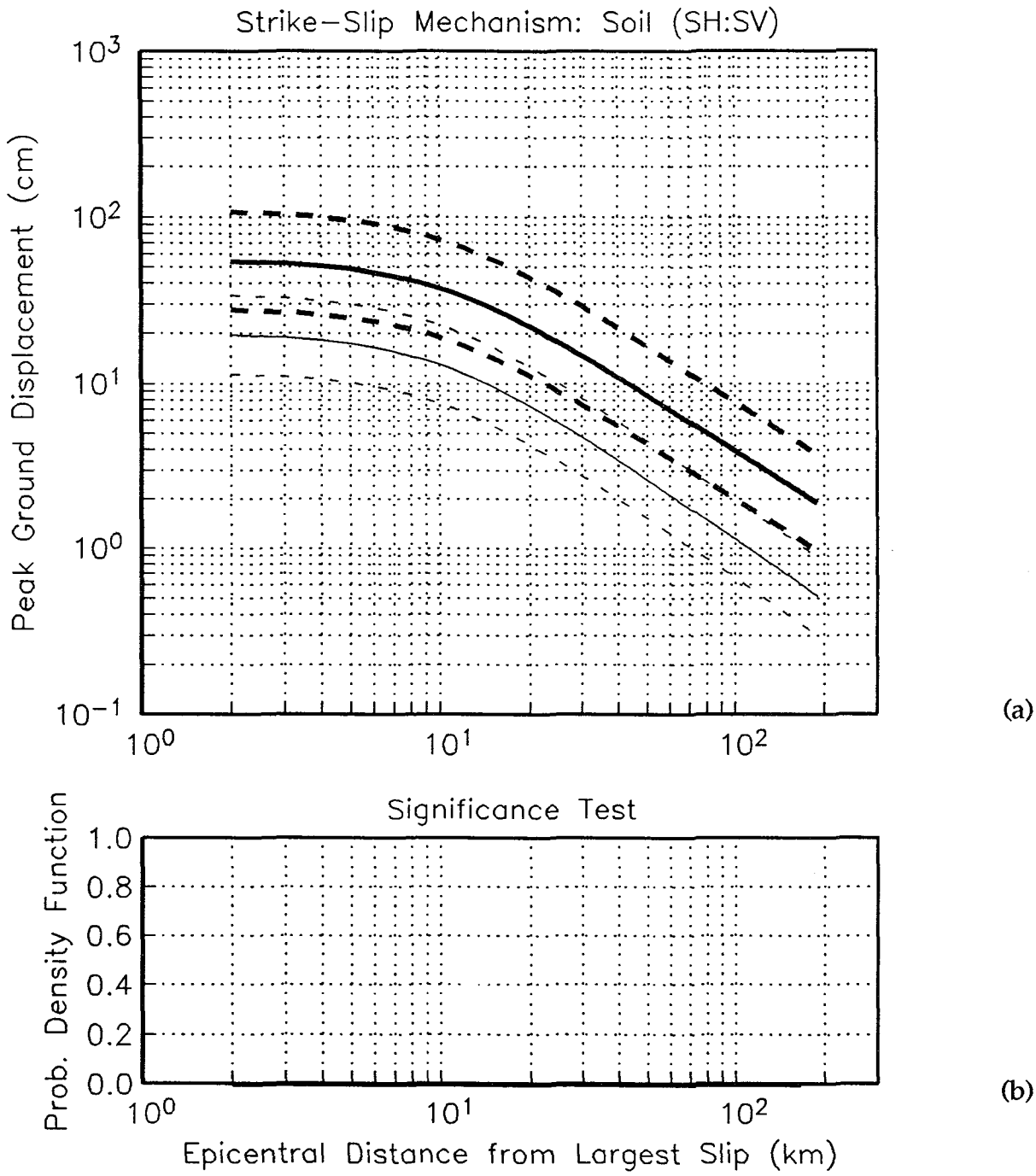

Figure 6.2 Comparison between SSHS (heavy line) and SSVS (light line) attenuation curves. The plus and minus one σ_T curves are drawn as dashed lines. The curves are for a $M_W = 7.0$ earthquake and are plotted over the applicable distance range based on the observations. (a) Peak ground displacement curves. (b) Probability density function from a student's t-test.

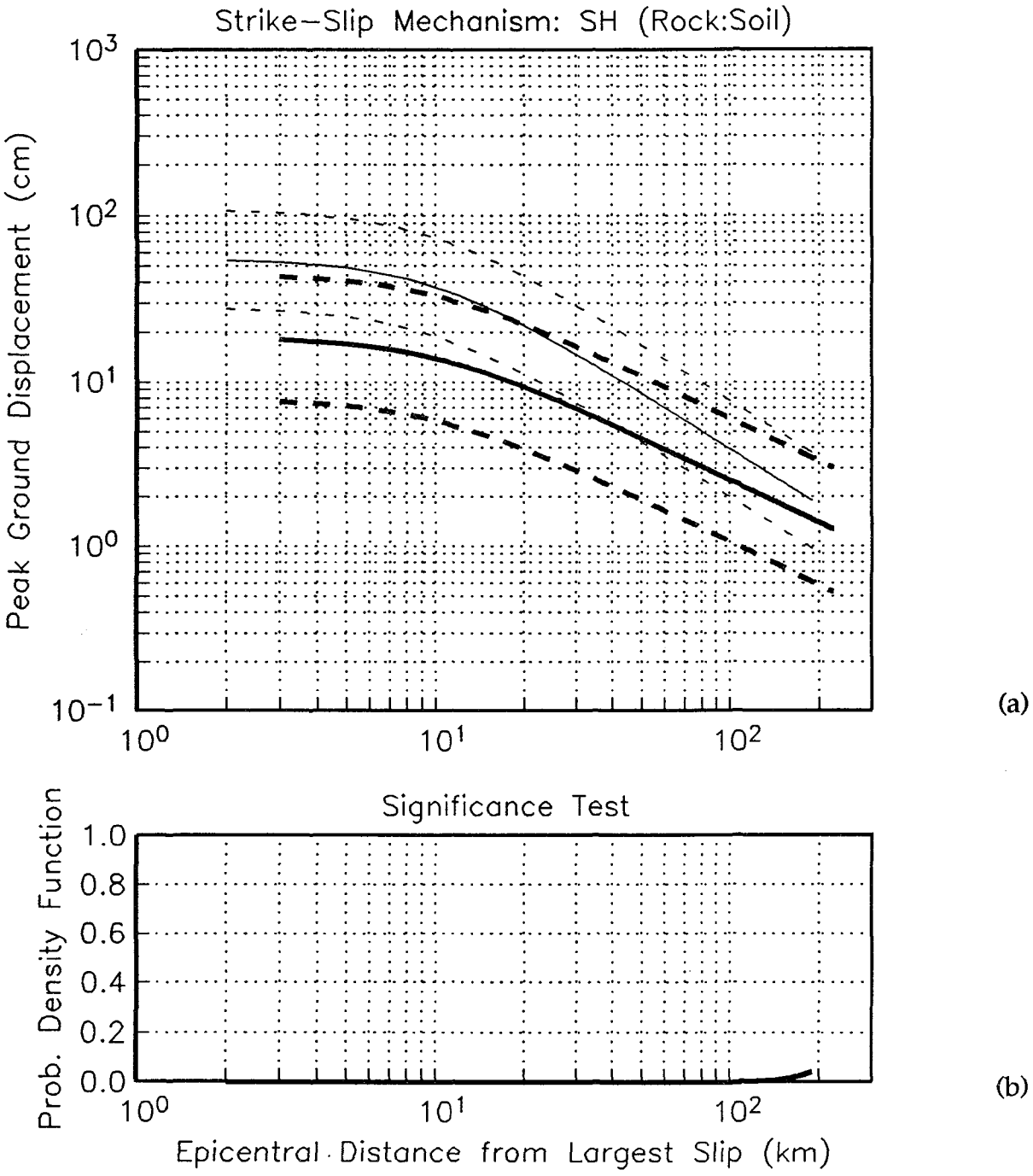

Figure 6.3 Comparison between SSHR (heavy line) and SSHS (light line) attenuation curves. The plus and minus one σ_T curves are drawn as dashed lines. The curves are for a $M_w = 7.0$ earthquake and are plotted over the applicable distance range based on the observations. (a) Peak ground displacement curves. (b) Probability density function from a student's t-test.

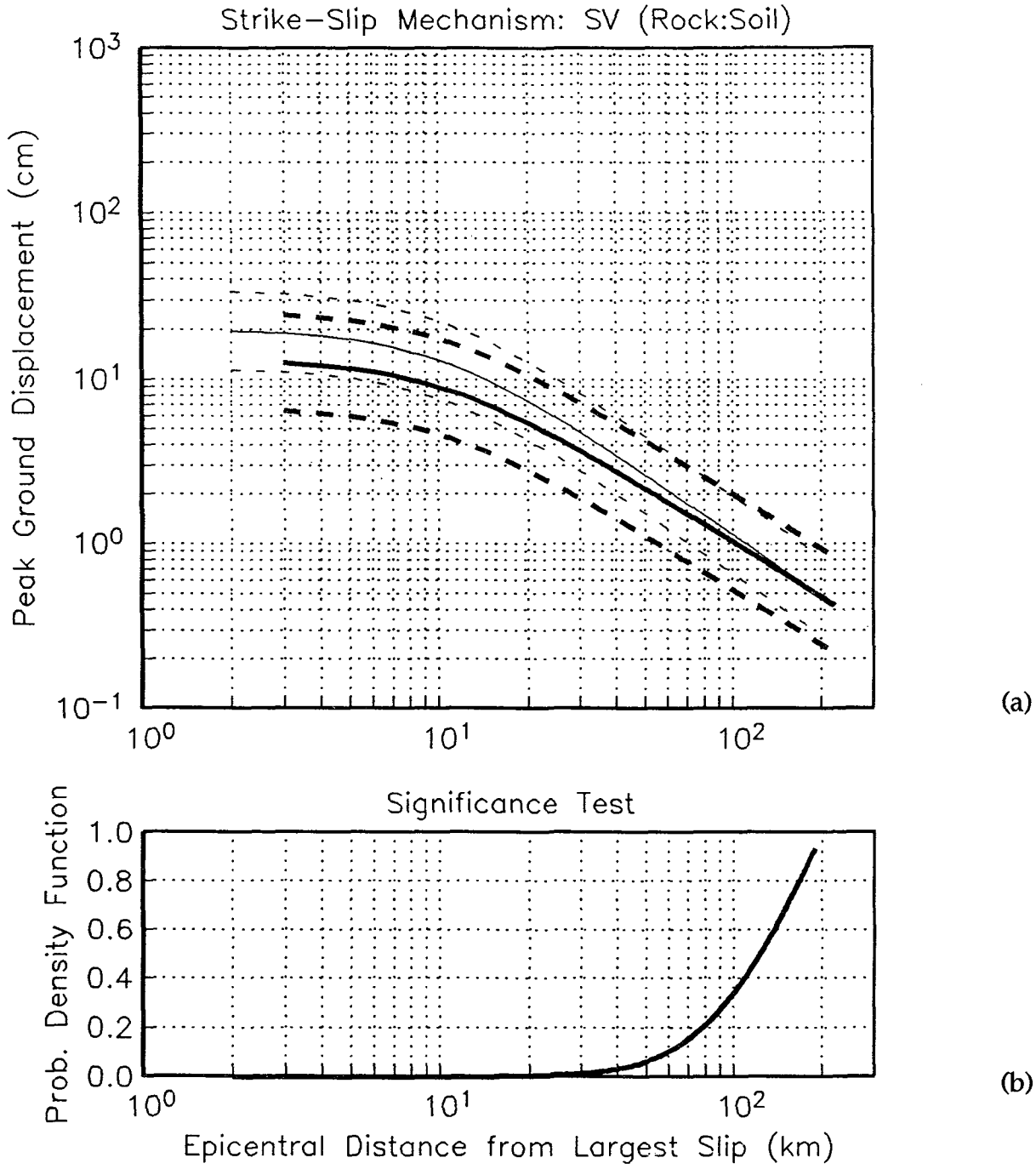

Figure 6.4 Comparison between SSVR (heavy line) and SSVS (light line) attenuation curves. The plus and minus one σ_T curves are drawn as dashed lines. The curves are for a $M_W = 7.0$ earthquake and are plotted over the applicable distance range based on the observations. (a) Peak ground displacement curves. (b) Probability density function from a student's t-test.

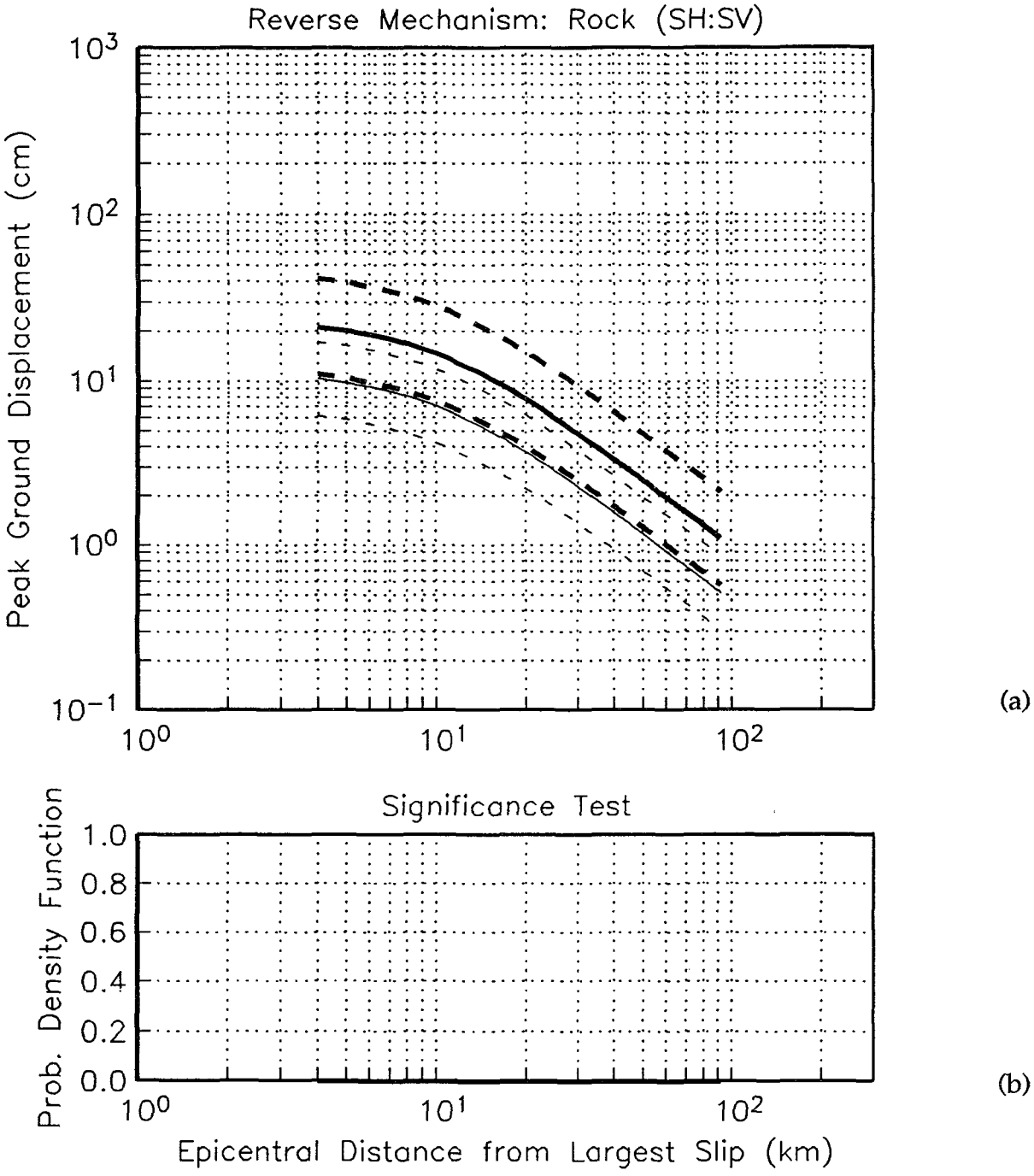

Figure 6.5 Comparison between RSHR (heavy line) and RSVR (light line) attenuation curves. The plus and minus one σ_T curves are drawn as dashed lines. The curves are for a $M_W = 7.0$ earthquake and are plotted over the applicable distance range based on the observations. (a) Peak ground displacement curves. (b) Probability density function from a student's t-test.

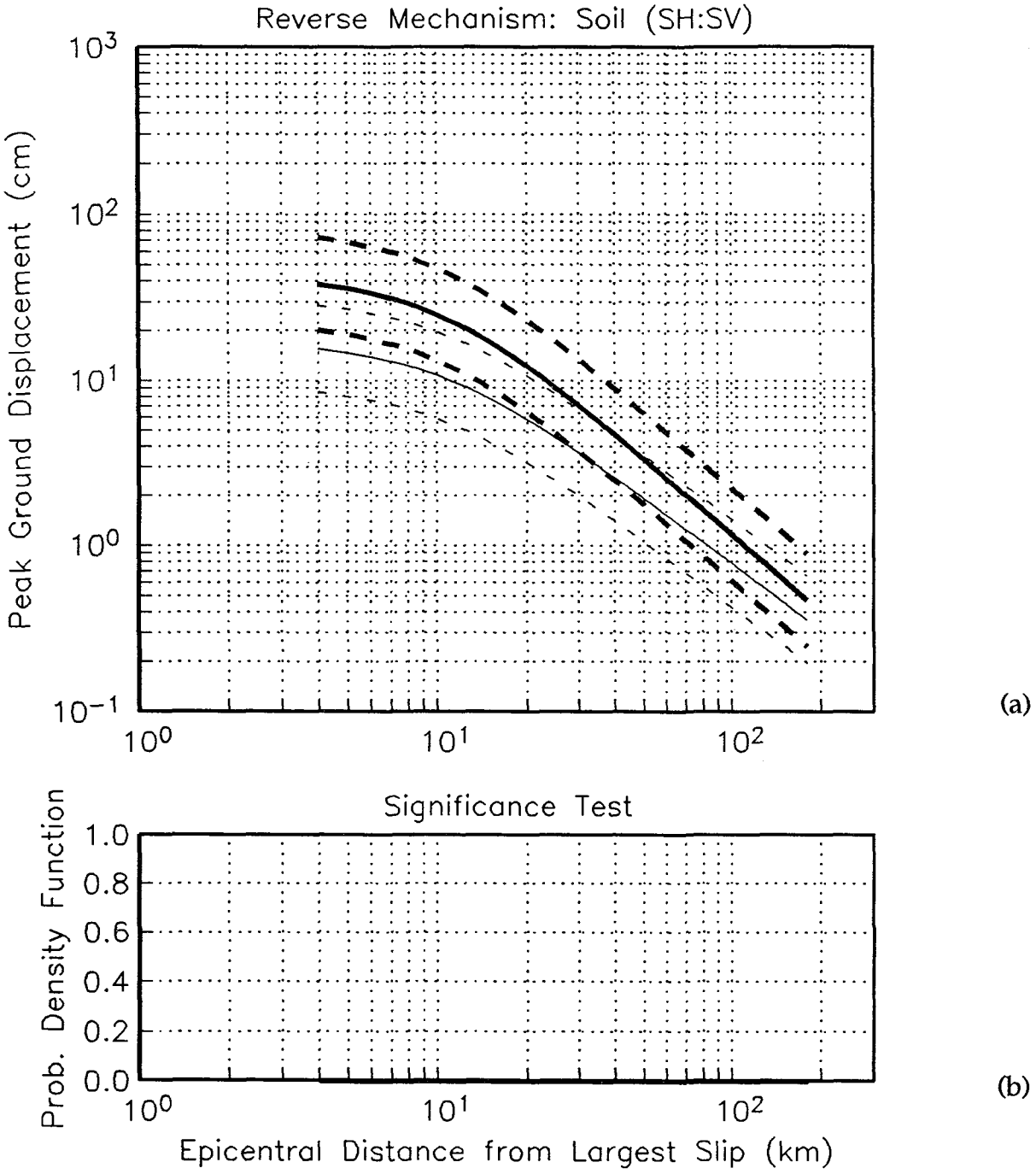

Figure 6.6 Comparison between RSHS (heavy line) and RSVS (light line) attenuation curves. The plus and minus one σ_T curves are drawn as dashed lines. The curves are for a $M_W = 7.0$ earthquake and are plotted over the applicable distance range based on the observations. (a) Peak ground displacement curves. (b) Probability density function from a student's t-test.

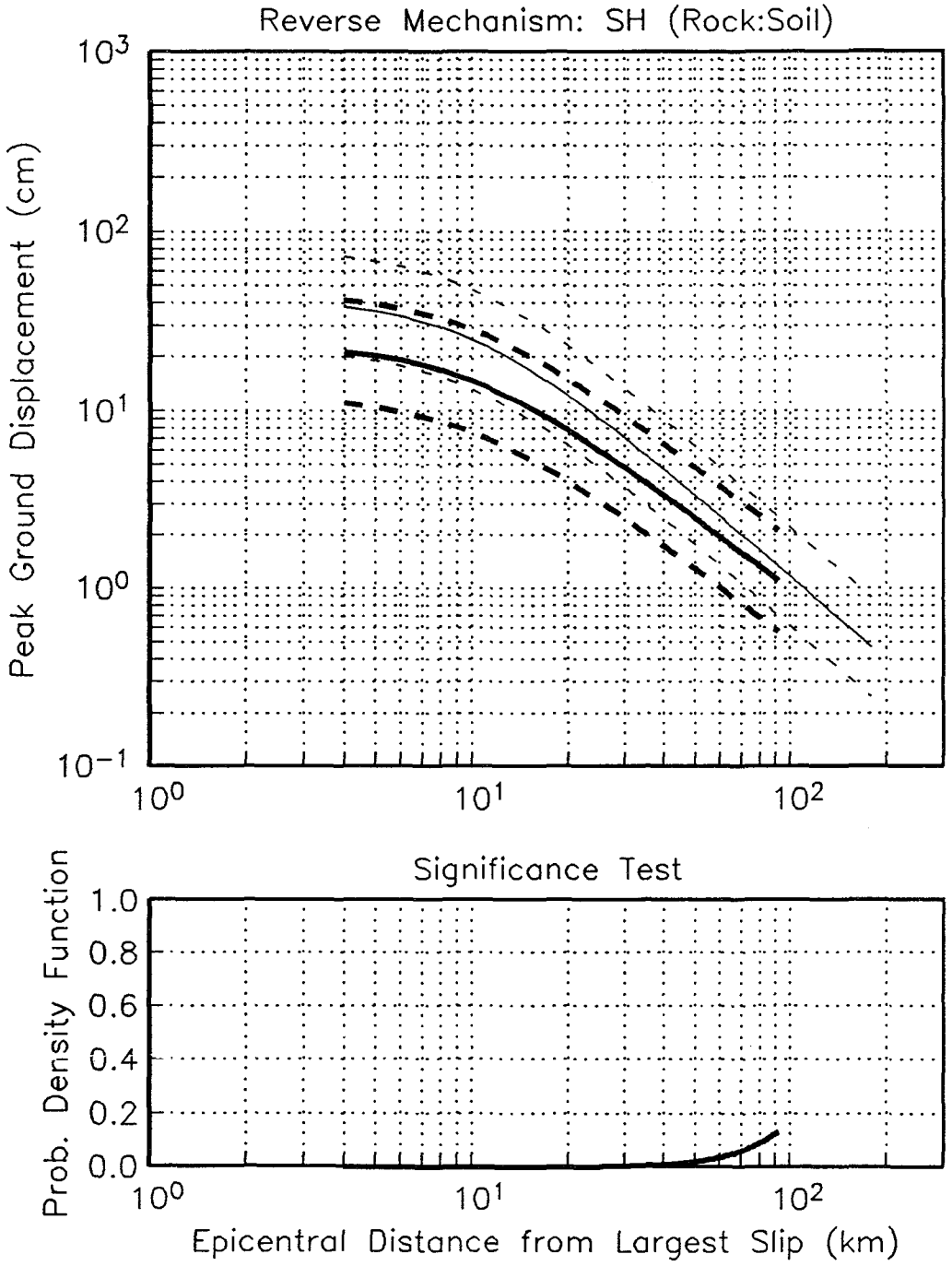

Figure 6.7 Comparison between RSHR (heavy line) and RSHS (light line) attenuation curves. The plus and minus one σ_T curves are drawn as dashed lines. The curves are for a $M_w = 7.0$ earthquake and are plotted over the applicable distance range based on the observations. (a) Peak ground displacement curves. (b) Probability density function from a student's t-test.

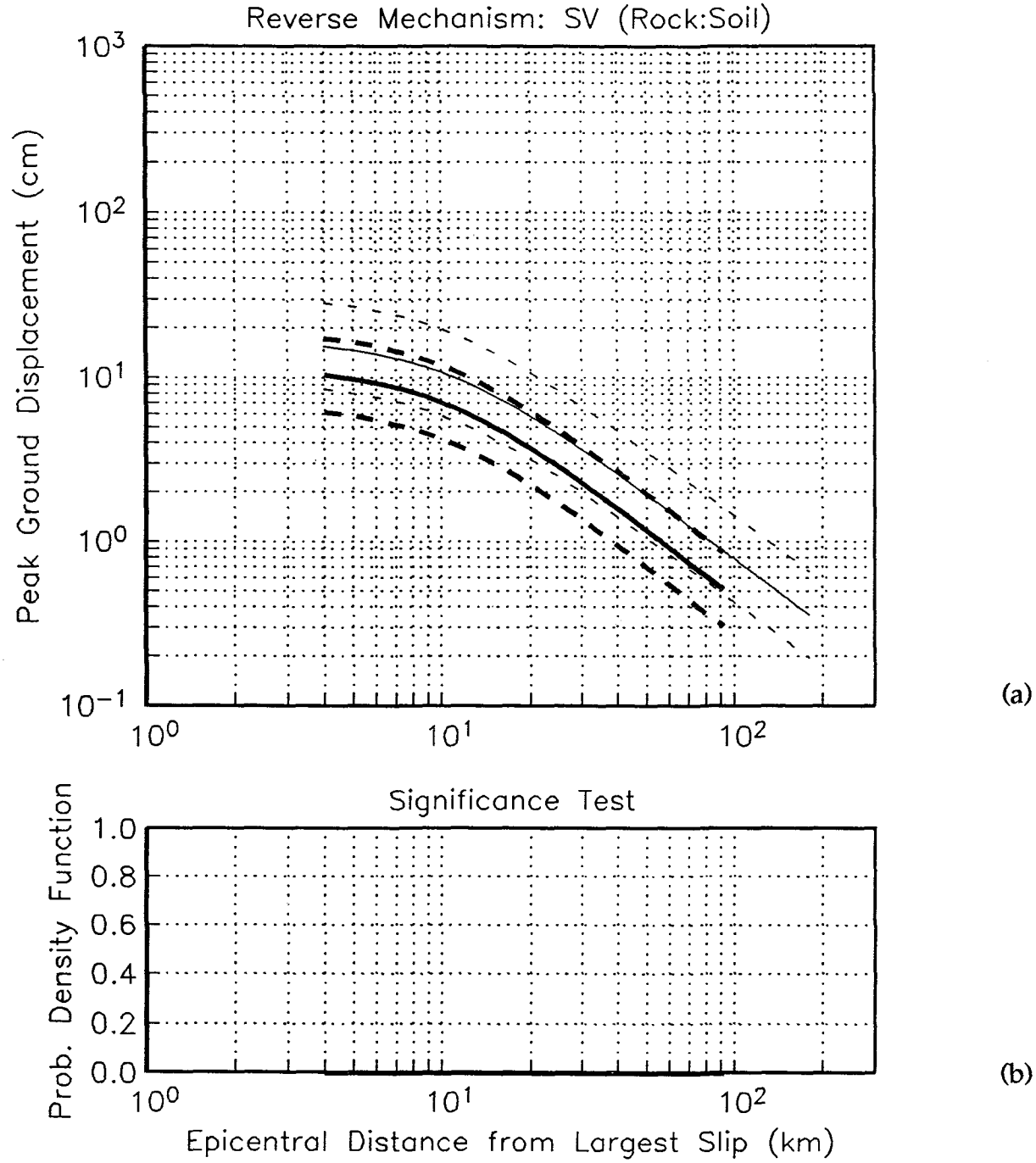

Figure 6.8 Comparison between RSVR (heavy line) and RSVS (light line) attenuation curves. The plus and minus one σ_T curves are drawn as dashed lines. The curves are for a $M_W = 7.0$ earthquake and are plotted over the applicable distance range based on the observations. (a) Peak ground displacement curves. (b) Probability density function from a student's t-test.

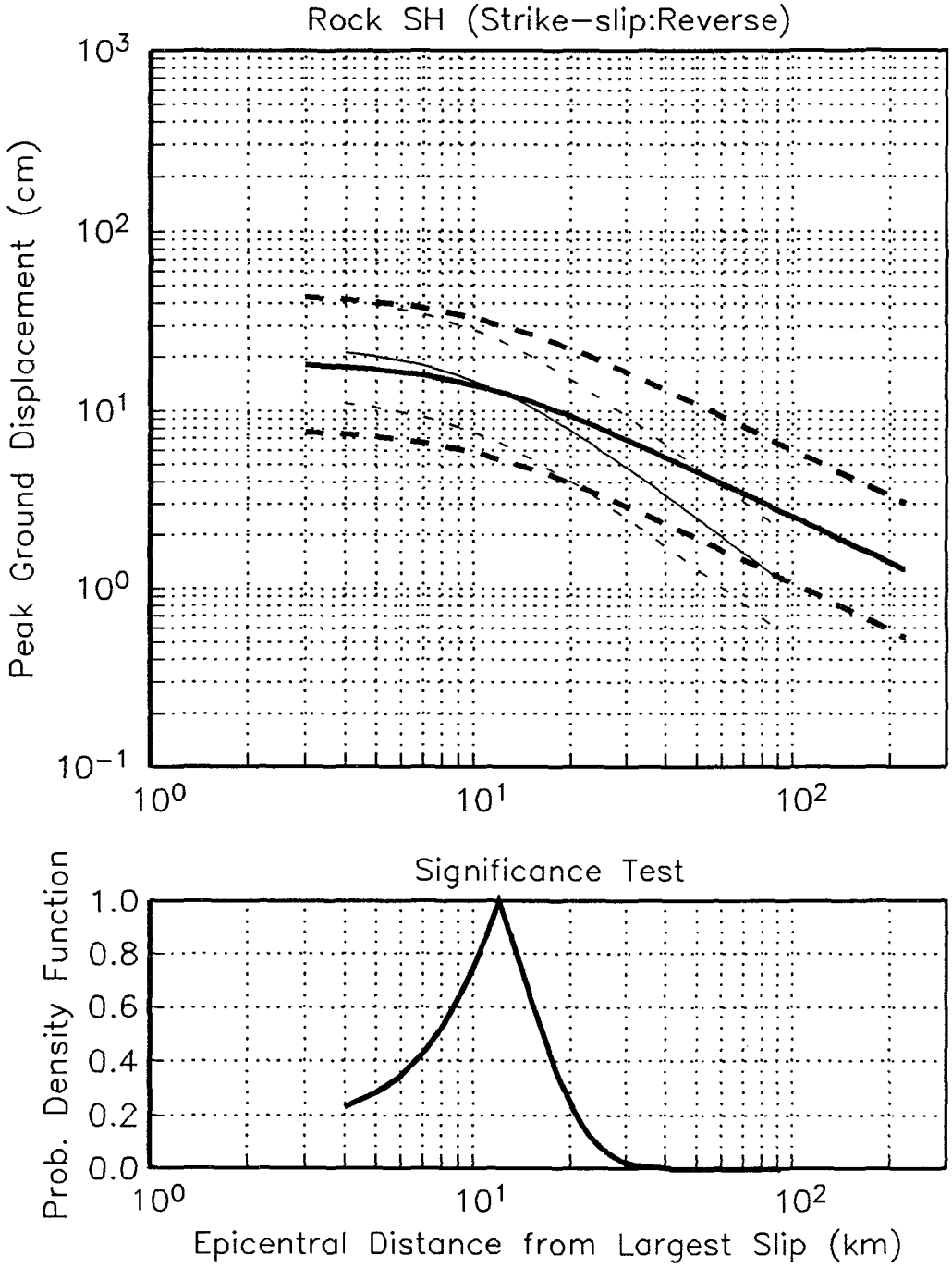

Figure 6.9 Comparison between SSHR (heavy line) and RSHR (light line) attenuation curves. The plus and minus one σ_T curves are drawn as dashed lines. The curves are for a $M_W = 7.0$ earthquake and are plotted over the applicable distance range based on the observations. (a) Peak ground displacement curves. (b) Probability density function from a student's t-test.

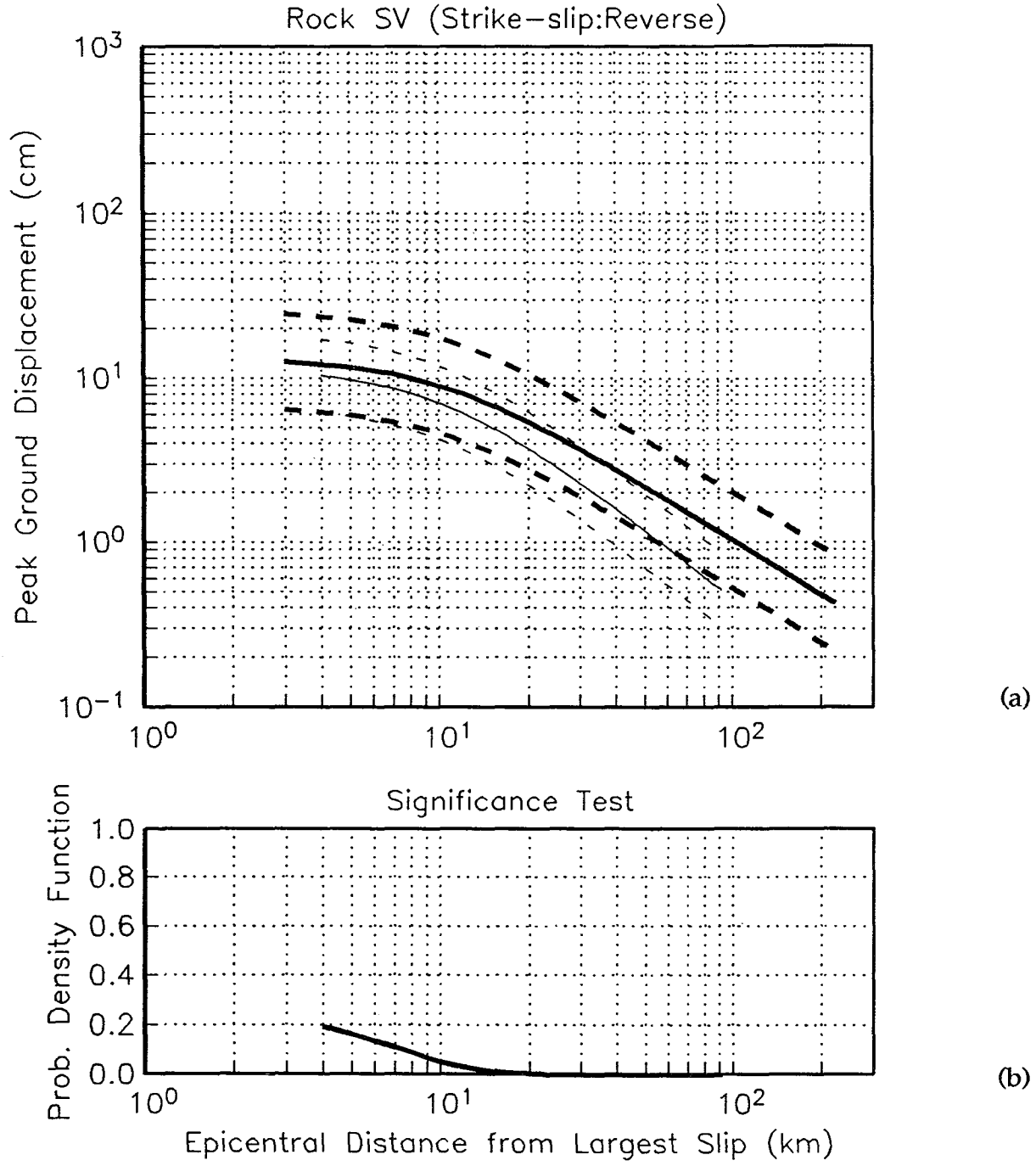

Figure 6.10 Comparison between SSVR (heavy line) and RSVR (light line) attenuation curves. The plus and minus one σ_T curves are drawn as dashed lines. The curves are for a $M_W = 7.0$ earthquake and are plotted over the applicable distance range based on the observations. (a) Peak ground displacement curves. (b) Probability density function from a student's t-test.

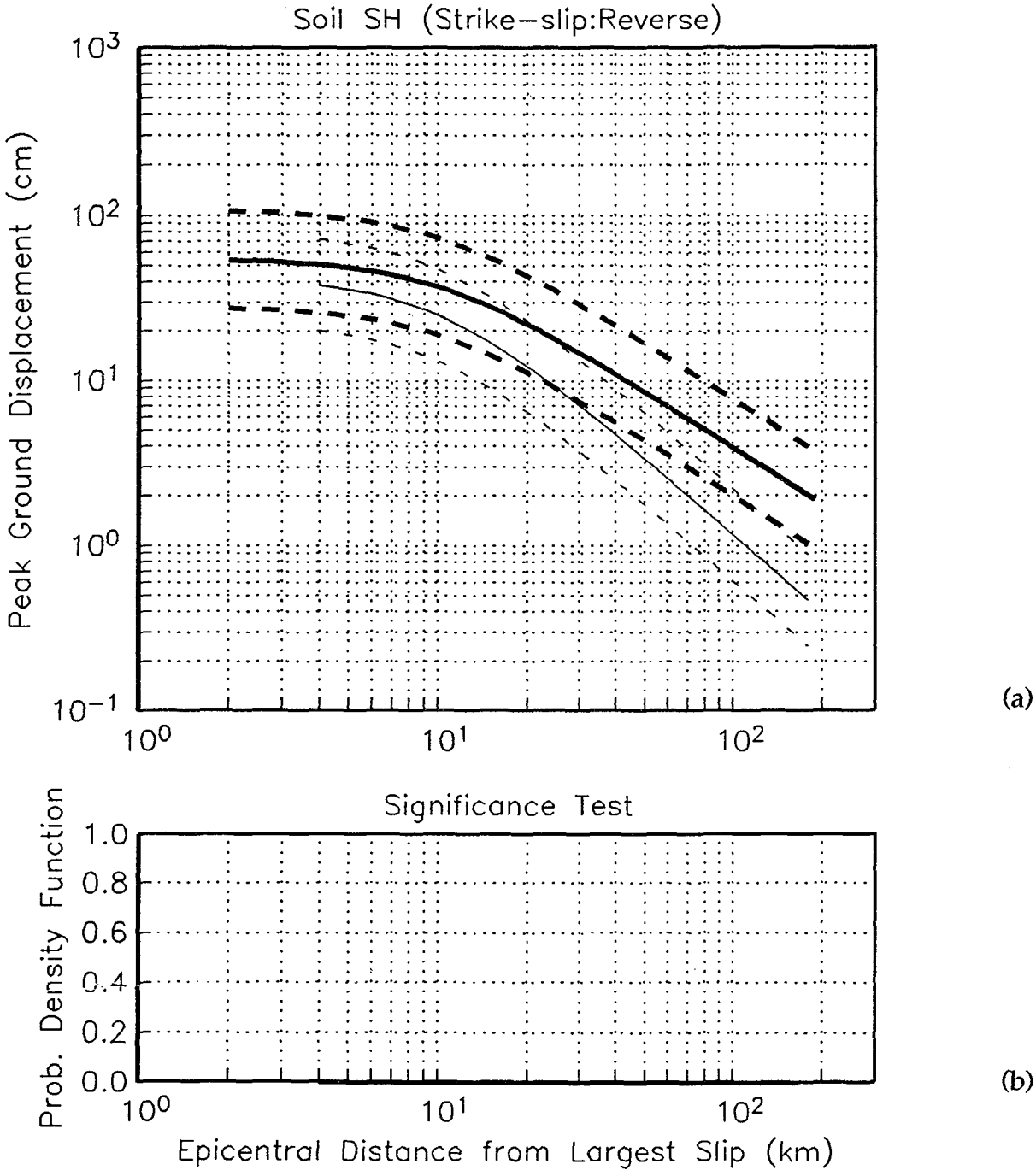

Figure 6.11 Comparison between SSHS (heavy line) and RSHS (light line) attenuation curves. The plus and minus one σ_T curves are drawn as dashed lines. The curves are for a $M_w = 7.0$ earthquake and are plotted over the applicable distance range based on the observations. (a) Peak ground displacement curves. (b) Probability density function from a student's t-test.

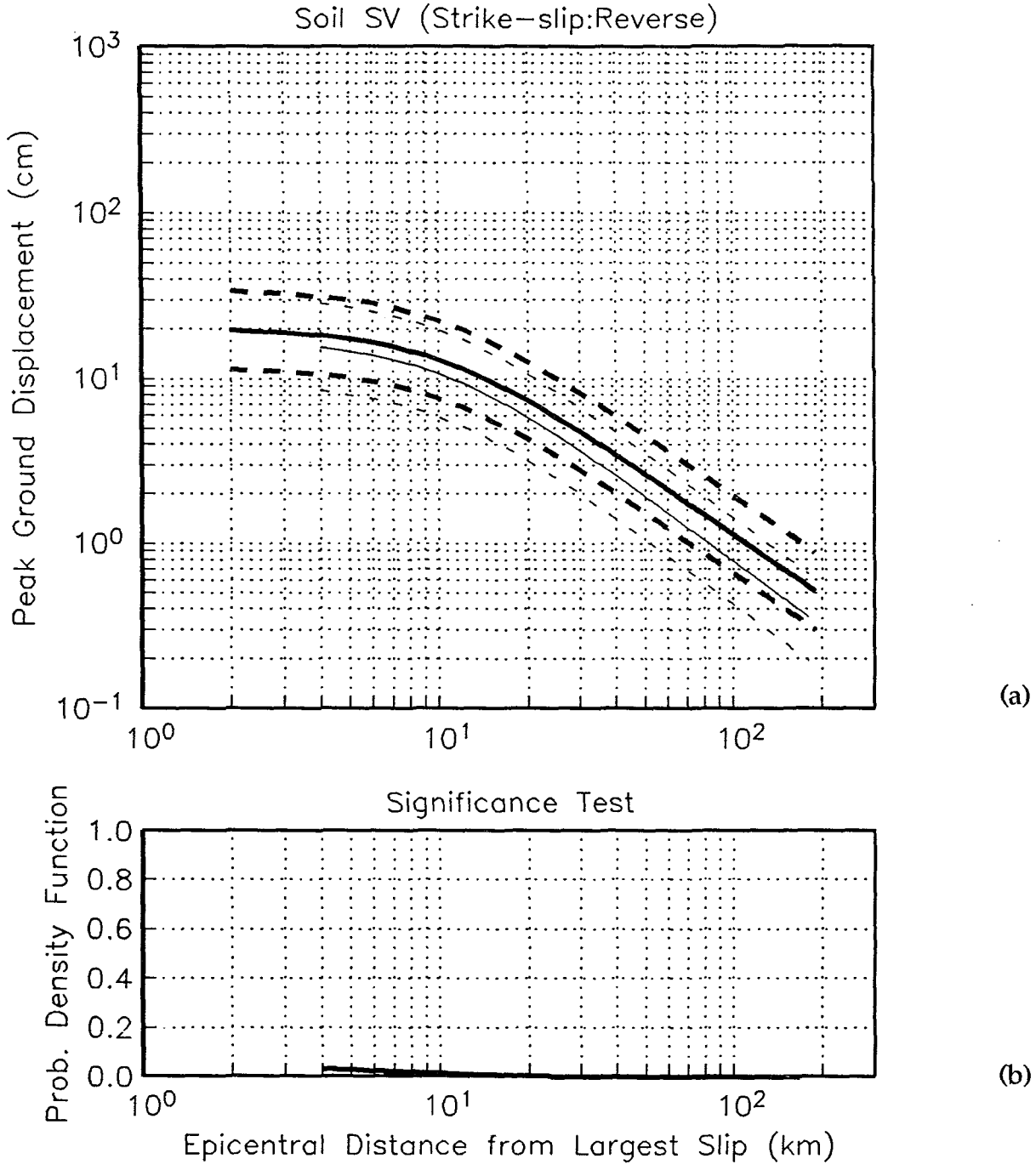

Figure 6.12 Comparison between SSVS (heavy line) and RSVS (light line) attenuation curves. The plus and minus one σ_T curves are drawn as dashed lines. The curves are for a $M_W = 7.0$ earthquake and are plotted over the applicable distance range based on the observations. (a) Peak ground displacement curves. (b) Probability density function from a student's t-test.

References

Abrahamson, N. A. and R. B. Darragh (1985). Observation of a Double Event at Regional Distances: The Morgan Hill Earthquake of 24 April 1984, *Bull. Seism. Soc. Am.* **75**, 1461-1464.

Abrahamson, N. A. and J. J. Litehiser (1989). Attenuation of Vertical Peak Acceleration, *Bull. Seism. Soc. Am.* **79**, 549-580.

Abrahamson, N. A. and R. R. Youngs (1992). A Stable Algorithm for Regression Analyses Using The Random Effects Model, *Bull. Seism. Soc. Am.* **82**, 505-510.

Aki, K (1988). Local Site Effects on Strong Ground Motion, in Earthquake Engineering and Soil Dynamics II - Recent Advances in Ground-Motion Evaluation, Park City, Utah.

Aki, K and P. G. Richards (1980). *Quantitative Seismology, Theory and Methods, Volume I*, W. H. Freeman and Company, New York, 557 pp.

Allen, C. R., T. C. Hanks, and J. H. Whitcomb (1975). Seismological Studies of the San Fernando Earthquake and Their Tectonic Implications, in San Fernando, California, Earthquake of 9 February 1971, California Division of Mines and Geology, Bulletin 196, 257-262.

Anderson, J. G., P. Bodin, J. N. Brune, J. Prince, S. K. Singh, R. Quaas, and M. Onate (1986). Strong Ground Motion from the Michoacan, Mexico, Earthquake, *Science* **233**, 1043-1049.

Archuleta, R. J., A. A. Tumarkina, A. G. Tumarkin (1994). SMDB Strong-Motion Database User's Guide, University of California, Santa Barbara.

Bakun, W. H., M. M. Clark, R. S. Cockerham, W. L. Ellsworth, A. L. Lindh, W. L. Prescott, A. F. Shakal, and P. Spudich (1984). The 1984 Morgan Hill California, Earthquake, *Science* **225**, 228-291.

Becker, A. M. (1993). Frequency Dependent Directivity Focusing of Strong Ground Motion, Ph. D. thesis, University of California, Berkeley, 163 pp.

Ben-Menahem, A. and S. J. Singh (1981). *Seismic Waves and Sources*, Springer-Verlag, New York Inc., New York, 1108 pp.

Bent, A. L. and D. V. Helmberger (1989). Source Complexity of the October 1, 1987, Whittier Narrows Earthquake, *J. Geophys. Res.* **94**, 9548-9556.

Beroza, G. C. (1991). Near-Source Modeling of the Loma Prieta Earthquake: Evidence for Heterogeneous Slip and Implications for Earthquake Hazard, *Bull. Seism. Soc. Am.* **81**, 1603-1621.

Boatwright, J. and D. M. Boore (1982). Analysis of the Ground Accelerations Radiated by the 1980 Livermore Valley Earthquakes for Directivity and Dynamic Source Characteristics, *Bull. Seism. Soc. Am.* **72**, 1843-1865.

Bolt, B. A. (1972). San Fernando Rupture Mechanism and the Pacoima Strong-Motion Record, *Bull. Seism. Soc. Am.* **62**, 1053-1061.

Bolt, B. A. and N. A. Abrahamson (1982). New Attenuation Relations for Peak and Expected Accelerations of Strong Ground Motion, *Bull. Seism. Soc. Am.* **72**, 2307-2321.

Bolt, B. A. and N. J. Gregor (1995). Discrimination of a Seismic Source Doublet in the Northridge, California Earthquake of 17 January 1994, submitted to *Geophs. Res. Lett.*

Bolt, B. A. and N. J. Gregor (1993). Synthesized Strong Ground Motions for the Seismic Condition Assessment of the Eastern Portion of the San Francisco Bay Bridge, Earthquake Engineering Research Center, *Report No. UCB/EERC-93/12.*

Bolt, B. A., T. V. McEvilly, and R. A. Uhrhammer (1981). The Livermore Valley, California, Sequence of January 1980, *Bull. Seism. Soc. Am.* **71**, 451-463.

Boore, D. M. and J. Boatwright (1984). Average Body-Wave Radiation Coefficients, *Bull. Seism. Soc. Am.* **74**, 1615-1621.

Boore, D. M., W. J. Joyner, and T. E. Fumal (1993). Estimation of Response Spectra and Peak Accelerations from Western North American Earthquakes: An Interim Report, *U. S. Geol. Surv., Open File Rept.* 93-509.

Boore, D. M., W. J. Joyner, and T. E. Fumal (1994). Estimation of Response Spectra and Peak Accelerations from Western North American Earthquakes: An Interim Report Part 2, *U. S. Geol. Surv., Open File Rept.* 94-127.

Boore, D. M., W. B. Joyner, A. A. Oliver, III, and R. A. Page (1980). Peak Acceleration, Velocity, and Displacement from Strong-Motion Records, *Bull. Seism. Soc. Am.* **70**, 305-321.

Bozorgnia, Y. and M. Niazi (1993). Distance Scaling of Vertical and Horizontal Response Spectra of the Loma Prieta Earthquake, *Earthquake Engineering and Structural Dynamics*, **22**, 695-707.

Brady, A. G. and P. N. Mork (1990). Loma Prieta, California, Earthquake October 18 (GMT) 1989, Processed Strong-Motion Records, *U. S. Geol. Surv., Open File Rept.* 90-247.

Brady, A. G., P. N. Mork, and L. C. Seekins (1988). Processed Strong-Motion Records, Whittier Narrows, California Earthquake, October 1, 1987, Volume I, USGS-NSMIN Stations within 15 km of the Epicenter, *U. S. Geol. Surv., Open File Rept.* 88-354.

Brady, A. G., P. N. Mork, and L. C. Seekins (1989). Processed Strong-Motion Records, Whittier Narrows, California Earthquake, October 1, 1987, Volume 2, USGS-NSMIN Stations between 11 and 31 km and the Santa Ana River Pipeline Bridge, *U. S. Geol. Surv., Open File Rept.* 89-122.

Brady, A. G., R. L. Porcella, G. N. Bycroft, E. C. Etheredge, P. N. Mork, B. Sliverstein, and A. F. Shakal (1987). Processing of Strong-Motion Recordings from the Main Shock, in the Morgan Hill, California Earthquake of April 24, 1984, *U. S. G. S. Bulletin 1639*, S. N. Hoose editor, 53-60.

Brady, A. G., R. L. Porcella, G. N. Bycroft, E. C. Etheredge, P. N. Mork, B. Sliverstein, and A. F. Shakal (1987). Computer Plots of Strong-Motion Results from the Main Shock, in the Morgan Hill, California Earthquake of April 24, 1984, *U. S. G. S. Bulletin 1639*, S. N. Hoose editor, 139-256.

Brillinger, D. R. and H. K. Preisler (1985). Further Analysis of the Joyner-Boore Attenuation Data, *Bull. Seism. Soc. Am.* **74**, 611-614.

Brune, J. N., F. L. Vernon III, R. S. Simons, J. Prince, and E. Mena (1982). Strong-Motion Data Recorded in Mexico During the Main Shock; in The Imperial Valley, California, Earthquake of October 15, 1979, *U. S. Geol. Prof. Paper* 1254, 319-350.

Buckle, I. G. (1988). Seismic Isolation of Buildings, prepared by Dynamic Isolation Systems, Inc., Berkeley, California.

Buckle, I. G. and R. L. Mayes (1990). Seismic Isolation: History, Application, and Performance - A World View, *Earthquake Spectra*, **6**, No. 2, 161-201.

Bullen, K. E. and B. A. Bolt (1985). *An Introduction to the Theory of Seismology*, Cambridge: Cambridge Univ. Press, 499 pp.

California Institute of Technology (1969-1974). "Bluebook" Series - Volume I: Strong Motion Earthquake Accelerograms - Uncorrected Accelerograms, *Earthquake Engineering Laboratory*, Pasadena.

Campbell, K. W. (1987). Predicting Strong Ground Motion in Utah, in Evaluation of Regional and Urban Earthquake Hazards and Risk in Utah, *U. S. Geol. Prof. Paper* 87-585, L1-L90.

Campbell, K. W. and Y. Bozorgnia (1994a). Empirical Analysis of Strong Ground Motion from the 1992 Landers, California, Earthquake, *Bull. Seism. Soc. Am.* 84, 573-588.

Campbell, K. W. and Y. Bozorgnia (1994b). Near- Source Attenuation of Peak Horizontal Acceleration from Worldwide Accelerograms Recorded from 1957 to 1993, in *Proc. Fifth U. S. National Conference on Earthquake Engineering*, Chicago, Illinois.

Choy, G. L. and J. Boatwright (1990). Source Characteristics of the Loma Prieta, California, Earthquake of October 18, 1989 from Global Digital Seismic Data, *Geophs. Res. Lett.* **17**, 1183-1189.

Choy, G. L. and R. Kind (1987). Rupture Complexity of a Moderate-Sized (mb 6.0) Earthquake: Broadband Body-Wave Analysis of the North Yemen Earthquake of 13 December 1982, *Bull. Seism. Soc. Am.* 77, 28-46.

Cockerham, R. S., F. W. Lester, and W. L. Ellsworth (1980). A preliminary Report on the Livermore Valley Earthquake Sequence, January 24 - February 26, 1980,*U. S. Geol. Surv., Open File Rept.* 80-714.

CSMIP Staff (1989). Plots of the Processed Data for the interim Set of 14 Records from the Santa Cruz Mountains (Loma Prieta), California Earthquake of 17 October 1989, Calif. Div. Mines and Geology, Office of Strong Motion Studies, Report No. OSMS 89-08.

CSMIP Staff (1992). Preliminary Processed Strong-Motion Data for the Landers Earthquake of 28 June 1992, Calif. Div. Mines and Geology, Office of Strong Motion Studies, Report No. OSMS 92-11.

Darragh, R., T. Cao, C. Cramer, M. Huang, and A. Shakal (1994a). Processed CSMIP Strong-Motion Records from the Northridge, California Earthquake of January 17, 1994: Release No. 1, Calif. Div. Mines and Geology, Office of Strong Motion Studies, Report No. OSMS 94-06B.

Darragh, R., T. Cao, C. Cramer, M. Huang, and A. Shakal (1994b). Processed CSMIP Strong-Motion Records from the Northridge, California Earthquake of January 17, 1994: Release No. 2, Calif. Div. Mines and Geology, Office of Strong Motion Studies, Report No. OSMS 94-08.

Darragh, R., T. Cao, C. Cramer, V. Graizer, M. Huang, and A. Shakal (1994a). Processed CSMIP Strong-Motion Records from the Northridge, California Earthquake of January 17, 1994: Release No. 3, Calif. Div. Mines and Geology, Office of Strong Motion Studies, Report No. OSMS 94-09.

Darragh, R., T. Cao, C. Cramer, V. Graizer, M. Huang, and A. Shakal (1994b). Processed CSMIP Strong-Motion Records from the Northridge, California Earthquake of January 17, 1994: Release No. 4, Calif. Div. Mines and Geology, Office of Strong Motion Studies, Report No. OSMS 94-10.

Darragh, R., T. Cao, M. Huang, and A. Shakal (1994a). Preliminary Processed Data for Tarzana - Cedar Hill Nursery A from the Northridge, California Earthquake of January 17, 1994, Calif. Div. Mines and Geology, Office of Strong Motion Studies, Report No. OSMS 94-12B.

Darragh, R., T. Cao, M. Huang, and A. Shakal (1994b). Processed CSMIP Strong-Motion Records from the Northridge, California Earthquake of January 17, 1994: Release No. 9, Calif. Div. Mines and Geology, Office of Strong Motion Studies, Report No. OSMS 94-16.

Darragh, R., T. Cao, C. Cramer, F. Su, M. Huang, and A. Shakal (1992). Processed Strong-Motion Data for the Landers Earthquake of 28 June 1992: Release No. 2, Calif. Div. Mines and Geology, Office of Strong Motion Studies, Report No. OSMS 92-13.

Darragh, R., T. Cao, M. Huang, and A. Shakal (1993). Processed Strong-Motion Data for the Landers Earthquake of 28 June 1992: Release No. 3, Calif. Div. Mines and Geology, Office of Strong Motion Studies, Report No. OSMS 93-01.

Dietz, L. D. and W. L. Ellsworth (1990). The October 17, 1989, Loma Prieta, California, Earthquake and its Aftershocks: Geometry of the Sequence from High-Resolution Locations, *Geophs. Res. Lett.* **17**, 1417-1420.

Drake, L. A. (1972). Love and Rayleigh Waves in Nonhorizontally Layered Media, *Bull. Seism. Soc. Am.* **62**, 1241-1258.

Drake, L. A. and B. A. Bolt (1980). Love Waves Normally Incident at a Continental Boundary, *Bull. Seism. Soc. Am.* **70**, 1103-1123.

Dreger, D. S. (1994). Empirical Green's Function Study of the January 17, 1994 Northridge, California Earthquake (M_W=6.7), *Geophs. Res. Lett.* **21**, 2633-2636.

Dreger, D. S. and D. V. Helmberger (1991). Source Parameters of the Sierra Madre Earthquake from Regional and Local Body Waves, *Geophs. Res. Lett.* **18**, 2015-2018.

Dreger, D., M. Pasyanos, S. Loper, R. McKenzie, N. Gregor, and B. Romanowicz (1994). The January 17, 1994 Northridge Earthquake: A Regional Perspective, *Northridge abstracts program for the 89th annual meeting of SSA*, No. 11.

Ehlig, P. L. (1975). Geologic Framework of the San Gabriel Mountains, in San Fernando, California, Earthquake of 9 February 1971, California Division of Mines and Geology, Bulletin 196, 7-18.

Etheredge, E. and R. Pocella (1987). Strong-Ground Motion Data from the October 1, 1987 Whittier Narrows Earthquake, *U. S. Geol. Surv., Open File Rept.* 87-616.

Geomatrix Consultants, (1992). Seismic Ground Motion Study for West San Francisco Bay Bridge, San Francisco, California, report for California Department of Transportation, Division of Structures, Project No. 2016G.

Graves, R. W. (1995). Preliminary Analysis of Long-Period Basin Response in the Los Angeles Region from the 1994 Northridge Earthquake, *Geophs. Res. Lett.* **22**, 101-104.

Gregor, N. J. (1995). Attenuation Relations for Peak Strong Ground Motion Displacement, Ph. D. thesis, University of California, Berkeley, 285 pp.

Hanks, T. C. and H. Kanamori (1979). A Moment Magnitude Scale, *J. Geophys. Res.* **84**, 2348-2350.

Hanks, T. C. and H. Krawinkler (1991). The 1989 Loma Prieta, California, Earthquake and Its Effects: Introduction to the Special Issue, *Bull. Seism. Soc. Am.* **81**, 1415-1423.

Hartzell, S. (1989). Comparison of Seismic Waveform Inversion Results for the Rupture History of a Finite Fault: Application to the 1986 North Palm Springs, California, Earthquake, *J. Geophys. Res.* **94**, 7515-7534.

Hartzell, S. H. and T. H. Heaton (1983). Inversion of Strong Ground Motion and Teleseismic Waveform Data for the Fault Rupture History of the 1979 Imperial Valley, California, Earthquake, *Bull. Seism. Soc. Am.* **73**, 1553-1583.

Hartzell, S. H. and T. H. Heaton (1986). Rupture History of the 1984 Morgan Hill, California, Earthquake from the Inversion of Strong Motion Records, *Bull. Seism. Soc. Am.* **76**, 649-674.

Hartzell, S. H. and M. Iida (1990). Source Complexity of the 1987 Whittier Narrows, California, Earthquake From the Inversion of Strong Ground Motion Records, *J. Geophys. Res.* **95**, 12,475-12,485.

Hartzell, S. H., G. S. Stewart, and C. Mendoza (1991). Comparison of L_1 and L_2 Norms in a Teleseismic Inversion for the Slip History of the Loma Prieta, California, Earthquake, *Bull. Seism. Soc. Am.* **81**, 1518-1539.

Hauksson, E. and L. M. Jones (1989). The 1987 Whittier Narrows Earthquake Sequence in Los Angeles, Southern California: Seismological and Tectonic Analysis, *J. Geophys. Res.* **94**, 9569-9589.

Hauksson, E. and R. S. Stein (1989). The 1987 Whittier Narrows, California Earthquake: A Metropolitan Shock, *J. Geophys. Res.* **94**, 9545-9547.

Heaton, T. H., J. F. Hall, D. J. Wald, M. W. Halling (1995). Response of High-Rise and Base-Isolated Buildings to a Hypothetical M_w=7.0 Blind Thrust Earthquake, *Science*, **267**, 206-211.

Heaton, T. H. and D. V. Helmberger (1979). Generalized Ray Models of the San Fernando Earthquake, *Bull. Seism. Soc. Am.* **69**, 1311-1341.

Heaton, T. H., F. Tajima, A. W. Mori (1986). Estimating Ground Motions Using Recorded Accelerograms, *Surveys in Geophysics*, **8**, 25-83.

Hoose, S. N. (1987). The Morgan Hill Earthquake: An Overview, in the Morgan Hill, California Earthquake of April 24, 1984, *U. S. G. S. Bulletin 1639*, S. N. Hoose editor, 1-14.

Housner, G. W. (1970). Strong Ground Motion, in *Earthquake Engineering*, Prentice-Hall, Inc., Englewood Cliffs, New Jersey, 518 p.

Huang, M. J., T. Q. Cao, D. L. Parke, A. F. Shakal (1989). Processed Strong-Motion Data from the Whittier, California Earthquake of 1 October 1987, Part I, Ground-Response Records, Calif. Div. Mines and Geology, Office of Strong Motion Studies, Report No. OSMS 89-03.

Huang, M. J., D. L. Parke, R. W. Sherburne, and A. F. Shakal (1987). Processed Strong Motion Data from the Palm Springs Earthquake of July 8, 1986: Part 1 Ground-Response Records, Calif. Div. Mines and Geology, Office of Strong Motion Studies, Report No. OSMS 87-01.

Huang, M., T. Cao, U. Vetter, and A. Shakal (1990a). Second Interim Set of CSMIP Processed Strong-Motion Records from the Santa Cruz Mountains (Loma Prieta), California Earthquake of 17 October 1989, Calif. Div. Mines and Geology, Office of Strong Motion Studies, Report No. OSMS 90-01.

Huang, M., T. Cao, U. Vetter, and A. Shakal (1990b). Third Interim Set of CSMIP Processed Strong-Motion Records from the Santa Cruz Mountains (Loma Prieta), California Earthquake of 17 October 1989, Calif. Div. Mines and Geology, Office of Strong Motion Studies, Report No. OSMS 90-05.

Iai, S. and Y. Matsunaga (1993). Comparison of Attenuation Relations and Response Spectra for Various Regions in the World, in *Proc. of the International Workshop on Strong Motion Data*, Menlo Park, California.

Idriss, I. M. (1985). Evaluating Seismic Risk in Engineering Practice, in *Proc. Eleventh International Conf. on Soil Mech. and Foundation Eng.*, San Francisco, California.

Iwan, W. D. and X. Chen (1994). Important Near-Field Ground Motion Data from the Landers Earthquake, *Proc. Tenth European Conference on Earthquake Engineering*, Vienna.

Jones, L. M., L. K. Hutton, D. D. Given, and C. R. Allen (1986). The North Palm Springs, California, Earthquake Sequence of July 1986, *Bull. Seism. Soc. Am.* **76**, 1830-1837.

Joyner, W. B. and D. M. Boore (1981). Peak Horizontal Acceleration and Velocity from Strong-Motion Records from the 1979 Imperial Valley, Earthquake, *Bull. Seism. Soc. Am.* **71**, 2011-2038.

Joyner, W. B. and D. M. Boore (1988). Measurement, Characterization, and Prediction of Strong Ground Motion, in Earthquake Engineering and Soil Dynamics II - Recent Advances in Ground-Motion Evaluation, Park City, Utah.

Joyner, W. B. and D. M. Boore (1991). Strong Earthquake Ground Motion and Engineering Design, *Geotechnical News*, **9**, No. 1, 21-26.

Kanamori, H. and K. Satake (1990). Broadband Study of the 1989 Loma Prieta Earthquake, *Geophs. Res. Lett.* **17**, 1179-1182.

Kanamori, H. and G. S. Stewart (1978). Seismological Aspects of the Guatemala Earthquake of February 4, 1976, *J. Geophys. Res.* **83**, 3427-3434.

Kawase, H. and K. Aki (1989). A Study on the Response of a Soft Basin for Incident S, P, and Rayleigh Waves with Special Reference to the Long Duration Observed in Mexico City, *Bull. Seism. Soc. Am.* **79**, 1361-1382.

Kawashima, K., K. Aizawa, and K. Takahashi (1986). Attenuation of Peak Ground Acceleration, Velocity, and Displacement Based on Multiple Regression Analysis of Japanese Strong Motion Records, *Earthquake Engineering and Structural Dynamics*, **14**, 199-215.

Kawashima, K. and K. Hasegawa (1994). New Seismic Design Specifications of Highway Bridges in Japan, *Earthquake Spectra*, **10**, No. 2, 333-356.

Kelly, J. M. (1990). Base Isolation: Linear Theory and Design, *Earthquake Spectra*, **6**, No. 2, 223-244.

Kelly, T. A. (1992). Landers Earthquake - Southern California Edison Accelerograph Records, personal memorandum.

Lahr, J. (1989). HYPOELLIPSE - A Computer Program for Determining Local Earthquake Hypocentral Parameters, Magnitude, and First Motion Pattern, *U. S. Geol. Surv., Open File Rept.* 89-116.

Langston, C. A. (1978). The February 9, 1971 San Fernando Earthquake: A Study of Source Finiteness in Teleseismic Body Waves, *Bull. Seism. Soc. Am.* 68, 1-29.

Lomax, A. J. and B. A. Bolt (1992). Broadband Waveform Modelling of Anomalous Strong Ground Motion in the 1989 Loma Prieta Earthquake Using Three-Dimensional Geologic Structures, *Geophs. Res. Lett.* 19, 1963-1966.

Maison, B. F. and C. E. Ventura (1992). Seismic Analysis of Base-Isolated San Bernardino County Building, *Earthquake Spectra*, 8, No. 4, 605-634.

Morse, P. M. and H. Feshbach (1953). *Methods of Theoretical Physics*, McGraw-Hill Inc., New York, 1978 pp.

Miranda, E. (1993). Evaluation of Seismic Design Criteria for Highway Bridges, *Earthquake Spectra*, 9, No. 2, 233-250.

Nakamura, Y., K. Hidaka, J. Saita, and S. Sato (1995). Strong Accelerations and Damage of the 1995 Hyogo-Ken-Nanbu Earthquake, *JR Earthquake Information* No. 23b.

Newmark, N. M. and W. J. Hall (1969). Seismic Design Criteria for Nuclear Reactor Facilities, *Proc. World Conf. Earthquake Eng., 4th Santiago*, 2, B4-37-B4-50.

Niazi, M. (1982). Source Dynamics of the 1979 Imperial Valley Earthquake from Near-Source Observations (of ground acceleration and velocity), in Proceedings of Workshop on the Dynamic Characteristics of Faulting Inferred from Recordings of Strong Ground Motion, *U. S. Geol. Surv., Open File Rept.* 82-591.

Perry, C. L., E. A. Fierro, H. Serdarat, and R. E. Scholl (1993). Supplemental Damping for Improved Seismic Performance, *Earthquake Spectra*, 9, No. 3, 559-580.

Ponti, D. J. and R. E. Wells (1991). Off-Fault Ground Ruptures in the Santa Cruz Mountains, California: Ridge-Top Spreading versus Tectonic Extension During the 1989 Loma Prieta Earthquake, *Bull. Seism. Soc. Am.* **81**, 1480-1510.

Porcella, R. L., R. B. Mattiesen, and R. P. Maley (1982). Strong-Motion Data Recorded in the United States, in the Imperial Valley, California, Earthquake of October 15, 1979, *U. S. Geol. Prof. Paper* 1254, 319-350.

Porcella, R., E. Etheredge, and R. Malley (1986). Some Strong-Motion Recordings of the 1986 North Palm Springs Earthquake, *Bull. Seism. Soc. Am.* **76**, 1844-1846.

Porcella, R., E. Etheredge, R. Maley, and J. Switzer (1987a). Strong-Motion Data from the July 8, 1986 North Palm Springs Earthquake and Aftershocks, *U. S. Geol. Surv. , Open File Rept.* 87-155.

Porcella, R., E. Etheredge, R. Maley, and J. Switzer (1987b). Strong-Motion Data from the Superstition Hills earthquakes of 0154 and 1315 (GMT), November 24, 1987, *U. S. Geol. Surv., Open File Rept.* 87-672.

Porter, L. D. (1982). Data Processing Procedures for Main-Shock Motions Recorded by the California Division of Mines and Geology Strong-Ground Motion Network; in The Imperial Valley, California, Earthquake of October 15, 1979, *U. S. Geol. Prof. Paper* 1254, 407-432.

Prescott, W. H., N. E. King, G. Guohua (1984). Preseismic and Coseismic Deformation Associated with the 1984 Morgan Hill, California Earthquake, in The Morgan Hill, California, Earthquake of April 24, 1984 (a Preliminary report), Vol. I, *U. S. Geol. Surv., Open File Rept.* 84-498-A, 50-59.

Sadigh, K. R. (1993). A Review of Attenuation Relationships for Rock Site Conditions from Shallow Crustal Earthquakes in an Interplate Environment, in *Proc. of the International Workshop on Strong Motion Data*, Menlo Park, California.

Scientists of the U.S.G.S. and the Southern California Earthquake Center (1994). "The Magnitude 6.7 Northridge, California, Earthquake of 17 January 1994," *Science*, **266**, 389-397.

Seekins, L. C., A. G. Brady, C. Carpenter, and N. Brown (1992). Digitized Strong-Motion Accelerograms of North and Central American Earthquakes 1933-1986, *U. S. Geol. Surv. Digital Data Series* DDS-7.

Seekins, L. C., A. G. Brady, and C. S. Muller (1989). Digitized Strong-Motion Accelerograms of North America Through 1986, *U. S. Geol. Surv., Open File Rept.* 89-93.

Schechter, B. (1981). Source Parameters and Directivity of the Livermore Earthquakes of 1980 (abstract), *Earthquake Notes*, **52**, 83.

Searle, S. R. (1971). *Linear Models*, Wiley, New York, 532 pp.

Shakal, A. F., M. J. Huang, D. L. Parke, and R. W. Sherburne (1986). Processed Data from the Strong-Motions Records of the Morgan Hill Earthquake of 24 April 1984, Part 1, Ground-Response Records, Calif. Div. Mines and Geology, Office of Strong Motion Studies, Report No. OSMS 85-04.

Shakal, A. F., M. J. Huang, C. E. Ventura, D. L. Parke, T. Q. Cao, R. W. Sherburne, and R. Blazquez (1987). CSMIP Strong-Motion Records from the Whittier, California Earthquake of October 1, 1987, Calif. Div. Mines and Geology, Office of Strong Motion Studies, Report No. OSMS 87-05.

Shakal, A., M. Huang, T. Cao, R. Sherburne, R. Sydnor, P. Fung, P. Malhotra, C. Cramer, F. Su, R. Darragh, and J. Wampole (1992). CSMIP Strong-Motion Records from the Landers, California Earthquake of 28 June 1992, Calif. Div. Mines and Geology, Office of Strong Motion Studies, Report No. OSMS 92-09.

Sharpe, R. V. (1982). Tectonic Setting of the Imperial Valley Region, in the Imperial Valley, California, Earthquake of October 15, 1979, *U. S. Geol. Prof. Paper* 1254, 5-14.

Singh, S. K., E. Mena, and R. Castro (1988). Some Aspects of Source Characteristics of the 19 September 1985 Michoacan Earthquake and Ground Motion Amplification in and Near Mexico City from Strong Motion Data, *Bull. Seism. Soc. Am.* **78**, 451-477.

Singh, J. P. and M. Tabatabaie (1991). Strong Motion Data - Application to Multiple Support Structures, *Geotechnical News*, 9, No. 1, 38-41.

Somerville, P. and J. Yoshimura (1990). The Influence of Critical Moho Reflections on Strong Ground Motions Recordings in San Francisco and Oakland During the 1989 Loma Prieta Earthquake, *Geophs. Res. Lett.* **17**, 1203-1206.

Spudich, P. and E. Cranswick (1982). Use of Near-Source Seismic-Array Data to Reveal Details of the Earthquake Rupture Process, *Earthquake Notes*, **53**, 39.

Spudich, P., M. Hellweg, and W. H. K. Lee (1995). Directional Topographic Site Response at Tarzana Observed in Aftershocks of the 1994 Northridge, California, Earthquake: Implications for Main Shock Motions, submitted to *Bull. Seism. Soc. Am. Special Issue on the 1994 Northridge, California, Earthquake.*

Steidl, J. H., R. J. Archuleta, and S. Hartzell (1991). Rupture History of the 1989 Loma Prieta, California, Earthquake, *Bull. Seism. Soc. Am.* **81**, 1573-1602.

Theodulidis, N. P. and B. C. Papazachos (1992). Dependence of Strong Ground Motion on Magnitude-Distance, Site Geology and Macroseismic Intensity for Shallow Earthquakes in Greece: I, Peak Horizontal Acceleration, Velocity, and Displacement, *Soil Dynamics and Earthquake Engineering*, **11**, 387-402.

Thio, H. K. and H. Kanamori (1994). Source Complexity of the 1994 Northridge Earthquake, *Northridge abstracts program for the 89th annual meeting of SSA*, No. 7.

Trifunac, M. D. and J. N. Brune (1970). Complexity of Energy Release During the Imperial Valley, California, Earthquake of 1940, *Bull. Seism. Soc. Am.* **60**, 137-160.

United States Geological Survey (1976). Seismic Engineering Data Report, Strong-Motion Earthquake Accelerograms, Digitization and Analysis, 1971 Records, *U. S. Geol. Surv., Open File Rept.* 76-609.

Vidale, J. E. and D. V. Helmberger (1988). Elastic Finite-Difference Modeling of the 1971 San Fernando, California Earthquake, *Bull. Seism. Soc. Am.* **78**, 122-141.

Wald, D. J. (1992). Strong Ground and Broadband Teleseismic Analysis of the 1991 Sierra Madre, California, Earthquake, *J. Geophys. Res.* **97**, 11,033-11,046.

Wald, D. J. and T. H. Heaton (1994a). Spatial and Temporal Distribution of Slip for the 1992 Landers, California, Earthquake, *Bull. Seism. Soc. Am.* **84**, 668-691.

Wald, D. J. and T. H. Heaton (1994b). A Dislocation Model of the 1994 Northridge, California, Earthquake Determined from Strong Ground Motions, *U. S. Geol. Surv., Open File Rept.* 94-278.

Wald, D. J., D. V. Helmberger, and S. H. Hartzell (1990). Rupture Process of the 1987 Superstition Hills Earthquake from the Inversion of Strong-Ground Motion Data, *Bull. Seism. Soc. Am.* **80**, 1079-1098.

Wald, D. J., D. V. Helmberger, and T. H. Heaton (1991). Rupture Model of the 1989 Loma Prieta Earthquake from the Inversion of Strong-Motion and Broadband Teleseismic Data, *Bull. Seism. Soc. Am.* **81**, 1540-1572.

Wyss, M. and J. N. Brune (1967). The Alaska Earthquake of 28 March 1964: A Complex Multiple Rupture, *Bull. Seism. Soc. Am.* **57**, 1017-1023.

EARTHQUAKE ENGINEERING RESEARCH CENTER REPORT SERIES

EERC reports are available from the National Information Service for Earthquake Engineering (NISEE) and from the National Technical Information Service (NTIS). Numbers in parentheses are Accession Numbers assigned by the National Technical Information Service; these are followed by a price code. Contact NTIS, 5285 Port Royal Road, Springfield Virginia, 22161 for more information. Reports without Accession Numbers were not available from NTIS at the time of printing. For a current complete list of EERC reports (from EERC 67-1) and availablity information, please contact University of California, EERC, NISEE, 1301 South 46th Street, Richmond, California 94804-4698.

UCB/EERC-84/01 "Pseudodynamic Test Method for Seismic Performance Evaluation: Theory and Implementation," by Shing, P.-S.B. and Mahin, S.A., January 1984, (PB84 190 644)A08.

UCB/EERC-84/02 "Dynamic Response Behavior of Kiang Hong Dian Dam," by Clough, R.W., Chang, K.-T., Chen, H.-Q. and Stephen, R.M., April 1984, (PB84 209 402)A08.

UCB/EERC-84/03 "Refined Modelling of Reinforced Concrete Columns for Seismic Analysis," by Kaba, S.A. and Mahin, S.A., April 1984, (PB84 234 384)A06.

UCB/EERC-84/04 "A New Floor Response Spectrum Method for Seismic Analysis of Multiply Supported Secondary Systems," by Asfura, A. and Der Kiureghian, A., June 1984, (PB84 239 417)A06.

UCB/EERC-84/05 "Earthquake Simulation Tests and Associated Studies of a 1/5th-scale Model of a 7-Story R/C Frame-Wall Test Structure," by Bertero, V.V., Aktan, A.E., Charney, F.A. and Sause, R., June 1984, (PB84 239 409)A09.

UCB/EERC-84/06 "Unassigned," by Unassigned, 1984.

UCB/EERC-84/07 "Behavior of Interior and Exterior Flat-Plate Connections Subjected to Inelastic Load Reversals," by Zee, H.L. and Moehle, J.P., August 1984, (PB86 117 629/AS)A07.

UCB/EERC-84/08 "Experimental Study of the Seismic Behavior of a Two-Story Flat-Plate Structure," by Moehle, J.P. and Diebold, J.W., August 1984, (PB86 122 553/AS)A12.

UCB/EERC-84/09 "Phenomenological Modeling of Steel Braces under Cyclic Loading," by Ikeda, K., Mahin, S.A. and Dermitzakis, S.N., May 1984, (PB86 132 198/AS)A08.

UCB/EERC-84/10 "Earthquake Analysis and Response of Concrete Gravity Dams," by Fenves, G.L. and Chopra, A.K., August 1984, (PB85 193 902/AS)A11.

UCB/EERC-84/11 "EAGD-84: A Computer Program for Earthquake Analysis of Concrete Gravity Dams," by Fenves, G.L. and Chopra, A.K., August 1984, (PB85 193 613/AS)A05.

UCB/EERC-84/12 "A Refined Physical Theory Model for Predicting the Seismic Behavior of Braced Steel Frames," by Ikeda, K. and Mahin, S.A., July 1984, (PB85 191 450/AS)A09.

UCB/EERC-84/13 "Earthquake Engineering Research at Berkeley - 1984," by EERC, August 1984, (PB85 197 341/AS)A10.

UCB/EERC-84/14 "Moduli and Damping Factors for Dynamic Analyses of Cohesionless Soils," by Seed, H.B., Wong, R.T., Idriss, I.M. and Tokimatsu, K., September 1984, (PB85 191 468/AS)A04.

UCB/EERC-84/15 "The Influence of SPT Procedures in Soil Liquefaction Resistance Evaluations," by Seed, H.B., Tokimatsu, K., Harder, L.F. and Chung, R.M., October 1984, (PB85 191 732/AS)A04.

UCB/EERC-84/16 "Simplified Procedures for the Evaluation of Settlements in Sands Due to Earthquake Shaking," by Tokimatsu, K. and Seed, H.B., October 1984, (PB85 197 887/AS)A03.

UCB/EERC-84/17 "Evaluation of Energy Absorption Characteristics of Highway Bridges Under Seismic Conditions - Volume I (PB90 262 627)A16 and Volume II (Appendices) (PB90 262 635)A13," by Imbsen, R.A. and Penzien, J., September 1986.

UCB/EERC-84/18 "Structure-Foundation Interactions under Dynamic Loads," by Liu, W.D. and Penzien, J., November 1984, (PB87 124 889/AS)A11.

UCB/EERC-84/19 "Seismic Modelling of Deep Foundations," by Chen, C.-H. and Penzien, J., November 1984, (PB87 124 798/AS)A07.

UCB/EERC-84/20 "Dynamic Response Behavior of Quan Shui Dam," by Clough, R.W., Chang, K.-T., Chen, H.-Q., Stephen, R.M., Ghanaat, Y. and Qi, J.-H., November 1984, (PB86 115177/AS)A07.

UCB/EERC-85/01 "Simplified Methods of Analysis for Earthquake Resistant Design of Buildings," by Cruz, E.F. and Chopra, A.K., February 1985, (PB86 112299/AS)A12.

UCB/EERC-85/02 "Estimation of Seismic Wave Coherency and Rupture Velocity using the SMART 1 Strong-Motion Array Recordings," by Abrahamson, N.A., March 1985, (PB86 214 343)A07.

UCB/EERC-85/03 "Dynamic Properties of a Thirty Story Condominium Tower Building," by Stephen, R.M., Wilson, E.L. and Stander, N., April 1985, (PB86 118965/AS)A06.

UCB/EERC-85/04 "Development of Substructuring Techniques for On-Line Computer Controlled Seismic Performance Testing," by Dermitzakis, S. and Mahin, S., February 1985, (PB86 132941/AS)A08.

UCB/EERC-85/05 "A Simple Model for Reinforcing Bar Anchorages under Cyclic Excitations," by Filippou, F.C., March 1985, (PB86 112 919/AS)A05.

UCB/EERC-85/06 "Racking Behavior of Wood-framed Gypsum Panels under Dynamic Load," by Oliva, M.G., June 1985, (PB90 262 643)A04.

UCB/EERC-85/07 "Earthquake Analysis and Response of Concrete Arch Dams," by Fok, K.-L. and Chopra, A.K., June 1985, (PB86 139672/AS)A10.

UCB/EERC-85/08 "Effect of Inelastic Behavior on the Analysis and Design of Earthquake Resistant Structures," by Lin, J.P. and Mahin, S.A., June 1985, (PB86 135340/AS)A08.

UCB/EERC-85/09 "Earthquake Simulator Testing of a Base-Isolated Bridge Deck," by Kelly, J.M., Buckle, I.G. and Tsai, H.-C., January 1986, (PB87 124 152/AS)A06.

UCB/EERC-85/10 "Simplified Analysis for Earthquake Resistant Design of Concrete Gravity Dams," by Fenves, G.L. and Chopra, A.K., June 1986, (PB87 124 160/AS)A08.

UCB/EERC-85/11 "Dynamic Interaction Effects in Arch Dams," by Clough, R.W., Chang, K.-T., Chen, H.-Q. and Ghanaat, Y., October 1985, (PB86 135027/AS)A05.

UCB/EERC-85/12 "Dynamic Response of Long Valley Dam in the Mammoth Lake Earthquake Series of May 25-27, 1980," by Lai, S. and Seed, H.B., November 1985, (PB86 142304/AS)A05.

UCB/EERC-85/13 "A Methodology for Computer-Aided Design of Earthquake-Resistant Steel Structures," by Austin, M.A., Pister, K.S. and Mahin, S.A., December 1985, (PB86 159480/AS)A10 .

UCB/EERC-85/14 "Response of Tension-Leg Platforms to Vertical Seismic Excitations," by Liou, G.-S., Penzien, J. and Yeung, R.W., December 1985, (PB87 124 871/AS)A08.

UCB/EERC-85/15 "Cyclic Loading Tests of Masonry Single Piers: Volume 4 - Additional Tests with Height to Width Ratio of 1," by Sveinsson, B., McNiven, H.D. and Sucuoglu, H., December 1985, (PB87 165031/AS)A08.

UCB/EERC-85/16 "An Experimental Program for Studying the Dynamic Response of a Steel Frame with a Variety of Infill Partitions," by Yanev, B. and McNiven, H.D., December 1985, (PB90 262 676)A05.

UCB/EERC-86/01 "A Study of Seismically Resistant Eccentrically Braced Steel Frame Systems," by Kasai, K. and Popov, E.P., January 1986, (PB87 124 178/AS)A14.

UCB/EERC-86/02 "Design Problems in Soil Liquefaction," by Seed, H.B., February 1986, (PB87 124 186/AS)A03.

UCB/EERC-86/03 "Implications of Recent Earthquakes and Research on Earthquake-Resistant Design and Construction of Buildings," by Bertero, V.V., March 1986, (PB87 124 194/AS)A05.

UCB/EERC-86/04 "The Use of Load Dependent Vectors for Dynamic and Earthquake Analyses," by Leger, P., Wilson, E.L. and Clough, R.W., March 1986, (PB87 124 202/AS)A12.

UCB/EERC-86/05 "Two Beam-To-Column Web Connections," by Tsai, K.-C. and Popov, E.P., April 1986, (PB87 124 301/AS)A04.

UCB/EERC-86/06 "Determination of Penetration Resistance for Coarse-Grained Soils using the Becker Hammer Drill," by Harder, L.F. and Seed, H.B., May 1986, (PB87 124 210/AS)A07.

UCB/EERC-86/07 "A Mathematical Model for Predicting the Nonlinear Response of Unreinforced Masonry Walls to In-Plane Earthquake Excitations," by Mengi, Y. and McNiven, H.D., May 1986, (PB87 124 780/AS)A06.

UCB/EERC-86/08 "The 19 September 1985 Mexico Earthquake: Building Behavior," by Bertero, V.V., July 1986.

UCB/EERC-86/09 "EACD-3D: A Computer Program for Three-Dimensional Earthquake Analysis of Concrete Dams," by Fok, K.-L., Hall, J.F. and Chopra, A.K., July 1986, (PB87 124 228/AS)A08.

UCB/EERC-86/10 "Earthquake Simulation Tests and Associated Studies of a 0.3-Scale Model of a Six-Story Concentrically Braced Steel Structure," by Uang, C.-M. and Bertero, V.V., December 1986, (PB87 163 564/AS)A17.

UCB/EERC-86/11 "Mechanical Characteristics of Base Isolation Bearings for a Bridge Deck Model Test," by Kelly, J.M., Buckle, I.G. and Koh, C.-G., November 1987, (PB90 262 668)A04.

UCB/EERC-86/12 "Effects of Axial Load on Elastomeric Isolation Bearings," by Koh, C.-G. and Kelly, J.M., November 1987, PB88-179015(A06).

UCB/EERC-87/01 "The FPS Earthquake Resisting System: Experimental Report," by Zayas, V.A., Low, S.S. and Mahin, S.A., June 1987, (PB88 170 287)A06.

UCB/EERC-87/02 "Earthquake Simulator Tests and Associated Studies of a 0.3-Scale Model of a Six-Story Eccentrically Braced Steel Structure," by Whittaker, A., Uang, C.-M. and Bertero, V.V., July 1987, (PB88 166 707/AS)A18.

UCB/EERC-87/03 "A Displacement Control and Uplift Restraint Device for Base-Isolated Structures," by Kelly, J.M., Griffith, M.C. and Aiken, I.D., April 1987, (PB88 169 933)A04.

UCB/EERC-87/04 "Earthquake Simulator Testing of a Combined Sliding Bearing and Rubber Bearing Isolation System," by Kelly, J.M. and Chalhoub, M.S., December 1990, PB92-192962(A09).

UCB/EERC-87/05 "Three-Dimensional Inelastic Analysis of Reinforced Concrete Frame-Wall Structures," by Moazzami, S. and Bertero, V.V., May 1987, (PB88 169 586/AS)A08.

UCB/EERC-87/06 "Experiments on Eccentrically Braced Frames with Composite Floors," by Ricles, J. and Popov, E., June 1987, (PB88 173 067/AS)A14.

UCB/EERC-87/07 "Dynamic Analysis of Seismically Resistant Eccentrically Braced Frames," by Ricles, J. and Popov, E., June 1987, (PB88 173 075/AS)A16.

UCB/EERC-87/08 "Undrained Cyclic Triaxial Testing of Gravels-The Effect of Membrane Compliance," by Evans, M.D. and Seed, H.B., July 1987, (PB88 173 257)A19.

UCB/EERC-87/09 "Hybrid Solution Techniques for Generalized Pseudo-Dynamic Testing," by Thewalt, C. and Mahin, S.A., July 1987, (PB 88 179 007)A07.

UCB/EERC-87/10 "Ultimate Behavior of Butt Welded Splices in Heavy Rolled Steel Sections," by Bruneau, M., Mahin, S.A. and Popov, E.P., September 1987, (PB90 254 285)A07.

UCB/EERC-87/11 "Residual Strength of Sand from Dam Failures in the Chilean Earthquake of March 3, 1985," by De Alba, P., Seed, H.B., Retamal, E. and Seed, R.B., September 1987, (PB88 174 321/AS)A03.

UCB/EERC-87/12 "Inelastic Seismic Response of Structures with Mass or Stiffness Eccentricities in Plan," by Bruneau, M. and Mahin, S.A., September 1987, (PB90 262 650/AS)A14.

UCB/EERC-87/13 "CSTRUCT: An Interactive Computer Environment for the Design and Analysis of Earthquake Resistant Steel Structures," by Austin, M.A., Mahin, S.A. and Pister, K.S., September 1987, (PB88 173 339/AS)A06.

UCB/EERC-87/14 "Experimental Study of Reinforced Concrete Columns Subjected to Multi-Axial Loading," by Low, S.S. and Moehle, J.P., September 1987, (PB88 174 347/AS)A07.

UCB/EERC-87/15 "Relationships between Soil Conditions and Earthquake Ground Motions in Mexico City in the Earthquake of Sept. 19, 1985," by Seed, H.B., Romo, M.P., Sun, J., Jaime, A. and Lysmer, J., October 1987, (PB88 178 991)A06.

UCB/EERC-87/16 "Experimental Study of Seismic Response of R. C. Setback Buildings," by Shahrooz, B.M. and Moehle, J.P., October 1987, (PB88 176 359)A16.

UCB/EERC-87/17 "The Effect of Slabs on the Flexural Behavior of Beams," by Pantazopoulou, S.J. and Moehle, J.P., October 1987, (PB90 262 700)A07.

UCB/EERC-87/18 "Design Procedure for R-FBI Bearings," by Mostaghel, N. and Kelly, J.M., November 1987, (PB90 262 718)A04.

UCB/EERC-87/19 "Analytical Models for Predicting the Lateral Response of R C Shear Walls: Evaluation of their Reliability," by Vulcano, A. and Bertero, V.V., November 1987, (PB88 178 983)A05.

UCB/EERC-87/20 "Earthquake Response of Torsionally-Coupled Buildings," by Hejal, R. and Chopra, A.K., December 1987, PB90-208638(A15).

UCB/EERC-87/21 "Dynamic Reservoir Interaction with Monticello Dam," by Clough, R.W., Ghanaat, Y. and Qiu, X-F., December 1987, (PB88 179 023)A07.

UCB/EERC-87/22 "Strength Evaluation of Coarse-Grained Soils," by Siddiqi, F.H., Seed, R.B., Chan, C.K., Seed, H.B. and Pyke, R.M., December 1987, (PB88 179 031)A04.

UCB/EERC-88/01 "Seismic Behavior of Concentrically Braced Steel Frames," by Khatib, I., Mahin, S.A. and Pister, K.S., January 1988, (PB91 210 898/AS)A11.

UCB/EERC-88/02 "Experimental Evaluation of Seismic Isolation of Medium-Rise Structures Subject to Uplift," by Griffith, M.C., Kelly, J.M., Coveney, V.A. and Koh, C.G., January 1988, (PB91 217 950/AS)A09.

UCB/EERC-88/03 "Cyclic Behavior of Steel Double Angle Connections," by Astaneh-Asl, A. and Nader, M.N., January 1988, (PB91 210 872)A05.

UCB/EERC-88/04 "Re-evaluation of the Slide in the Lower San Fernando Dam in the Earthquake of Feb. 9, 1971," by Seed, H.B., Seed, R.B., Harder, L.F. and Jong, H.-L., April 1988, (PB91 212 456/AS)A07.

UCB/EERC-88/05 "Experimental Evaluation of Seismic Isolation of a Nine-Story Braced Steel Frame Subject to Uplift," by Griffith, M.C., Kelly, J.M. and Aiken, I.D., May 1988, (PB91 217 968/AS)A07.

UCB/EERC-88/06 "DRAIN-2DX User Guide.," by Allahabadi, R. and Powell, G.H., March 1988, (PB91 212 530)A12.

UCB/EERC-88/07 "Theoretical and Experimental Studies of Cylindrical Water Tanks in Base-Isolated Structures," by Chalhoub, M.S. and Kelly, J.M., April 1988, (PB91 217 976/AS)A05.

UCB/EERC-88/08 "Analysis of Near-Source Waves: Separation of Wave Types Using Strong Motion Array Recording," by Darragh, R.B., June 1988, (PB91 212 621)A08.

UCB/EERC-88/09 "Alternatives to Standard Mode Superposition for Analysis of Non-Classically Damped Systems," by Kusainov, A.A. and Clough, R.W., June 1988, (PB91 217 992/AS)A04.

UCB/EERC-88/10 "The Landslide at the Port of Nice on October 16, 1979," by Seed, H.B., Seed, R.B., Schlosser, F., Blondeau, F. and Juran, I., June 1988, (PB91 210 914)A05.

UCB/EERC-88/11 "Liquefaction Potential of Sand Deposits Under Low Levels of Excitation," by Carter, D.P. and Seed, H.B., August 1988, (PB91 210 880)A15.

UCB/EERC-88/12 "Nonlinear Analysis of Reinforced Concrete Frames Under Cyclic Load Reversals," by Filippou, F.C. and Issa, A., September 1988, (PB91 212 589)A07.

UCB/EERC-88/13 "Implications of Recorded Earthquake Ground Motions on Seismic Design of Building Structures," by Uang, C.-M. and Bertero, V.V., November 1988, (PB91 212 548)A06.

UCB/EERC-88/14 "An Experimental Study of the Behavior of Dual Steel Systems," by Whittaker, A.S. , Uang, C.-M. and Bertero, V.V., September 1988, (PB91 212 712)A16.

UCB/EERC-88/15 "Dynamic Moduli and Damping Ratios for Cohesive Soils," by Sun, J.I., Golesorkhi, R. and Seed, H.B., August 1988, (PB91 210 922)A04.

UCB/EERC-88/16 "Reinforced Concrete Flat Plates Under Lateral Load: An Experimental Study Including Biaxial Effects," by Pan, A. and Moehle, J.P., October 1988, (PB91 210 856)A13.

UCB/EERC-88/17 "Earthquake Engineering Research at Berkeley - 1988," by EERC, November 1988, (PB91 210 864)A10.

UCB/EERC-88/18 "Use of Energy as a Design Criterion in Earthquake-Resistant Design," by Uang, C.-M. and Bertero, V.V., November 1988, (PB91 210 906/AS)A04.

UCB/EERC-88/19 "Steel Beam-Column Joints in Seismic Moment Resisting Frames," by Tsai, K.-C. and Popov, E.P., November 1988, (PB91 217 984/AS)A20.

UCB/EERC-88/20 "Base Isolation in Japan, 1988," by Kelly, J.M., December 1988, (PB91 212 449)A05.

UCB/EERC-89/01 "Behavior of Long Links in Eccentrically Braced Frames," by Engelhardt, M.D. and Popov, E.P., January 1989, (PB92 143 056)A18.

UCB/EERC-89/02 "Earthquake Simulator Testing of Steel Plate Added Damping and Stiffness Elements," by Whittaker, A., Bertero, V.V., Alonso, J. and Thompson, C., January 1989, (PB91 229 252/AS)A10.

UCB/EERC-89/03 "Implications of Site Effects in the Mexico City Earthquake of Sept. 19, 1985 for Earthquake-Resistant Design Criteria in the San Francisco Bay Area of California," by Seed, H.B. and Sun, J.I., March 1989, (PB91 229 369/AS)A07.

UCB/EERC-89/04 "Earthquake Analysis and Response of Intake-Outlet Towers," by Goyal, A. and Chopra, A.K., July 1989, (PB91 229 286/AS)A19.

UCB/EERC-89/05 "The 1985 Chile Earthquake: An Evaluation of Structural Requirements for Bearing Wall Buildings," by Wallace, J.W. and Moehle, J.P., July 1989, (PB91 218 008/AS)A13.

UCB/EERC-89/06 "Effects of Spatial Variation of Ground Motions on Large Multiply-Supported Structures," by Hao, H., July 1989, (PB91 229 161/AS)A08.

UCB/EERC-89/07 "EADAP - Enhanced Arch Dam Analysis Program: Users's Manual," by Ghanaat, Y. and Clough, R.W., August 1989, (PB91 212 522)A06.

UCB/EERC-89/08 "Seismic Performance of Steel Moment Frames Plastically Designed by Least Squares Stress Fields," by Ohi, K. and Mahin, S.A., August 1989, (PB91 212 597)A05.

UCB/EERC-89/09 "Feasibility and Performance Studies on Improving the Earthquake Resistance of New and Existing Buildings Using the Friction Pendulum System," by Zayas, V., Low, S., Mahin, S.A. and Bozzo, L., July 1989, (PB92 143 064)A14.

UCB/EERC-89/10 "Measurement and Elimination of Membrane Compliance Effects in Undrained Triaxial Testing," by Nicholson, P.G., Seed, R.B. and Anwar, H., September 1989, (PB92 139 641/AS)A13.

UCB/EERC-89/11 "Static Tilt Behavior of Unanchored Cylindrical Tanks," by Lau, D.T. and Clough, R.W., September 1989, (PB92 143 049)A10.

UCB/EERC-89/12 "ADAP-88: A Computer Program for Nonlinear Earthquake Analysis of Concrete Arch Dams," by Fenves, G.L., Mojtahedi, S. and Reimer, R.B., September 1989, (PB92 139 674/AS)A07.

UCB/EERC-89/13 "Mechanics of Low Shape Factor Elastomeric Seismic Isolation Bearings," by Aiken, I.D., Kelly, J.M. and Tajirian, F.F., November 1989, (PB92 139 732/AS)A09.

UCB/EERC-89/14 "Preliminary Report on the Seismological and Engineering Aspects of the October 17, 1989 Santa Cruz (Loma Prieta) Earthquake," by EERC, October 1989, (PB92 139 682/AS)A04.

UCB/EERC-89/15 "Experimental Studies of a Single Story Steel Structure Tested with Fixed, Semi-Rigid and Flexible Connections," by Nader, M.N. and Astaneh-Asl, A., August 1989, (PB91 229 211/AS)A10.

UCB/EERC-89/16 "Collapse of the Cypress Street Viaduct as a Result of the Loma Prieta Earthquake," by Nims, D.K., Miranda, E., Aiken, I.D., Whittaker, A.S. and Bertero, V.V., November 1989, (PB91 217 935/AS)A05.

UCB/EERC-90/01 "Mechanics of High-Shape Factor Elastomeric Seismic Isolation Bearings," by Kelly, J.M., Aiken, I.D. and Tajirian, F.F., March 1990.

UCB/EERC-90/02 "Javid's Paradox: The Influence of Preform on the Modes of Vibrating Beams," by Kelly, J.M., Sackman, J.L. and Javid, A., May 1990, (PB91 217 943/AS)A03.

UCB/EERC-90/03 "Earthquake Simulator Testing and Analytical Studies of Two Energy-Absorbing Systems for Multistory Structures," by Aiken, I.D. and Kelly, J.M., October 1990, (PB92 192 988)A13.

UCB/EERC-90/04 "Unassigned," by Unassigned, 1990.

UCB/EERC-90/05 "Preliminary Report on the Principal Geotechnical Aspects of the October 17, 1989 Loma Prieta Earthquake," by Seed, R.B., Dickenson, S.E., Riemer, M.F., Bray, J.D., Sitar, N., Mitchell, J.K., Idriss, I.M., Kayen, R.E., Kropp, A., Harder, L.F., Jr. and Power, M.S., April 1990, (PB 192 970)A08.

UCB/EERC-90/06 "Models of Critical Regions in Reinforced Concrete Frames Under Seismic Excitations," by Zulfiqar, N. and Filippou, F.C., May 1990.

UCB/EERC-90/07 "A Unified Earthquake-Resistant Design Method for Steel Frames Using ARMA Models," by Takewaki, I., Conte, J.P., Mahin, S.A. and Pister, K.S., June 1990, PB92-192947(A06).

UCB/EERC-90/08 "Soil Conditions and Earthquake Hazard Mitigation in the Marina District of San Francisco," by Mitchell, J.K., Masood, T., Kayen, R.E. and Seed, R.B., May 1990, (PB 193 267/AS)A04.

UCB/EERC-90/09 "Influence of the Earthquake Ground Motion Process and Structural Properties on Response Characteristics of Simple Structures," by Conte, J.P., Pister, K.S. and Mahin, S.A., July 1990, (PB92 143 064)A15.

UCB/EERC-90/10 "Experimental Testing of the Resilient-Friction Base Isolation System," by Clark, P.W. and Kelly, J.M., July 1990, (PB92 143 072)A08.

UCB/EERC-90/11 "Seismic Hazard Analysis: Improved Models, Uncertainties and Sensitivities," by Araya, R. and Der Kiureghian, A., March 1988, PB92-193010(A08).

UCB/EERC-90/12 "Effects of Torsion on the Linear and Nonlinear Seismic Response of Structures," by Sedarat, H. and Bertero, V.V., September 1989, (PB92 193 002/AS)A15.

UCB/EERC-90/13 "The Effects of Tectonic Movements on Stresses and Deformations in Earth Embankments," by Bray, J. D., Seed, R. B. and Seed, H. B., September 1989, PB92-192996(A18).

UCB/EERC-90/14 "Inelastic Seismic Response of One-Story, Asymmetric-Plan Systems," by Goel, R.K. and Chopra, A.K., October 1990, (PB93 114 767)A11.

UCB/EERC-90/15 "Dynamic Crack Propagation: A Model for Near-Field Ground Motion.," by Seyyedian, H. and Kelly, J.M., 1990.

UCB/EERC-90/16 "Sensitivity of Long-Period Response Spectra to System Initial Conditions," by Blasquez, R., Ventura, C. and Kelly, J.M., 1990.

UCB/EERC-90/17 "Behavior of Peak Values and Spectral Ordinates of Near-Source Strong Ground-Motion over a Dense Array," by Niazi, M., June 1990, (PB93 114 833)A07.

UCB/EERC-90/18 "Material Characterization of Elastomers used in Earthquake Base Isolation," by Papoulia, K.D. and Kelly, J.M., 1990, PB94-190063(A08).

UCB/EERC-90/19 "Cyclic Behavior of Steel Top-and-Bottom Plate Moment Connections," by Harriott, J.D. and Astaneh-Asl, A., August 1990, (PB91 229 260/AS)A05.

UCB/EERC-90/20 "Seismic Response Evaluation of an Instrumented Six Story Steel Building," by Shen, J.-H. and Astaneh-Asl, A., December 1990, (PB91 229 294/AS)A04.

UCB/EERC-90/21 "Observations and Implications of Tests on the Cypress Street Viaduct Test Structure," by Bollo, M., Mahin, S.A., Moehle, J.P., Stephen, R.M. and Qi, X., December 1990, (PB93 114 775)A13.

UCB/EERC-91/01 "Experimental Evaluation of Nitinol for Energy Dissipation in Structures," by Nims, D.K., Sasaki, K.K. and Kelly, J.M., 1991.

UCB/EERC-91/02 "Displacement Design Approach for Reinforced Concrete Structures Subjected to Earthquakes," by Qi, X. and Moehle, J.P., January 1991, (PB93 114 569/AS)A09.

UCB/EERC-91/03 "A Long-Period Isolation System Using Low-Modulus High-Damping Isolators for Nuclear Facilities at Soft-Soil Sites," by Kelly, J.M., March 1991, (PB93 114 577/AS)A10.

UCB/EERC-91/04 "Dynamic and Failure Characteristics of Bridgestone Isolation Bearings," by Kelly, J.M., April 1991, (PB93 114 528)A05.

UCB/EERC-91/05 "Base Sliding Response of Concrete Gravity Dams to Earthquakes," by Chopra, A.K. and Zhang, L., May 1991, (PB93 114 544/AS)A05.

UCB/EERC-91/06 "Computation of Spatially Varying Ground Motion and Foundation-Rock Impedance Matrices for Seismic Analysis of Arch Dams," by Zhang, L. and Chopra, A.K., May 1991, (PB93 114 825)A07.

UCB/EERC-91/07 "Estimation of Seismic Source Processes Using Strong Motion Array Data," by Chiou, S.-J., July 1991, (PB93 114 551/AS)A08.

UCB/EERC-91/08 "A Response Spectrum Method for Multiple-Support Seismic Excitations," by Der Kiureghian, A. and Neuenhofer, A., August 1991, (PB93 114 536)A04.

UCB/EERC-91/09 "A Preliminary Study on Energy Dissipating Cladding-to-Frame Connection," by Cohen, J.M. and Powell, G.H., September 1991, (PB93 114 510)A05.

UCB/EERC-91/10 "Evaluation of Seismic Performance of a Ten-Story RC Building During the Whittier Narrows Earthquake," by Miranda, E. and Bertero, V.V., October 1991, (PB93 114 783)A06.

UCB/EERC-91/11 "Seismic Performance of an Instrumented Six-Story Steel Building," by Anderson, J.C. and Bertero, V.V., November 1991, (PB93 114 809)A07.

UCB/EERC-91/12 "Performance of Improved Ground During the Loma Prieta Earthquake," by Mitchell, J.K. and Wentz, Jr., F.J., October 1991, (PB93 114 791)A06.

UCB/EERC-91/13 "Shaking Table - Structure Interaction," by Rinawi, A.M. and Clough, R.W., October 1991, (PB93 114 917)A13.

UCB/EERC-91/14 "Cyclic Response of RC Beam-Column Knee Joints: Test and Retrofit," by Mazzoni, S., Moehle, J.P. and Thewalt, C.R., October 1991, (PB93 120 277)A03.

UCB/EERC-91/15 "Design Guidelines for Ductility and Drift Limits: Review of State-of-the-Practice and State-of-the-Art in Ductility and Drift-Based Earthquake-Resistant Design of Buildings," by Bertero, V.V., Anderson, J.C., Krawinkler, H., Miranda, E. and The CUREe and The Kajima Research Teams, July 1991, (PB93 120 269)A08.

UCB/EERC-91/16 "Evaluation of the Seismic Performance of a Thirty-Story RC Building," by Anderson, J.C., Miranda, E., Bertero, V.V. and The Kajima Project Research Team, July 1991, (PB93 114 841)A12.